Rapid Phase-contrast Magnetic Resonance Imaging Using Spiral Trajectories and Parallel Imaging

Jennifer Anne Steeden

A dissertation submitted in partial fulfillment of the requirements for the degree of
Doctor of Philosophy
of
University College London.

Department of Medical Physics and Bioengineering University College London
2011

I, Jennifer Anne Steeden confirm that the work presented in this thesis is my own. Where information has been derived from other sources, I confirm that this has been indicated in the thesis.

ABSTRACT

Phase contrast (PC) MRI is a proven method of measuring blood flow in the clinical environment. Traditionally, PCMR data is acquired using cardiac gated Cartesian sequences. However, these sequences are time consuming and difficult to perform in patients with irregular heart rates. The work of my thesis covers three alternative PC sequences, all using undersampled spiral sequences with SENSE reconstruction algorithms.

The first piece of work investigates real-time spiral PCMR. The spiral flow sequence was validated at rest by comparing stroke volumes in the aorta of healthy volunteers, against a retrospectively gated Cartesian sequence. By combining flow data with simultaneous blood pressure measurements during exercise, this sequence was used to quantify the hemodynamic response to physical stress.

The second piece of work investigates improvements in spatial or temporal resolution for real-time PCMR, by splitting the acquisition of flow-compensated and flow-encoded data into separate short blocks. The data is then retrospectively matched in cardio-respiratory space, to remove background phase offsets. This sequence was validated (at rest) in an adult population. The improved spatial resolution was shown to provide more accurate flow measurements than standard real-time flow measurements, in a paediatric population.

The third piece of work investigates prospectively triggered spiral PCMR to achieve high spatio-temporal resolution, within a short breath-hold. Flow volumes, regurgitation fraction and shunt ratios were compared from a high spatial-resolution, free breathing retrospectively gated Cartesian sequence with 3 averages (~2.5 minute scan time), a low spatial-resolution breath-hold retrospectively gated Cartesian sequence (~20 second scan time), and the (high spatial-resolution) prospectively triggered spiral sequence (~6 second scan time). It was shown that accurate flow

measurements can be made in the aorta, pulmonary artery and pulmonary branches, within manageable breath-hold times for children and sick adults. This sequence may improve patient compliance and increase patient throughput.

ACKNOWLEDGEMENTS

First and foremost I would like to thank Vivek Muthurangu for all of his help, support and advice over the last two years. His continuous enthusiasm, dedication and never-ending supply of ideas has provided great encouragement and motivation. Vivek has been especially helpful in proof-reading manuscripts and is always pushing me to do the best that I can. Without his help none of these studies would have been possible.

I would also like to thank David Atkinson for his endless support, physics knowledge and for proof-reading all of my long-winded documents. His patience and ability to teach have been greatly appreciated.

In addition I would like to thank the following people for their support and advice during my work: Michael Hansen, for all of his help in the early days; Andrew Taylor, for his continued support and proof-reading of manuscripts; Freddy Odille, for his efficiency and brilliant segmentation tool (which has saved many hours of tedious circle-drawing time); and Peter Gatehouse, for all of his help in anything MRI-related. Furthermore, I would like to thank the radiographers at ICH, who have helped with scanning during these 3 years: Wendy Norman, Rod Jones, Catherine Bull and Romina Linton.

I am also grateful to all of the volunteers and patients who have taken part in the studies described in this thesis, and to the British Heart Foundation for providing financial support towards the running of the scanner. Additional thanks must go to EPSRC for funding my PhD.

Last, but by no means least, I would like to thank Mike and my family, without whom none of this would have been possible. And of course, the Caterham for keeping Mike out of my hair whilst writing my thesis!

CONTENTS

LIST OF FIGURES

LIST OF TABLES

LIST OF ABBREVIATIONS

1D	One dimensional
2D	Two dimensional
3D	Three dimensional
4D	Four dimensional
AAO	Ascending aorta
ACL	Auto-calibration lines
ANOVA	Analysis of variance
BP	Blood pressure
bpm	Beats per minute
BW	Bandwidth
C	Compliance
CG	Conjugate gradient
CPU	Central processing unit
ECG	Electrocardiogram
EPI	Echo planar imaging
effTE	Effective echo time
FAE	Fourier acceleration encoding
FFT	Fast Fourier transform
FOV	Field-of-view
FVE	Fourier velocity encoding
GRAPPA	Generalized autocalibrating partially parallel acquisitions
GPU	Graphics processing unit
HSR	High spatial resolution
HTR	High temporal resolution
ICH	Institute of Child Health
IVC	Inferior vena cava
LPA	Left pulmonary artery

LV	Left ventricle
MIST	Montreal Imaging Stress Task
MPA	Main pulmonary artery
MRI	Magnetic resonance imaging
NFFT	Non-equispaced fast Fourier transform
NMR	Nuclear magnetic resonance
NSA	Number of signal averages
PC	Phase contrast
PCMR	Phase contrast magnetic resonance
PVR	Pulmonary vascular resistance
Q_p/Q_s	Ratio of flow in the pulmonary artery to flow in the aorta
R	Resistance
RF	Radio-frequency
ROI	Region of interest
RPA	Right pulmonary artery
RV	Right ventricle
SENSE	Sensitivity encoding
SNR	Signal-to-noise ratio
SV	Stroke volume
SVC	Superior vena cava
SVR	Systemic vascular resistance
TE	Echo time
TR	Repetition time
TSENSE	Temporal filtering combined with spatial sensitivity encoding
UCL	University College London
UI	User interface
UNFOLD	UNaliasing by Fourier-encoding the Overlaps using the temporaL Dimension
VENC	Velocity encoding
VNR	Velocity-to-noise ratio
VOI	Vessel of interest

CHAPTER 1

Principles of Magnetic Resonance Imaging

1.1 Introduction

The fundamental physical principles of nuclear magnetic resonance (NMR) were discovered independently by Felix Bloch (1) and Edward Purcell (2), in 1946. They theorized that any spinning charged particle creates an electromagnetic field.

Paul Lauterbur produced the first magnetic resonance (MR) images using the principles of NMR in 1973 (3), and Peter Mansfield developed the principles of signal localisation in 1974 (4). Since then MRI has become a common method of medical imaging, which is used clinically in a wide variety of specialties.

MRI is a non-invasive, non-ionising medical imaging modality, which;

- Allows an arbitrary selection of scan plane
- Has good penetration depth
- Can produce truly 3D images with high resolution
- Has good inherent soft tissue contrast
- Allows visualization of structures
- Allows quantification of function, e.g. flow

1.2 Nuclear Magnetic Resonance

NMR can be described in terms of quantum mechanics or more simply using a classical description.

1.2.1 Quantum Mechanics Description of NMR

Elementary particles possess an intrinsic angular momentum, $\vec{J}$, called *spin*. As a nucleus, such as a proton has an electric charge, this spinning charged particle has a magnetic moment (1, 2). The magnetic moment, $\vec{\mu}$, is related to the angular momentum, by;

$$\vec{\mu} = \gamma \vec{J} \qquad \textit{Equation 1.1}$$

where γ is a nucleus dependent, physical constant, called the *gyromagnetic ratio*. The magnitude of the spins magnetic momentum, $|\mu|$, can be calculated by;

$$|\mu| = \gamma \hbar \sqrt{I(I+1)} \qquad \textit{Equation 1.2}$$

where $\hbar$ is Planck's constant (1.055×10^{-34} Js), and I is the nuclear spin quantum number.

A commonly used constant related to the gyromagnetic ratio is $\not\gamma$, where;

$$\not\gamma = \frac{\gamma}{2\pi} \qquad \textit{Equation 1.3}$$

Values of NMR-relevant I and $\not\gamma$ are given in Table 1.1. Note: Nuclei are only NMR-active if $I \neq 0$, i.e. the nuclei must have an odd mass number, or an odd charge number.

Nucleus	Spin, *I*	Gyromagnetic ratio, γ (MHz/T)
^{1}H	1/2	42.58
^{13}C	1/2	10.71
^{19}F	1/2	40.05
^{31}P	1/2	11.26

Table 1.1: Properties of some relevant NMR-active nuclei

Due to thermal random motion there is no net-magnetic moment in the absence of an external magnetic field. However, when an external magnetic field is applied, the spins become quantized into $(2I+1)$ energy levels. These quantum levels, m_I, are;

$$m_I = -I, -I+1, \ldots, I \qquad \textit{Equation 1.4}$$

The most common nuclei used in MRI is hydrogen (^{1}H), as this has a natural abundance in the body. From Table 1.1 it can be seen that for a hydrogen nuclei; I = ½. From Equation 1.4 we can see that ^{1}H has two energy states when an external magnetic field is applied; +½ and -½. These two states are aligned in opposite directions, often referred to as *parallel* and *anti-parallel* (to the external magnetic field), or *spin-up* and *spin-down*. While the orientation of $\vec{\mu}$ is quantized along the direction of the magnetic field, the spins continue to precess randomly about the z-axis, at an angular frequency, ω_0, where;

$$\omega_0 = \gamma B_0 \qquad \textit{Equation 1.5}$$

This is the *Larmor equation*, which underpins NMR.

The energy states, E, are proportional to the strength of the external magnetic field applied, B_0, by;

$$E = -I\gamma\hbar B_0 \qquad \textit{Equation 1.6}$$

Therefore, for ^{1}H a transition between the two states represents a change in energy of;

$$\Delta E = \gamma \hbar B_0 \qquad \textit{Equation 1.7}$$

This non-zero difference in energy levels is known as *Zeeman splitting*;

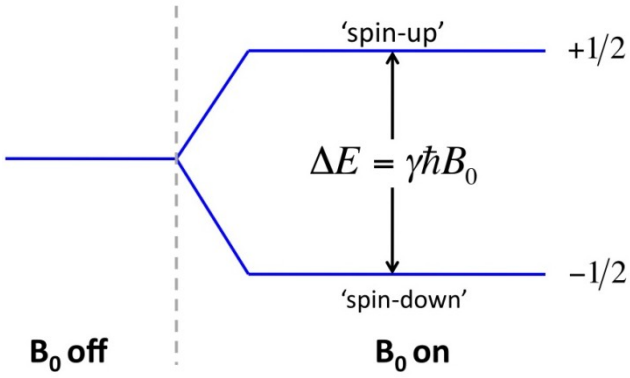

Figure 1.1: Zeeman splitting for a spin-½ system

A transition between the two energy states can be induced by absorption or emission of electromagnetic radiation of frequency, ω_0, such that;

$$\hbar\omega_0 = \Delta E = \gamma \hbar B_0 \qquad \textit{Equation 1.8}$$

This is known as the *resonance condition*.

In reality there is not just one, but are many nuclei all of which occupy a particular spin state. According to the Boltzmann relationship;

$$\frac{N_{+1/2}}{N_{-1/2}} = \exp\left(\frac{\Delta E}{kT_S}\right) \qquad \textit{Equation 1.9}$$

$$= \exp\left(\frac{\gamma \hbar B_0}{kT_S}\right) \qquad \text{(from Equation 1.7)} \qquad \textit{Equation 1.10}$$

$$\approx 1 + \frac{\gamma \hbar B_0}{kT_S} \qquad \text{(providing } kT_S >> \gamma \hbar B_0\text{)} \qquad \textit{Equation 1.11}$$

$$N_{+1/2} - N_{-1/2} \approx N_S\left(\frac{\gamma \hbar B_0}{2kT_S}\right) \qquad \textit{Equation 1.12}$$

where k is the Boltzmann constant (1.38×10^{-23} J/K), T_S is the absolute temperature of the spin system (in Kelvin), $N_{+1/2}$ is the number of spins in the higher energy state, $N_{-1/2}$ is the number of spins in the lower energy state, and N_S is the total number of spins in the spin system. From Equation 1.12 it can be seen that there are slightly more spins in the lower energy state. The resulting bulk magnetization, $\vec{M}$, can be calculated as;

$$\vec{M} = \sum_{n=1}^{N_S} \vec{\mu}_n \qquad \textit{Equation 1.13}$$

$$= \left(\sum_{n=1}^{N_S} \vec{\mu}_{x,n} \right) \vec{x} + \left(\sum_{n=1}^{N_S} \vec{\mu}_{y,n} \right) \vec{y} + \left(\sum_{n=1}^{N_S} \vec{\mu}_{z,n} \right) \vec{z} \qquad \textit{Equation 1.14}$$

Assuming B_0 is applied on the z-axis, the $\vec{x}$ and $\vec{y}$ terms are zero. This is because the projection of $\vec{\mu}_n$ onto the transverse plane has a random phase, while it precesses about $\vec{z}$. Therefore, by substituting Equation 1.2 into Equation 1.14 we get;

$$\vec{M} = \left(\sum_{n=1}^{N_{+1/2}} \frac{1}{2} \gamma \hbar - \sum_{n=1}^{N_{-1/2}} \frac{1}{2} \gamma \hbar \right) \vec{z} \qquad \textit{Equation 1.15}$$

$$= \frac{1}{2} \left(N_{+1/2} - N_{-1/2} \right) \gamma \hbar \vec{z} \qquad \textit{Equation 1.16}$$

Equation 1.16 shows that $\vec{M}$ points exactly along the positive direction of the z-axis at thermal equilibrium.

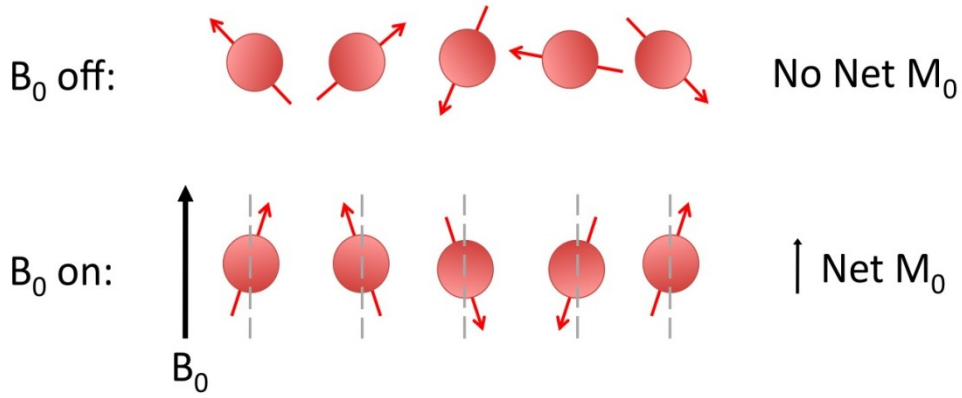

Figure 1.2: Magnetic moment vectors. Top: spins precess with random phase, bottom; spins align in direction of an external magnetic field

It is not possible to measure $\vec{M}$ when it is aligned with the main magnetic field, however each magnetic moment vector also has a microscopic transverse component. It is possible to achieve phase coherence between the spins (thereby introducing a transverse component of $\vec{M}$), by introducing an oscillating magnetic field (B_1) perpendicular to the main field. The frequency of B_1 must be such that it induces a change in the energy state of the spins (see Equation 1.5 and Equation 1.8), i.e. it must have a frequency equal to ω_0. As ω_0 is in the radio-frequency range, B_1 is often referred to as an *RF-pulse*.

Treating the behaviour of all the spins in the system in terms of the net magnetic vector, $\vec{M}$, allows us to transfer to the classical description of NMR.

1.2.2 Classical Description of NMR

When $\vec{M}$ is aligned with an external magnetic field, it continues to precess about the z-axis, at the frequency ω_0, as shown in Figure 1.3;

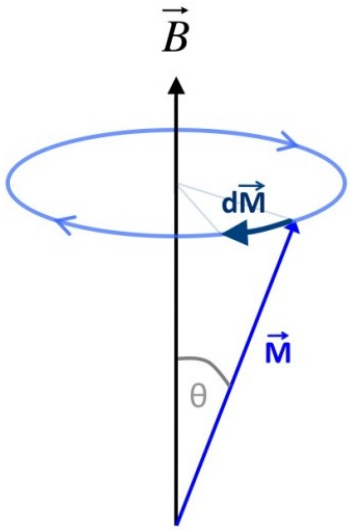

Figure 1.3: Precession of the spin-vector about a static magnetic field

This time-dependent behaviour of $\overrightarrow{M}$, in the presence of an applied magnetic field, $\vec{B}$, can be described by the Bloch equation;

$$\frac{d\overrightarrow{M}}{dt} = \gamma \overrightarrow{M} \times \vec{B} \qquad \textit{Equation 1.17}$$

When a constant field, B_0, is applied on the z-axis, $\vec{B} = B_0 \vec{z}$, Equation 1.17 can be written as the following component equations;

$$\left.\begin{aligned} \frac{dM_x}{dt} &= \gamma M_y \cdot B_0 \\ \frac{dM_y}{dt} &= -\gamma M_x \cdot B_0 \\ \frac{dM_z}{dt} &= 0 \end{aligned}\right\} \qquad \textit{Equation 1.18}$$

Where $\omega_0 = \gamma B_0$, the complete set of solutions is;

$$\left.\begin{aligned} M_x(t) &= M_x(0)\cos(\omega_0 t) + M_y(0)\sin(\omega_0 t) \\ M_y(t) &= -M_x(0)\sin(\omega_0 t) + M_y(0)\cos(\omega_0 t) \\ M_z(t) &= M_z(0) \end{aligned}\right\} \qquad \textit{Equation 1.19}$$

These equations describe the precession of $\overrightarrow{M}$ about the z-axis, at frequency ω_0, as previously shown in Figure 1.3.

1.2.2.1 Rotating Frame of Reference

In order to simplify the effect of RF-pulses and relaxation mechanisms, the *rotating frame of reference* is commonly used (denoted as x', y', and z'). This reference frame rotates about the z-axis at the Larmor frequency, ω_0. It is mathematically related to the stationary frame by;

$$\left.\begin{aligned} \vec{x}' &\equiv \vec{x}\cdot\cos(\omega t) - \vec{y}\cdot\sin(\omega t) \\ \vec{y}' &\equiv \vec{x}\cdot\sin(\omega t) + \vec{y}\cdot\cos(\omega t) \\ \vec{z}' &\equiv \vec{z} \end{aligned}\right\} \qquad \textit{Equation 1.20}$$

In this rotating frame, spins which are rotating at the Larmor frequency appear to be stationary, while those at a higher or lower frequency gain or lose phase, respectively. $\vec{M}$ can now be viewed as a static vector, $\vec{M}'$.

1.2.2.2 RF-Pulses

In the static frame of reference, a typical B_1 field takes the form;

$$\vec{B}_1(t) = 2B_1^e(t)\cos(\omega_{rf}t)\vec{x} \qquad \textit{Equation 1.21}$$

where B_1^e is the pulse envelope function. Mathematically this can be decomposed into two circularly polarized fields (perpendicular to the z-axis). Assuming the counter-clockwise rotation exerts negligible effects, Equation 1.21 can be re-written as;

$$\vec{B}_1(t) = B_1^e(t)\left[\ \vec{x}\cdot\cos(\omega_{rf}t) - \vec{y}\cdot\sin(\omega_{rf}t)\right] \qquad \textit{Equation 1.22}$$

By viewing the RF-pulse in the rotating frame of reference (see Equation 1.20), Equation 1.22 can be re-written as;

$$\vec{B}_1'(t) = B_1^e(t)\ \vec{x}' \qquad \textit{Equation 1.23}$$

Substituting Equation 1.23 into the Bloch equation (Equation 1.17), gives;

$$\left.\begin{aligned} \frac{dM_{x'}}{dt} &= 0 \\ \frac{d\,M_{y'}}{d\,t} &= \gamma\, B_1^e(t) M_{z'} \\ \frac{dM_{z'}}{dt} &= -\gamma\, B_1^e(t) M_{y'} \end{aligned}\right\} \qquad \textit{Equation 1.24}$$

For an RF-pulse under the starting conditions $M_{x'}(0) = M_{y'}(0) = 0$ and $M_{z'}(0) = M_z^0$, the bulk magnetization is therefore;

$$\left.\begin{aligned} M_{x'}(t) &= 0 \\ M_{y'}(t) &= M_z^0 \sin\left(\int_{t=0}^{\tau} \gamma\, B_1^e(t)dt\right) \\ M_{z'}(t) &= M_z^0 \cos\left(\int_{t=0}^{\tau} \gamma\, B_1^e(t)dt\right) \end{aligned}\right\} \qquad \textit{Equation 1.25}$$

where τ is the RF-pulse duration. Combining these equations with Equation 1.20 it can be seen that the bulk magnetization vector precesses (or *nutates*) about the x'-axis with angular velocity;

$$\vec{\omega}_1 = -\gamma \vec{B}_1 \qquad \textit{Equation 1.26}$$

This is called *forced precession*. As a result, the bulk magnetization vector is tipped onto the *x*-*y* plane, where it can be measured.

The flip angle (α) of an RF-pulse is defined as the angle between $\vec{M}$ and the *z*-axis immediately after the RF-pulse has terminated. From Equation 1.25 it can be seen that α depends on the magnitude of B_1 and τ, by;

$$\alpha = \int_{t=0}^{\tau} \gamma\, B_1^e(t)dt \qquad \textit{Equation 1.27}$$

1.2.2.3 Signal Detection

After $\overrightarrow{M}$ has been excited using an RF-pulse, it can be measured on the *x*-*y* plane. By placing RF-receive coils in the *x*-*y* plane, the time-varying bulk magnetization vector induces a voltage in these coils, proportional to $\overrightarrow{M}_{xy}$.

The voltage induced varies at the Larmor frequency and decays exponentially with time due to magnetization relaxation. In the absence of any additional magnetic gradients, this signal is known as the *free induction decay*.

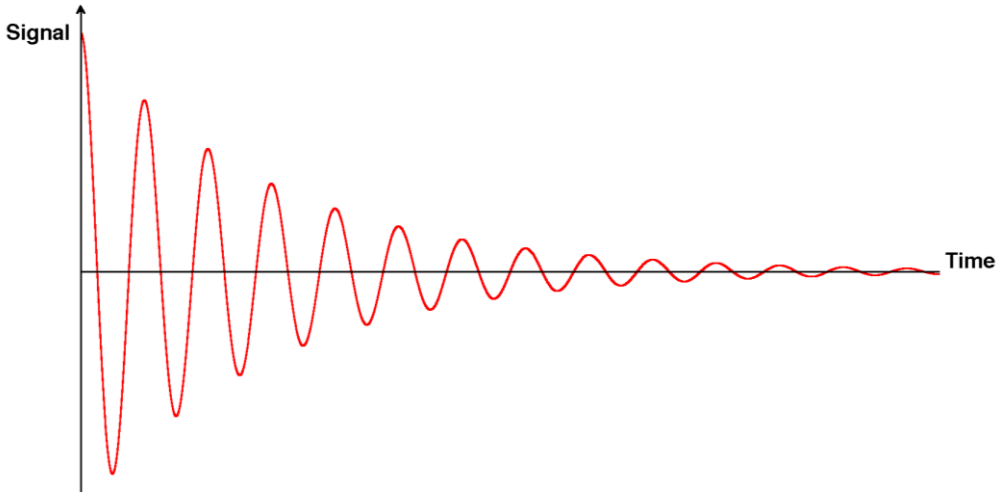

Figure 1.4: Free induction decay simulated in MATLAB

1.3 Magnetic Resonance Imaging

The signal received in MRI is the sum of the magnetization from all of the excited spins within the object (see Equation 1.13). In a static homogeneous field, after an RF-pulse, $\overrightarrow{M'}$ remains along the x'-axis – this reveals no information about the location of the individual spins.

1.3.1 Spatial Encoding

By manipulating the spatial variation of the magnetic field in a known way using gradient coils, it is possible to achieve spatial encoding of the MR signal. These gradient coils vary the magnetic field linearly across the imaging volume. By extending the Larmor equation (Equation 1.5) it can be seen that the addition of a linearly varying gradient $\overrightarrow{G_r}$ across an imaging volume has the effect of altering the precessional frequency of the spins depending on their position ($\vec{r}$);

$$\omega(\vec{r}) = \gamma\left(B_0 + \overrightarrow{G_r} \cdot \vec{r}\right) \qquad \textit{Equation 1.28}$$

This is shown in Figure 1.5.

1.3.2 K-space

The received signal (after demodulation) from an object after a single RF-excitation is now seen to be related to its 3D position;

$$S(t) = \iiint \rho(\vec{r}) \exp\left(-j\gamma \overrightarrow{G_r} \cdot \vec{r}t\right) d\vec{r} \qquad \textit{Equation 1.29}$$

where ρ is the proton density. The reciprocal space is defined, $\vec{k}$, where;

$$\vec{k}(t) = \gamma \int_0^t \overrightarrow{G}(\tau)\, d\tau \qquad \textit{Equation 1.30}$$

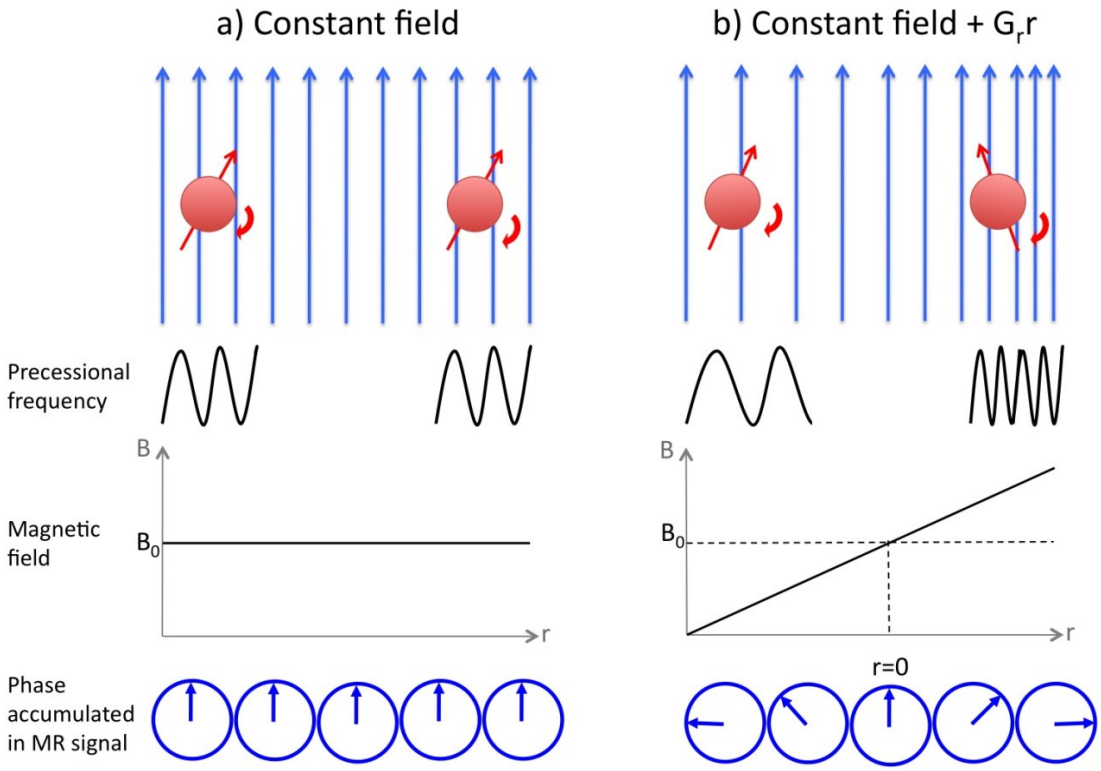

Figure 1.5: Effect of gradients on the precessional frequency of spins. a) In a constant field all of the spins precess at the same frequency – there is no difference in the phase of the MR signal. b) When a linear gradient is applied, the precessional frequency is dependent on position – the phase of the MR signal is proportional to the spins position

The Fourier relationship between the received signal and the position of the spins (the proton density) is obvious from Equation 1.29;

$$S(\vec{k}) = \iiint \rho(\vec{r}) \exp(-j2\pi \vec{k}\vec{r})\, d\vec{r} \qquad \textit{Equation 1.31}$$

$$\rho(\vec{r}) = \iiint S(\vec{k}) \exp(j2\pi \vec{k}\vec{r})\, d\vec{k} \qquad \textit{Equation 1.32}$$

The raw data is therefore collected in *k-space*, where the centre of k-space contains low spatial frequencies and at the periphery contains high spatial frequencies. To transform this raw data from k-space into image space, the inverse Fourier transform must be used. Normally the *fast Fourier transform* (FFT) is used, due to its computational efficiency.

There are some MRI techniques which sample k-space in 3D as described in Equation 1.31 and Equation 1.32, however most techniques reduce the problem to 2D by applying slice selection (see section 1.3.3), in the *z*-direction.

1.3.3 Slice Selection

In order to selectively excite spins in a single imaging plane, a linear gradient is applied simultaneously with the RF-pulse. As described in section 1.2.1 an RF-pulse only affects spins, which are precessing at the frequency of the RF-pulse. Therefore by applying a linear gradient (shown in Figure 1.6 on the *z*-axis) at the same time as the RF-pulse, only a band of spins are excited (along the *z*-axis). The slice thickness is dependent on the bandwidth of the RF-pulse and the gradient strength, as seen in Figure 1.6;

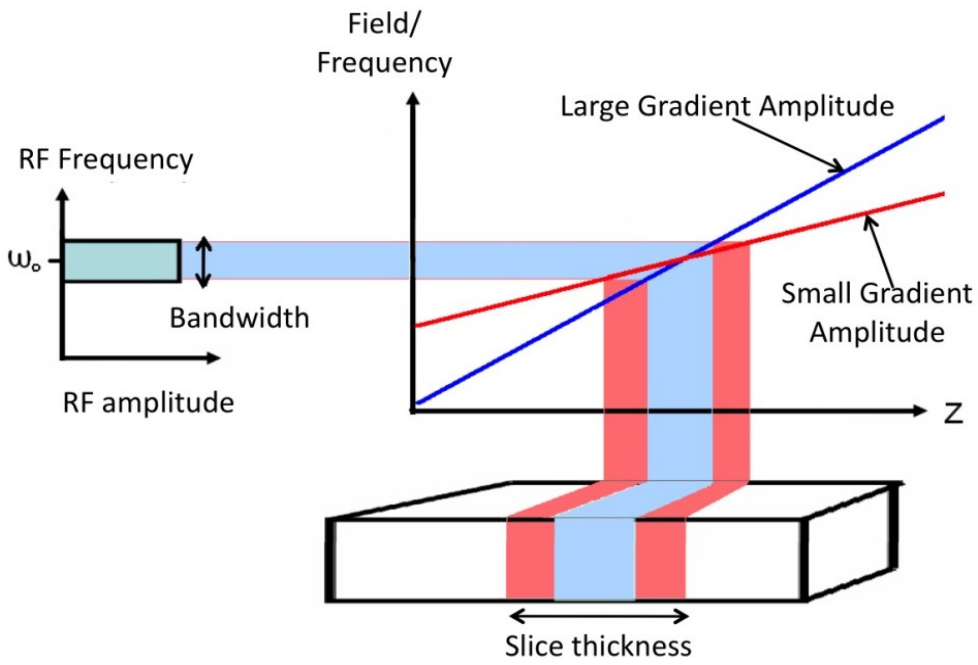

Figure 1.6: Slice selection; an RF-pulse is applied simultaneously with a linear gradient on the *z*-axis

1.3.4 Fourier Imaging

After slice selection, the problem has been reduced to just two dimensions. From Equation 1.30 it can be seen that the position in k-space is proportional to the time-integral of the gradient vector (also known as the *zeroth-order gradient moment*). This means that the (*x* and *y*) gradients that are applied, define our trajectory in (2D) k-space. In conventional Cartesian imaging, data is acquired one row at a time (see Figure 1.7). After slice selection, a *phase-encoding gradient* is first applied on the *y*-axis – this moves us up/down in k-space. A *readout gradient* is then applied on the *x*-axis to move us across k-space, while the ADC is on (i.e. data is acquired). This sequence of gradients is repeated with a different phase-encoding gradient for each row in k-space.

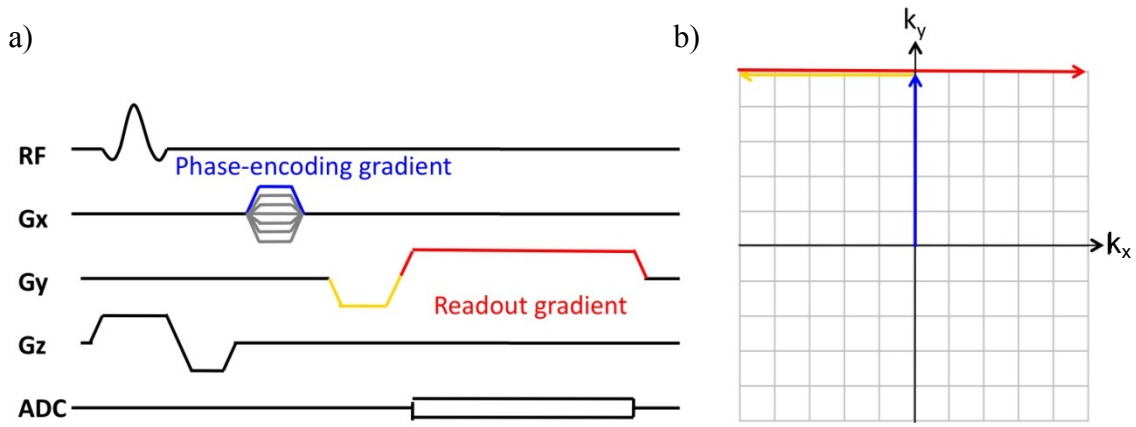

Figure 1.7: a) Sequence diagram of a basic Cartesian gradient echo sequence. b) Corresponding k-space trajectory

1.3.4.1 Frequency-Encoding

In Cartesian imaging *frequency-encoding* is often used to explain how the signal is encoded in the *x*-direction. As described in section 1.3.1, the application of the readout gradient on the *x*-axis, causes the frequency of the spins to be linearly related to their spatial location (in the *x*-direction) (see Equation 1.28).

From Equation 1.29 the signal resulting from the readout gradient (G_x) can be written as;

$$S(t) = \int_{object} \rho_0 \exp\left(-j\gamma \vec{G}_x \cdot \vec{x}\ t \right) d\vec{x} \qquad \textit{Equation 1.33}$$

1.3.4.2 Phase-Encoding

In Cartesian imaging *phase-encoding* is often used to explain how the signal is encoded in the *y*-direction. The phase-encoding gradient is applied before the readout (see Figure 1.7). Like the frequency-encoding (or readout) gradient, this causes the frequency of the spins to be linearly related to their spatial location (in the *y*-direction), while the gradient is on. When the phase-encoding gradient is turned off, spins from different *y*-positions have accumulated different phase angles. The signal during and after the phase-encoding gradient, can be written as;

$$dS(y,t) = \begin{cases} \rho(y)\exp\left(-j\gamma G_y \cdot y t \right) & 0 \le t \le T_{pe} \\ \rho(y)\exp\left(-j\gamma G_y \cdot y T_{pe} \right) & T_{pe} \le t \end{cases} \qquad \textit{Equation 1.34}$$

where T_{pe} is the total time of the phase-encoding gradient. It can be seen that the signal after the phase-encode gradient will have an initial phase (ϕ) of;

$$\phi(y) = -\gamma G_y \cdot y T_{pe} \qquad \textit{Equation 1.35}$$

1.3.4.3 General Localization

Describing frequency and phase encoding differently does not translate well to non-Cartesian imaging. In fact, frequency and phase encoding are the same.

Expanding Equation 1.31 for a 2D problem we get;

$$S(k_x,k_y)=\iint \rho(x,y)\exp\left(-j2\pi x k_x\right)\exp\left(-j2\pi y k_y\right)\,dxdy \qquad \textit{Equation 1.36}$$

Combining Equation 1.30 and Equation 1.36 we get;

$$S(k_x,k_y)=\iint \rho(x,y)\cdot\exp\left(-j\gamma x\int_0^x G_x(\tau)\,d\tau\right)\cdot\exp\left(-j\gamma y\int_0^y G_y(\tau)\,d\tau\right)\,dxdy \qquad \textit{Equation 1.37}$$

It can be seen that the rate at which the spins dephase depends on their position (in x and y) and the amplitude of the gradient waveforms (G_x and G_y) at time τ. Therefore, spins accumulate a phase over time depending on their 2D location, according to the equation;

$$\phi(x,y)=-\gamma\left(x\int_0^x G_x(\tau)\,d\tau+y\int_0^y G_y(\tau)\,d\tau\right) \qquad \textit{Equation 1.38}$$

1.3.5 Pulse Sequences

A pulse sequence is a set of defined RF and gradient pulses, which control how k-space is filled. Parameters normally used when describing pulse sequences include *echo time* (TE) and *repetition time* (TR). TE is defined as the time between the RF-pulse and the point we pass through the centre of k-space. TR is defined as the time between excitatory RF-pulses.

1.3.6 K-space Trajectories

There are many different paths that can be taken, to acquire all of the data in k-space. Collecting data in a Cartesian grid (see Figure 1.7) is popular because the gradient design is simple and the data is robust to many artefacts. Also, k-space data must be on a uniform rectilinear grid in order to use the FFT. Acquiring data in this way is very slow as only a small portion of k-space is covered after each excitation, and there are a large number of excitations (equal to the number of lines in k_y).

Methods of speeding up acquisition, while maintaining data on a Cartesian grid include the use of *echo planar imaging* (EPI), see Figure 1.8. Single shot EPI is possible where the entire k-space is filled after one excitation, or segmented EPI can be used where a part of k-space is filled after each excitation.

Non-Cartesian trajectories may offer more efficient methods of covering k-space, or non-uniform coverage of k-space. The most common non-Cartesian trajectories include radial and spiral acquisitions (see Figure 1.8);

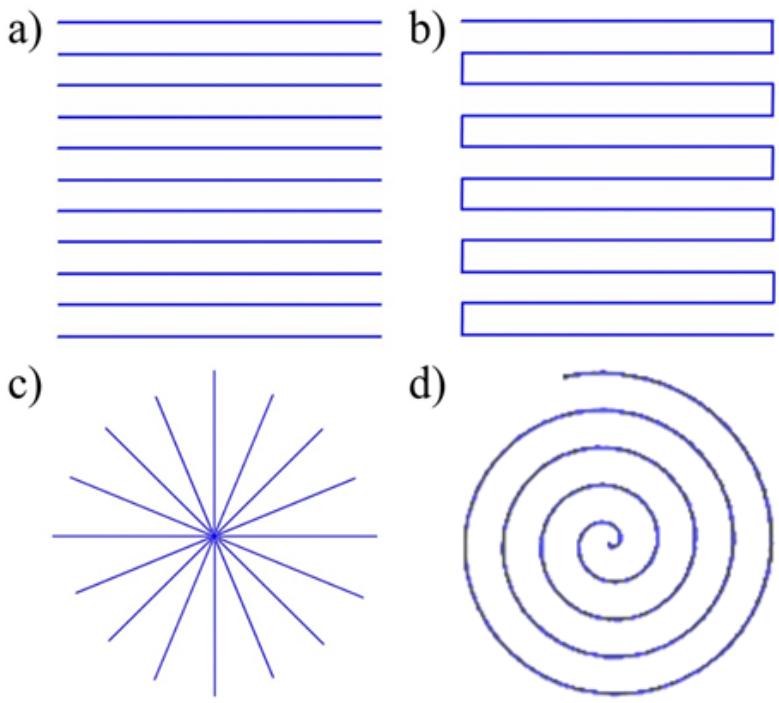

Figure 1.8: Common k-space trajectories; a) Cartesian, b) EPI, c) Radial, d) Spiral

Both radial and spiral sequences oversample the centre of k-space, which reduces their sensitivity to motion, and can be useful when using parallel imaging techniques (see section 1.4). In this work we will focus on the use of spiral trajectories, as they have desirable properties for flow imaging (see section 1.6)

1.3.7 Spiral Trajectories

Spiral trajectories (5, 6) provide a highly efficient method of traversing k-space, as a large proportion of k-space can be covered after just one excitation. As spiral trajectories start in the centre of k-space they have a very short effective TE (effTE), therefore spins have very little time to dephase due to motion, before the centre of k-space is acquired – this is especially important in flow imaging (7, 8).

To acquire data on a spiral trajectory, the required gradient waveforms are sinusoidal in shape and must be both frequency and amplitude modulated. The Archimedean spiral (where the radius is directly proportional to the amount of rotation) is a popular trajectory design, as the resulting k-space density is fairly uniform. The desired Archimedes spiral trajectory can be designed using the following formula (6);

$$\vec{k}(t) = \lambda\theta(t) \cdot \exp(j\theta(t)) \qquad \textit{Equation 1.39}$$

where $\theta(t)$ describes the azimuth angle evolution over time (in radians), and λ is a constant which describes the rate of spiral growth towards the edge of k-space.

To prevent aliasing, the distance between two spiral arms (Δk) should not be greater than the Nyquist sampling ratio;

$$\Delta k = \frac{1}{FOV} = \lambda 2\pi \qquad \textit{Equation 1.40}$$

$$\lambda = \frac{N_{\text{int}}}{2\pi \cdot FOV} \qquad \textit{Equation 1.41}$$

where N_{int} is the total number of desired interleaves. A spiral trajectory that has multiple interleaves uses the same trajectory for each interleave, however each interleave is rotated by a multiple of $2\pi/N_{\text{int}}$ radians.

To ensure we reach the edge of k-space, the final value of θ must equal to;

$$\theta_{final} = \frac{k_{\max}}{\lambda} = \frac{1}{2\Delta\, x \cdot \lambda} \qquad \textit{Equation 1.42}$$

It is possible to design spiral trajectories with constant angular velocity, or with constant linear velocity, however the gradient amplitude is not great enough to fulfil either of these trajectories. To achieve the most efficient spiral trajectory the gradients must be limited by the slew rate at the start of the readout, however once the maximum gradient amplitude has been reached, this then limits the gradient waveforms (as seen in Figure 1.9).

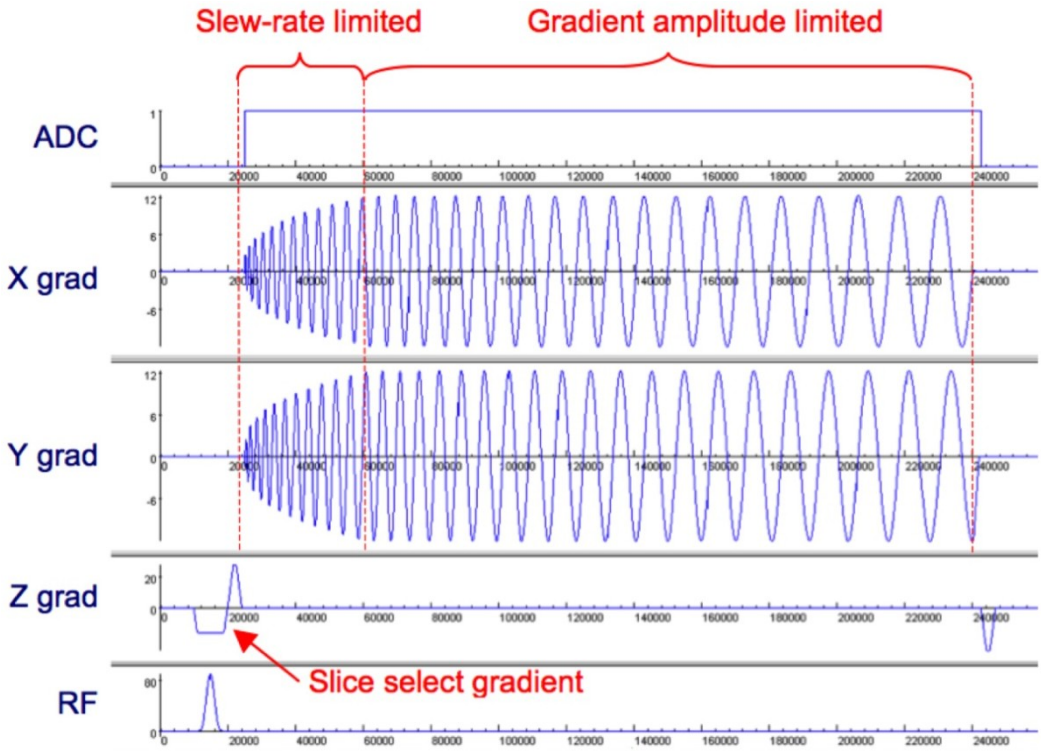

Figure 1.9: Example of an efficient spiral trajectory. The gradients are slew-rate limited in the centre of k-space, and gradient amplitude limited at the edge of k-space

Equation 1.39 can be solved by differentiation (6, 9). There are many ways to optimise the spirals. One solution can be realized by (5, 6, 10);

$$\theta(t) = \frac{t}{\sqrt{\alpha + (1-\alpha)t}} \qquad \textit{Equation 1.43}$$

where α is used to tune the spiral between constant angular velocity (when α = 1, $\theta \propto t$) and constant linear velocity (when α = *0*, $\theta \propto \sqrt{t}$). Unfortunately it is difficult to optimise α so that the resulting trajectories cover k-space as efficiently as possible (10). A more efficient solution is obtained by solving for the gradient amplitude and slew rate given the hardware limitations (6, 9). Unfortunately there is no analytical solution to these equations making them computationally expensive, as they must be solved iteratively. This is discussed further in section 2.3.1.1.

1.3.8 Gridding

K-space data that is acquired using non-Cartesian trajectories (or non-uniform trajectories), requires the data to be re-sampled onto a uniform rectangular grid before reconstruction using the FFT. It is possible to perform nearest neighbour interpolation or bilinear interpolation of the data onto a Cartesian grid, however this is prone to artefacts. Alternatively, *gridding* can be used (11, 12).

Gridding uses a window function, $\hat{C}$, which is convolved with the measured data, $\hat{M}$, and sampled onto a unit-spaced grid;

$$\hat{G} = \left(\hat{C} * \hat{M}\right) \cdot III \qquad \textit{Equation 1.44}$$

where the 2D comb function, *III*, is defined as;

$$^{2}III(x,y) = \sum_{i}\sum_{j}\delta(x-i, y-j) \qquad \textit{Equation 1.45}$$

The ideal window function (or *convolution kernel*) is a *sinc* kernel, however as this is an infinite function the computation is impractical. The choice of kernel is a trade-off between processing time and interpolation accuracy (13). In MRI a *Kaiser-Bessel* kernel is commonly used (typical width: 3-5 grid points) (13, 14), as it has minimal residual aliasing and allows a relatively short computation time. It also has an analytic expression for its properties in the Fourier domain. The Kaiser-Bessel kernel is defined as (13);

$$C(u) = \frac{1}{w} I_0\left[\beta\sqrt{1-(2u/w)^2}\right] \qquad \textit{Equation 1.46}$$

$$c(x) = \frac{\sinh\sqrt{\pi^2 w^2 x^2 - \beta^2}}{\sqrt{\pi^2 w^2 x^2 - \beta^2}} \qquad \textit{Equation 1.47}$$

where $C(u) \overset{FT}{\Leftrightarrow} c(x)$, w is the window width, $I_0[\ ]$ is the modified Bessel function, and β is a constant that determines the shape of the window. After gridding has been performed, the data can be transformed into image space using a 2D inverse FFT. It is necessary to divide the resultant image by the Fourier transform of the convolution kernel, to remove the apodization caused by the convolution.

For non-uniform sampling patterns it is also necessary to perform density correction to account for undersampling/oversampling. This correction is performed by multiplying the data by a set of weights (an area density function), prior to convolution with the widow function. For a spiral trajectory these weights (W) can be numerically estimated (7) as;

$$W(t) = \left| \vec{G}(t) \right| \cdot \left| \left[\sin\left(\arg\left(\vec{G}(t)\right)\right) - \sin\left(\arg\left(\vec{k}(t)\right)\right) \right] \right| \qquad \textit{Equation 1.48}$$

1.4 Parallel Imaging

It is possible to speed up MR acquisition by undersampling the data. In Cartesian imaging this is normally achieved by missing out entire lines in k-space (in the phase-encode direction) as seen in Figure 1.10;

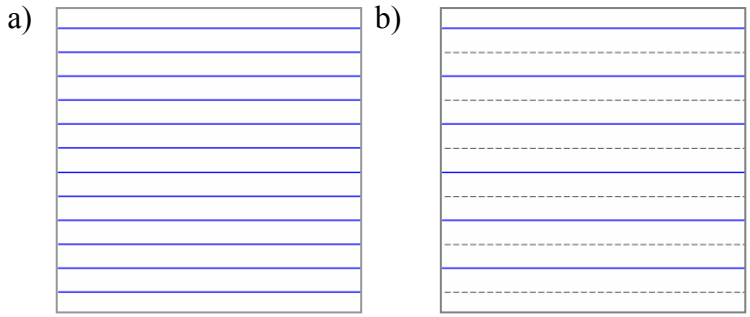

Figure 1.10: Undersampling of Cartesian k-space data a) Fully sampled data, b) corresponding 2-fold undersampled data

The increase in distance between the k-space lines causes an effective decrease in the FOV, as;

$$\Delta k = \frac{1}{FOV} \qquad \textit{Equation 1.49}$$

This causes aliasing to occur in the reconstructed images, as replicas of the subject appear along the phase-encode direction, spaced at FOV/acceleration factor, as seen in Figure 1.11;

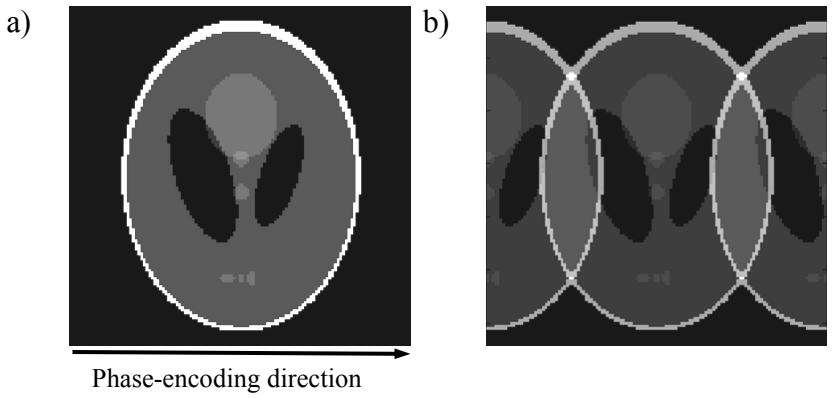

Figure 1.11: Simulated effect of Cartesian undersampling, performed in MATLAB. a) Fully-sampled, b) 2-fold acceleration

Parallel-imaging, so called because data is acquired simultaneously (i.e. in parallel) using multiple coils, can be used to remove aliasing from undersampled data. Parallel-imaging uses the spatial dependence of the individual coils (the *coil sensitivities*) to imply information about origin of the signal, and unwrap the aliasing.

There are many different parallel-imaging algorithms, however they can be divided into two main categories;

- Those that unwrap the data in the image domain
- Those that unwrap the data in the Fourier domain

Parallel-imaging algorithms that unwrap data in image space include;

- SENSE (sensitivity encoding) (15)
- K-t SENSE (16)
- TSENSE (temporal filtering combined with spatial sensitivity encoding) (17)

Parallel-imaging algorithms that unwrap data in k-space include;

- SMASH (Simultaneous acquisition of spatial harmonics) (18)
- GRAPPA (Generalized autocalibrating partially parallel acquisitions) (19)
- K-t GRAPPA (20)

In this work we will focus on the use of SENSE.

1.4.1 Coil Sensitivities

To measure the coil sensitivities low resolution, full FOV images are required from each of the coils, and from a homogeneous coil (15). The complex coil sensitivity, C_γ of the γ^{th} coil, is calculated by dividing the low resolution, full FOV complex image from the γ^{th} coil (I_γ), by the low resolution, full FOV complex image from the homogeneous coil (I_H);

$$C_\gamma = I_\gamma / I_H \qquad \textit{Equation 1.50}$$

The homogeneous image, I_H, may be acquired using the body coil. Alternatively, an estimated homogeneous image can be formed from the complex sum-of-squares of all coil images;

$$I_H(x,y) = \sqrt{\sum_{\gamma=1}^{n_c} I_{\gamma(x,y)} I^*_{\gamma(x,y)}} \qquad \textit{Equation 1.51}$$

The low-resolution images necessary to calculate the coil sensitivities may be acquired in a separate scan, however this requires additional scan time and is prone to errors if the subject moves between the scans.

Alternatively, the coil sensitivities can be calculated from the acquired data itself. This can be achieved in many different ways, as reviewed in (21). Commonly self-calibrated SENSE is used, where variable density k-space data is acquired (22-24). A small number of fully sampled lines in the centre of k-space are used to produce low-resolution reference images. However, the need for additional scan lines decreases the temporal resolution or increases the scan time.

Another approach is TSENSE (17) which uses the UNFOLD method (25) to provide temporal filtering. The UNFOLD technique interleaves the k-space lines in sequential images. The images reconstructed from any single frame contain aliasing, however the aliased component is shifted between frames. This means that the aliasing can be removed by temporal low-pass filtering of the data.

Using the sum-of-squares method to calculate the homogeneous coil (see Equation 1.51), TSENSE allows all coil sensitivity information to be calculated without any additional scans, or additional scan lines. In order to ensure high signal-to-noise coil sensitivity information, the un-aliased images may be averaged over multiple measurements as is performed in k-t SENSE (16).

1.4.2 SENSE

SENSE (15) uses a linear encoding matrix, E, to describe the transformation from the ideal image ρ (matrix size: $n_m \times n_m$) to the acquired aliased values from each coil, S_γ (number of samples: n_k);

$$S_\gamma = E_\gamma \rho \qquad \textit{Equation 1.52}$$

In Cartesian SENSE, E includes the inverse FFT at the k-space positions used to acquire the data (this defines the aliasing), and the coil sensitivity information. E (size: $n_c n_k \times n_m^2$) can be written as;

$$E_{(\gamma,k),\rho} = C_\gamma\left(r_\rho\right)\exp\left(j2\pi K_k r_\rho\right) \qquad \textit{Equation 1.53}$$

where r_ρ denotes the position of the ρ^{th} voxel and K_k, is the k^{th} sampling position in k-space.

The reconstruction of ρ is performed using a linear reconstruction matrix, F, where;

$$\rho = \sum_\gamma S_\gamma F_\gamma \qquad \textit{Equation 1.54}$$

F (size: $n_m^2 \times n_c n_k$) is estimated under a *weak voxel criterion*, which approximates the shape of the voxel function by the unit impulse function. This gives;

$$FE = Id \qquad \textit{Equation 1.55}$$

where Id denotes an identity matrix (size: $n_m \times n_m$). F is therefore, often over-determined ($n_c n_k - n_m^2$ remaining degrees of freedom). The least squares method is used to chose the solution with minimum errors in every equation, by;

$$F = \left(E^H E\right)^{-1} E^H \qquad \textit{Equation 1.56}$$

where E^H is the complex conjugate transpose of E.

By combining Equation 1.54 and Equation 1.56, we get the least-squares SENSE algorithm;

$$\rho = \left(E^H E\right)^{-1} E^H S \qquad \textit{Equation 1.57}$$

In this work we have omitted the noise matrix to simplify the reconstruction. This results in an SNR penalty, however the unfolding is still ensured (15).

1.4.2.1 Cartesian SENSE

SENSE reconstruction of an accelerated Cartesian data set, can be efficiently performed by direct unfolding of the aliased images in the image domain, as seen in Figure 1.12. The formula derived in Figure 1.12, is a simplified version of Equation 1.57, where the reconstruction matrix (*E*) is just the inverse of the coil sensitivity data.

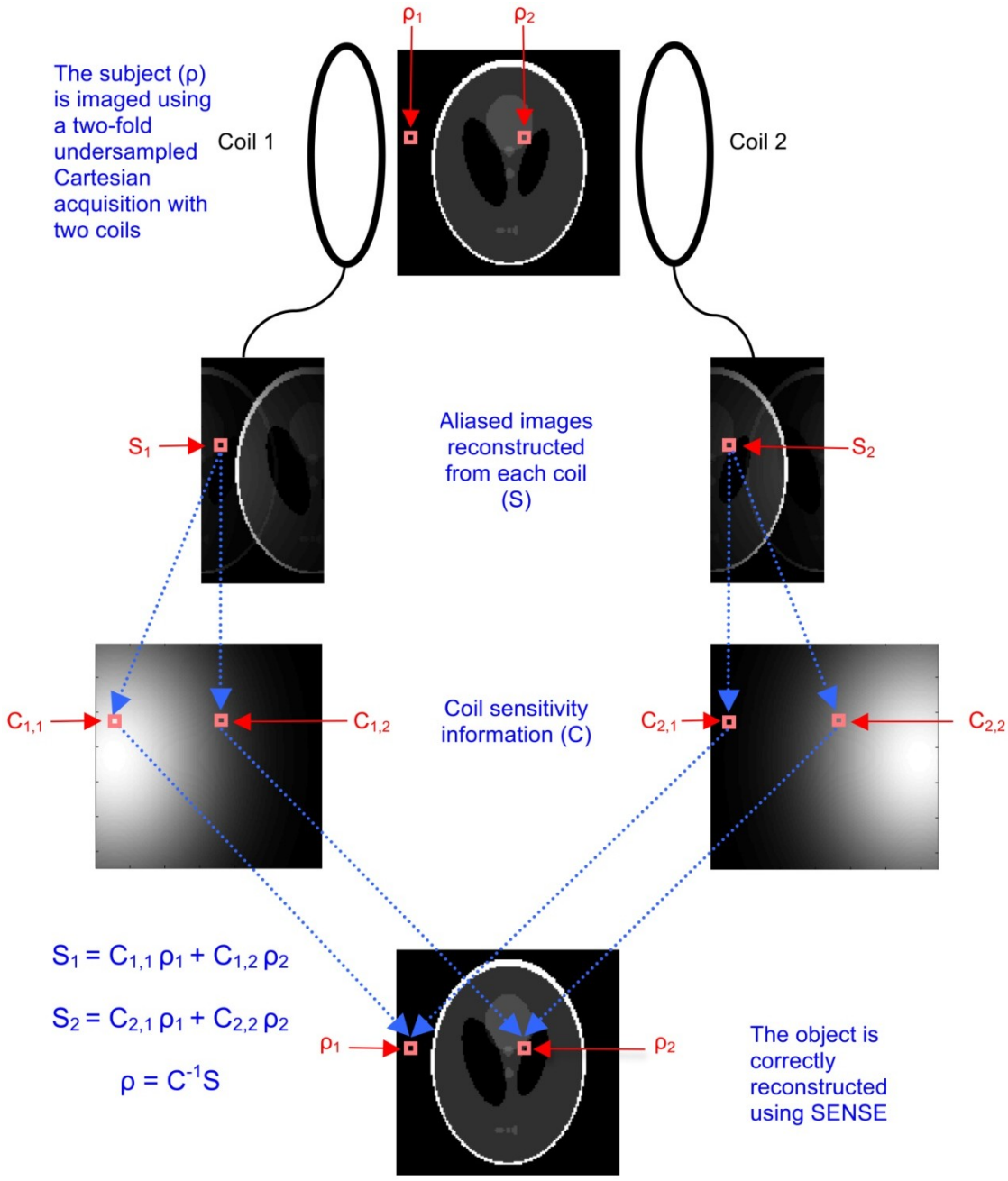

Figure 1.12: Basic Cartesian SENSE by direct unfolding. Simulation made in MATLAB

1.4.2.2 Non-Cartesian SENSE

It is also possible to perform parallel-imaging for data acquired using non-Cartesian trajectories. For example, in an interleaved spiral sequence it is possible to miss out entire spiral readouts, as seen in Figure 1.13.

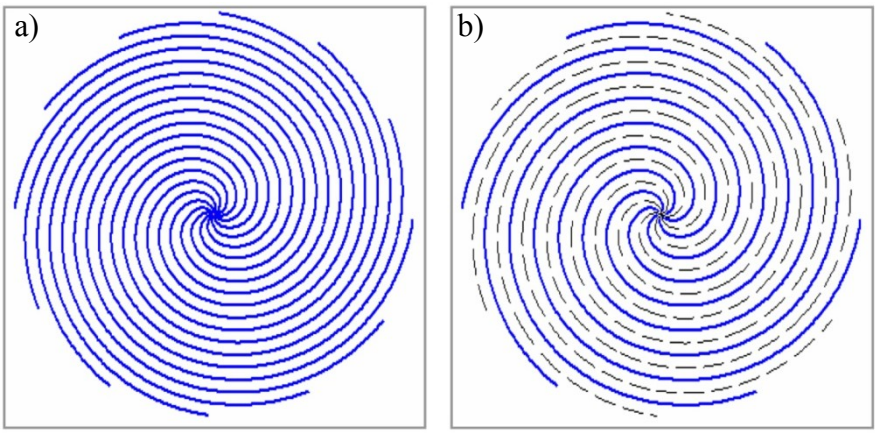

Figure 1.13: Undersampling of spiral k-space data a) Fully sampled data, b) corresponding 2-fold undersampled spiral data

However, undersampled spiral data causes aliasing in the form of streaks and swirls that are not related to the anatomical region that generated the aliasing;

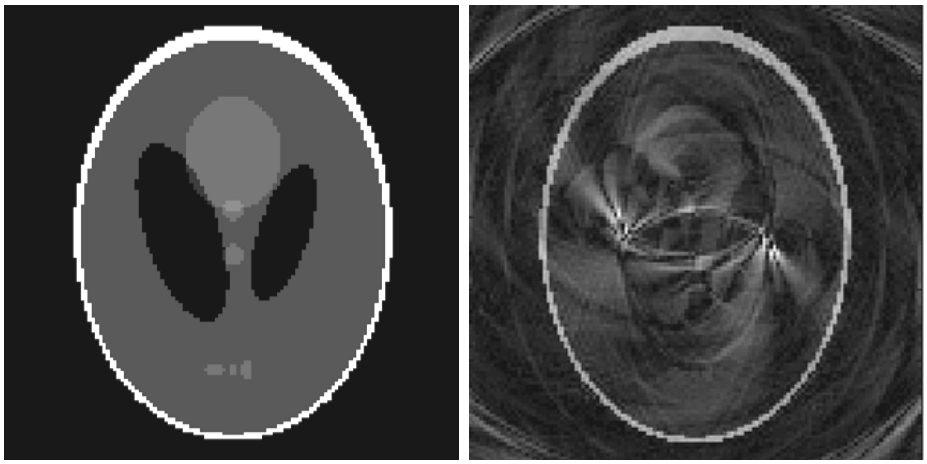

Figure 1.14: Simulated effect of spiral undersampling, performed in MATLAB. a) Fully sampled with 12 spiral interleaves, b) corresponding 2-fold undersampled data

This makes direct unfolding of the data, as seen in Figure 1.12, impossible. Solving Equation 1.57 is numerically challenging as the matrices are very large. A more efficient solution is to solve Equation 1.57 iteratively (14). Typically, the conjugate-gradient (CG) method is used, which solves linear systems in the form;

$$Ax = b \qquad \textit{Equation 1.58}$$

where x is an unknown vector, and A is a coefficient matrix. The CG converges safely given that A is square, symmetric and positive-definite.

The CG is an iterative method, which can be summarized (14, 26, 27) as;

$$
\begin{aligned}
& d_{(0)} = r_{(0)} = b - Ax_{(0)} \\
& \textit{for (i = 0, 1, 2...)} \\
& \quad \alpha_{(i)} = \frac{r_{(i)}^T r_{(i)}}{r_{(i)}^T r_{(i)}} && \textit{\{compute step length\}} \\
& \quad x_{(i+1)} = x_{(i)} + \alpha_{(i)} d_{(i)} && \textit{\{update solution\}} \\
& \quad r_{(i+1)} = r_{(i)} - \alpha_{(i)} A d_{(i)} && \textit{\{compute new residual\}} \\
& \quad \beta_{(i+1)} = \frac{r_{(i+1)}^T r_{(i+1)}}{r_{(i)}^T r_{(i)}} \\
& \quad d_{(i+1)} = r_{(i+1)} + \beta_{(i+1)} d_{(i)} && \textit{\{compute new search direction\}} \\
& \textit{end}
\end{aligned}
\qquad \textit{Equation 1.59}
$$

where i is the iteration number, d is the search direction, r is the residual (how far we are away from the correct b, which also indicates the direction of steepest descent), α is a scalar determining the step length and β is the Gram-Schmidt orthogonal basis. The initial guess at the solution, $x_{(0)}$, is commonly a matrix of zeros (size: $n_m \times n_m$).

Each iteration of the conjugate gradient results in a refined approximation of x to the exact solution. A convergence check is often performed to limit the time taken for the iterative process. This convergence check is based on the value of α. When the required accuracy (ε) is reached ($\alpha < \varepsilon$), or the number of iterations exceeds a predefined maximum number of iterations, then the current estimate is used.

From Equation 1.57 and Equation 1.58, for the CG SENSE algorithm;

$$A = E^H E \qquad \textit{Equation 1.60}$$

$$x = \rho \qquad \textit{Equation 1.61}$$

$$b = E^H S \qquad \textit{Equation 1.62}$$

In non-Cartesian SENSE, the encoding matrix, E, consists of;

- Multiplication with the coil sensitivities
- Deapodization; division by the Fourier transform of the gridding kernel (see section 0)
- Transformation to k-space using the inverse FFT
- Back-gridding of the data onto the experimental k-space trajectory, by convolution with a gridding kernel

The conjugate of the encoding matrix, E^H, therefore consists of;

- Multiplication by weights, W, to perform density correction (see section 0)
- Gridding onto a Cartesian grid, using convolution with a gridding kernel (see section 0)
- Transformation into the image domain using the FFT
- Deapodization; division by the Fourier transform of the gridding kernel (see section 0)
- Multiplication by the complex conjugate of the coil sensitivities

The implementation of the iterative CG SENSE algorithm is shown in Figure 1.15.

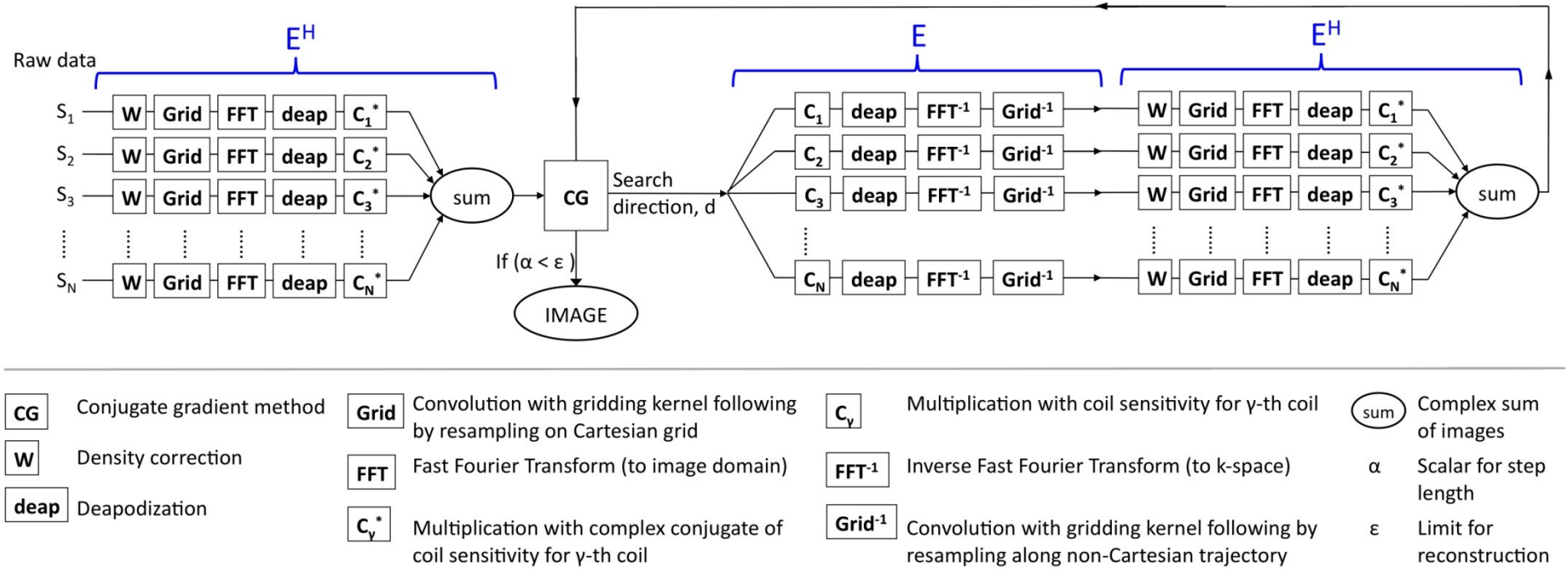

Figure 1.15: Implementation of iterative CG image reconstruction

1.4.2.3 Regularization

The image reconstruction problem often becomes ill-conditioned (28) due to high acceleration factors and/or sub-optimal geometry of the coils, which leads to amplification of noise. It is possible to improve the conditioning of the problem with the use of regularization, which constrains the solution based on some prior knowledge (29). From Equation 1.52 it can be seen that we desire a solution that satisfies;

$$\min\left\|E\rho - S\right\|_2 \qquad \textit{Equation 1.63}$$

where $\left\|\bullet\right\|_2$ is the L2-norm. By adding a constraint, we can look for a solution that satisfies (30);

$$\rho_\lambda = \arg\ \min_\rho \left\{ \ \left\|E\rho - S\right\|_2 + \lambda\left\|L\left(\rho - \rho_0\right)\right\|_2 \ \right\} \qquad \textit{Equation 1.64}$$

where λ controls the trade-off between data consistency and regularization, L is a linear transform (chosen to reduce the sensitivity to noise), and ρ_0 is a prior estimate of the solution. This is called *Tikhonov regularization* (29, 30).

The simplest form of Tikhonov regularization is called *zeroth-order regularization*, where L is an identity matrix (30-32). However, the optimal choice of L is a diagonal matrix, with the inverse of the expected signal along the diagonal;

$$L^H L = \theta^{-1} \qquad \textit{Equation 1.65}$$

where θ is the signal covariance matrix (33, 34).

Equation 1.64 can be re-written as;

$$\left.\begin{aligned} E\left(\rho - \rho_0\right) &= S - E\rho_0 \\ \lambda L\left(\rho - \rho_0\right) &= 0 \end{aligned}\right\} \qquad \textit{Equation 1.66}$$

Writing Equation 1.66 in stacked form we get;

$$\widetilde{E}\widetilde{\rho} = \widetilde{S} \qquad \textit{Equation 1.67}$$

where;

$$\left.\begin{aligned} \widetilde{E} &= \begin{bmatrix} E \\ \lambda L \end{bmatrix} \\ \widetilde{\rho} &= \rho - \rho_0 \\ \widetilde{S} &= \begin{bmatrix} S - E\rho_0 \\ 0 \end{bmatrix} \end{aligned}\right\} \qquad \textit{Equation 1.68}$$

Equation 1.67 can be solved using the least squares algorithm, in a similar fashion to Equation 1.57;

$$\widetilde{\rho} = \left(\widetilde{E}^H \widetilde{E}\right)^{-1} \widetilde{E}^H \widetilde{S} \qquad \textit{Equation 1.69}$$

Substituting Equation 1.68 into Equation 1.69 we get;

$$\widetilde{\rho} = \left(E^H E + \lambda^2 L^H L\right)^{-1} E^H \left(S - E\rho_0\right) \qquad \textit{Equation 1.70}$$

$$\rho = \rho_0 + \left(E^H E + \lambda^2 L^H L\right)^{-1} E^H \left(S - E\rho_0\right) \qquad \textit{Equation 1.71}$$

1.4.2.4 Preconditioning

In addition to regularization, it is possible to incorporate preconditioning into the iterative SENSE algorithm (35). Preconditioning aims to make Equation 1.62 closer to the desired solution, therefore reducing the number of iterations in the CG. The addition of a diagonal preconditioning matrix (*D*), to Equation 1.70 gives;

$$D^{-1}\widetilde{\rho} = D\left(E^H E D + \lambda^2 L^H L D\right)^{-1} D E^H \left(S - E\rho_0\right) \qquad \textit{Equation 1.72}$$

D can be calculated from the coil sensitivity information, and the regularization information (35) by;

$$D_{(x,y)} = \sqrt{\frac{1}{N_{ft}\sum_{\gamma=1}^{N_c} C_{\gamma,xy} C^*_{\gamma,xy} + diag\left(\lambda^2 L^H L\right)_{xy}}} \qquad \textit{Equation 1.73}$$

where N_{ft} is the number of elements in the final image.

The final CG algorithm with regularization and preconditioning, can be written as;

$$D_{(x,y)} = \sqrt{\frac{1}{N_{ft}\sum_{\gamma=1}^{N_c} C_{\gamma,xy} C^*_{\gamma,xy} + diag\left(\lambda^2 \theta^{-1}\right)_{xy}}} \qquad \textit{\{from Equation 1.73 \& Equation 1.65\}}$$

$$d_{(0)} = r_{(0)} = D\left(E^H\left(S - E\rho_{(0)}\right)\right)$$

for (i = 0, 1, 2...)

$$q_{(i)} = D\left(E^H E D d_{(i)} + \lambda^2 \theta^{-1} D d_{(i)}\right)$$

$$\alpha_{(i)} = \frac{r^T_{(i)} r_{(i)}}{d^T_{(i)} q_{(i)}}$$

$$\widetilde{\rho}_{(i+1)} = \widetilde{\rho}_{(i)} + \alpha_{(i)} d_{(i)}$$

$$r_{(i+1)} = r_{(i)} - q_{(i)}$$

$$\beta_{(i+1)} = \frac{r^T_{(i+1)} r_{(i+1)}}{r^T_{(i)} r_{(i)}}$$

$$d_{(i+1)} = r_{(i+1)} + \beta_{(i+1)} d_{(i)}$$

end

$$\rho = D\widetilde{\rho}_{final} + \rho_0$$

Equation 1.74

1.5 Cardiac Imaging

MRI is an inherently slow imaging methodology, hence it can take seconds to acquire a single two-dimensional image. This makes MR data susceptible to artefacts caused by cardiac and respiratory motion (36). These artefacts must be minimized to obtain images of diagnostic quality

1.5.1 Respiratory Motion

There are three main techniques to reduce respiratory artefacts;

- Multiple signal averages
- Breath-hold imaging
- Respiratory gating

The simplest way to minimize respiratory artefacts is to increase the *number of signal averages* (NSA's). This technique reinforces the signal intensity in static anatomy, however reduces the signal intensity of ghosts caused by the moving anatomy. To achieve good artefact reduction the number of NSA's is often set to 3 (or greater), giving a three-fold increase in total scan time.

If the total imaging time is short (< 25 seconds), it may be possible to perform the scan within a single breath-hold. For certain applications it is also possible to split the acquisition into multiple breath-holds (e.g. for multiple slices), however the breath-hold positions may vary, resulting in inconsistent data. Additionally, many children and sick adults are unable to complete long breath-holds.

Respiratory gating uses navigator information (from respiratory bellows or from a respiratory navigator signal) to only acquire data when the subject is in the same respiratory position. The success of this technique is dependent on the regularity of the patient's respiratory pattern. Generally respiratory gating also results a three-fold increase in total scan time (37).

1.5.2 Cardiac Motion

Cardiac motion is normally compensated by the use of cardiac gating. Normally an electrocardiogram (ECG) signal is used to synchronize the acquisition of data with the cardiac motion. This enables multiple phases of the cardiac cycle to be sampled. There are two main types of cardiac gating;

- Prospective gating
- Retrospective gating

In prospective gating the R-wave of the ECG signal is used to trigger the start of the data acquisition, over multiple heart-beats. Within each RR-interval there is an operator-selected trigger-delay, an acquisition window, and a trigger-window, as shown in Figure 1.16;

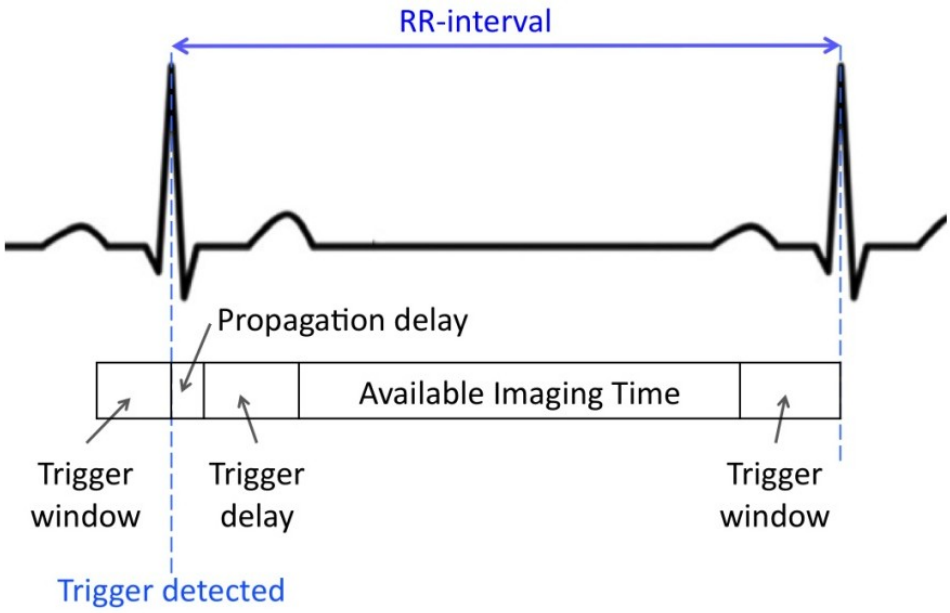

Figure 1.16: Prospective Cardiac gating; the RR-interval is divided into sub-sections

The trigger-window is the time after the data acquisition, when the pulse sequence is waiting for a valid trigger. This is necessary to account for heart rate variability. Once an R-wave is detected the trigger-window closes. A subsequent trigger-delay may be selected by the user to restrict acquisition of data to diastole, however this may be set to zero to maximize acquisition efficiency. In the remainder of the RR-interval, the pulse sequence is played out. Prospectively gated sequences always exclude late diastole, because of the need for a trigger-window.

In retrospective gating, data is continuously acquired over multiple heart-beats, and stored with the simultaneous ECG data. As the MRI data is sampled at arbitrary points in the cardiac cycle, post-processing is required to retrospectively interpolate the data to pre-determined, fixed points in the cardiac cycle. The benefit of retrospective gating is that it can provide data from the whole cardiac cycle.

In both prospective and retrospective gating, the detection of an R-wave causes a change in the line, or group of lines (known as a segment) that is acquired (38), as seen in Figure 1.17.

Common problems with ECG-gated acquisitions include;

- Inaccurate R-wave detection
- Irregular heart rates (arrhythmias)

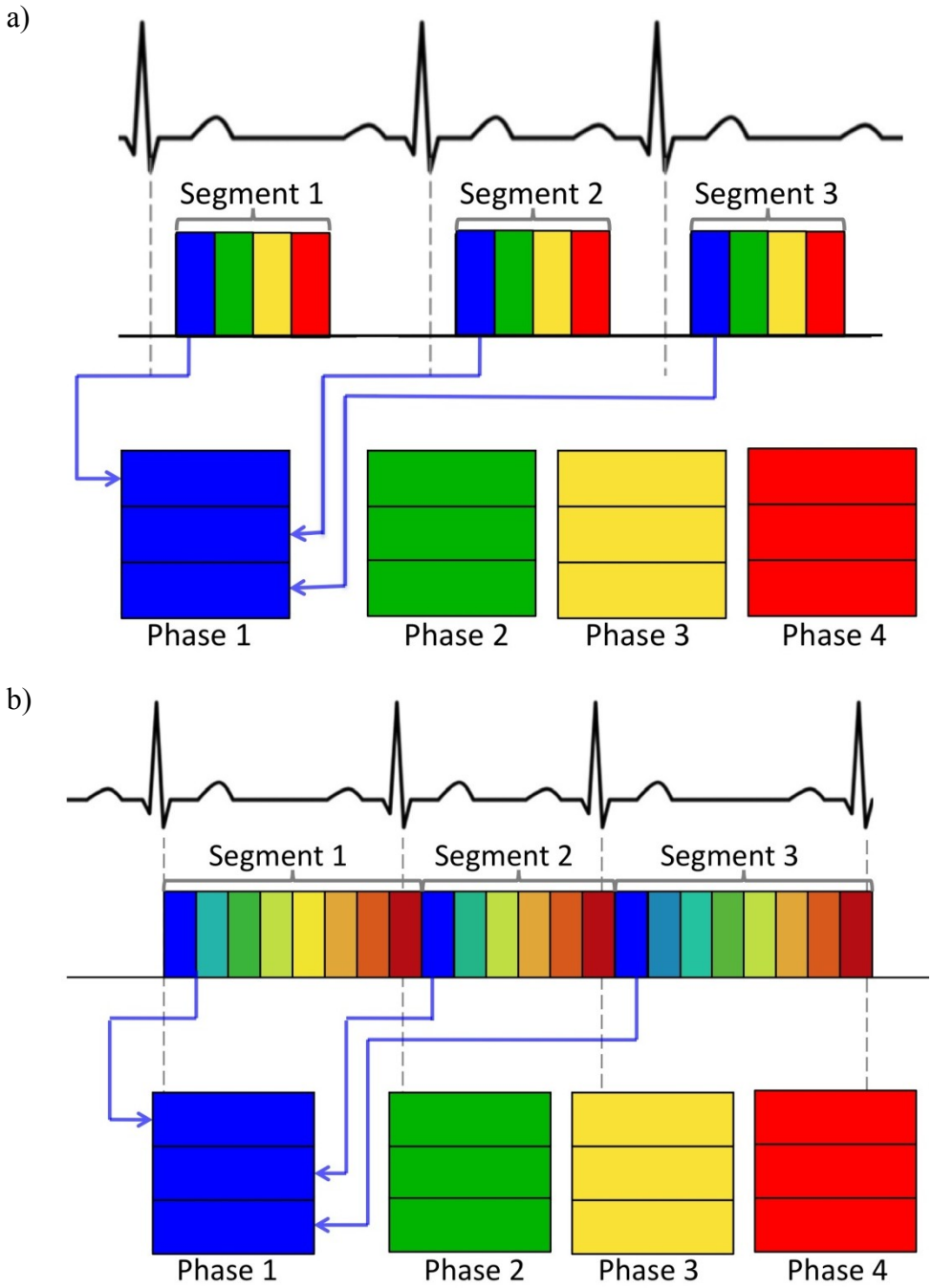

Figure 1.17: Data acquisition in; a) prospective ECG gating, b) retrospective ECG gating. In both sequences one segment is acquired repeatedly in each R-wave and detection of an R-wave resulting in a change in the segment. The colours represent different cardiac phases within each RR-interval. In prospective gating the final images are created by combining the segments depending on their position after the R-wave, i.e. the first segment collected after each R-wave are combined to make the image for the first phase. In retrospective gating the final images are created by sorting the data depending on when it was acquired with respect to the R-wave, then combining the segments which fall into the retrospectively sorted time bins.

1.6 Flow Measurements

As described in section 1.3.1 the linear magnetic gradients used for spatial encoding in MRI alter the resonant frequency of spins depending on their position, $\vec{r}$ (see Equation 1.28). This makes MRI inherently motion sensitive. As previously demonstrated, spatial encoding is achieved as spins accumulate a phase over time depending on their location. In its general form Equation 1.38 can be written as;

$$\phi(t) = \gamma \int_{t_0}^{t} \vec{G}(\tau)\vec{r}(\tau)\, d\tau \qquad \textit{Equation 1.75}$$

By performing a Taylor expansion of Equation 1.75, it can be seen that the phase accumulated by a spin is linearly proportional to its velocity (39);

$$\phi(t) = \gamma \vec{r}_0 \int_{t_0}^{t} \vec{G}(\tau)\, d\tau + \gamma \vec{v}_0 \int_{t_0}^{t} \vec{G}(\tau)\tau\, d\tau + \ \ldots\ + \gamma \frac{1}{n!} \int_{t_0}^{t} \vec{G}(\tau)\tau^n\, d\tau \qquad \textit{Equation 1.76}$$

where r_0 is the initial displacement of the spin along the direction of the gradient, and v_0 is the initial velocity of the spin in the direction of the gradient.

As the n^{th}-order moment of a gradient, M_n, is defined as;

$$M_n = \int_{t_0}^{t} \vec{G}(\tau)\tau^n\, d\tau \qquad \textit{Equation 1.77}$$

it can be seen that the sensitivity of MRI to the velocity of spins is related to the first-order gradient moment (M_1);

$$\phi(t) = \gamma \left(\vec{r}_0 M_0 + \vec{v}_0 M_1 + \ \ldots\ + \frac{1}{n!} \left(\frac{d^n r}{dt^2} \right)_{t=0} M_n \right) \qquad \textit{Equation 1.78}$$

The encoding of velocity into the phase of an MR signal is known as *phase-contrast* (PC) imaging (40).

1.6.1 Implementation of Phase-Contrast Imaging

Assuming there is no accelerative or higher order motion of spins, Equation 1.78 simplifies to;

$$\phi(t) = \gamma\left(\vec{r}_0 M_0 + \vec{v}_0 M_1\right) \qquad \textit{Equation 1.79}$$

It is possible to remove the effect of displacement (r_0) on the phase of signal, with the use of a bi-polar gradient with two lobes of equal area but opposite polarity. The net area of the bi-polar gradient is therefore zero, i.e. M_0 is zero. In this case Equation 1.79 can be simplified to;

$$\phi(t) = \gamma\vec{v}_0 M_1 \qquad \textit{Equation 1.80}$$

From Equation 1.80 it can be seen that the resulting phase is only related to the velocity of the spins;

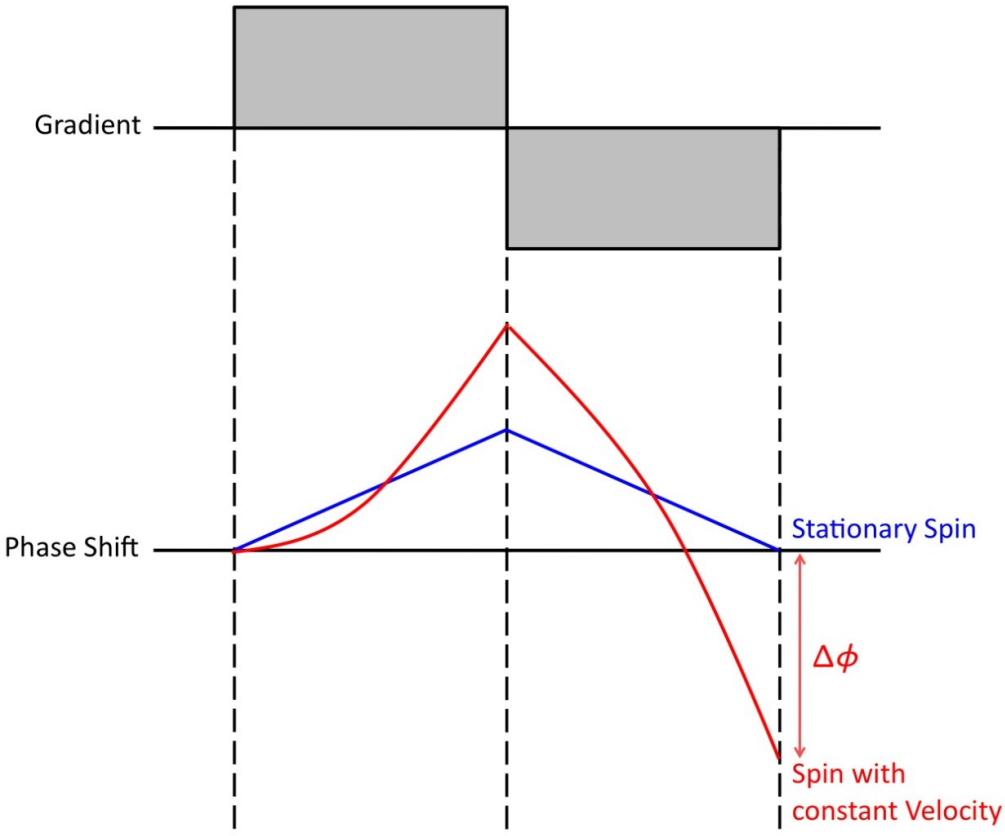

Figure 1.18: A balanced bipolar gradient causes a phase shift which is proportional to the velocity of the spins

Unfortunately phase offsets may arise from additional sources, e.g. B_0 inhomogeneities, susceptibility effects, concomitant gradients (from the imaging gradients) or eddy currents. In order to remove these additional phase offsets, normally two interleaved measurements are made with different first-order gradient moments. The phase of the resultant images is subtracted, thereby subtracting out the background phase offsets. The phase difference in PCMR is therefore commonly expressed as a difference in the first-order moments of the two images, ΔM_1;

$$\Delta\phi = \gamma\, \vec{v}_0 \cdot \Delta M_1 \qquad \textit{Equation 1.81}$$

The value of ΔM_1 determines the maximum velocity that can correctly be encoded in PCMR before aliasing occurs – this is often referred to as the *velocity encoding* (VENC). A spin travelling at ±VENC (m/s) will cause a phase shift of ± π radians, as;

$$VENC = \frac{\pi}{\gamma\, \Delta M_1} \qquad \textit{Equation 1.82}$$

Although alternative encoding strategies are possible, it is common to acquire one data set with velocity-compensated gradients (i.e. with a VENC of zero) and the other data set with velocity-encoded gradients (i.e. with the desired VENC). This is called *asymmetric encoding*.

It is possible to measure flow in any direction, however most commonly flow is measured through-plane. This is achieved by placing the flow gradients on the *z*-axis after the slice-select gradient. Here the flow gradients can be combined with the slice-select rewinder gradient to minimize the TE. Conventionally each line in k-space is acquired using flow-compensated gradients, and then with flow-encoded gradients, before moving to the next line in k-space, as seen for a Cartesian sequence in Figure 1.19.

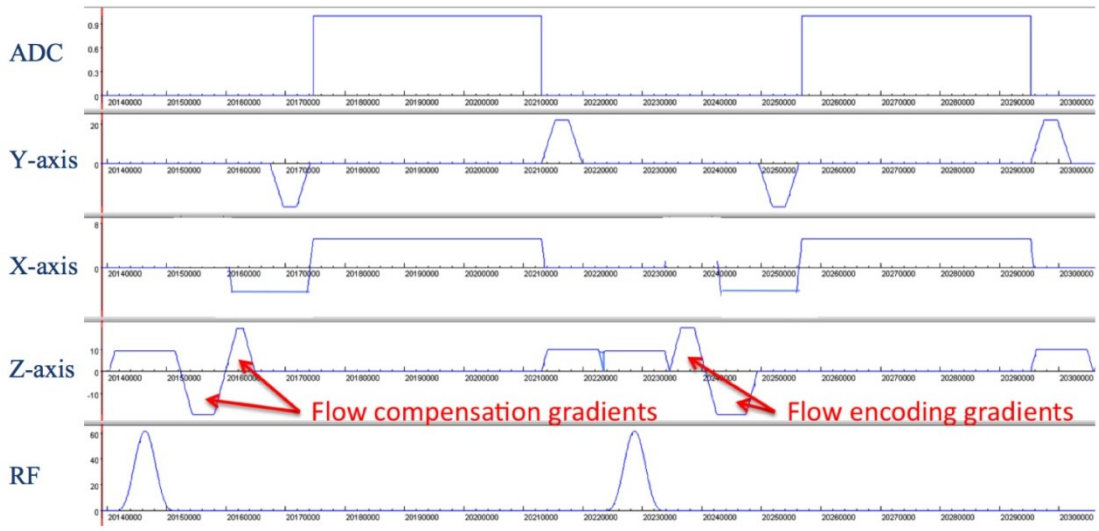

Figure 1.19: Example of a Cartesian PC sequence. Each line is acquired with flow-compensated and flow-encoded gradients before moving to the next line in k-space

Every PC acquisition yields a magnitude image and a phase image. The magnitude image gives information about the anatomy and is used for segmentation. The phase image gives the velocity of blood in each voxel and can be used to calculate flow volumes.

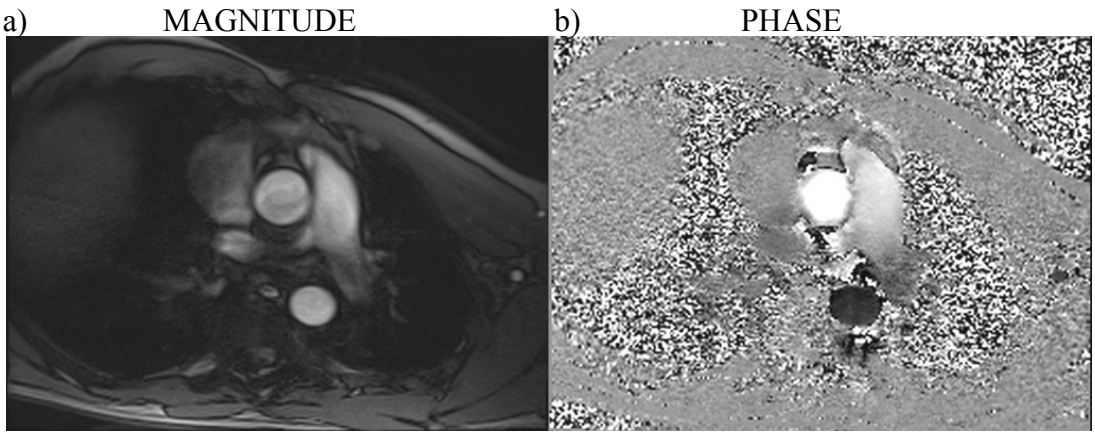

Figure 1.20: Example of a PC data in the ascending aorta of a healthy volunteer

1.6.2 Accuracy of PCMR

In the clinical environment, measures of stroke volume, cardiac output and regurgitation fraction from flow measurements are used to determine patient diagnosis and treatment.

The accuracy of PCMR depends on;

- Adequate temporal resolution to accurately detect the peak velocities
- Adequate spatial resolution to prevent partial-volume effects (see below)
- The spins within each voxel to be travelling at the same velocity, to prevent intravoxel dephasing (see below)
- A suitable match between the velocities in the vessel of interest and the chosen VENC;
    - If the VENC is too small, then wrap occurs where the phase shift is greater than $\pm \pi^c$
    - If the VENC is too large, then noise may mask the true velocities
- The angle of the imaging plane to the main direction of flow – for through-plane flow the most precise measurements are obtained if the plane is orthogonal to the direction of flow
- Complete subtraction of background phase offsets
- The accuracy of vessel segmentation

Partial-volume effects are observed when there are both stationary and flowing spins within a voxel, e.g. in voxels that are on vessel boundaries. This results in overestimation of flow because the signal intensity from the blood pool is greater than that from surrounding tissue, causing the velocity of the flowing spins to be weighted more heavily than the stationary spins (known as *in-flow enhancement*). The smaller the vessel (or the larger the pixels), the larger the relative number of pixels influenced by partial-volume effects.

Intravoxel dephasing occurs when there are spins with different velocities within a voxel, causing destruction of phase coherence. Intravoxel dephasing may be caused by accelerative spins, turbulent spins or magnetic field inhomogeneity. Both partial-volume effects and intravoxel dephasing can be reduced by increasing the spatial resolution of the images.

Greil, et al. (41) investigated the effect of the above parameters on the accuracy of PCMR in a pulsatile flow phantom (with a maximum instantaneous velocity of 0.65 m/s). They found that mean percentage error did not differ significantly with;

- Slice thickness (4, 6, 8 mm, p = 0.4)
- Slice inclination (0°, 10°, 20°, 30°, 40°, p = 0.09)
- RF-flip angle (10°, 15°, 20°, 30°, 40°, p = 0.19)
- VENC (1.0, 1.5, 2.0, 2.5, 3.0, 3.5, 4.0 m/s, p = 0.82)

However, they found that as the spatial resolution was decreased (by increasing the FOV), the error percentage grew linearly ($y = 0.35x - 7.6$), as shown in Figure 2.21;

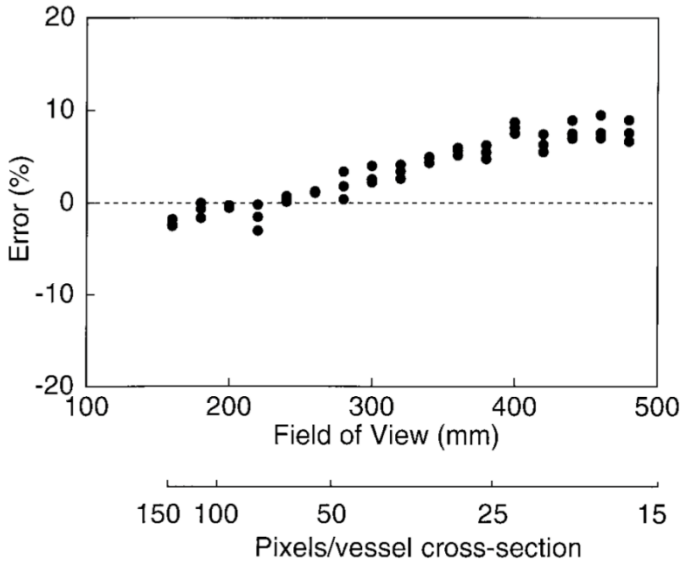

Figure 1.21: From Greil, et al. (41). A linear relationship was found between the number of pixels in the vessel of interest and the percentage flow error

Where there were only 16 pixels in the cross section of the vessel, the flow velocity was overestimated by an average of 9.0 %. Greil, et al. concluded that providing the spatial resolution is great enough, PCMR is an accurate and robust method of measuring flow (41).

Tang, et al. (42) have also shown that the accuracy of flow measurements improves as spatial resolution increases. They showed that there must be at least 16 isotropic voxels within the vessel of interest to achieve flow measurements within 10 % of the true value.

1.6.3 Concomitant Gradients in Flow Imaging

Concomitant gradients (also known as *Maxwell* gradients) are unintentional gradients with nonlinear spatial dependence, which occur in addition to the desired linear magnetic field gradients. These concomitant gradients are instantaneous with the applied gradients (unlike eddy currents which can last beyond the applied gradients), and are a consequence of Maxwell's equations for the divergence and curl of the magnetic field.

Concomitant gradients cause undesired phase offsets in images and therefore incorrect velocity measurements in PCMR. The concomitant gradient field can be calculated (43) as;

$$B_c(x,y,z,t) = \frac{1}{2B_0}\left\{ \begin{array}{r} G_x^2 z^2 + G_y^2 z^2 + G_z^2 \dfrac{x^2+y^2}{4} \\ -G_x G_z xz - G_y G_z yz \end{array} \right\} \qquad \textit{Equation 1.83}$$

Causing a phase accumulation of;

$$\Delta\phi_c(x,y,z,t) = \gamma \int B_c(x,y,z,t)\ dt \qquad \textit{Equation 1.84}$$

From Equation 1.83 and Equation 1.84 the residual phase in PCMR caused by concomitant gradients (after the phase difference calculation) can be calculated as (43);

$$\Delta\phi_c(x,y,z) = Az^2 + B\left(x^2+y^2\right) + Cxz + Dyz \qquad \textit{Equation 1.85}$$

$$\left.\begin{array}{l} A = \dfrac{\gamma}{2B_0}\int\left\{ \left[G_x^2(t)+G_y^2(t)\right]_{fe1} - \left[G_x^2(t)+G_y^2(t)\right]_{fe2} \right\} dt \\ B = \dfrac{\gamma}{8B_0}\int\left\{ G_z^2(t)_{fe1} - G_z^2(t)_{fe2} \right\} dt \\ C = \dfrac{\gamma}{2B_0}\int\left\{ \left[G_x(t)G_z(t)\right]_{fe1} - \left[G_x(t)G_z(t)\right]_{fe2} \right\} dt \\ D = \dfrac{\gamma}{2B_0}\int\left\{ \left[G_y(t)G_z(t)\right]_{fe1} - \left[G_y(t)G_z(t)\right]_{fe2} \right\} dt \end{array}\right\} \qquad \textit{Equation 1.86}$$

where *fe1* is the first flow image and *fe2* is the second flow image. The integrals in Equation 1.86 are evaluated over a time period from the end of the RF-excitation pulse, to the beginning of the ADC readout (this is because all other gradients are the same in both flow images and so any additional phase caused by Maxwell gradients will be subtracted out).

Maxwell gradients also affect all imaging gradients, and may play an important part in spiral imaging (44). In spiral imaging the effect of concomitant gradients is much harder to correct, as each point in the readout has to be corrected by a different phase offset. Although these Maxwell gradients may lead to blurring of the spiral images, they will be the same in both of the flow images and so do not contribute to additional phase offsets in spiral PCMR.

1.6.4 Additional Phase Offsets

Additional phase offsets in PC imaging have been widely observed after phase subtraction (45-49). These phase offsets may arise from inhomogeneities in the magnetic field or eddy current effects. They are affected by the imaging position, VENC, maximum gradient amplitude and maximum gradient slew rate, amongst others. Like concomitant gradients, these phase offsets cause incorrect velocity measurements in PCMR.

Gatehouse, et al. (49) performed a multi-centre, multi-vendor study into background phase offsets in PC acquisitions from 12 systems. In this study no post-processing was carried out to correct for phase offsets. In a static phantom, located up to 70 mm from the magnet isocenter, the phase offset over a circular region-of-interest with 30 mm diameter, gave a velocity offset from 0.4 cm/s to 4.9 cm/s. Over all planes and systems the average velocity offset was 2.7 cm/s – this represents 1.8 % of the 150 cm/s VENC used.

Gatehouse, et al. (49) suggest a 5 % error in volume to be the limit of acceptability. Therefore in an 80 mL/cycle stroke volume, the limit of acceptability is 4 mL/cycle error. In theory, in a great vessel of diameter 30 mm, an average velocity offset of 2.7 cm/s would cause a 19.1 mL/cycle error in stroke volume (with a heart rate of 60 bpm). This is ~5 times the 4 mL/cycle limit of acceptability, demonstrating the importance of background phase correction in PCMR.

Commonly manual post processing techniques are used to remove additional phase offsets. One such method involves estimation of the phase offset from a region of stationary tissue near to the vessel of interest (41, 47, 50). Unfortunately this method does not work well in the great vessels, as there is very little surrounding stationary tissue.

Alternatively, a separate scan can be performed on a stationary phantom with identical imaging parameters (46, 51, 52). From these images the phase offsets in the same region as the vessel can be calculated. This method is time consuming and inconvenient in clinical practice, as it must be carried out for every PC image acquired.

A semi-automated method described by Walker, et al. assumes the phase offsets vary linearly in space (53). The phase offsets can be predicted by fitting a plane through the stationary pixels in the phase image. This plane is subtracted from the velocity images to correct for phase offsets. This technique is widely used however the phase offsets are often assumed to be of a low-order (41, 47, 48, 54, 55). This technique can be completely automated, however it does not work for very noisy data or in images where there is very little stationary tissue. This is discussed further in section 4.3.7.

CHAPTER 2

Real-time Flow Measurements

2.1 Introduction

Exercise is a powerful stimulator of the cardiovascular system and can be used to unmask subtle changes in early hypertensive disease (56). Exercise testing is a common medical exam carried out to assess for cardiac disease, where the patient is placed on a treadmill and the level of exercise is progressively increased. Routinely, only blood pressure (BP) and heart rate response are measured during exercise (56). These are not sensitive markers of early vascular dysfunction and thus the full potential of exercise stress testing is not achieved. It would be advantageous if systemic vascular resistance (R) and total arterial compliance (C) could also be measured during exercise (see section 2.2.4). This requires quantification of flow, as well as blood pressure measurements.

Cardiac gated PCMR is a proven method of measuring blood flow at rest (57-60). However, gated flow sequences are not reliable during exercise due to excessive motion. Additionally, gated sequences average data from multiple heart-beats, which prohibits the assessment of short-term changes in flow patterns which occur during exercise.

A pharmacological stress test can be used instead of exercise, to increase the load on the heart, e.g. using Dobutamine or Adenosine. Pharmacological stress tests are important in subjects with physical limitations, e.g. severe arthritis, prior injury or reduced exercise tolerance. However, exercise testing is advantageous over pharmacological stress tests due to the physiologic effects of exercise. Although, there are possible side-effects to both exercise and pharmacological agents, generally fewer side effects are observed in response to exercise than to pharmacological agents. Table 2.1 shows a comparison of side effects from exercise testing and Dobutamine testing in the same group of patients (N=136) as found by Beleslin, et al. (61). In this study at least one symptom was observed in 46% of patients during exercise and in 79% of patients during pharmacological stress tests using Dobutamine. Of these, serious symptoms were found in 3% of patients during exercise and in 11% of patients during pharmacological stress tests using Dobutamine.

	Exercise (%)	Dobutamine (%)
Any symptom	46	79
Shivering/chilling	0	52
Flushing	0	8
Shortness of breath	14	7
Headache	10	4
Premature Ventricular Contractions	13	32
Serious symptom	3	11
Hypotension	1	6
Tachycardia	2	3
Atrial Fibrillation	0	1
Atrioventricular block	0	1

Table 2.1: Adapted from Beleslin, et al. (61), showing comparison of side effects from exercise and Dobutamine in the same group of patients

Previous exercise studies have been carried out using MRI. These have mostly used cardiac gated sequences, hence required suspension of exercise during imaging (see section 2.2.2). This is non-physiological (62) and makes ramped exercise protocols difficult to perform (where the exercise intensity is increased throughout the exam). A better approach may be to use real-time imaging where data is acquired within one heart-beat, rather than averaging data over many heart-beats (see section 2.2.1). Real-time MR is less susceptible to motion (caused either by exercise or breathing) and can be performed without cardiac gating, making it more suited to imaging during exercise. However, real-time imaging may come at the cost of low temporal or low spatial resolution, which may affect its accuracy at high heart rates present during exercise.

The high temporal resolution required for real-time imaging during exercise can be achieved through efficient k-space filling, combined with parallel imaging. In this study we investigated the use of an undersampled spiral PCMR sequence, reconstructed using an iterative SENSE algorithm, to measure the hemodynamic response to exercise.

2.1.1 Aims

The aims of this study were to:

- Develop a real-time spiral SENSE PCMR sequence with a high temporal resolution
- Develop an iterative CG SENSE, PCMR reconstruction algorithm
- Validate the real-time flow sequence in-vitro and in-vivo
- Demonstrate the feasibility of using this sequence to measure cardiac output during exercise
- Combine the flow measurements from the real-time spiral SENSE PCMR sequence with non-invasive pressure measurements to calculate vascular resistance and compliance

2.1.2 Personal Contribution

To fulfil the above aims I have:

- Designed and developed a uniform density spiral sequence with data undersampling, for PCMR measurements (see section 2.3.1) in the Siemens, IDEA environment. The spiral trajectory is calculated based on code developed by Brian Hargreaves (63)
- Optimised the spiral sequence to achieve a high temporal resolution with adequate image quality (see section 2.3.5), as well as reducing background phase offsets (see section 2.3.4)
- Designed and developed an iterative CG reconstruction for spiral SENSE PCMR data (see section 2.3.2) in the Siemens, ICE environment (also prototyped in MATLAB). This is based on code for iterative CG reconstruction of radial k-t SENSE data, developed by Michael Hansen. Specifically, it uses Michael Hansen's gridding algorithm
- Implemented concomitant gradient correction (see section 2.3.3)
- Performed in-vitro validation of the sequence, in a pulsatile flow pump (see section 2.4)

- Performed in-vivo validation of the sequence, in 20 healthy volunteers, at rest (see section 2.5.5)
- Used the sequence to measure flow in 20 healthy volunteers at rest and at two different exercise levels (see section 2.5). This data was combined with simultaneous blood pressure measurements to quantify resistance and compliance (see section 2.5.6)
- Developed a plug-in for OsiriX (the OsiriX Foundation, Geneva, Switzerland), to analyse real-time flow data (see section2.3.6.1)
- Developed a plug-in for OsiriX to quantify resistance and compliance (see section 2.3.6.2)

The results from this work have been published by J. Steeden, D. Atkinson, A. Taylor and V. Muthurangu, in the Journal of Magnetic Resonance Imaging, 2010, **31**(4), entitled; "Assessing vascular response to exercise using a combination of real-time spiral phase-contrast MR and noninvasive blood pressure measurements" (64) (see Appendix 1).

2.2 Literature Overview

In this section, literature on the following areas will be discussed:

- Real-time flow measurements
- Performing MRI during exercise
- Assessment of hemodynamic parameters using MRI

This is not an exhaustive review on all previous real-time flow studies or all studies measuring flow immediately after exercise, however highlights some relevant papers. These papers were found using a combination of the search engines *GoogleScholar* and *PubMed*, The search terms used included (a combination of):

- MRI
- Real-time
- Fast
- Flow
- Phase contrast
- Spiral
- Echo planar
- SENSE
- Exercise
- Ergometer

When a relevant paper was found, the referenced papers were followed up and any subsequent papers which have cited this paper were also followed up.

2.2.1 Real-time Flow Measurements

Real-time flow measurements have been achieved through the use of efficient trajectories (including EPI and spirals) and more recently through the use of parallel imaging.

2.2.1.1 Efficient Trajectories

In 2000, Nayak, et al. (65) developed a real-time PCMR sequence using spiral trajectories, with a sliding window reconstruction. Sliding window is a view sharing technique where intermediate images are formed whenever a new line is acquired.

A water-selective spectral-spatial excitation pulse (duration 7 ms) was used to avoid blurring from off-resonant fat signals. The sequence parameters are shown in Table 2.2.

Nayak, et al. showed a good correlation (within 5 %) between a reference standard PCMR sequence and the spiral flow sequence, in a constant flow phantom with through-plane and in-plane flow measurements. Experiments in a pulsatile flow pump showed that the spiral sequence was able to accurately capture the shape and peak of the velocity waveform, compared to continuous-wave Doppler ultrasound.

Sequence Parameters	
TE/TR	8/30 ms
Spiral interleaves	3
Flip angle	30°
FOV	200 mm
Matrix	87×87
VENC	242 cm/sec
Temporal resolution	180 ms (~6 frames/sec)
Spatial resolution	2.4×2.4 mm

Table 2.2: Sequence parameters used by Nayak, et al. (65)

The temporal resolution achieved by Nayak, et al. is low, meaning that the sequence is unlikely to accurately detect the peak flow. The low temporal resolution is partly due to the long spectral-spatial excitation pulse (7 ms), as well as long spiral readouts (16 ms), giving a long TR of 30 ms. The long excitation and long readout may also cause signal reduction in areas of flow, as high velocity spins may not experience the

full excitation, or may move significantly during the readout. However, the use of a spectral-spatial pulse does allow for a small FOV without wrap artefacts.

Non-spiral trajectories have also been used for real-time flow imaging. Klein, et al. (66) used a turbo gradient-echo EPI PCMR sequence to measure flow in 47 patients. In large and medium sized vessels (with diameters 20-55 mm and 6-13 mm, respectively) vessel diameter, peak velocity and flow volumes were quantified. The sequence parameters for the real-time EPI sequence are shown in Table 2.3, where the EPI factor is the number of lines acquired per EPI readout. The flow results were compared to a reference standard (free-breathing, retrospectively-gated) PCMR sequence.

Sequence Parameters	
TE/TR	6.8/15.5 ms
EPI factor	9
Flip angle	20°
FOV	200-350 mm
Matrix	64×128
VENC	200 cm/sec
Temporal resolution	124 ms (~8 frames/sec)
Spatial resolution	~4.7×2.3 mm

Table 2.3: Sequence parameters used by Klein, et al. (66).

Klein, et al. found a reasonably good agreement between the reference standard PCMR sequence and their EPI flow sequence, for large and medium size vessels in terms of vessel diameter ($r = 0.97$ and $r = 0.71$, relative difference; 4 % and 16 % respectively) and peak velocity ($r = 0.88$ and $r = 0.81$, relative difference; 10 % and 14 % respectively). The flow volumes correlated reasonably well in large vessels ($r = 0.87$, relative difference; 16 %) but not in the medium size vessels ($r = 0.64$, relative difference; 31 %).

This study achieved low temporal and low spatial resolution imaging, without any data undersampling or data sharing. The sequence was not accurate in terms of stroke volume, in medium vessels. This significant difference is most likely to be due to low spatial resolution of the EPI sequence, which resulted in ~6 cross sectional pixels within the vessel. As discussed in section 1.6.2, Tang, et al. (42) have shown that that there must be at least 16 voxels within the vessel of interest to achieve flow measurements within 10 % of the true value. This study demonstrates the need for good spatial resolution to prevent partial volume effects and ensure accurate flow volume measurements.

From these studies it can be seen that the temporal resolution achieved by efficient trajectories alone, is not adequate for real-time imaging.

2.2.1.2 Parallel Imaging

Further increases in temporal resolution for real-time PCMR have been achieved by combining efficient trajectories with parallel imaging, including SENSE.

In 2004 Körperich, et al. (67) developed a free-breathing, real-time, single-shot EPI PCMR sequence, accelerated with SENSE. The sequence parameters were;

Sequence Parameters	
TE/TR	4.9/19.4 ms
EPI factor	19
Half-scan factor	0.6
SENSE factor	4
Flip angle	40°
FOV	300×340 mm
Matrix	112×128
VENC	200 cm/sec
Temporal resolution	39 ms (~25 frames/sec)
Spatial resolution	~2.7×2.7 mm

Table 2.4: Sequence parameters used by Körperich, et al. (67)

The *half-scan factor* used in this study (also known as *partial-Fourier acquisition*) indicates how much of k-space is filled. A half-scan factor of 0.6, only acquires 60 % of k-space (one entire half and only a small proportion of the other half). The remaining lines are zero padded (a more advanced *homodyne reconstruction* cannot be used for PCMR as this results in the loss of the phase data (37)). If the object is real, its Fourier transform is Hermitian, i.e.

$$S(-k_x,-k_y)=S^*(k_x,k_y) \qquad \textit{Equation 2.1}$$

where * denotes the complex conjugation. Unfortunately this assumption is never true because unwanted phase shifts cause the reconstructed object to be complex. As flowing spins cause phase shifts, PCMR data is always complex, hence its Fourier transform is not Hermitian. Bernstein, et al. (37) state that partial-Fourier acquisition is likely to result in errors in the phase of PCMR data if the half-scan factor is lower than 75 %.

Körperich, et al. validated this real-time EPI PCMR sequence using a pulsatile flow phantom, by comparison of 6 flow volumes with the *bucket and stopwatch* method. Despite the low half-scan factor used, a good correlation was found ($r = 0.999$) with a moderate overestimation ($y = 1.26x + 0.03$) and relative differences of 12.8-28.1 % ($p < 0.006$).

In-vivo experiments were carried out in 14 paediatric patients (age: 5.2 ± 2.0 years) with cardiac left-to-right shunt. The Q_P/Q_S ratio (ratio of flow in the pulmonary artery to flow in the aorta) was calculated from a reference standard (free-breathing, retrospectively-gated) PCMR sequence and from the real-time EPI PCMR sequence (Q_P/Q_S ratio; 1.91 ± 0.64 vs. 1.94 ± 0.68, respectively). Comparison of the stroke volumes from the two sequences found negligible difference in the pulmonary artery (3 %) and aorta (2 %).

By combining a SENSE factor of 4 with a half-Fourier technique, Körperich, et al. were able to achieve high temporal resolution imaging (39 ms). However, in this study it was necessary to perform a separate scan (< 1 minute) to calculate the coil sensitivities.

Körperich, et al. performed 1D SENSE (as the data was only undersampled in the phase-encode direction) using a 5-element cardiac coil for signal detection. Four-fold acceleration seems to be very high for 1D SENSE, as the acceleration factor in SENSE is bound by the number of independent coils used in the direction of the undersampling (15, 68). However it is likely that the technique was successful due to the large FOV used (300×340 mm) in small children (average age: 5.2 years). As these children are likely to be much smaller than the FOV, this means that in the undersampled images, many pixels will have less than 4 aliases (i.e. the acceleration factor is effectively less than 4), simplifying the reconstruction.

In 2005 Nezafat, et al. (69) described a real-time auto-calibrated spiral TSENSE sequence. In this study the spiral interleaves were rotated in each phase, so that by combining the raw data from *R* (acceleration factor) frames, a fully sampled, full FOV image could be reconstructed. This allowed adaptive coil sensitivities to be calculated from the acquired data, removing the need for an additional scan (see section 1.4.1).

Nezafat, et al. measured flow in the ascending aorta and in the aortic value of one healthy volunteer, using the sequence parameters shown in Table 2.5. No validation of the spiral sequence is shown.

There are several limitations to this study, including;

- Demonstration of the technique in just one healthy volunteer
- No validation of the sequence
- Low temporal resolution achieved, especially in the aortic valve (91.2 ms)
- Reconstruction of data offline, in MATLAB

Sequence Parameters	Ascending Aorta	Aortic Valve
TE/TR	2.3/15.2 ms	15.2 ms
Spiral interleaves	8	?
SENSE factor	4	3
Flip angle	30°	30°
FOV	340×340 mm	260×260 mm
Slice thickness	10 mm	10 mm
Matrix	?	256×256
VENC	150 cm/sec	150 cm/sec
Temporal resolution	60.8 ms (~16 frames/sec)	91.2 ms (~11 frames/sec)
Spatial resolution	?	1.8×1.8 mm

Table 2.5: Sequence parameters used by Nezfat, et al. (70)

From these studies it can be seen that by combining efficient trajectories with parallel imaging, it is possible to achieve high temporal and spatial resolution imaging. Körperich, et al. (67) demonstrated high resolution imaging in small children with the use of partial-Fourier EPI trajectories, undersampled by SENSE. Unfortunately, EPI trajectories have a long TE which is not optimal for flow imaging, as moving spins have a long time to dephase before the centre of k-space is sampled. Spiral trajectories have a much shorter effTE , as they start in the centre of k-space, making them optimal for flow imaging (7, 8). Additionally spiral sequences allow undersampling in 2D, unlike EPI. Nezafat, et al. (70) used spiral trajectories undersampled by SENSE, however the temporal resolution achieved (60.8-91.2 ms) is not adequate for imaging high heart rates expected during exercise.

We wish to achieve high temporal resolution real-time PCMR imaging, using spiral trajectories because of the short effTE's possible. We wish to calculate the coil sensitivities from the data itself, not from a separate pre-scan as performed by Körperich, et al. (67). We will also reconstruct the data on-line, unlike Nezafat, et al. (70), as this will allow the user to view the images and repeat the scan if necessary. Reconstructing the data on-line will make the real-time sequence clinically useful, and allows all images to be stored and backed-up with the remaining images from the study.

2.2.2 Performing MRI During Exercise

Studies investigating the response to exercise with MRI often use supine ergometers, as it is not possible for subjects to be upright within a conventional MRI scanner. Most studies require ECG gating to achieve suitable spatial and temporal resolution. In these studies the subjects are normally required to suspend exercise, in order to perform MRI measurements. This is non-physiological, as cardiac dynamics change rapidly after exercise (62). Studies have shown a greater sensitivity to disease at peak exercise than post-exercise, e.g. Dymond, et al. (71) found 100 % vs. 70 % sensitivity using radionuclide angiography and by Hecht, et al. (72) found 100 % vs. 78 % sensitivity using echocardiography. Suspension of exercise also makes ramped exercise protocols difficult to perform.

Studies that have performed PCMR with gated sequences, immediately after supine exercise include Mohiaddin, et al. in 1999 (73), Pedersen, et al. in 1999 (74) and 2002 (75) and Jekic, et al in 2008 (76).

Studies by Taylor, et al. in 2002 (77), Cheng, et al. in 2003 (78), 2004 (79), 2005 (80) and Tenforde, et al. in 2010 (81) have performed cardiac gated flow measurements during the continuation of upright exercise (using a 0.5 T open-bore MRI system). This upright cycling position enables higher levels of exercise than supine exercise, and subjects are able to achieve a higher cardiac output when they are upright. Upright cycling also offers a more natural and comfortable exercise position, however there are very few vertical, open-bore magnet systems. Additionally, the low magnetic field strength used results in low SNR images.

There are very few studies that use real-time PCMR sequences (without the use of ECG gating) to acquire data during continuation of exercise. One such study was performed by Hjortdal, et al. (82). They used a real-time, segmented EPI sequence to investigate the influence of exercise on flow, in 11 paediatric patients (age: 12.4 ± 4.6 years).

The sequence parameters were;

Sequence Parameters	
TE/TR	4-5/12-13 ms
EPI segments	13
Half-scan factor	0.8
FOV	90×136 mm
Slice thickness	5-7 mm
Matrix	26×64
VENC	50-120 cm/sec
Temporal resolution	48-56 ms (~20 frames/sec)
Spatial resolution	3.4×2.1 mm

Table 2.6: Sequence parameters used by Hjortdal, et al. (82)

Flow was measured at rest and at two exercise levels (0.5 and 1.0 W/kg) in the inferior vena cava (IVC), superior vena cava (SVC) and in the ascending aorta. For each real-time flow measurement 120 consecutive PC images were acquired. Blood flow and stroke volume were quantified over two respiratory cycles. It was found that mean aortic and IVC flow rates increased significantly with increased exercise, however SVC flow was unchanged. The study was able to separately quantify inspiratory and expiratory flow to demonstrate that in total Cavopulmonary connection (TCPC) patients, inspiration facilitates IVC flow at rest but less so during exercise.

In this study high temporal resolution real-time imaging was achieved using efficient EPI trajectories, without parallel-imaging – this was possible due to the very small imaging matrix used. Additionally, partial-Fourier acquisition was used which may introduce errors into the PCMR phase data. However, the combined IVC and SVC flow was comparable to the measured aortic flow (< 6 % difference), indicating the accuracy of the sequence. The separate quantification of flow during inspiration and expiration would not have been possible without the use of a real-time sequence.

Hjortdal, et al. (82) were able to use a small FOV (90×136 mm) with a small matrix (26×64) as they were imaging paediatric patients (mean age: 12.4 years) with a single 18-cm receiver coil.

In 2010, Pedersen, et al. (83) extended the sequence developed by Hjortdal, et al. to use parallel-imaging. A five-element cardiac coil was used, to allow SENSE factors of 2-3. The acceleration of data acquisition was used to image over a larger FOV using a bigger matrix, while maintaining the temporal and spatial resolution. The actual FOV or matrix size are not stated, however the remaining sequence parameters are assumed to be the same as (82) in Table 2.6, unless otherwise stated in Table 2.7.

Sequence Parameters	
TE	4.8-5.0 ms
SENSE factor	2-3
Temporal resolution	48-52 ms (~20 frames/sec)
Spatial resolution	3.20×2.0 mm

Table 2.7: Sequence parameters used by Pedersen, et al. (83)

In 7 patients (median age: 18 years) and in 7 control subjects (median age: 19 years), flow was measured in the ascending aorta and in the descending aorta. Real-time flow measurements were acquired at rest and at two exercise levels (0.5 and 1.0 W/kg). No validation of the sequence has been carried out, and there are very few details on the implementation. However, Pedersen, et al. have achieved a relatively high temporal and spatial resolution with the use of efficient EPI trajectories, a half-scan factor of 0.8, plus a SENSE acceleration of 2-3.

We wish to develop a real-time PCMR sequence, to measure flow during continuation of exercise as performed by Hjortdal, et al. (82) and Pedersen, et al. (83). Instead of using an EPI sequence, we will use a spiral trajectory with a short effTE. We do not want to use a partial-Fourier acquisition, as this is known to introduce errors into the phase of PCMR measurements (37). It is felt that the temporal resolution of the studies described here, is still too low to ensure that the peak flow is accurately captured during exercise.

Gatehouse, et al. (84) suggest that at rest, the accuracy of PCMR is retained if the temporal resolution is less than 60 ms. At a heart rate of 70 bpm, this is the equivalent of ~14 frames/cycle. At a heart rate of 104 bpm (as found by Hjortdal, et al. (82) at 1.0 W/kg of exercise), to ensure 14 frames/cycle a temporal resolution of ~40 ms would be necessary.

2.2.3 Measurement of Ventricular Function During Exercise

In addition to PCMR measurements during exercise, previous studies have quantified ventricular volumes using MRI, during exercise. Again, most studies use gated sequences and require suspension of exercise, including Roest, et al. in 2001 (85) and 2003 (86).

However, Lurz, et al. (87) measured right and left ventricular volumes using two real-time sequences;

- A Cartesian SSFP sequence, with 75% partial-Fourier, accelerated 2-fold using GRAPPA ("standard real-time" sequence)
- A radial sequence, accelerated 8-fold using k-t SENSE ("radial k-t real-time" sequence)

The sequence parameters are shown in Table 2.8.

GRAPPA is a parallel-imaging method that removes the aliasing in k-space. The centre of k-space is fully sampled, by acquiring additional auto-calibration lines (ACL), which are used to calculate the coil sensitivity information.

K-t SENSE is a variant of SENSE, which also uses spatiotemporal correlations to constrain the reconstruction (16), allowing higher acceleration factors to be achieved than is possible with SENSE. These spatiotemporal correlations are derived from a low spatial resolution alias-free training data set.

	Standard real-time	Radial k-t real-time
TE/TR	0.9/2.0 ms	1.1/2.3 ms
Half-scan factor	0.75	-
GRAPPA (ACL)	2 (16)	-
k-t SENSE factor	-	8
Flip angle	41-47^{o}	43-65^{o}
FOV	~380×320 mm	~380×380 mm
Rectangular FOV	~85 %	100 %
Slice thickness	10 mm	10 mm
Number of slices	10-12	10-12
Matrix	128×82	128×128
Temporal resolution	~80 ms (~13 frames/sec)	~35.5 ms (~28 frames/sec)
Spatial resolution	3.1×3.9 mm	3.0×3.0 mm

Table 2.8: Sequence parameters used by Lurz, et al. (87)

For the radial k-t SENSE sequence, 16 radial projections were acquired in each frame. The sampling pattern was rotated in each frame so that 8 consecutive frames comprised a fully sampled k-space (with 128 radial projections). The centre 1/8th of each frame was used as a low resolution, alias-free, training data for the k-t SENSE algorithm. This sequence has previously been validated at rest (88). These studies were carried out at UCL Institute of Child Health (ICH), and this sequence is used in section 2.5.2.3 to validate our real-time flow sequence.

Lurz, et al. measured ventricular volumes using both real-time sequences in 12 healthy volunteers (mean age: 32.5 years), at rest and during continuation of exercise (at 7.5 W, 15.0 W and 22.5 W). Accuracy of the sequences was determined by assessing the agreement between right ventricular (RV) stroke volume and left ventricular (LV) stroke volume. The agreement of RV to LV stroke volumes was found to be greater during exercise with the radial k-t real-time sequence than with the standard real-time sequence (standard deviation of difference: ±3.43 vs. ±8.97 mL/cycle, respectively; $F = 6.85$, $p < 0.001$). Bland Altman analyses for both of the sequences are seen in Figure 2.1, showing a smaller bias and lower limits of agreement for the radial k-t sequence, compared to the standard real-time sequence.

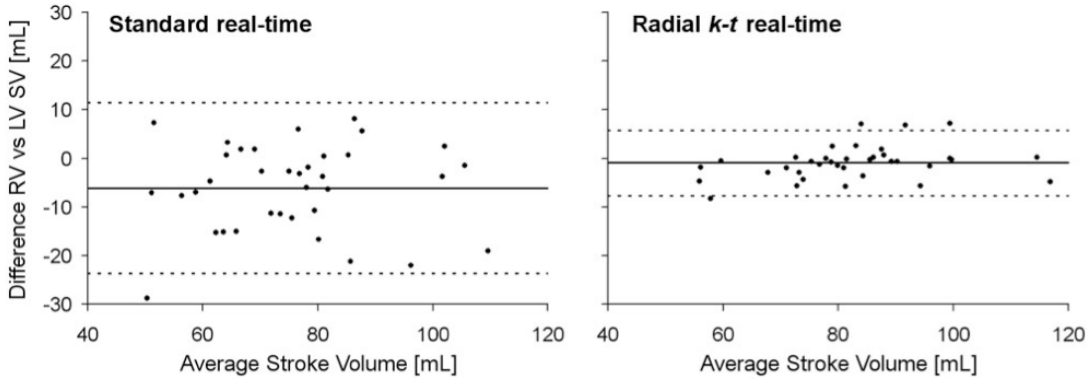

Figure 2.1: From Lurz, et al. (87). Agreement in RV to LV stroke volumes for; a) standard real-time and b) radial k-t real-time sequences

Lurz, et al. also found that the image quality and motion fidelity of the radial k-t real-time sequence was greater than that of the standard real-time sequence. This was because of the higher temporal resolution achieved by the radial k-t real-time sequence. Additionally the artefacts caused by the radial sequence (radial streaks) were less visually disturbing.

This study achieved high temporal and spatial resolution imaging with the use of radial trajectories, undersampled by a factor of 8. The data was reconstructed using an iterative CG k-t SENSE algorithm. The sequence was demonstrated to be accurate in adults, even during exercise.

Lurz. et al, demonstrated that high temporal resolution is important in real-time imaging to ensure accurate quantification of ventricular volumes during exercise. The agreement in LV and RV stroke volume was significantly worse from the standard real-time sequence than the radial k-t real-time sequence (temporal resolution; 80 ms vs. 35 ms). The average heart rates found in this study at 22.5 W of exercise was 154 bpm – at this heart rate the standard real-time sequence could only capture ~5 frames/cycle, whereas the radial k-t real-time sequence could capture ~11 frames/cycle.

2.2.4 Assessment of Hemodynamic Parameters Using MRI

In this study we are interested in quantifying systemic vascular resistance (R) and vascular compliance (C). R (measured in mmHg/L/min, also known as *Woods units*, WU) is the amount of resistance to flow that must be overcome to push blood through the peripheral circulatory system. R is calculated by;

$$R = \frac{mean\ arterial\ blood\ pressure}{cardiac\ output} \qquad \textit{Equation 2.2}$$

Compliance is a measure of the ability of the wall of a blood vessel to distend and increase volume, with increasing transmural pressure. A simple approximation of compliance (C_{SV}) is;

$$C_{SV} = \frac{stroke\ volume}{pulse\ \ pressure} \qquad \textit{Equation 2.3}$$

however C_{SV} is thought to overestimate true arterial compliance (89). The pulse pressure method (C_{PPM}) is thought to give a more accurate estimation of true compliance by parameter optimization of the two-element Windkessel model (90). The two-element Windkessel model is;

$$\dot{Q}(t) = \frac{P(t)}{R} + C\frac{dP(t)}{dt} \qquad \textit{Equation 2.4}$$

where P is pressure and $\dot{Q}(t)$ is the flow curve.

Normally R and C are calculated using invasive catheter manometers to measure pressure, and using the Fick method to quantify flow from invasive oximetry data. Unfortunately, the Fick method is considered to be inaccurate, especially in the presence of high blood flow and high concentrations of oxygen.

In the pulmonary vasculature, accurate PCMR flow measurements have been combined with invasive pressure measurements to calculate vascular resistance (91) and compliance (92).

2.2.4.1 Measuring Vascular Resistance Using MRI

In 2004 Muthurangu, et al. (91) measured pulmonary vascular resistance by combining PCMR flow measurements with simultaneous invasive pressure measurements. PCMR was carried out using a retrospectively-gated, Cartesian sequence during free-breathing. Three NSA's were used to reduce respiratory artefacts. Imaging was performed at the midpoint of the pulmonary artery.

The vascular resistance measurements derived from MR were compared to those derived from the Fick method in 15 patients. Muthurangu. et al, showed reasonable agreement between Fick and MRI–derived resistance at 30 % oxygen ($r = 0.91$, bias = 2.3 %), however at 100 % oxygen there was less agreement between the methods ($r = 0.59$, bias = 54.2 %). It was believed that these errors were from inaccuracies in the Fick method, rather than the MR. This study by Muthurangu, et al. demonstrated the feasibility of quantifying vascular resistance using PCMR.

We wish to use this principle to quantifying vascular resistance, by combining non-invasive cuff-based oscillometric blood pressure measurements with real-time PCMR measurements. By acquiring data during exercise we will be able to analyse the response of vascular resistance to exercise – this has not been previously carried out.

2.2.4.2 Measuring Vascular Compliance Using MRI

Muthurangu, et al. (92) also measured vascular compliance using the same protocol as described above. C_{SV} (Equation 2.3) was compared to C_{PPM} calculated from parameter optimization of the two-element Windkessel model (Equation 2.4). In this study C_{PPM} was found by generating a series of modelled pressure curves (*P*) using values of C between 0.001 and 7.0 mL/mmHg. C_{PPM} was taken to be the value that produced the best match with the actual pulse pressure. This is discussed further in section 2.3.6.2.

Compliance was measured in 17 patients. Correlation between C_{SV} and C_{PPM} was found to be excellent ($r > 0.97$), however there was a systemic bias (of 61 %), giving a significant difference between the two methods. This overestimation of C_{SV} has been previously observed (89, 90), due to oversimplification of the model. This study by Muthurangu, et al. demonstrated the feasibility of quantifying vascular compliance using PCMR.

We wish to use this principle to quantifying vascular compliance using the pulse pressure method, by combining non-invasive cuff-based oscillometric blood pressure measurements with real-time PCMR measurements. By acquiring data during exercise we will be able to analyse the vascular compliance response to exercise – this has not been previously carried out.

2.2.5 Summary

From the literature overview it can be seen that:

- Spiral trajectories have previously been combined with PCMR to successfully measure flow in real-time with MRI
- Without the use of data undersampling, the temporal resolution achieved is insufficient for real-time imaging
- Data undersampling with a SENSE reconstruction algorithm have been successfully used to measure flow in real-time with a high temporal resolution

- A few studies have measured flow-volume response to exercise using MRI, however many of these studies do not acquire data in real-time
- A few studies have combined MRI flow measurements with invasive blood pressure measurement in order to quantify pulmonary vascular resistance and compliance

We wish to combine these principles to develop a high temporal resolution real-time undersampled spiral PCMR sequence, with a SENSE reconstruction algorithm. We will use this sequence to measure flow volume response to continued exercise in the ascending aorta. By combining non-invasive blood pressure measurements with the real-time PCMR data we aim to measure the hemodynamic response to exercise using MRI, for the first time.

We aim to achieve a higher temporal resolution than most of the studies described, to ensure that peak flow is accurately captured during the high heart rates expected during exercise. As described above, we aim to achieve a temporal resolution of ~40 ms, as this would ensure ~14 frames/cycle a heart rate of 110 bpm.

2.3 Development

This section discusses what was developed for this study.

2.3.1 Real-time PCMR Sequence

It is possible to accelerate the acquisition of MR data by the use of efficient trajectories (section 1.3.6) as well as parallel imaging (section 1.4).

2.3.1.1 Spiral Sequence

In this study a uniform density spiral sequence was developed by integrating code by Brain Hargreaves (63) to calculate the spiral trajectories, into an MRI pulse sequence. This code takes into account the required;

- FOV
- Number of interleaves
- Maximum slew rate
- Maximum gradient amplitude
- Sampling period (Bandwidth)
- K-space radius

The equations describing spiral trajectories have been presented in section 1.3.7. The code by Hargreaves calculates an Archimedes spiral trajectory (Equation 1.39) solving θ (which describes the azimuth angle evolution over time) as a function of time using an iterative process. This iterative process is described below.

By differentiation of Equation 1.39 we get an expression for the gradient amplitude vector;

$$\vec{G} = \frac{2\pi\lambda}{\gamma} e^{j\theta}\left(\dot{\theta} + j\theta\dot{\theta}\right) \qquad \textit{Equation 2.5}$$

where $\dot{\theta}$ is the first derivative of θ with respect to time. Differentiation again gives an expression for the slew-rate vector;

$$\vec{S} = \frac{2\pi\lambda}{\gamma} e^{j\theta}\left[\left(\ddot{\theta} - \theta\dot{\theta}^2\right) + j\left(2\dot{\theta}^2 + \theta\ddot{\theta}\right)\right] \qquad \textit{Equation 2.6}$$

where $\ddot{\theta}$ is the second derivative of θ with respect to time.

At first the trajectory is slew rate limited, and so Equation 2.5 is solved for $\ddot{\theta}$ (as the maximum slew rate is known), giving $\dot{\theta}$ and θ by discrete integration. The iterative loop then uses these values to solve for $\ddot{\theta}$ at the next time point. Once the maximum gradient amplitude is reached, Equation 2.6 is solved for $\dot{\theta}$. The iterative calculation repeats until the maximum k-space radius is reached.

The same spiral trajectory is used for each interleave, however for the m^{th} interleave (where there are N interleaves in total) the trajectory is rotated by an angle, α (radians);

$$\alpha = \frac{2\pi\ m}{N} \qquad \textit{Equation 2.7}$$

The resultant spiral trajectories have been presented in Figure 1.9.

The maximum slew rate is set at 95 % of the slew rate achievable by the system (obtained from the system properties in run time). As the maximum gradient amplitude determines our sampling frequency, the maximum gradient amplitude is calculated (from the Bandwidth/pixel as on the UI) as;

$$G_{\max} = \frac{bandwidth\ per\ pixel}{pixel\ \ size \times \gamma} \qquad \textit{Equation 2.8}$$

A check is performed to ensure that this value does not exceed 80 % of the maximum gradient amplitude achievable by the system. The maximum k-space radius is calculated in run time as;

$$k_r^{\max} = \frac{matrix\ \ size}{2 \cdot FOV} \qquad \textit{Equation 2.9}$$

In our implementation a non-selective RF-excitation (*sinc*) pulse is used, with a short duration (of 600 μs) to ensure a short effTE. We do not apply rewinder gradients after the spiral readouts, as it is possible to achieve a shorter TR without these gradients. However, gradient spoiling (on the *z*-axis) and RF-spoiling are carried out to reduce residual transverse magnetisation. Gradient spoilers are applied at the end of each TR – these large gradients cause the transverse magnetisation to dephase along the direction of the gradient, leading to signal cancellation in a pixel. RF-spoiling works by phase cycling the RF excitation – in our sequence this implemented as an increase of 50^o in the phase of the RF pulse with each excitation. This phase cycling prevents signals from previous excitations from adding coherently.

To prevent a flash artefact in the first few frames, we applied 1 second of dummy pulses (where the gradients are played out but the ADC is not turned on), prior to the start of data acquisition.

2.3.1.2 Flow Encoding

The flow encoding gradients were added to the spiral sequence. We decided to use an asymmetric encoding, as this allowed coil sensitivity data to be calculated from just the flow-compensated data. In this way the magnitude of the coil sensitivity data is free of flow artefacts, and the phase is independent of the flow.

The flow-compensated and flow-encoded readouts were interleaved in their acquisition to maintain temporal coherence. This means that each spiral interleave is acquired once with flow-compensated gradients and once with flow-encoding gradients, before moving to the next spiral interleave (as presented in Figure 1.19).

As we are interested in through-plane flow, the flow-encoding gradients were added to the slice-select axis. To minimize the effTE, the flow-encoding gradients were combined with the slice-select rewinder gradient. The resulting sequence diagram can be seen in Figure 2.2;

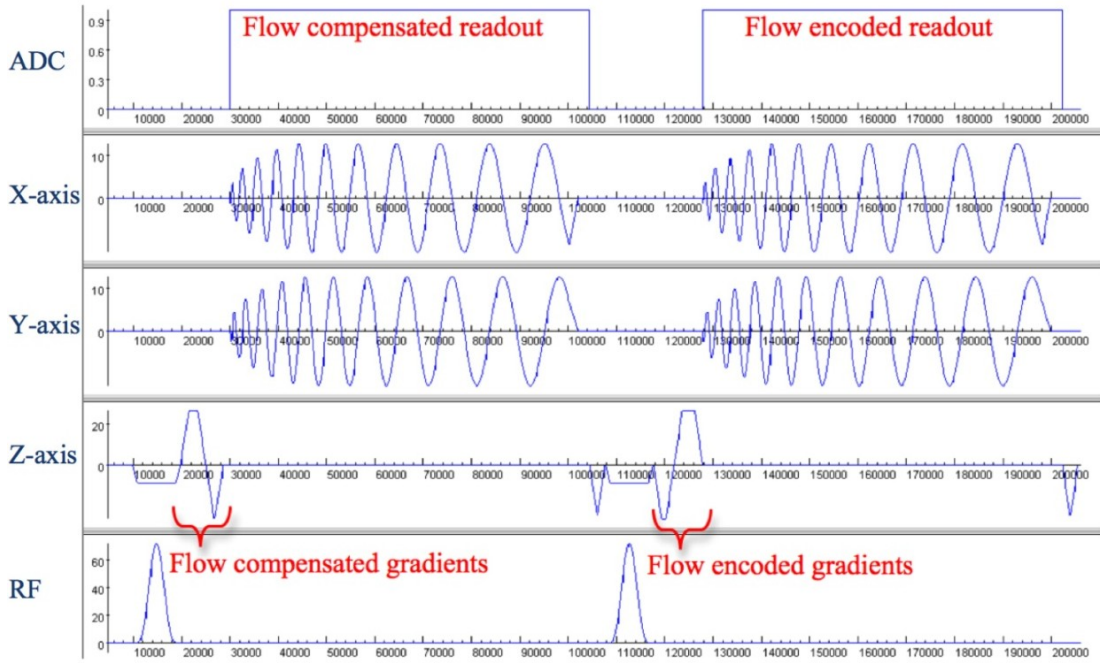

Figure 2.2: A sequence diagram showing the interleaved flow-compensated and flow-encoded readouts for one spiral interleave

2.3.1.3 Data Undersampling

In this study we wanted to calculate the coil sensitivity data from the undersampled data itself, rather than from a separate pre-scan (see section 1.4.1). As we are using uniform density spiral trajectories the centre of k-space is not fully sampled, therefore cannot be used to calculate the coil sensitivity maps. It was decided to use a variant of TSENSE (17) (see section 1.4.1) where the k-space lines in sequential repetitions are interleaved (see Figure 2.8).

In this implementation the desired acceleration factor, is specified by the user from the UI;

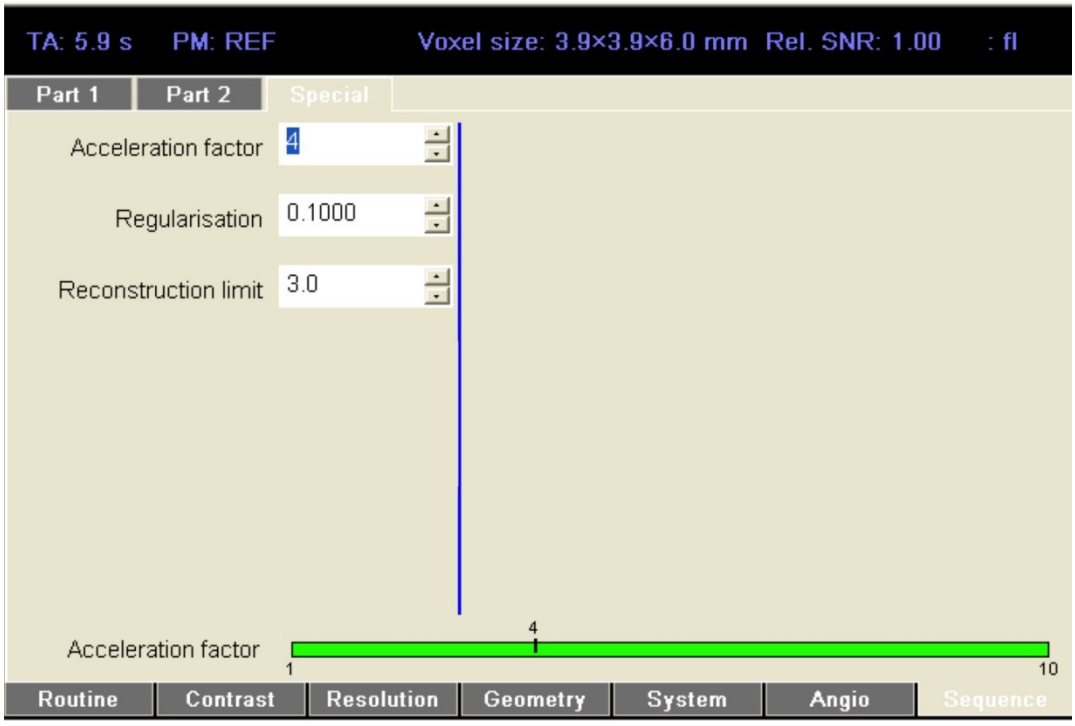

Figure 2.3: The sequence->special tab on the UI contains user-defined parameters; including the desired acceleration factor, the regularisation factor (λ) and reconstruction limit (ε).

2.3.2 SENSE Reconstruction

In order for the sequence to be clinically useful, it is necessary for the undersampled data to be reconstructed online, in the Siemens ICE environment (ICE VB15, two AMD Opteron processors, clock-speed: 3.2GHz, cache: 6MB). An iterative SENSE algorithm was used (section 1.4.2.2), with regularization (section 1.4.2.3) and preconditioning (section 1.4.2.4) to improve the speed of convergence. The conjugate gradient algorithm described in Equation 1.75 was implemented in ICE, however in this study we did not use any prior information (this is the same as setting ρ_0 to zero in Equation 1.75).

Gridding (see section 0) was performed by convolution with a Kaiser-Bessel kernel (see Equation 1.46 and Equation 1.47). The kernel width was chosen at $w = 4$, to give a good compromise between image quality and calculation time, where $\beta = 5.7567$ from the optimal values in (13). To remove aliasing at the edges of the images, an oversampling factor of 1.25 was used. This means that the FOV was increased by a factor of 1.25, by gridding the data onto a smaller grid, and the outer portion of the image was ignored. A look-up-table was used to store the gridding kernel (with 10000 steps), to optimise calculation time. This code was written by Michael Hansen, but I adapted it to handle spiral trajectories (rather than radial trajectories).

The spiral trajectory is calculated within the ICE environment by calling the trajectory function used in the sequence, with the same input parameters. The gridding weights (see section 0) are calculated analytically using Equation 1.48 within ICE.

2.3.2.1 Calculation of Coil Sensitivity Information

The coil sensitivity data and signal covariance (θ) required for the reconstruction algorithm (see section 1.4.1) were calculated directly from the raw data. Specifically, using just the flow-compensated data, the following steps were carried out to calculate the coil sensitivity data;

- For all repetitions and all channels;
    - Grid the undersampled data
    - Perform 2D inverse FFT to image space
- For all channels;
    - Calculate average image from all repetitions*
    - Perform 2D FFT to k-space
    - Apply 2D Tukey Filter (see below) to smooth the image
    - Perform 2D inverse FFT to image space (we will denote these images as I_γ)
- Calculate homogeneous image (I_H) (see Equation 1.51) as the complex square-root-sum-of-squares of all coil images, I_γ
- Calculate the coil sensitivities for each coil, $C_{\gamma;}$
    - Divide I_γ by I_H

Examples of images from the steps above are shown in Figure 2.4.

In TSENSE adaptive coil sensitivity maps are used, by combining just R frames (in the step marked with a *). However these coil sensitivity maps tend to be noisy and this noise propagates through the reconstruction. We propose to calculate the coil sensitivity maps from all frames (similar to k-t SENSE (16)) so that high SNR coil sensitivity maps are achieved.

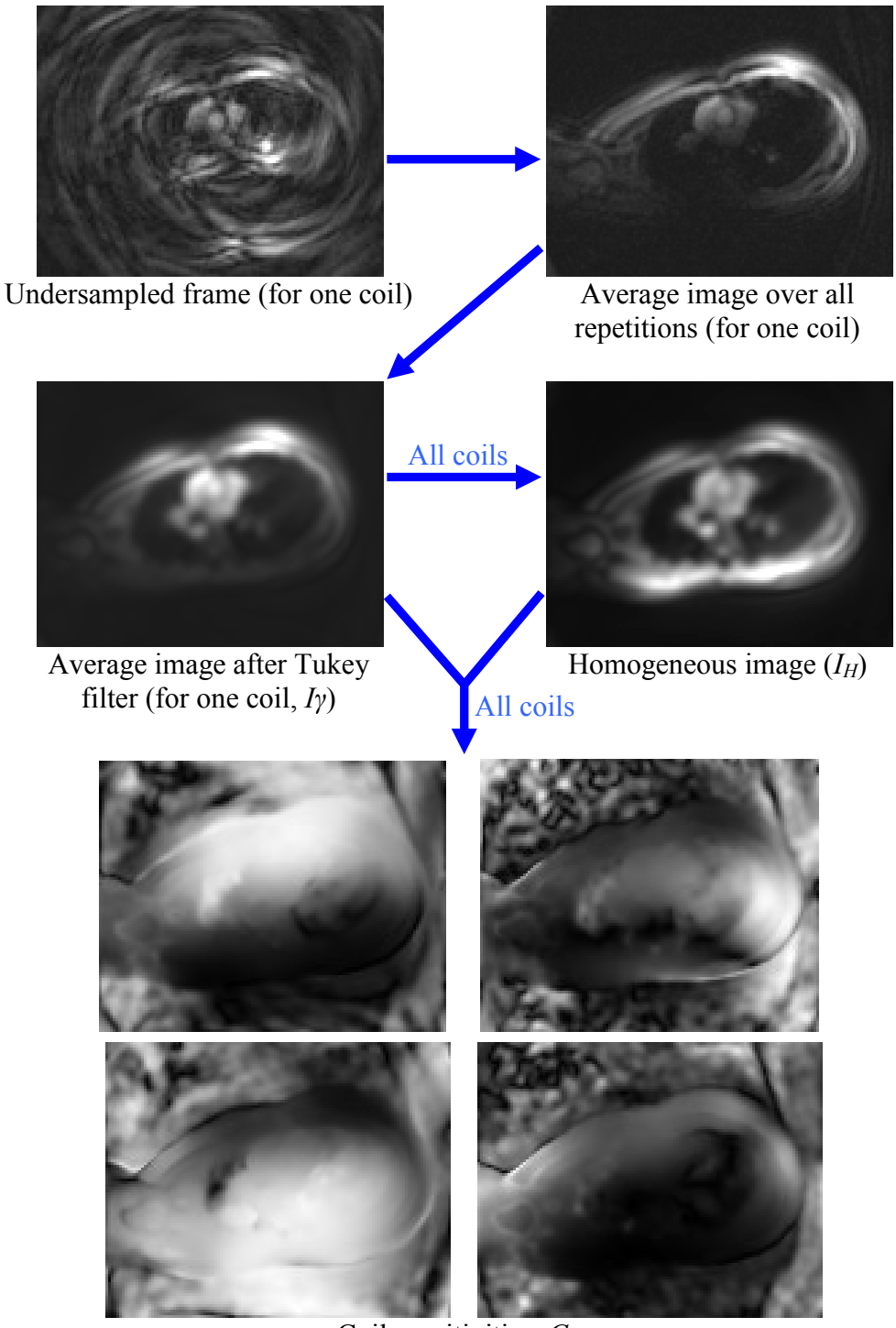

Figure 2.4: Calculation of coil sensitivity information from an undersampled spiral sequence (SENSE ×4). The coil sensitivities are calculated by dividing of the filtered average image for each coil by the homogeneous image

An adapted Tukey filter was used to generate low-resolution images, by weighting the k-space data to maintain low frequency data and attenuate high frequency data. In this Tukey filter the user can control the flat top radius (r) and transition width (T), as shown in Figure 2.5;

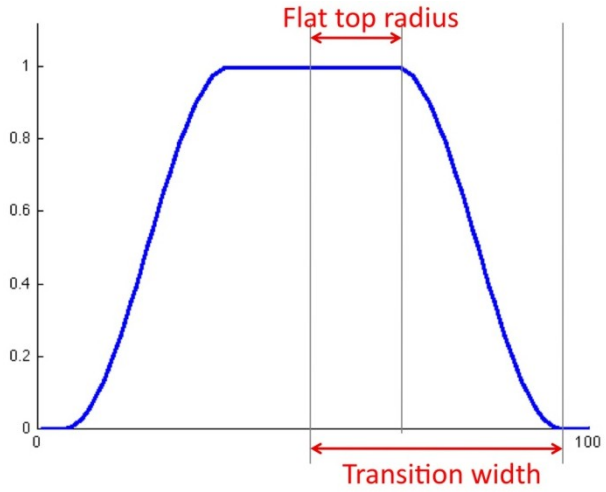

Figure 2.5: A Tukey filter, simulated in MATLAB

This filter is described as;

$$\omega_0(n) = \begin{cases} 1 & \text{when } n < r \\ \frac{1}{2} + \left(\frac{\cos\left(\pi \left| \frac{n-r}{T} \right| \right)}{2} \right) & \text{when } r \le n \le (r+T) \\ 0 & \text{when } n > (r+T) \end{cases} \qquad \text{Equation 2.10}$$

The Tukey filter used to calculate the coil sensitivity data uses parameters: $r = 0$ and $T = matrix\_size/2$.

The signal covariance (θ) used in the regularisation and preconditioning (see section 1.4.2.3 and section 1.4.2.4) was found from the expected signal, L (see Equation 1.65). In this study L was calculated in the same way as I_H except without the Tukey filtering.

2.3.3 Concomitant Gradient Correction

The effect of the concomitant field (see section 1.6.3) is small (52 ppm at 1.5 T with a gradient amplitude of 10 mT/m and a 20 cm distance from isocenter), and is thus largely neglected in most imaging situations (43). However in this study we are using a 1.5 T system with a high amplitude gradient system (40 mT/m) and for this application are generally interested in performing off-centre imaging. Therefore, concomitant magnetic fields were observed to be important in the resultant PCMR images, as seen in Figure 2.6. Maxwell correction was performed to remove the effects of concomitant gradients originating from the flow encoding gradients (43).

The residual phase in PCMR caused by concomitant gradients (after the phase difference calculation) has been presented in Equation 1.84 and Equation 1.85. In Figure 2.6 residual phase offsets result in velocity errors up to 20 cm/s at the edge of the image – this is one-fifth of the 100 cm/s VENC used to acquire these images.

In Figure 2.6 Maxwell correction is observed to remove the phase offset in transverse, coronal and sagittal slices. The phase offset in the double oblique slice shown in Figure 2.6 is not removed by Maxwell correction, implying that this offset may be from a different cause (see section 2.3.4).

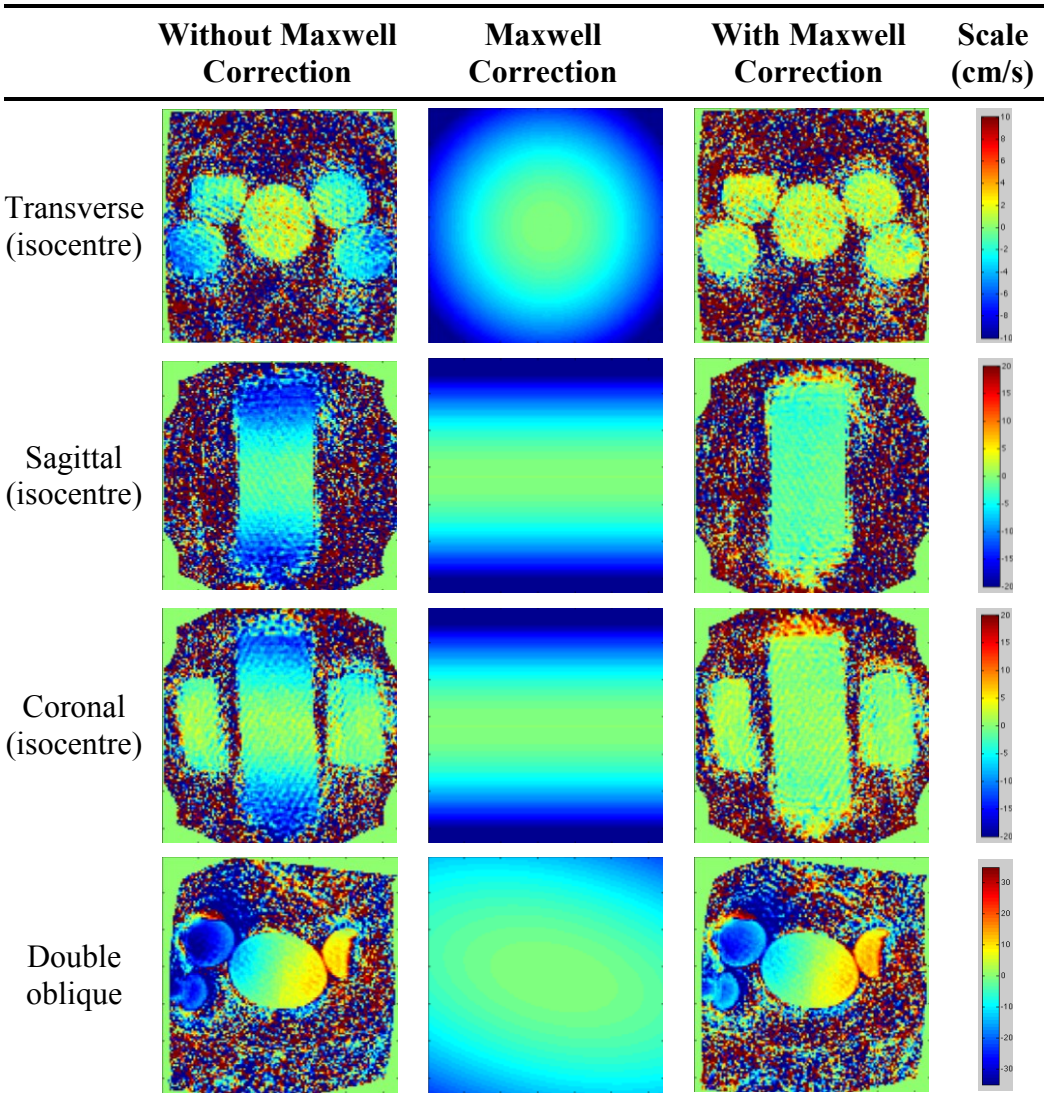

Figure 2.6: Effect of Maxwell correction on water phantoms imaged with 12 spiral interleaves, undersampled by a factor of 2, VENC = 100cm/s. Note the different scales

2.3.4 Residual Phase Offsets

Maxwell correction did not completely remove background phase offsets when imaging a double oblique slice. This suggests that there may be additional residual background phase offsets from other sources (as discussed in section 1.6.4).

It was observed that by varying the effTE and the slew rate of the flow encoding gradients, it was possible to alter these additional phase offsets (see Figure 2.7).

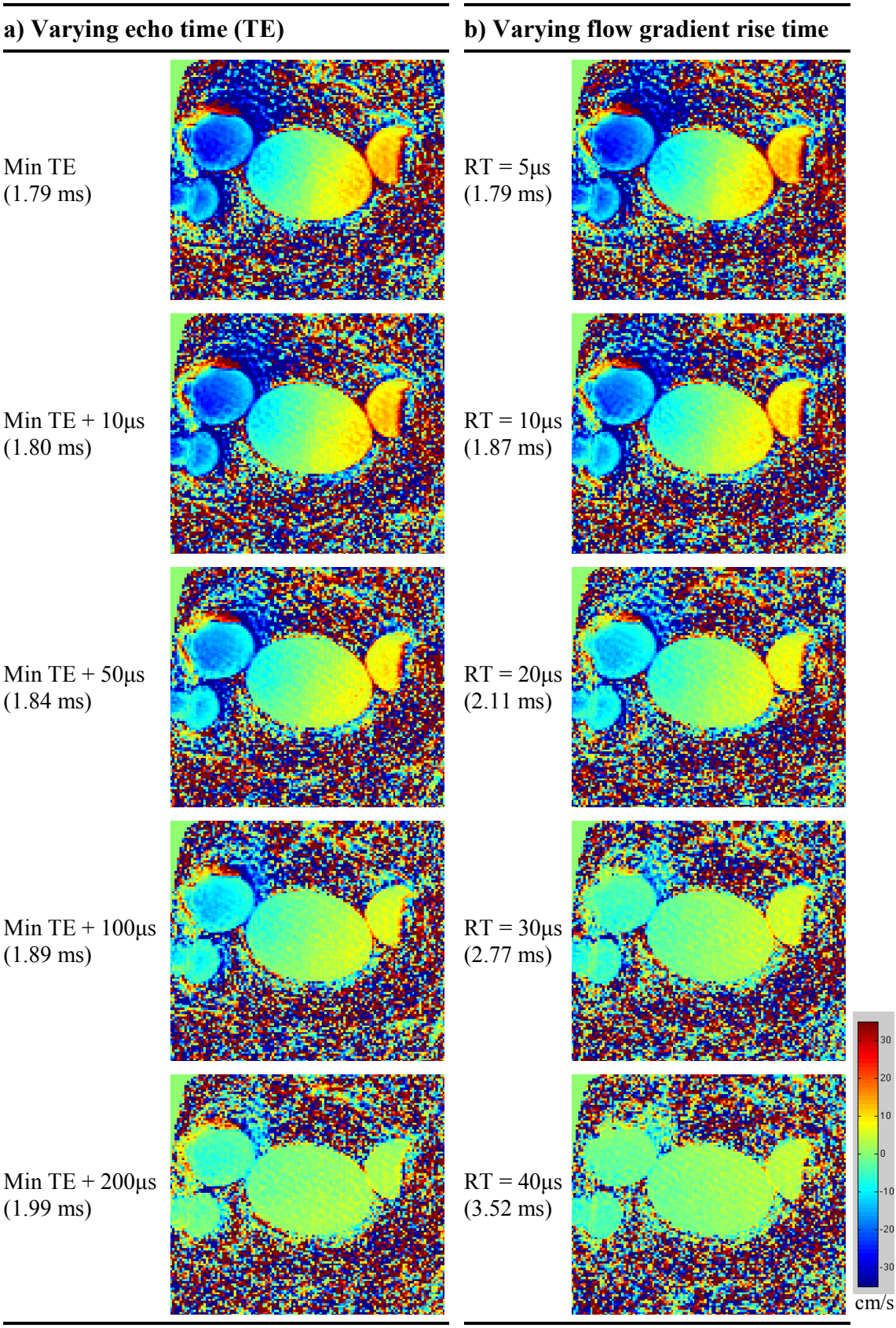

Figure 2.7: Residual phase offsets (after Maxwell correction) from an oblique slice in a water phantom, VENC: 100cm/s. Effect of varying; a) TE, b) rise time (RT) of the flow-encoding gradients. Values in brackets give the actual effTE

Figure 2.7a) shows that the phase offsets decreased when a delay was inserted between the end of the flow gradients and the beginning of the readout. Figure 2.7b shows that (with no additional TE delay) the phase offsets could be decreased, by lengthening the rise time of the flow gradients – this is the same as reducing the slew rate of the flow gradients. These observations imply that these additional phase offsets may be a result of residual eddy currents from the flow-compensation/flow-encoding gradients. Alternatively these phase offsets may be caused by waveform pre-emphasis gradients played out by the scanner to reduce the effect of eddy currents (37). These gradients may still be active after the end of the intended gradient. By introducing a TE delay, these eddy currents/waveform pre-emphasis gradients have time to decay before the beginning of the readout. By decreasing the slew rate of the gradients, less eddy currents are produced (hence the waveform pre-emphasis gradients will also be smaller).

Optimisation of the TE delay and ramp-up times, found that we were able to achieve low residual phase offsets for most imaging planes (when imaging the aorta) using a ramp-up time of 10 μs, with an additional TE delay of 400 μs, within a short TE (TE = 2.27 ms for the experiment shown in Figure 2.7 with a VENC of 100 cm/s).

2.3.5 Optimisation of Sequence Parameters

Adequate temporal resolution is essential to ensure accurate flow measurements. In this study we wanted to acquire each phase-contrast frame in ~40 ms (as discussed in section 2.2.2).

As we do not use a 2D spatially selective excitation, when imaging the ascending aorta the RF-pulse also excites spins in the arms of the subject. If the FOV is smaller than the subject, the reconstruction algorithm would not be able to distinguish between aliasing caused by undersampling of data and aliasing caused by wrapping of signal from outside the FOV. Therefore in this study it was necessary to use a large FOV, to also include the arms of all subjects. The FOV was therefore set at 500 mm, as we were imaging adult subjects.

In spiral imaging it is necessary to keep the readout times relatively short to ensure signal throughout the entire readout, and to reduce cumulative trajectory errors (which were observed to lead to image rotation and blurring).

With these requirements we were able to optimise the sequence parameters for our application. This was done by varying the sequence parameters, and comparing the resultant temporal resolution and image quality (by visual inspection). The parameters for the optimised sequence were;

- 128 matrix
- 8 spiral interleaves
- 4-fold acceleration
- 1775 Hz/pixel bandwidth
- 7 mm slice thickness
- 15^{o} Flip angle
- 10^{-3} reconstruction limit (ε)
- 0.1 regularisation factor (λ)

With these settings a temporal resolution of 40.4 ms (with a VENC of 200 cm/s) and a spatial resolution of 3.9×3.9 mm was achieved. In this optimised sequence, data is acquired according to Figure 2.8.

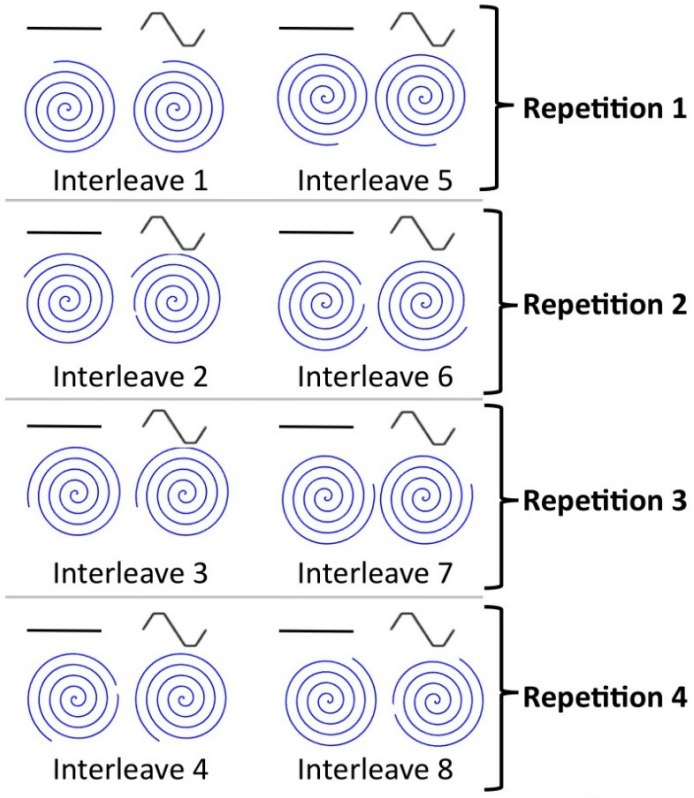

Figure 2.8: Acquisition of data for the optimised sequence with 8 spiral interleaves, undersampled by a factor of 4. ⎯⎯ represents flow-compensated data, and ∿ represents flow-encoded data. Note the rotation of the spiral interleaves

The resulting images from a resolution phantom can be seen in Figure 2.9;

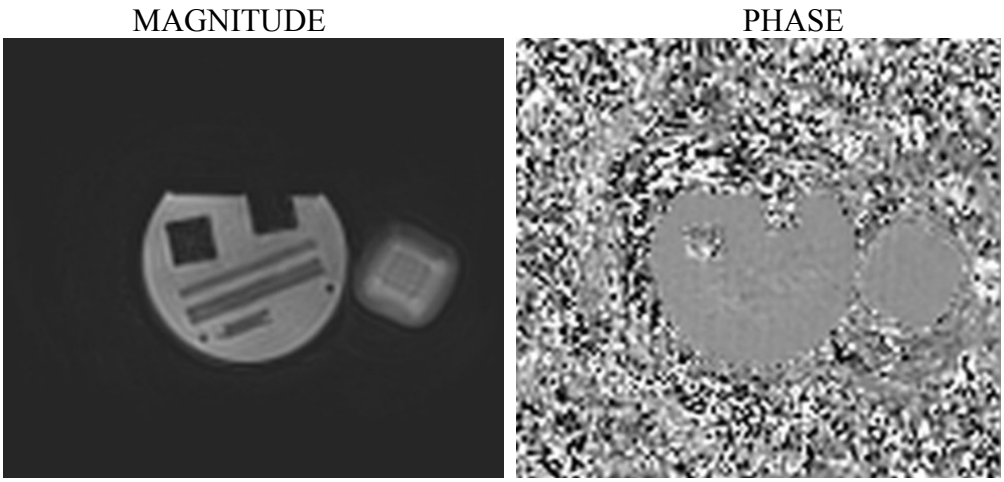

Figure 2.9: Resultant image quality from the optimised sequence in a resolution phantom (circular object on left of image), with a bottle of oil (square object on right of image)

2.3.6 Development of OsiriX Plug-ins

In order to analyse the resultant phase-contrast data, a plug-in was developed for the open-source software, OsiriX. This allows calculation of the flow velocities, flow volumes, as well as vascular resistance and compliance.

2.3.6.1 Analysis of Flow Data

When analysing flow data, segmentation is performed on the magnitude images, and then copied across to the phase images. As already discussed, the pixel intensities in the phase image are proportional to the velocity of the blood. The flow volume is therefore calculated by multiplying the velocity in each pixel by the pixel area. The flow volume of a vessel, is calculated by summing the flow volumes from all pixels within the vessel.

To calculate the stroke volume (or net forward flow) for a vessel, it is necessary to integrate the flow volume over one cardiac cycle. As the data is acquired in real-time, we must first select one cardiac cycle and calculate the stroke volume for this cycle. This is done automatically in the plug-in by;

- Detecting the peaks within the flow volume curve (these are plotted in green dots on the plug-in, see Figure 2.10. The peak-threshold can be adjusted by the user if the peaks are not correctly detected)
- Calculating the RR-interval, as the time per PC frame (temporal resolution) multiplied by the average number of frames per cycle
- For the cardiac cycle selected by the user (from the UI);
    - Find the points in the flow curve which represent the relevant cardiac cycle (these points can be adjusted by the user if the algorithm does not correctly detect the cycle, see Figure 2.10)
    - Integrating the flow volume curve for the selected cardiac cycle to a temporal resolution of 1 ms (by Fourier interpolation)
    - Calculate forward flow by summing the positive flow values in the integrated flow curve
    - Calculate backward flow by summing the negative flow values in the integrated flow curve
    - Calculate net forward flow by summing the all flow values in the integrated flow curve

The plug-in for analyzing the real-time flow data is shown in Figure 2.10.

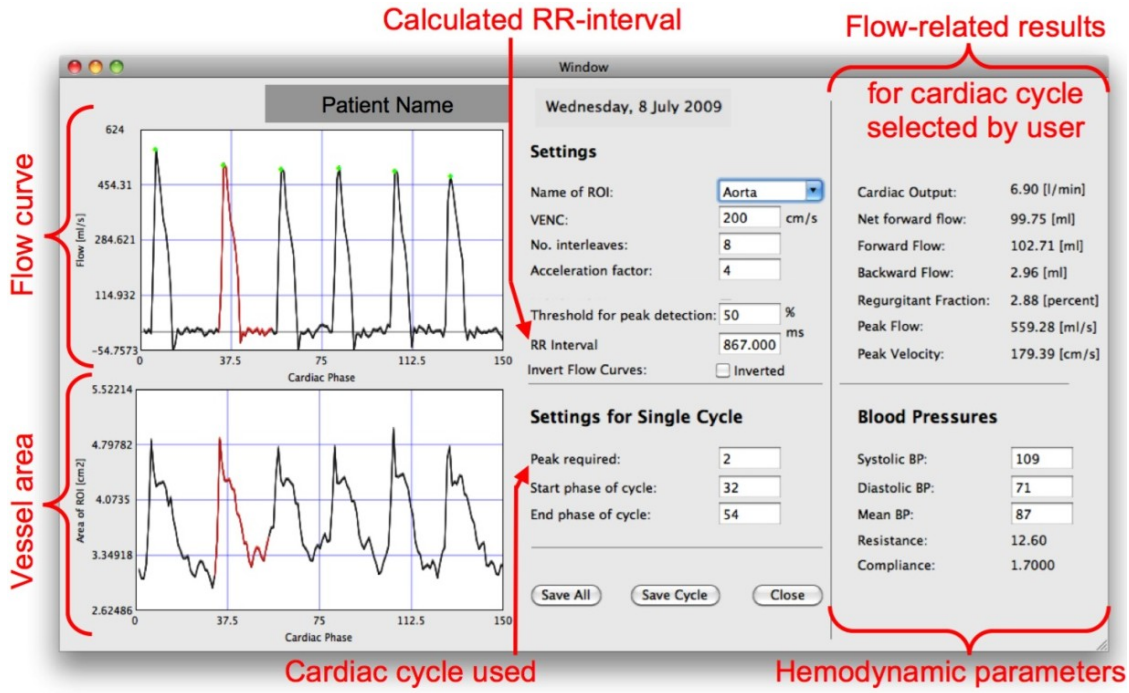

Figure 2.10: In-house plug-in developed for analysis of real-time flow data using OsiriX

2.3.6.2 Analysis of Hemodynamic Parameters

This plug-in can also be used to calculate the vascular resistance and compliance by combining the flow data (from the single cycle selected), with the blood pressure measurements (as seen in Figure 2.10).

Vascular resistance is calculated by dividing the mean blood pressure by the cardiac output (see section 2.2.4.1). Compliance was calculated using an optimization of the two-element Windkessel model (Equation 2.4), in the same way as Muthurangu, et al. (92) (see section 2.2.4.2). Specifically, a flow curve $\dot{Q}(t)$ with 50 cardiac cycles was created by repeating the single flow curve selected from the UI. $\dot{Q}(t)$ and the calculated resistance (R) were used as inputs to the Windkessel model. A series of modelled pressure curves (P) were generated using values of compliance (C) between 0.1 and 5.0 mL/mmHg in increments of 0.01. For a given C, Equation 2.4 was integrated using the initial condition $P(0) = 0$. This generated a 50-cycle pressure curve, which had stabilized and was independent of the initial condition by the 40th cycle. Therefore the modelled systolic and diastolic pressures ($P_{systole\_computed}$ and $P_{diastole\_computed}$) were calculated from the maximum and minimum pressures

respectively, between the 40th and 50th cycles. The modelled pulse pressure ($PP_{computed}$) was calculated as $P_{systole\_computed}$ minus $P_{diastole\_computed}$. Compliance was taken to be the value that produced the best match between $PP_{computed}$ and the actual pulse pressure (PP_{actual}) as seen in Figure 2.11;

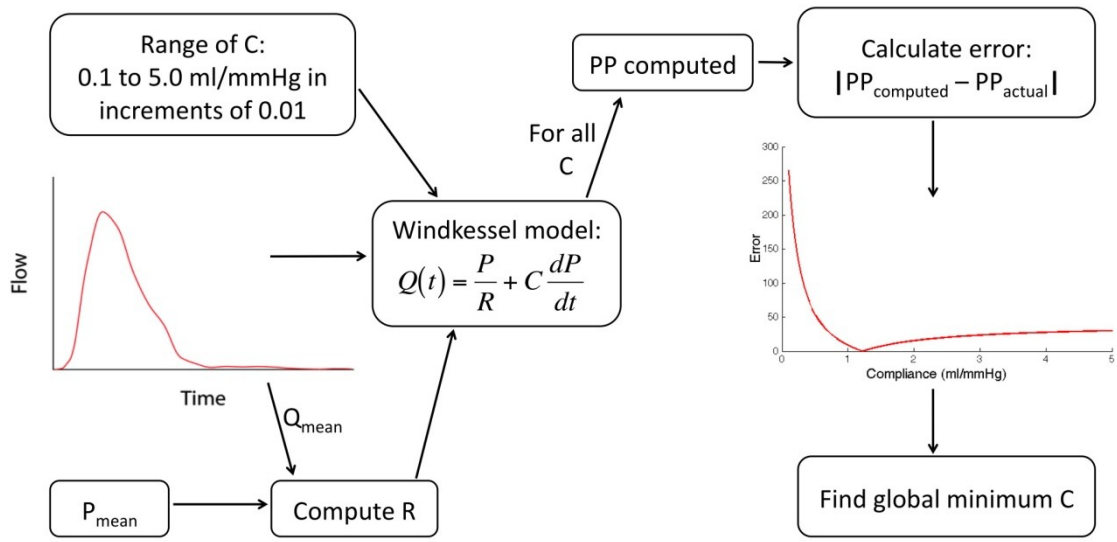

Figure 2.11: Figure from (64). Calculation of compliance, by optimisation of two-element Windkessel model

2.4 In-vitro Validation

To validate the undersampled spiral PCMR sequence, an experiment was carried out using tap water within a pulsatile flow pump (Harvard Medical Systems) connected to a distensible rubber tubing vessel phantom, as seen in Figure 2.12;

Figure 2.12: Photograph of rubber tubing vessel phantom used for in-vitro validation

The output from the pump was varied from 2.8-6.8 L/min, by changing the stroke volume (50-90 mL/cycle) and the pump rate (60-85 bpm). Flow was quantified at 14 different output volumes.

PCMR images were acquired using a standard, retrospectively-gated Cartesian sequence and the real-time spiral sequence, at the mid-point of the phantom with a transverse imaging plane. Two three-element spine coils (below the phantom) and two three-element body-matrix coils (above the phantom) were used for imaging.

2.4.1 Standard Flow Sequence

Standard flow quantification was performed using a (vendor supplied) retrospectively-gated, velocity-encoded gradient echo sequence with sequence parameters shown in Table 2.9. The sequence was gated from an external square wave signal generated by the flow pump.

This sequence has been well validated in many previous studies against the gold-standard stop-watch cylinder method of measuring flow (58, 60, 91, 93, 94). Therefore in this study the flow volumes measured from this sequence are assumed to be the true flow volumes.

Sequence Parameters	
TE/TR	3.4/7.0 ms
GRAPPA (ACL)	2 (24)
Flip angle	30^{o}
FOV	320×240 mm
Rectangular FOV	75 %
Asymmetric echo	77 %
Slice thickness	7 mm
Matrix	256×192
Pixel Bandwidth	390 Hz/pixel
VENC	50 cm/s
NSA	2
Temporal resolution	27.9 ms (36 frames/sec)
Spatial resolution	1.3×1.3 mm
Scan Time	~2.0 mins

Table 2.9: Standard PCMR sequence parameters, in-vitro

Asymmetric echo uses the same principle as partial-Fourier but in the readout dimension.

2.4.2 Real-time Spiral Sequence

Real-time flow quantification was performed using the in-house real-time spiral PCMR sequence (optimised in section 2.3.5). The sequence parameters are shown in Table 2.10.

Sequence Parameters	
TE/TR	2.7/11.2 ms
Spiral Interleaves	8
SENSE factor	4
Flip angle	15^{o}
FOV	300 mm
Slice thickness	7 mm
Matrix	128×128
Pixel Bandwidth	1775 Hz/pixel
VENC	50 cm/s
Temporal resolution	44.8 ms (22 frames/sec)
Spatial resolution	2.3×2.3 mm
Scan Time	~4 sec

Table 2.10: Real-time Spiral PCMR sequence parameters, in-vitro

For each scan, 80 consecutive frames were acquired. Reconstruction time online for each scan was ~3 minutes.

2.4.3 Image Analysis

All images were processed in OsiriX. Flow images were manually segmented (by J.A.S. using the modulus images) and the pump output was measured. For the real-time sequence a single cycle was used for calculation of flow volumes.

Results are expressed as the mean ± standard deviation. Measurements of agreement between the standard flow sequence and the real-time flow sequence were performed using Bland-Altman analysis, as well as calculation of correlation coefficients. All statistical analysis was performed using GraphPad Prism (GraphPad Software Inc., San Diego, CA).

2.4.4 In-vitro Results

For each experiment pump output was calculated using both sequences.

2.4.4.1 Flow Assessment

There was good agreement between the standard gated flow sequence and the real-time flow sequence, throughout the cycle as seen in Figure 2.13;

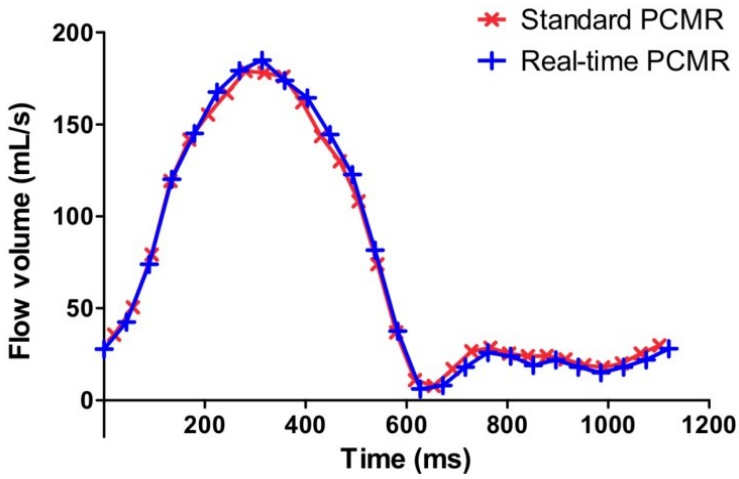

Figure 2.13: Comparison of flow profiles in-vitro

Figure 2.14 shows the use of the OsiriX plug-in (described in section 2.3.6.1) for analysis of the real-time PCMR data for one experiment.

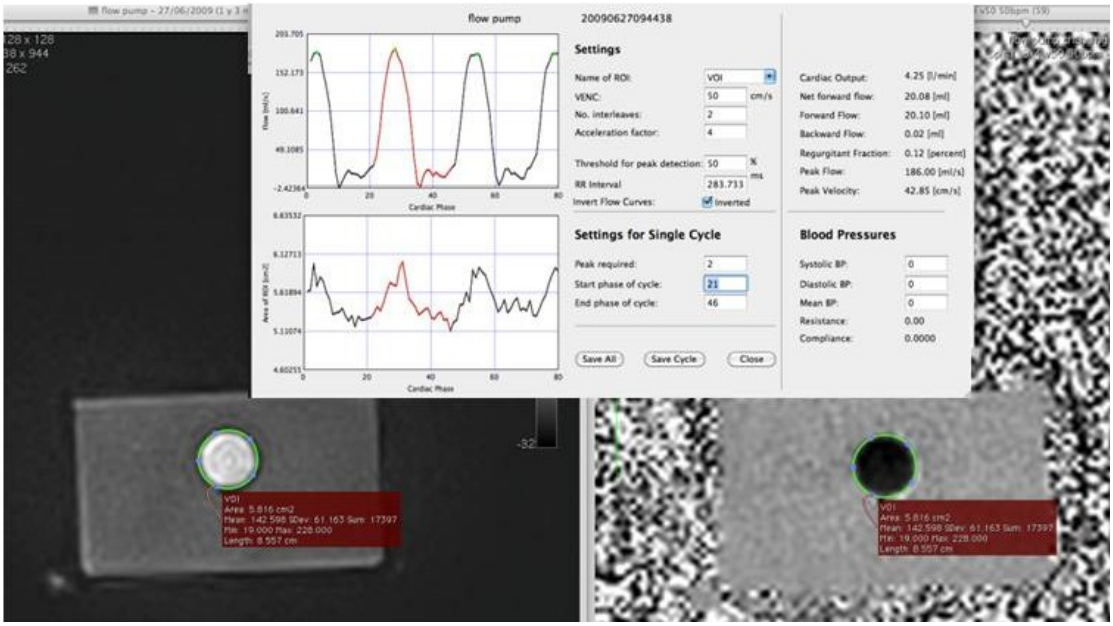

Figure 2.14: Example of data analysis for real-time sequence using the OsiriX plug-in

A good agreement was found between the pump output calculated from the reference PCMR and real-time PCMR sequence (5.09 ± 1.28 L/min vs. 5.17 ± 1.30 L/min, respectively). Bland-Altman analysis of the pump output found the bias was -0.08 L/min, with 95% limits of agreement from -0.34 to 0.18 L/min (as seen in Figure 2.15). The correlation coefficient was 0.995 ($p < 0.005$).

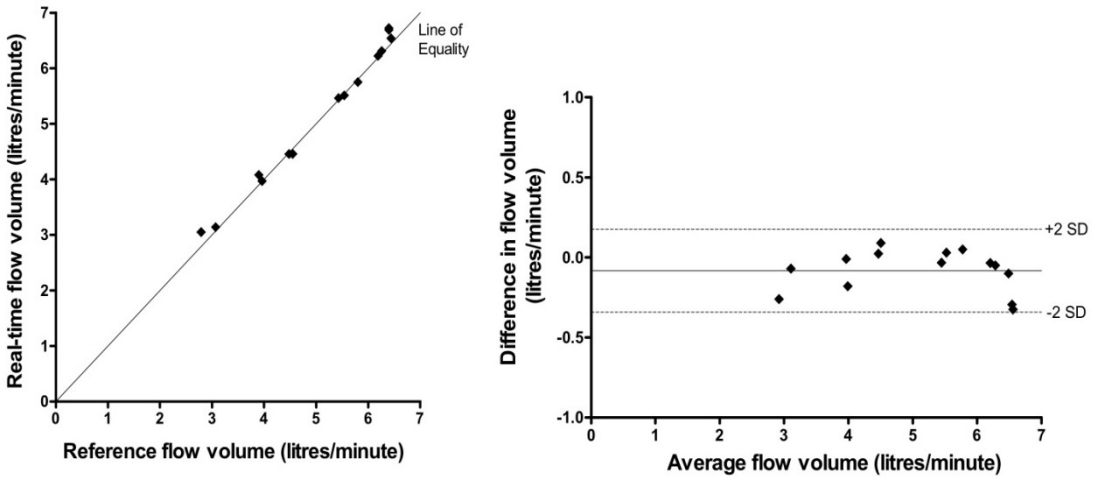

Figure 2.15: Comparison of pump output in-vitro between the reference flow sequence and real-time flow sequence. a) Correlation of flow measured from both techniques. b) Bland-Altman plot of the difference in flow measured using both techniques

2.4.4.2 Image Quality

Small residual aliasing artefacts were visible at the edges of all real-time spiral flow images, however no aliasing was seen over the vessel phantom. Additionally, some image blurring was observed and this is attributed to the sensitivity of spiral trajectories to off-resonance effects and small k-space trajectory errors. Figure 2.16 shows an example of the image quality from the standard PCMR sequence and the real-time PCMR sequence.

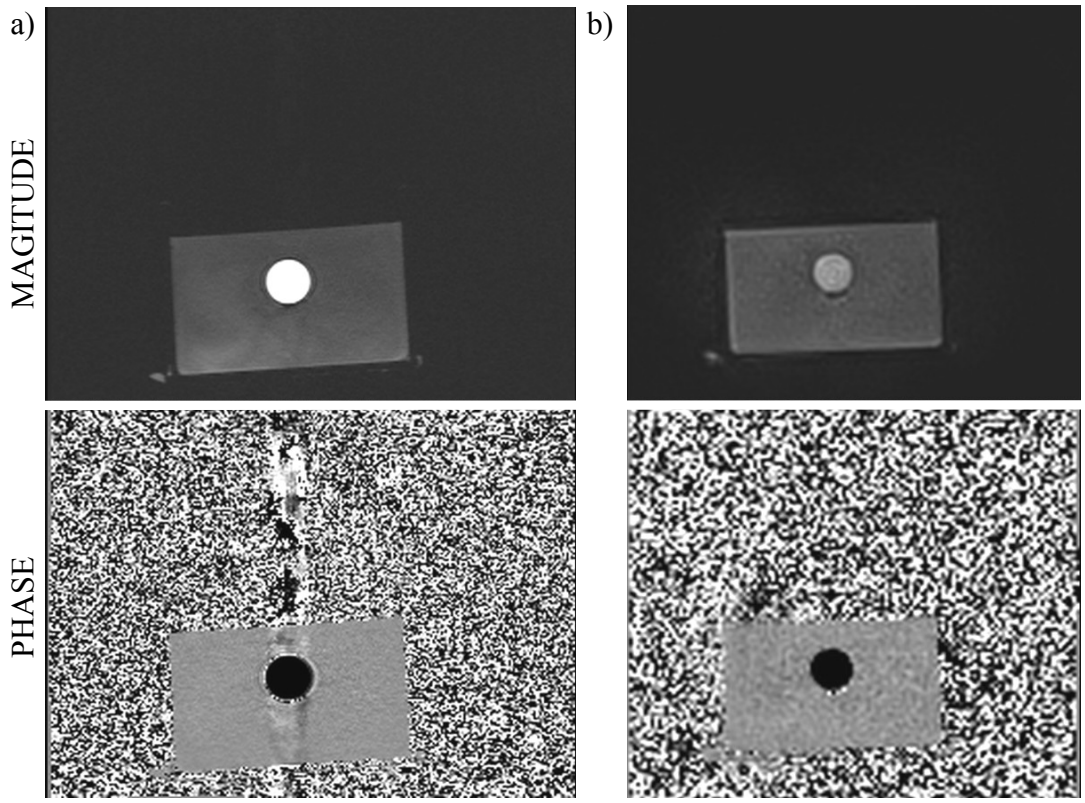

Figure 2.16: Examples of images acquired in-vitro from; a) the standard PCMR sequence and b) the real-time sequence

2.5 In-vivo Experiments

Validation of the real-time flow sequence, as well as hemodynamic response to exercise was performed in-vivo.

2.5.1 Study Population

Twenty healthy volunteers (9 Male: 11 Female) were recruited for this study between May and July 2009. The median age was 27.6 ± 6.8 years (range: 21.9-49.2 years). Exclusion criteria were;

i. Cardiovascular disease (assessed by clinical history)
ii. Illness that prevented exercise (i.e. joint disease)
iii. Contraindications for MR such as MR-incompatible implants, or pregnancy

The local research ethics committee approved the study and written consent was obtained from all volunteers.

2.5.2 MR Protocol

Exercise was performed with an MR-compatible ergometer (MR cardiac ergometer Up/Down, Lode, Groningen, Netherlands), as seen in Figure 2.18 and Figure 2.17. The participants were placed supine in the MR scanner, with their feet strapped into the peddles and the upper leg strapped to supports on the ergometer, prior to the scan. Exercise consisted of an up-ward and down-ward motion of the pedals. This type of exercise is designed to minimize motion artefacts, as motion is restricted to the lower legs.

Figure 2.17: Photograph of a subject performing exercise on the ergometer, within the MRI scanner at ICH

All imaging was performed using two six-element body-matrix coils (one on top of the subject and one underneath the subject), as seen in Figure 2.18. It is not possible to use the standard spine coil underneath the subject, as this coil must be removed to accommodate the exercise ergometer on the scanner table.

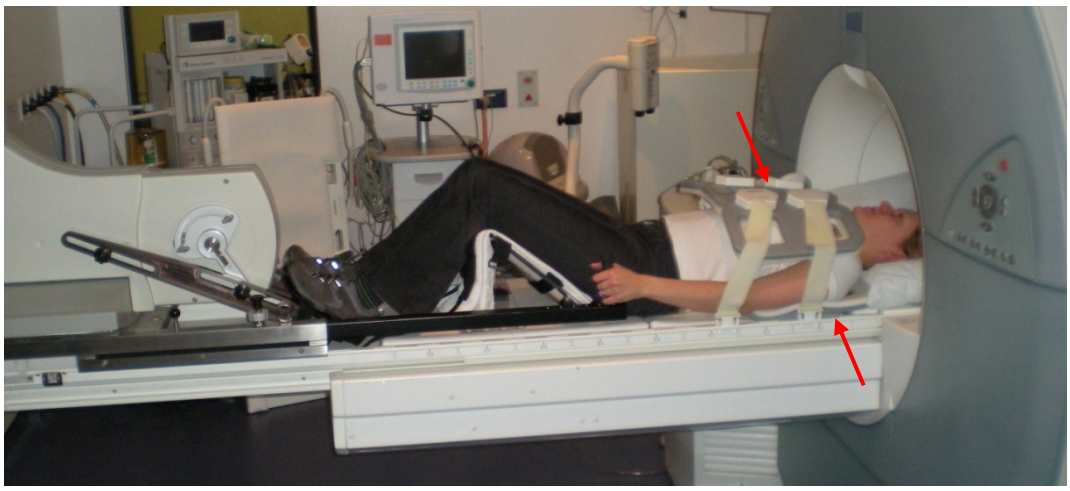

Figure 2.18: Coils used for imaging in-vivo; one body-matrix coil on top of the subject, and one underneath

The imaging protocol at rest and at two exercise levels (4W and 8W) is shown in Figure 2.19;

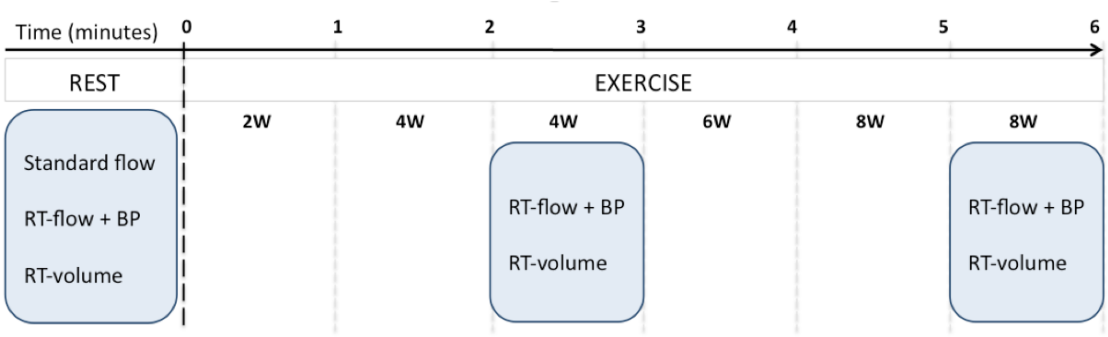

Figure 2.19: Figure from (64). The timeline of the MRI protocol at rest and during each exercise level

Exercise intensity was increased incrementally during the scan. All exercise data was acquired during free breathing and during the course of exercise. Brachial artery systolic, mean and diastolic blood pressure was measured with a cuff based oscillometric device (Datex Ohmeda, Finland) during acquisition of all real-time PCMR data.

2.5.2.1 Standard Flow Assessment

Standard aortic flow quantification was performed at rest using a retrospectively-gated, velocity-encoded gradient echo sequence (as previously described for the in-vitro experiment in section 2.4.1). The parameters are assumed to be the same as Table 2.9 unless otherwise stated in Table 2.11.

The imaging plane was located in the ascending aorta, as it passes the bifurcation of the pulmonary arteries. The scan was performed during free breathing. In this study the flow volumes measured from this sequence are assumed to be the true flow volumes.

Sequence Parameters	
TE/TR	3.2/7.0 ms
FOV	~320×240 mm
VENC	180 cm/s
NSA	3
Temporal resolution	27.1 ms (37 frames/sec)
Spatial resolution	~1.3×1.3 mm
Scan Time	~2.5 mins

Table 2.11: Standard PCMR sequence parameters, in-vivo

2.5.2.2 Real-time Flow Assessment

Real-time flow quantification was performed using the spiral PCMR sequence (as previously described in the in-vitro experiment in section 2.4.2). The parameters are assumed to be the same as Table 2.10 unless otherwise stated;

Sequence Parameters	
TE/TR	1.8/10.1 ms
FOV	500 mm
VENC	200 cm/s
Temporal resolution	40.4 ms (25 frames/sec)
Spatial resolution	3.9×3.9 mm
Scan Time	~6 sec

Table 2.12: Real-time spiral PCMR sequence parameters, in-vivo

The imaging plane was the same as the reference PCMR sequence. For each scan, 152 consecutive frames were acquired over ~6 seconds to ensure that an accurate RR-interval could be retrospectively calculated from the resulting flow profiles. Reconstruction for each scan took ~5 minutes.

2.5.2.3 Real-time Volume Assessment

Ventricular volumes were assessed using the real-time radial k-t SENSE sequence described in section 2.2.3. The sequence parameters are shown in Table 2.13;

Sequence Parameters	Radial k-t real-time
TE/TR	1.2/2.5 ms
k-t SENSE factor	8
Flip angle	38^{o}
FOV	~380×380 mm
Slice thickness	10 mm
Number of slices	11-13
Matrix	128×128
Radial Spokes	128
Pixel Bandwidth	1500 Hz/pixel
Temporal resolution	~35.5 ms (~28 frames/sec)
Spatial resolution	3.0×3.0 mm
Scan time	~30 sec

Table 2.13: Real-time volume assessment sequence parameters, in-vivo

Eleven to 13 contiguous slices were acquired in the short axis to ensure coverage of the ventricle. Real-time data for each slice was acquired for 1.5 seconds and the slice was then automatically moved down the ventricle. This sequence has previously been validated at rest (88) and during exercise (87).

2.5.3 Data Analysis

All images were processed using in-house plug-ins for OsiriX. Measurement of ventricular stroke volume was performed by Vivek Muthurangu, as described in (87, 88). Flow images were manually segmented (by J.A.S. using the modulus images) and stroke volume and cardiac output were measured. By combining the flow data with blood pressure measurements, resistance and compliance were quantified (as described in 2.3.6.2).

All results are expressed as the mean ± standard deviation. Measurements of agreement between the standard flow sequence and the real-time flow sequence, and also between the real-time k-t ventricular volume sequence and the real-time flow sequence, were performed using Bland-Altman analysis, as well as calculation of correlation coefficients. Two-tailed Student's t-tests were used to compare the hemodynamic responses at different exercise levels. All statistical analysis was performed using GraphPad Prism.

2.5.4 Image Quality

Small residual aliasing artefacts were visible in all real-time spiral flow images. Motion artefacts due to free breathing and continuation of exercise were not significant between images acquired at rest and at 8 W of continuous exercise. This is due to the very high temporal resolution achieved and because there is limited motion in the torso during the up-down exercise performed.

Additionally some image blurring was observed, which is attributed to the sensitivity of spiral trajectories to off-resonance effects and small k-space trajectory errors. Figure 2.20 shows examples of the image quality from the real-time flow sequence at rest and during exercise.

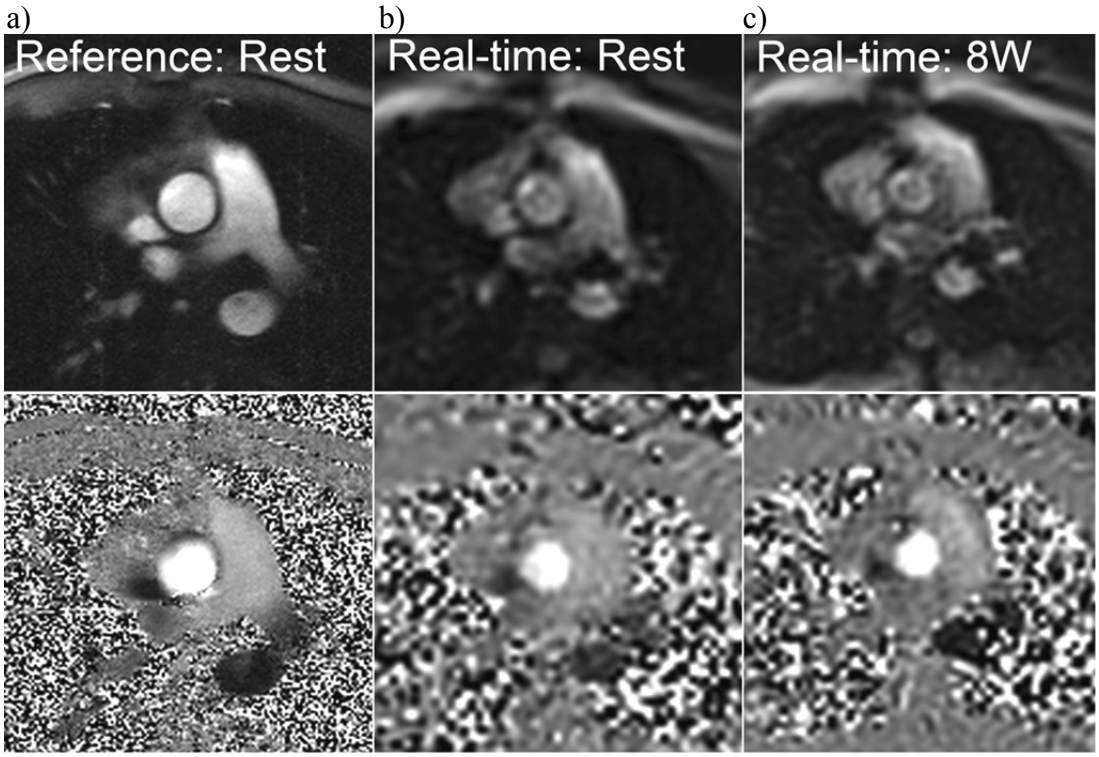

Figure 2.20: Figure from (64). Magnitude (top) and phase (bottom) images from; a) reference gated flow sequence at rest, b) real-time flow sequence at rest, and c) real-time flow sequence during exercise at 8W

2.5.5 In-vivo Validation

At rest the flow volumes calculated from the real-time spiral PCMR sequence were compared to those from the standard PCMR sequence. A good agreement in stroke volumes was found, $r = 0.994$, $p < 0.005$. Bland Altman analysis found a bias of -0.58 mL/cycle and 95% limits of agreement from -4.71 to 3.56 mL/cycle, as shown in Figure 2.21.

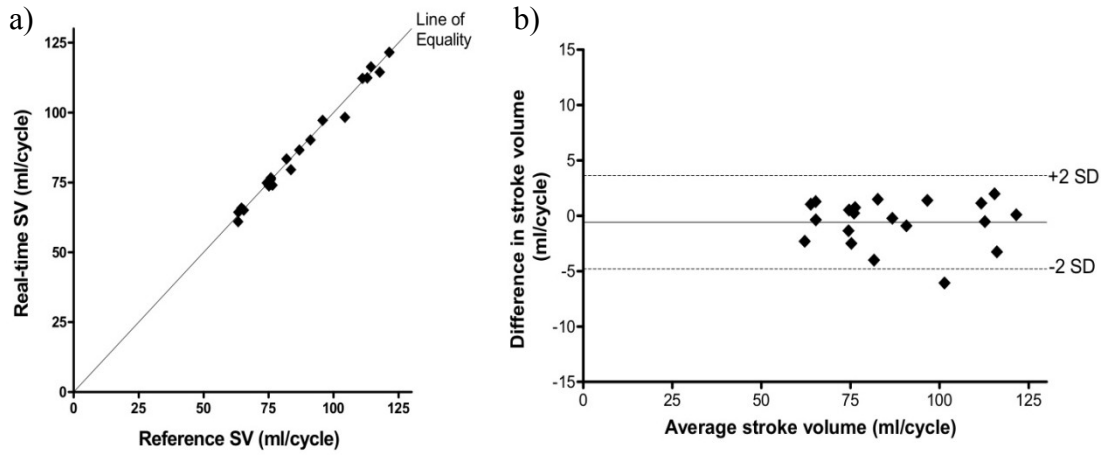

Figure 2.21: Figure from (64). Comparison of aortic stroke volumes from reference standard PCMR and real-time spiral PCMR, at rest. a) Correlation of flow measured from both techniques. b) Bland-Altman plot of the difference in flow measured using both techniques

At rest and during exercise, aortic flow volumes calculated from the real-time spiral PCMR sequence were compared with left ventricular stroke volumes from the real-time k-t SENSE volume measurements. At rest, Bland-Altman assessment found a bias of -2.04 mL/cycle and 95% limits of agreement from -8.29 to 4.21 mL/cycle. The correlation coefficient between the two data sets was 0.988 ($p < 0.005$), as seen in Figure 2.22;

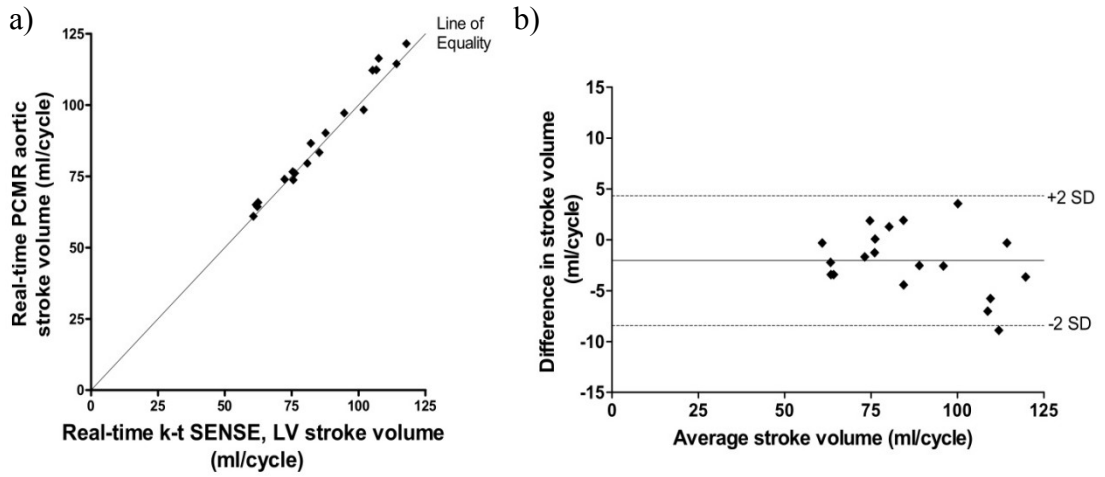

Figure 2.22: Comparison of stroke volumes in-vivo, at rest calculated from real-time k-t SENSE (LV stroke volume) and real-time spiral PCMR (aortic stroke volume). a) Correlation of flow measured from both techniques. b) Bland-Altman plot of the difference in flow measured using both techniques

During exercise at 8W, Bland-Altman assessment found a bias of 0.83 mL/cycle, with 95% limits of agreement from -4.18 to 5.84 mL/cycle and a correlation coefficient of 0.984 ($p < 0.005$), as seen in Figure 2.23;

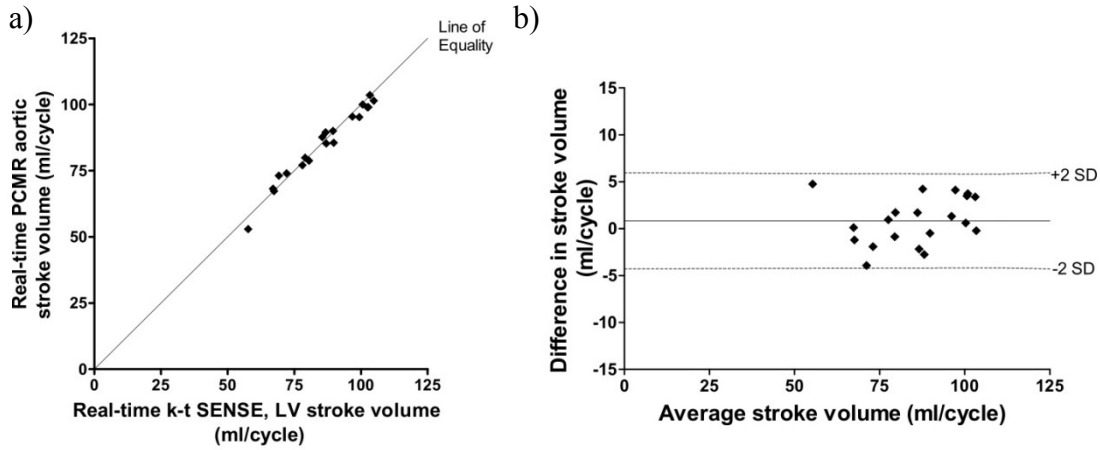

Figure 2.23: Comparison of stroke volumes in-vivo, at 8W of exercise calculated from real-time k-t SENSE (LV stroke volume) and real-time spiral PCMR (aortic stroke volume). a) Correlation of flow measured from both techniques. b) Bland-Altman plot of the difference in flow measured using both techniques

2.5.6 Vascular Response To Exercise

All participants successfully completed the exercise protocol. Blood pressure and MR flow data was measured on all subjects at rest, and at 4 W and 8 W of exercise. This data was used to calculate vascular resistance and compliance successfully in all subjects, at rest and during exercise.

Table 2.14 and Figure 2.24 show the average measured responses to exercise, which demonstrate the expected behaviour (95). Heart rate, cardiac output, and systolic and mean blood pressure increased significantly between rest and 4 W of exercise. Conversely, R and C decreased significantly between rest and 4 W. Between 4 W and 8 W heart rate, cardiac output and R changed significantly. There was no change in stroke volume or diastolic blood pressure during either stage of exercise.

	Rest+	4W+	8W+	P* (0W-4W)	P* (4W-8W)	P* (0W-8W)
Heart rate (bpm)	68.2 (12.5)	99.2 (15.8)	108.6 (21.2)	<.001	< .001	< .001
Stroke volume (ml/cycle)	87.2 (19.5)	85.1 (16.2)	85.2 (13.6)	0.3	0.97	0.41
Cardiac output (L/min)	5.8 (1.4)	8.3 (1.6)	9.1 (1.7)	< .001	0.002	< .001
Systolic BP (mmHg)	112.5 (10.4)	137.2 (15.2)	134.6 (21.0)	< .001	0.5	< .001
Diastolic BP (mmHg)	64.8 (6.0)	66.3 (12.3)	64.3 (13.1)	0.54	0.46	0.85
Mean BP (mmHg)	83.9 (6.8)	95.5 (9.4)	95.3 (8.9)	< .001	0.91	< .001
Vascular resistance (WU)	15.2 (2.9)	11.8 (2.5)	10.7 (1.7)	< .001	0.007	< .001
Arterial compliance (mL/mmHg)	1.00 (0.23)	0.62 (0.23)	0.63 (0.21)	< .001	0.8	< .001

+ Mean from all volunteers (standard deviation) * Paired t-test

Table 2.14: Response to Exercise

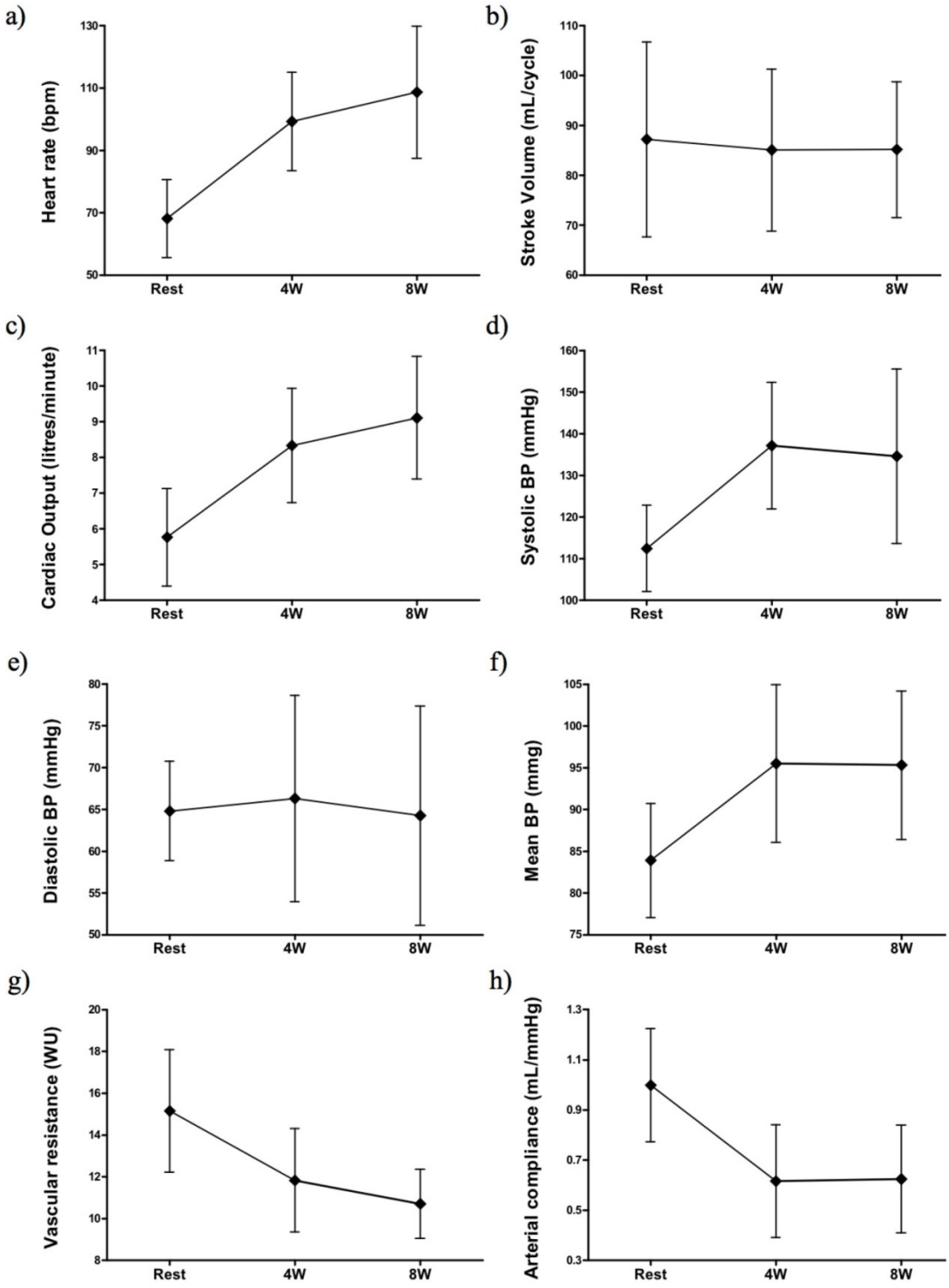

Figure 2.24: Measured responses to exercise. All points are mean values, and standard deviation is shown with error bars. Effect of exercise on a) heart rate, b) stroke volume, c) cardiac output, d) systolic BP, e) diastolic BP, f) mean BP, g) systemic vascular resistance, and h) arterial compliance. Figures a)c)g)h) from (64)

2.6 Discussion

The main findings of this study were;

i) Real-time PCMR, achieved using an undersampled spiral sequence reconstructed using SENSE, is an accurate method of measuring aortic flow at rest and during exercise

ii) MR flow data can be successfully combined with simultaneous blood pressure measurements to quantify hemodynamic responses to exercise in healthy volunteers

Exercise may be used to unmask early signs of vascular disease in at-risk groups. The ability to non-invasively measure vascular resistance and compliance further improves the sensitivity of exercise testing. Thus, this technique may allow the identification of at-risk individuals (91, 92). Impedance Cardiography offers an alternative method of measuring flow in real-time, however it is often unreliable and is not as accurate as MRI (96).

Gated flow sequences are unreliable during exercise due to excessive motion. A more robust solution is real-time imaging (82, 87). However, real-time sequences generally have a lower temporal resolution than gated sequences. This is problematic for exercise studies due to the high heart rates arising during physical stress. In this study adequate temporal resolution was achieved in three ways;

1. Spatial resolution was sacrificed, requiring less coverage of k-space and thus allowing quicker filling of k-space
2. A spiral trajectory was used, which allowed more efficient filling of k-space
3. K-space was undersampled and reconstructed using a SENSE algorithm

The resultant images have a low spatial resolution with an improved high temporal resolution, and minimal residual aliasing. Increased breathing during exercise caused little visual difference in image quality between scans acquired at rest and in exercise due to the high temporal resolution achieved. However, breathing is known to affect the stroke volume (97). In the standard flow sequence, variations in stroke volume

from breathing are averaged out, however when analyzing the real-time stroke volumes, a single flow cycle was chosen for comparison. This may explain some of the differences in flow volumes found between the two techniques.

Despite compromising the spatial resolution and using an undersampled non-Cartesian trajectory, there was good agreement with the reference flow sequence and the real-time ventricular volumes. Thus, this sequence is a robust method for assessing aortic flow during exercise.

2.6.1 Hemodynamic Response to Exercise

Using the real-time flow sequence we were able to demonstrate an increase in cardiac output at 4 W and 8 W, driven by an increase in heart rate rather than stroke volume. It has previously been observed that in raised leg supine exercise at a low intensity level, increased cardiac output was driven by heart rate rather than stroke volume (98). The low exercise levels undertaken may explain why stroke volume did not significantly change, compared to previous supine exercise studies which have used higher exercise levels including 7.5 W, 15.0 W and 22.5 W (87). Nevertheless, we were able to elicit a fall in R and C in this normal population.

To our knowledge, this is the first time vascular resistance and compliance have been quantified using MR during exercise. Previously, R and C have been assessed in the pulmonary vasculature by combining MR flow data at rest and simultaneous invasive blood pressure measurements (91, 92). We have extended these well-validated techniques to the systemic vasculature during exercise. It has been hypothesized that a lower than normal fall in R, in response to exercise is an indicator of early vascular disease (95, 99). An excessive drop in C during exercise may also predispose to vascular disease. Further work is required to demonstrate abnormal vascular responses in a patient population using this technique.

2.6.2 Limitations

In this study vascular response was only measured during mild, supine exercise. Increasing the exercise intensity may increase the sensitivity to subtle vascular abnormalities. Unfortunately, as exercise intensity increases it may become more difficult to accurately measure blood pressure non-invasively. However, it should be noted that we were able elicit a response during mild exercise.

The other limitations of this technique are the low spatial resolution and long reconstruction times. Spatial resolution could be increased by the use of a smaller FOV, which here was set high to include the arms. This could be achieved by the use of spatially-selective excitations or saturation bands, which would conversely decrease temporal resolution (see section 5.2.1). Additionally, RF-shielding of the arms and torso or improved coil configurations, may allow a smaller FOV without affecting the temporal resolution (see section 5.2.1). Alternative reconstruction algorithms, which take advantage of spatiotemporal correlations (e.g. k-t SENSE (100)), may allow an increase in matrix size without a large temporal penalty. Reconstruction times could be improved by the use of newer multi-processor graphics cards (101), which are well suited to complex iterative reconstruction (see section 5.2.2).

There are very few centres with MR compatible ergometers. Although this may limit the use of this technique in the general cardiology clinic, as stress testing becomes more important and alternative methods of exercising within the MRI environment become available (e.g. isometric exercise (102)) it is felt that this technique of non-invasively measuring the hemodynamic response to exercise will become increasingly common.

2.6.3 Conclusion

In conclusion, we have shown that it is possible to measure the hemodynamic response to exercise using a combination of real-time MR flow and simultaneous blood pressure measurements. It is hoped that this technique could be used to identify individuals at risk of developing cardiovascular disease and thus allow early medical intervention.

2.7 Automatic Segmentation Propagation of Real-Time PCMR

Post-processing of real-time PCMR images is challenging as they have low spatial resolution, low SNR, as well as misalignments from frame to frame due to free breathing. The high temporal resolution means that hundreds of frames can be acquired in a few seconds. This makes computer-assisted segmentation tools desirable.

Existing methods for automated segmentation of vessels include;

- Adaptive thresholding (103)
- Graph searching (104)
- Active contours (105)
- Model-based approaches for small vessels (106)

Transferring these approaches to real-time images is challenging.

Freddy Odille (107) investigated the use of accurate, fully deformable nonrigid registration for segmentation of the real-time data acquired in section 2.5. The results from this work have been published in the Journal of Magnetic Resonance Imaging, 2010; 33(1) p.232, by F. Odille, J. Steeden, V. Muthurangu and D. Atkinson, entitled; "Automatic Segmentation Propagation of the Aorta in Real-Time Phase Contrast MRI using Nonrigid Registration" (107) (see Appendix 2).

The registration provides displacement fields that describe motion between a reference frame and every other frame of the temporal series. A contour drawn manually in the reference frame can therefore be automatically propagated to the other frames, resulting in a fast segmentation of the whole real-time sequence of images.

The registration-based segmentation was integrated into an OsiriX plug-in. The registration was limited to a rectangular region-of-interest (ROI), of size 9×9 cm^2, selected around the reference contour to save computation time. To decrease the sensitivity of the algorithm to intensity changes from inflow enhancement, a histogram matching was applied to all images of the time series before running the registration.

For ten randomly selected volunteer data sets from section 2.5 (at rest and exercise at 4 W), two observers (F.O. and J.A.S.) performed manual segmentation (M1 and M2) and automatic segmentation (A1 and A2). The segmentation errors were quantified using Dice score (108) (the intersection area divided by the mean area of the ROI's) and stroke volume measurements.

A high Dice score (of 0.886 ± 0.039) was found when comparing automatic and manual segmentations. Additionally, a good correlation coefficient between SV measurements was found at rest and exercise, as seen in Table 2.15.

	M1 vs. M2	A1 vs. A2	M vs. A[a]
Rest			
Correlation coefficient	0.988	0.983	0.987
Bias (mL/cycle)	2.64 ± 3.31	0.54 ± 3.94	– 0.82 ± 3.83 -1.36 ± 3.07 1.82 ± 3.11 1.28 ± 3.73
Wilcoxon signed rank test	p = 0.02	p = 0.23	– p = 1.00 p = 0.28 p = 0.11 p = 0.28
Exercise			
Correlation coefficient	0.960	0.945	0.958
Bias (mL/cycle)	3.24 ± 4.10	1.17 ± 5.04	– -1.47 ± 4.52 -2.64 ± 5.43 1.77 ± 3.35 0.60 ± 3.70
Wilcoxon signed rank test	p = 0.01	p = 0.49	– p = 0.23 p = 0.28 p = 0.11 p = 0.63

[a] Results from all combinations: M_1 vs. A_1, M_1 vs. A_2, M_2 vs. A_1, M_2 vs. A_2.

Table 2.15: Results from (107) showing stroke volumes calculated from manual vs. automatic segmentations

Figure 2.25 shows an example of manual and semi-automatic segmentations from the two observers;

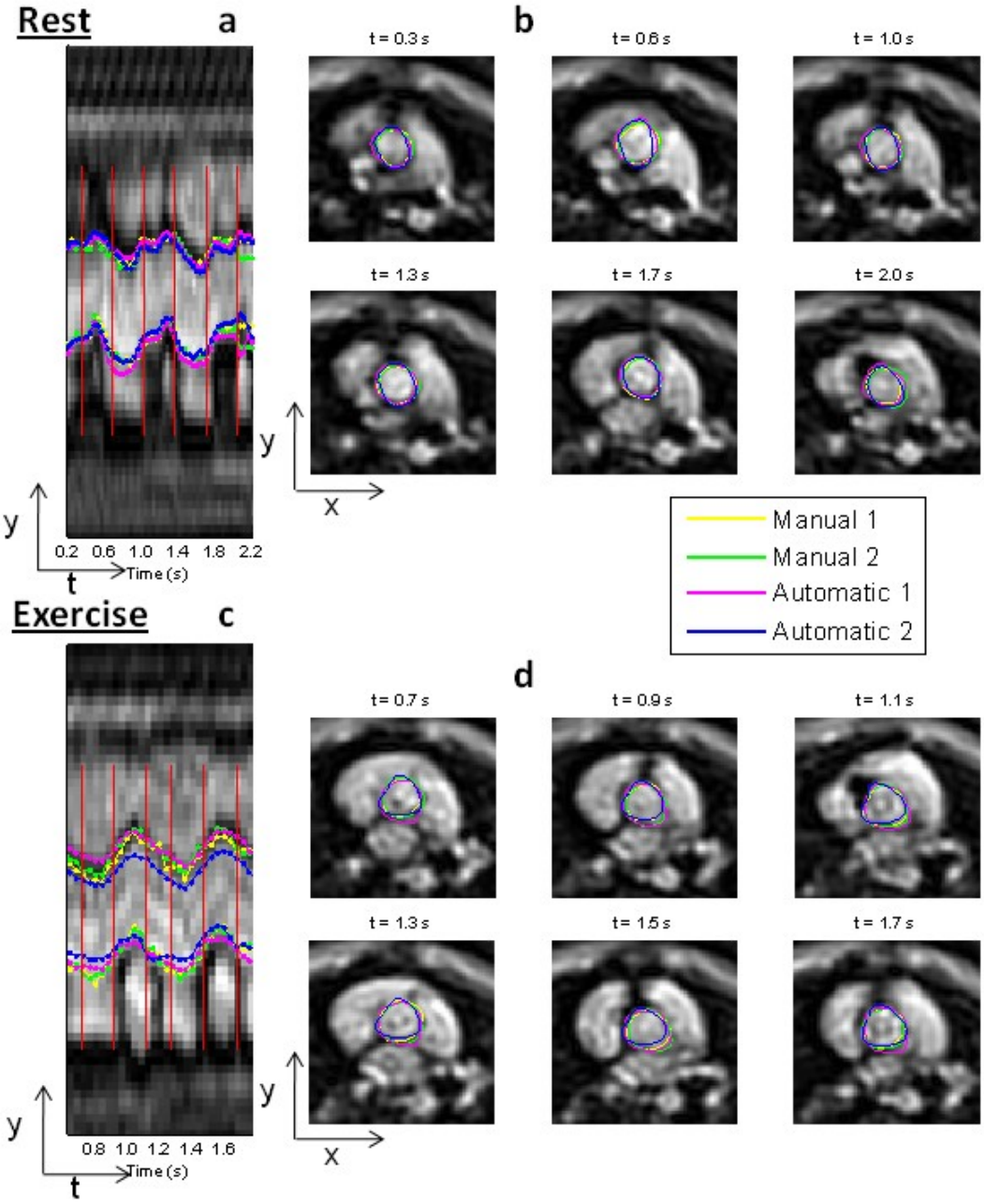

Figure 2.25: Figure from (107). Example of manual and semi-automatic segmentations from two observers, at rest (a, b) and during exercise (c,d). Segmentations are show in a hybrid space-time view (a, c) and in multiple frames (c,d) chosen at times indicated by the red vertical lines

It can be seen that the semi-automatic segmentations were accurate when compared to manually drawn ROI's, in terms of Dice score and stroke volume measures. This is true at rest and in exercise, demonstrating that this technique works even in the presence of significant movement in the vessel of interest. The variability of the semi-automatic segmentation is partly limited by the intrinsic variability of the initial manual segmentation. This may explain why the semi-automatic method does not provide a better reproducibility. The lower A1 vs. A2 bias suggests that the semi-automatic segmentation technique is less likely to suffer from systematic inter-observer error.

The main advantage of this technique is the possibility to accurately segment all 148 images in ~10 seconds. This is compared to up to 30 minutes when segmenting all 148 frames manually.

2.8 Hemodynamic Response To Mental Stress Using Real-time PCMR

This novel real-time PCMR sequence was also used in the first study to measure the hemodynamic response to mental stress using MRI, by Alexander Jones (109). This work aims to help understand the underlying links between mental stress and the development of cardiovascular disease. The results from this work have been published in Journal of Magnetic Resonance Imaging, 2011; 33(2) p.448, by A. Jones, J. Steeden, J. Pruessner, A. Taylor, A. Deanfield and V. Muthurangu, entitled; "Detailed Assessment of The Hemodynamic Response to Psychosocial Stress using Real-Time MRI" (109) (see Appendix 3).

Standard cardiac-gated sequences are unsuitable for mental stress studies, due to their;

- Long acquisition times
- Motion intolerance
- Insensitivity to short-term changes in flow patterns

Therefore, real-time measurements are necessary when imaging during mental stress tasks.

In this study the Montreal Imaging Stress Task (MIST) (110) was used to evoke a neuroendocrine stress response, while the subject was in the scanner. Mental arithmetic tasks were displayed on a computer screen (Figure 2.26), visible to the participants using a mirror. Answers were selected from a circularly arranged set of numbers (0-9) using a fibre-optic mouse. Regardless of the participant's performance, the 'performance bar' was negatively biased such that they appeared to perform poorly in comparison to the average score.

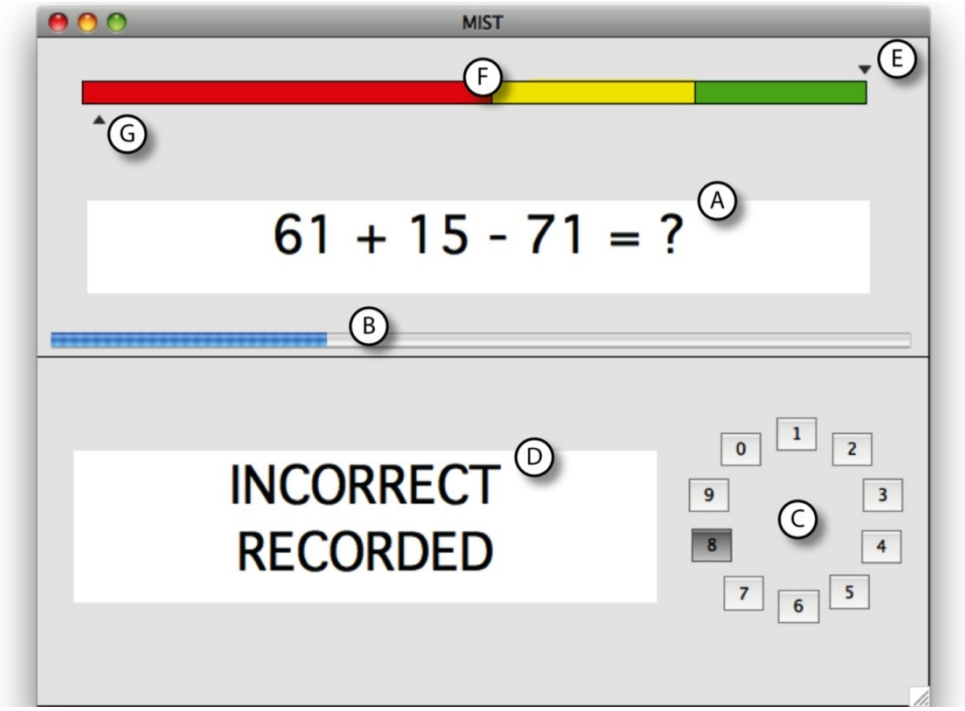

Figure 2.26: Figure from (109). A screenshot of the MIST test, showing; a) an example mathematical problem, b) a timer bar, c) possible answers (0-9) and d) feedback box. f) The 'performance bar', shows the 'average' score e) marked above the bar and the participants score g) below the bar

Flow was measured using the real-time spiral SENSE PCMR sequence using the same parameters as in Table 2.10, unless otherwise stated;

Sequence Parameters	
TE/TR	1.93/9.63 ms
Flip angle	25^{o}
Pixel bandwidth	1860 Hz/pixel
VENC	180 cm/s
Temporal resolution	38.5 ms (~26 frames/sec)

Table 2.16: Sequence parameters used in mental stress study by Jones, et al. (109)

For each measurement, 76 consecutive frames were acquired over ~3 seconds. Simultaneous oscillometric blood pressure measures were used to calculate systemic vascular resistance and arterial compliance.

Twenty-two healthy, non-smoking volunteers (11 male: 11 female) with a median age of 36.2 (range: 25.9-63.7) years were recruited. It was found that in response to stress, blood pressure increased due to increased cardiac output and reduced compliance. As stroke volume did not significantly change, the increase in cardiac output was solely due to the increase in heart rate. Greater blood pressure responses were observed in male subjects, than in female subjects, due to a greater increase in cardiac output and higher vascular resistance. Older participants were observed to have greater blood pressure responses, due to a greater decrease in total arterial compliance.

This study showed the possibility of comprehensively assessing the cardiovascular response to mental stress using a combination of the MIST test and real-time PCMR. The findings suggest stress exposes relationships of cardiovascular function with age and sex, which were not seen at rest. It is thought that this method may be used to provide a greater understanding of the mechanisms underlying the links between mental stress and the development of cardiovascular disease.

2.9 Clinical Use

In addition to the research studies described here, this real-time PCMR sequence is used in the clinical environment at ICH to measure flow in subjects with an irregular heart rate. Previously flow could not be measured in these subjects as conventional methods of measuring blood flow, using cardiac gating, fail. Figure 2.27 shows an example of flow data acquired using the real-time spiral PCMR sequence, in a patient with an irregular heart rate.

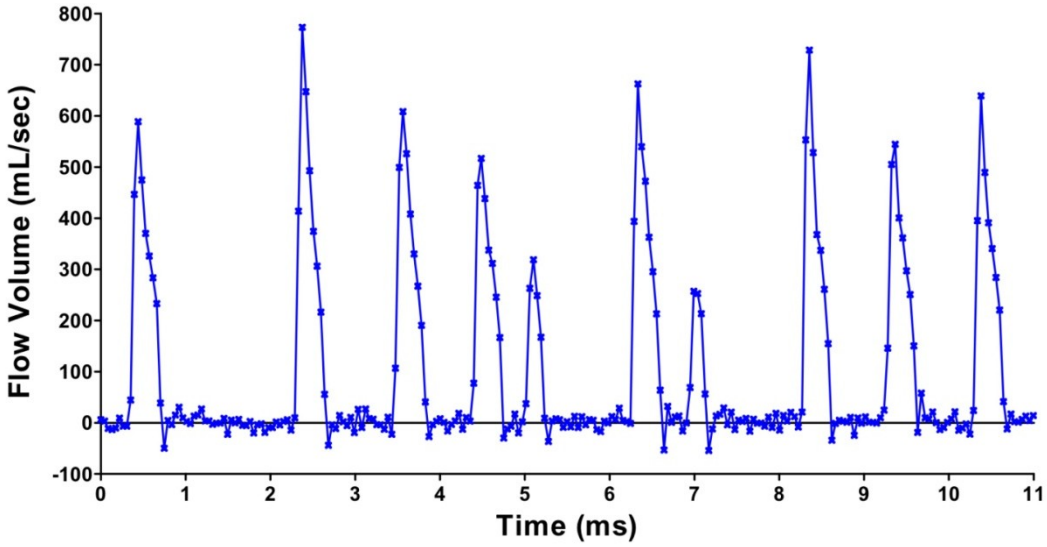

Figure 2.27: Flow curve measured using the real-time PCMR sequence, in a subject with an irregular heart rate

CHAPTER 3

Split-Acquisition Flow Measurements

3.1 Introduction

The fundamental problem with PCMR is the need to acquire two phase images to produce a single PC flow image. This limits the available spatial or temporal resolution, which is particularly problematic for real-time imaging. In children with congenital heart disease, high resolution imaging is necessary to ensure accuracy at higher heart rates and in smaller vessels. Thus, real-time imaging is not commonly used in this population. Although the real-time PCMR sequence developed in chapter 2 has a high temporal resolution, the low spatial resolution makes this sequence unsuitable for imaging small vessels. Nevertheless, fast, free breathing acquisitions are still desirable for children as they could significantly improve patient compliance and diagnostic effectiveness.

Reference-less PCMR sequences that use a single flow-encoded data set to measure flow, have been previously investigated (see section 3.2.1). In these studies, background phase offsets are predicted by fitting a low order model through the phase of static tissue surrounding the vessel of interest. Unfortunately, these methods do not perform well for intra-thoracic vessels due to the lack of stationary, surrounding tissue.

In this study, an alternative split-acquisition real-time CINE approach is considered (see section 3.3.1) for measurement of flow at rest. Flow-encoded and flow-compensated data are acquired continuously at high temporal resolution in separate short blocks. By comparing magnitude images, the closest flow-compensated frame in the cardio-respiratory cycle is determined for each flow-encoded frame. These matched flow-compensated frames are used to subtract out background phase offsets from the flow-encoded phase data. Thus, the data is acquired in real-time but with the background phase correction originating from a different heart beat. This effectively doubles the frame rate compared to conventional interleaved real-time PCMR, allowing either higher temporal or spatial resolution.

3.1.1 Aims

The aims of this study were to;

- Develop a split-acquisition spiral SENSE PCMR sequence
- Develop a fast and accurate matching algorithm
- Validate the split-acquisition flow sequence in-vivo
- Demonstrate the utility of the split-acquisition flow sequence in a paediatric population

3.1.2 Personal Contribution

To fulfil the above aims I have:

- Designed and developed a split-acquisition sequence (see section 3.3.1) developed in the Siemens, IDEA environment. This is based on the undersampled spiral SENSE sequence developed in chapter 2
- Optimised the sequence parameters (see section 3.4)
- Designed a matching algorithm (see section 3.3.2) which was subsequently developed in the Siemens, ICE environment (also prototyped in MATLAB)
- Performed validation of the matching technique (see section 3.6)
- Assessed image quality of the split-acquisition technique, by quantification of signal-to-noise ratio (SNR), velocity-to-noise ratio (VNR) and edge sharpness (see section 3.7). These measures were calculated using plug-ins developed for OsiriX (see section 3.3.3)
- Performed in-vivo validation of the sequence, in an adult population (see section 3.8)
- Showed the utility of the sequence in a paediatric population (see section 3.9)

The results from this work have been published by J. Steeden, D. Atkinson, A. Taylor and V. Muthurangu, in Magnetic Resonance In Medicine, 2010, **64**(6), entitled; "Split-Acquisition Real-time CINE Phase-Contrast MR Flow Measurements" (111) (see Appendix 4).

3.2 Literature Overview

In this section, literature on the following areas will be discussed:

- Reference-less flow measurements
- Splitting the acquisition of flow data
- Matching MR images

The studies described here do cover most reference-less flow studies. These papers were found using a combination of the search engines *GoogleScholar* and *PubMed*, The search terms used included (a combination of):

- MRI
- Referenceless
- Nonsubtractive
- Fast
- Flow
- Phase contrast

When a relevant paper was found, the referenced papers were followed up and any subsequent papers which have cited this paper were also followed up.

3.2.1 Reference-less Flow Measurements

Previous studies have investigated the use of reference-less flow imaging. These studies acquire just flow-encoded data and then predict the background phase offsets. This allows a doubling in the achievable temporal resolution.

In 1999, Man, et al. (112) described the use of a spiral sequence for non-subtractive flow measurements. By assuming that the background phase varies slowly in space, these offsets are predicted from the flow-encoded data itself.

In this method a fourth-order polynomial is fitted separately to the real and imaginary parts of the flow-encoded data (in areas of sufficient SNR). The resulting phase is assumed to be the global trend of the phase offset, and is subtracted from the flow-encoded phase image. A 2D median filter (with approximately twice the size of the vessel of interest) was then applied separately to the normalized real and imaginary parts of the resultant image. This filter is used to prevent phase caused by flowing blood, from affecting the background phase estimate. The resulting phase from the median filter is used as an additional background phase correction to the polynomial phase-corrected image.

Man, et al. showed this non-subtractive technique to have a good correlation with a standard PCMR sequence and the *bucket and stopwatch* method in a steady flow phantom (average velocity errors: ±1.7 cm/s and ±2.5 cm/s, respectively). Flow was also measured in one volunteer, where the average discrepancy in velocities was found to be up to ±6 cm/sec.
The method by Man, et al. was shown to have a reduced accuracy in velocity measurements and increased artefacts compared to a conventional PCMR sequence. Additionally, this non-subtractive method is not suitable for measuring bulk flow in the heart chambers, or in vessels which are surrounded by air.

An extension of this work was carried out in 2009 by Nielson, et al. (113) who used a balanced steady-state free-precession (SSFP), flow-encoded, Cartesian sequence (with TE = TR/2) to perform reference-less PCMR imaging. Nielson, et al. manually selected stationary tissue in close proximity to the vessel of interest (VOI). A low order polynomial was then fitted through these pixels and this was subsequently subtracted from the phase of the flow-encoded images, as seen in Figure 3.1;

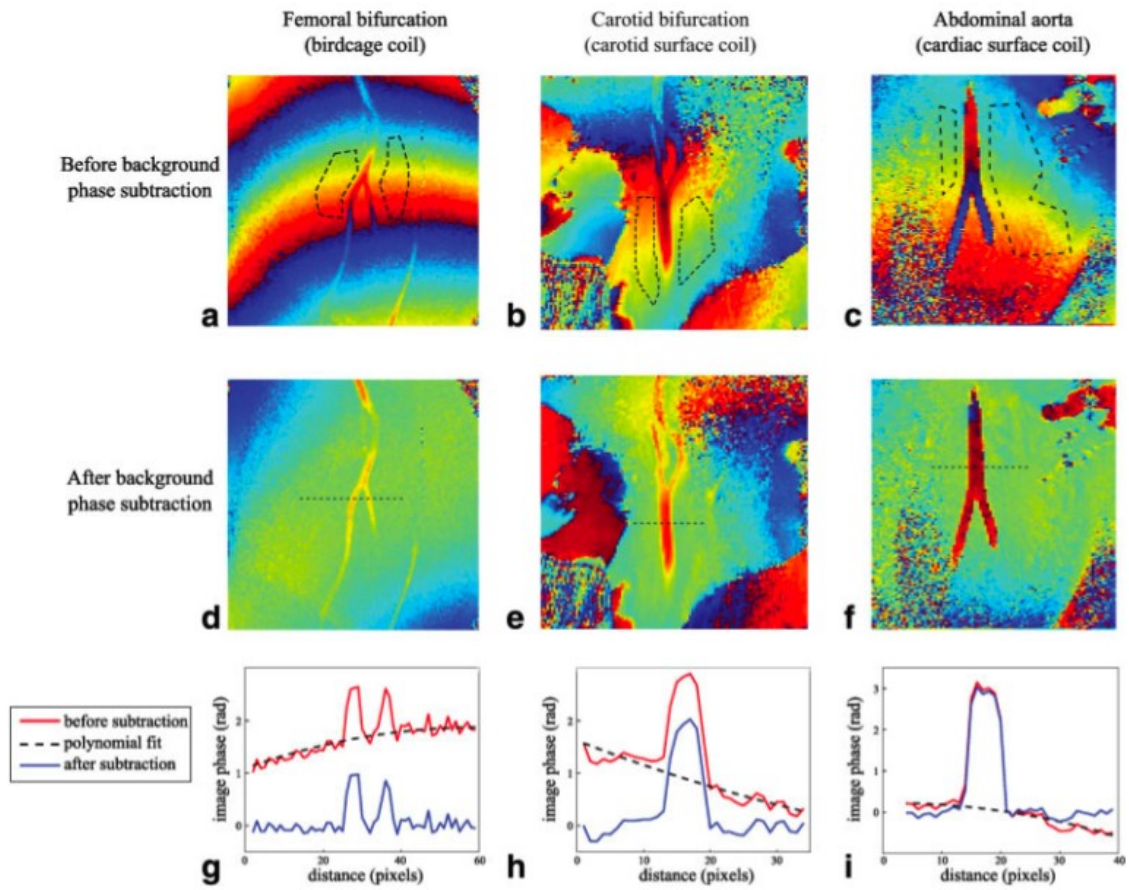

Figure 3.1: From Nielson, et al. (113). Top row shows manually drawn ROI's through the smooth background phase offsets. These images were corrected using a 2nd order polynomial fit (middle and bottom row)

Using the mean-squared error as a measure of goodness-of-fit, in two subjects it was observed that a 3rd or lower order polynomial fit could be used to adequately approximate the background phase.

Nielson, et al. demonstrated the possibility of predicting phase offsets from static regions close to the vessel of interest, to enable accurate flow quantification. The proposed technique requires manual segmentation of stationary tissue for every measurement – this is not feasible in clinical practise as it is very time consuming. This technique is also not possible where there is no or little stationary tissue near the vessel, e.g. in cardiac flow.

Both of these studies have demonstrated the possibility of acquiring just flow-encoded data and predicted the background phase offsets from stationary tissue. Unfortunately, these techniques have been demonstrated on a very limited number of volunteers, and little validation of either technique is shown. Neither of these techniques are suitable in areas where the vessel is surrounded by air, as there is no static tissue for phase reference. As we are interested in measuring flow in the aorta, which is surrounded by the lungs and non-static tissue, neither the techniques by Man, et al. or Nielsen, et al. could be used.

We wish to develop a technique which allows an effective doubling in temporal resolution, as achieved in reference-less flow measurements, however which is suitable to measure flow in the aorta. We wish to make our technique fully automated, unlike Nielson, et al. to make it clinically useful.

3.2.2 Splitting the Acquisition of Flow Data

A few studies have investigated splitting the acquisition of different flow data over multiple cardiac cycles.

A simple technique used by Mohiaddin et al. (114) to measure blood flow in the thigh, acquired a single flow-compensated image at the start of the entire study. All subsequent flow measurements were performed by acquiring just flow-encoded data. Each flow-encoded frame was corrected by subtracting the velocity-compensated image. This technique relies on the vessel of interest remaining stationary throughout the scan. This single flow-compensated image approach is therefore unsuitable for accurate flow quantification in the thoracic arteries due to the motion of the heart.

In 1994, Gatehouse, et al. (8) measured flow volumes using an ECG-triggered, single shot, spiral sequence. In this study the flow-compensated data was acquired in one heart-beat and the flow-encoded data acquired in the following heart-beat. The resulting phase-contrast data was formed by temporal matching of the flow-compensated and flow-encoded data. This approach allows an effective doubling of temporal resolution, compared to standard phase-contrast imaging.

Gatehouse, et al. measured flow using this technique in the descending aorta of normal volunteers, using the sequence parameters shown in Table 3.1;

Sequence Parameters	
TE/TR	6/50 ms
Spiral interleaves	1
Flip angle	45°
FOV	350 mm
Matrix	64×64
Slice thickness	10 mm
Effective Temporal resolution	50 ms (20 frames/sec)
Spatial resolution	5.5 mm

Table 3.1:Sequence parameters used by Gatehouse, et al. (8)

Lower velocities were measured using this sequence compared to a standard PCMR sequence. This was thought to be due to the low spatial resolution of the spiral sequence, as the large voxels cause a greater partial volume effect and also make the area measurement unreliable.

Similarly, Nayak, et al. (115) studied the possibility of acquiring different flow-encoding directions over multiple heart-beats. Continuous “triggered” real-time data was acquired, where the flow-encoding direction was modified in response to a detected R-wave. The spiral PCMR sequence, with sliding window reconstruction, by Nayak, et al. (65) described in section 2.2.1.1, was used to acquire data in one healthy volunteer. By acquiring data over three RR-intervals (breath-hold of 4 sec), flow was measured in three directions.

Additionally, Nayak, et al. (115) measured flow in six parallel slices by acquiring data (in a single flow-encoding direction) over six RR-intervals (breath-hold of 7 sec), showing how this technique could be used for multi-slice coverage. The accuracy of these techniques was not demonstrated.

These studies by Gatehouse, et al. (8) and Nayak, et al. (115) demonstrate that it is possible to acquire phase-contrast data over multiple heart-beats, and retrospectively combine the data to obtain flow measurements. However, validation of these techniques is limited. Both studies used cardiac gating to trigger the start of a new flow-encoding. We do not wish to use cardiac gating, as this is susceptible to inaccurate R-wave detection, and is not feasible for subjects with irregular heart-beats. Additionally by removing the need for ECG monitoring, we are in keeping with a philosophy of a more simple MRI (116).

3.2.3 Matching MR images

When considering how best to match flow-compensated and flow-encoded data from different cardiac cycles, we wished for a simple, fast and accurate method. In the MR literature, matching of images has previously been performed for catheter tracking. When performing catheter tracking using MRI, a thick slab is dynamically imaged and a baseline image subtracted. The baseline image is used to highlight the movement of devices and must be reacquired if any motion occurs, if scan geometry changes or if other parameters are changed.

A modified catheter tracking technique was developed by Bakker, et al. (117) where a set of dynamic reference images were acquired, instead of a single baseline image. The most suitable reference image was selected automatically for each acquired image, and used for subtraction. This method is called *adaptive subtraction*. Bakker, et al. selected the most suitable reference image, as the frame with the minimum least square error with the acquired image pixels.

This technique was validated in-vitro and in-vivo, where it was observed that the adaptive subtraction method was not sensitive to motion (of the phantom in-vitro, or respiratory motion in-vivo) or modified scan parameters, whereas with a conventional baseline subtraction, the images remained severely degraded by artefacts.

This study showed that *adaptive subtraction* can be used in-vivo to accurately track catheters, by matching images from different RR-intervals. This matching method is very simple, and hence matching can be performed rapidly with very little computational delay.

3.2.4 Summary

From the literature review it can be seen that:

- Previous studies have investigated using reference-less PCMR techniques, where just flow-encoded data is acquired and background phase offsets are predicted from stationary tissue. Unfortunately these techniques do not work well where there is little stationary tissue near to the vessel of interest
- Previous studies have investigated splitting the different encoding gradients for PCMR over multiple RR-intervals. These studies use cardiac gating, and match the flow data according to their temporal position
- In catheter tracking, an adaptive subtraction technique has been developed to successfully match images from different subsets of data

3.3 Development

In this study we investigated the possibility of splitting the acquisition of flow-compensated and flow-encoded data, and retrospectively matching these images to remove background phase offsets. Data was acquired using the real-time spiral SENSE sequence developed in chapter 2. However, an alternative acquisition scheme and an accurate matching technique, were developed.

3.3.1 Split-acquisition Scheme

Accurate phase subtraction relies on correct spatial alignment (matching in the cardio-respiratory cycle) of flow-compensated and flow-encoded data. The proposed split-acquisition strategy relies on the fact that the cardiac and respiratory cycles have different frequencies. Thus, data from adjacent RR-intervals is likely to be in similar positions in the respiratory cycle. This means that flow-compensated and flow-encoded data can be acquired continuously in consecutive short blocks and still be matched in the cardio-respiratory cycle.

As it is necessary to capture one whole cardiac cycle in each block, each block must be longer than one RR-interval. However, to ensure adjacent blocks are in a similar position in the respiratory cycle, each block must be as short as possible. Therefore, in this study the split-acquisition sequence was divided into three blocks of two seconds each (compensated – encoded – compensated), as seen in Figure 3.2;

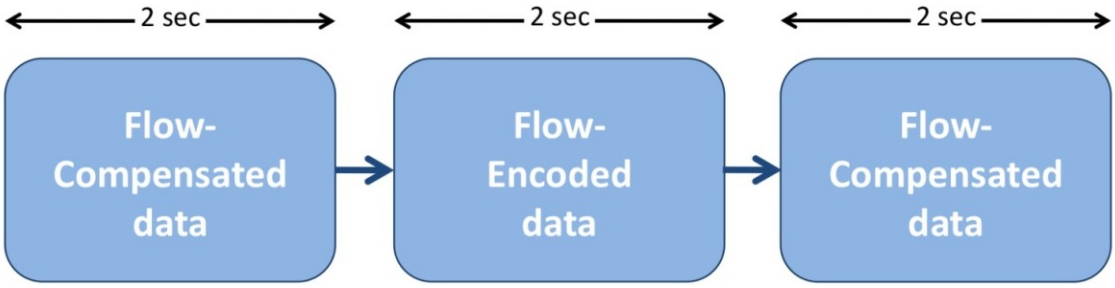

Figure 3.2: Acquisition of flow data for split-acquisition technique

Two flow-compensated blocks were used to increase the likelihood of at least one flow-compensated measurement being acquired at a similar point in the respiratory cycle to each flow-encoded measurement.

3.3.2 Matching Technique

Precise matching of flow-compensated and flow-encoded data is necessary to ensure accurate flow measurements. In this study we propose to use a variation of the adaptive subtraction technique used by Bakker, et al. (117) (section 3.2.3), to retrospectively match the flow-compensated and flow-encoded data.

In this study we are interested in accurate quantification of flow in the aorta. It is therefore important that the flow-encoded and selected flow-compensated images align well in the vessel of interest. By planning the scan position so that the vessel of interest was in the centre of the resultant images, it was possible to apply an adapted 2D Tukey window (as described in section 2.3.2.1) to all magnitude images before matching, to attenuate signal at the edge of the image. This weights the matching more heavily on the vessel of interest. The optimal filter parameters (as found in preliminary group of 10 volunteers) were found to be; flat top radius = FOV/6, transition width = FOV/8. The effect of this Tukey filter can be seen in Figure 3.3;

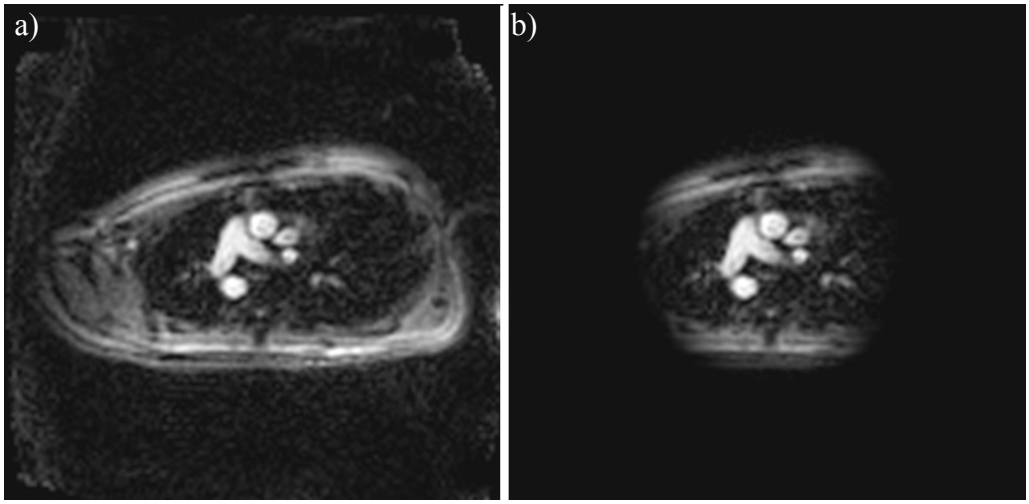

Figure 3.3: Effect of the Tukey filter on the magnitude images. a) Magnitude image before Tukey filter, b) Windowed magnitude image after Tukey Filter

Each windowed flow-encoded frame was then matched to a windowed flow-compensated frame from either of the two blocks, using the following scheme (also see Figure 3.4);

- Pixel-wise subtraction of the flow-encoded frame (windowed magnitude reconstruction) from every flow-compensated frame (windowed magnitude reconstruction, from both blocks) to produce a set of difference images
- A matching error metric (ε) was calculated by summing all of the absolute pixel values in each difference image
- Identification of the 'matched' flow-compensated frame that is associated with the lowest ε value
- Phase subtraction of the flow-encoded frame with its matched flow-compensated frame to remove background phase offsets and produce the final PC image

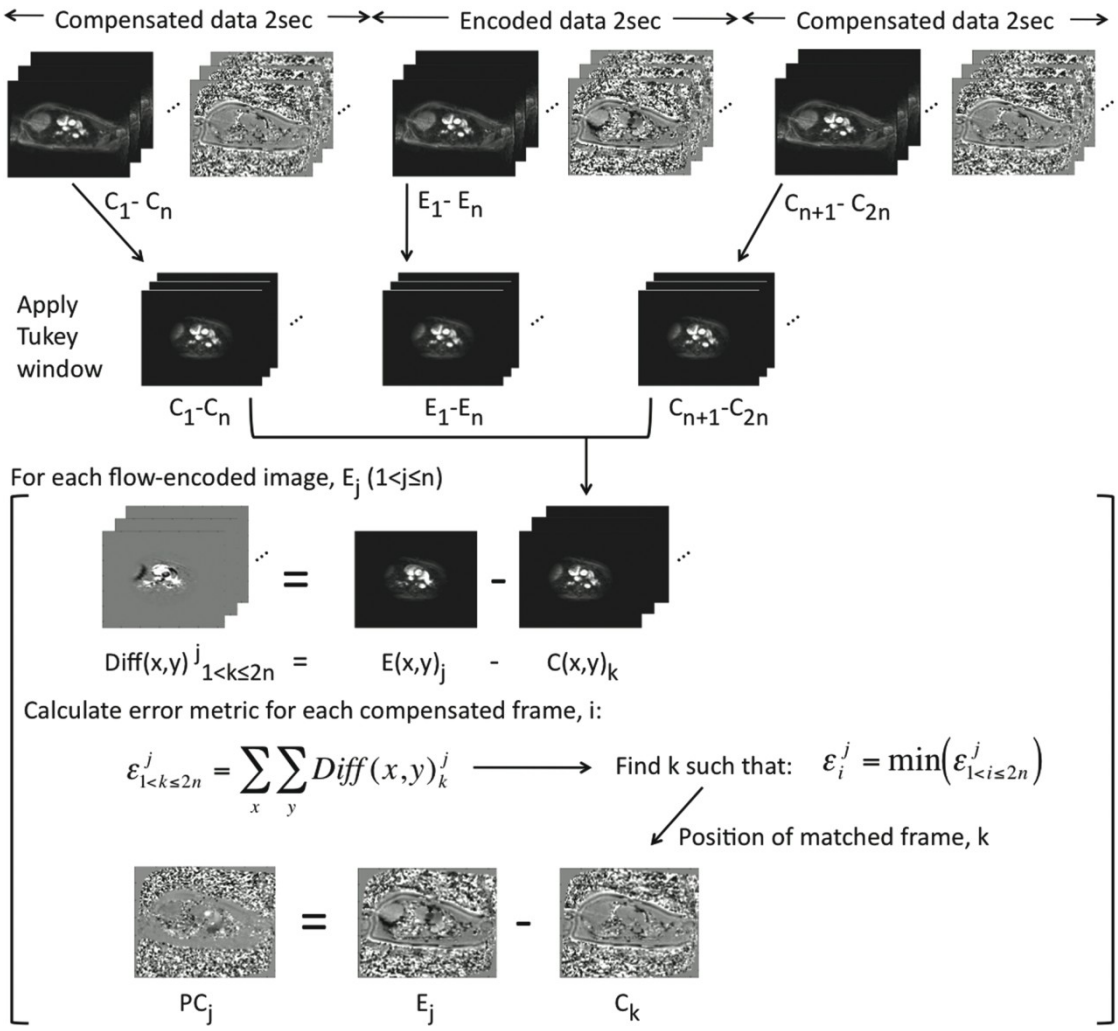

Figure 3.4: Figure from (111). Pipeline of data acquisition and reconstruction for the proposed split-acquisition real-time CINE PCMR technique

3.3.3 Development of Image Quality Assessment Tools

We wished to quantify the image quality of the resultant split-acquisition sequence. Parallel imaging is known to affect the SNR by;

$$SNR_{SENSE} = \frac{SNR_{NORMAL}}{g\sqrt{R}} \qquad \textit{Equation 3.1}$$

where SNR_{NORMAL} is the SNR achieved in a non-acceleration acquisition and g is the *geometry factor* which determines how independent the coils are (15).

In this study image quality was assessed using measures of SNR, VNR and edge sharpness – this allowed us to assess the effect of matching data from different RR-intervals on the resultant image quality. True quantification of SNR and VNR in images acquired using non-Cartesian parallel imaging is non-trivial due to the uneven distribution of noise (88, 118). Therefore in this study estimated SNR and estimated VNR were calculated. Due to time restrictions these estimated SNR and VNR measurements were not compared to true SNR and VNR measurements.

3.3.3.1 Calculation of Estimated SNR

Noise in the signal intensity (σ_S) was estimated from a ROI manually drawn in approximately stationary tissue as close to the vessel of interest as possible (note: this ROI is only used for the SNR and VNR calculations and not for background correction). For each pixel within the ROI, the standard deviation of the magnitude data was calculated over all measurements. The estimated signal noise, σ_S, was calculated as the average standard deviation over all pixels. The estimate of SNR was then calculated by dividing the mean pixel intensity inside the vessel of interest (during peak systole) by the estimated signal noise.

3.3.3.2 Calculation of Estimated VNR

Similarly, an estimate of VNR was calculated by dividing the mean velocity inside the vessel of interest (during peak systole) by an estimate of velocity noise (σ_V). The estimated velocity noise was calculated from the same ROI in stationary tissue as used above. For each pixel within the ROI, the standard deviation of the phase data was calculated over all measurements and averaged over all pixels to provide an estimated velocity noise, σ_V. This is the same method as used by Nielsen, et al. (113).

3.3.3.3 OsiriX Plug-in Implementation

The calculation of estimated SNR and estimated VNR was implemented as a plug-in for OsiriX. In this plug-in;

- An average magnitude image is formed from all phase-contrast magnitude frames
- The user manually segments an area of stationary tissue near to the vessel of interest in the average image (see Figure 3.5a). This ROI is copied to all phase-contrast magnitude frames
- The user manually segments the vessel of interest in the average image (see Figure 3.5b). The semi-automated segmentation described in section 2.7 is used to propagate this ROI through all phase-contrast magnitude frames
- The user opens the corresponding phase series, and the ROI's are automatically copied from the magnitude images to the phase images
- The frame with maximum flow in the vessel of interest is found (this can be changed by user from the UI) and the SNR and VNR are calculated for this frame (as described above) and output to the UI (see Figure 3.5c)

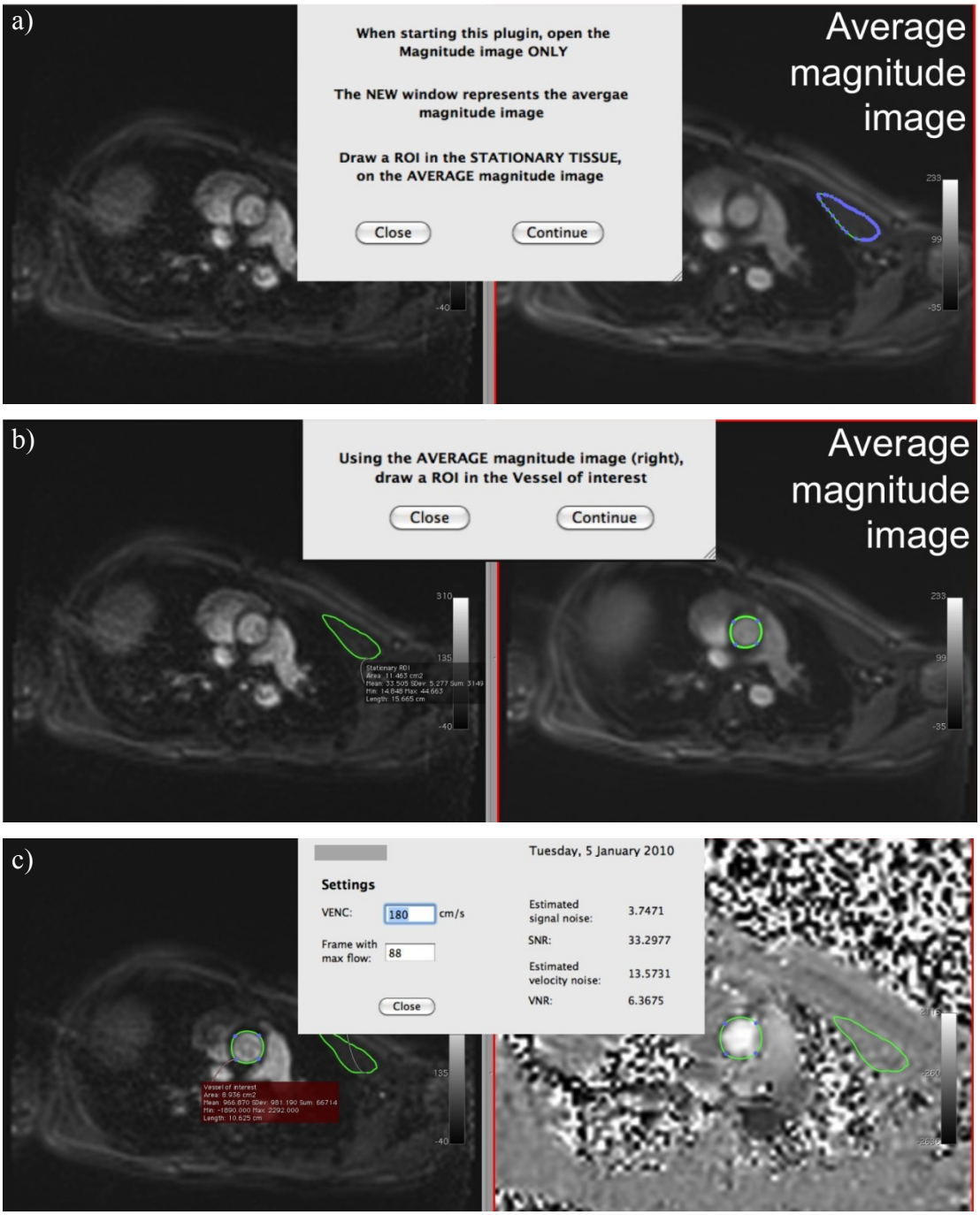

Figure 3.5: OsiriX plug-in developed for calculation of estimated SNR and VNR. a) First a ROI drawn in stationary tissue in an average magnitude image. b) The stationary ROI is copied to all magnitude frames (left). A ROI is then drawn in the vessel of interest in the average magnitude image. c) The semi-automatic segmentation tool is used to propagate the segmentation of the vessel through all magnitude frames. Estimated SNR and VNR are calculated in the frame with maximum flow (as indicated on the UI)

3.3.3.4 Calculation of Edge Sharpness

A quantitative edge sharpness measure was calculated by measuring the maximum relative gradient of pixel intensities across the border of the vessel of interest, as previously been carried out by Muthurangu, et al. (88). In this measure, sharp edges in the images are represented by a high gradient of the pixel intensities. To prevent noise providing artificially high gradients, the pixel intensities were fitted to a fifth-order polynomial prior to differentiation (88).

A plug-in was implemented for OsiriX, where the user draws a line over the border of the vessel in the frame during peak systole (as seen in Figure 3.6). The pixel values at 1 mm intervals along this line are found, and a 5th order polynomial fit is made to the data. The original pixel intensities and the fitted pixel intensities are plotted (in red and black, respectively) in the top graph on the plug-in (see Figure 3.6) allowing the user to assess how well the polynomial fit has worked.

The relative gradient of pixel intensities was calculated by differentiation of the polynomial data, and dividing the result by the pixel intensities – this is plotted on the bottom graph of the plug-in (see Figure 3.6). Edge sharpness is taken to be the maximum gradient of the pixel intensities along the ROI.

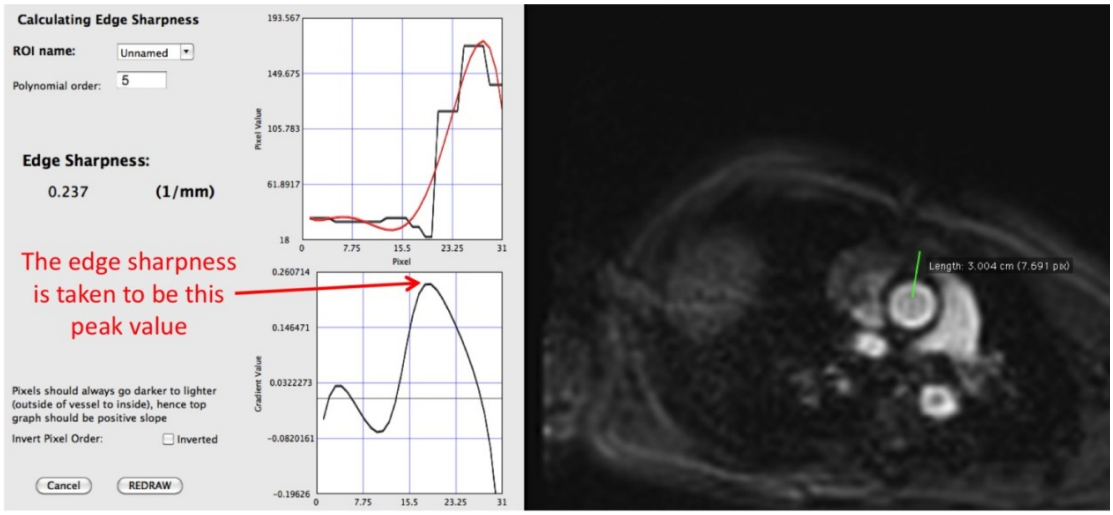

Figure 3.6: OsiriX plug-in used to calculated edge sharpness

3.4 Optimisation of Sequence Parameters

In this study we wished to demonstrate the effective doubling in temporal resolution achieved using a split-acquisition technique, and also the ability to achieve increased spatial resolution.

To demonstrate the effective doubling in temporal resolution, a high temporal resolution (HTR) split-acquisition sequence was developed and compared to the standard interleaved real-time sequence developed in chapter 2. These two sequences were run with the same scan parameters, including a 128 matrix (giving a spatial resolution of 3.9×3.9 mm, with a FOV of 500 mm). After optimisation the split-acquisition sequence achieved a temporal resolution of 22 ms, and the standard real-time sequence achieved a temporal resolution of 44 ms (using 12 spiral interleaves accelerated by a factor of 4 – see Table 3.2 for all imaging parameters).

To demonstrate the ability to increase the spatial resolution whilst still maintaining a high temporal resolution, a high spatial resolution (HSR) split-acquisition sequence was also tested. This sequence used a 192 matrix. It was found that 24 spiral interleaves accelerated by a factor of 4 gave the best compromise between image quality and adequate temporal resolution. With these settings a split-acquisition sequence with a spatial resolution of 2.6×2.6 mm (and a temporal resolution of 38 ms) was achieved (see Table 3.2 for all imaging parameters).

The resulting image quality from the two split-acquisition sequences in a resolution phantom, can be seen in Figure 3.7.

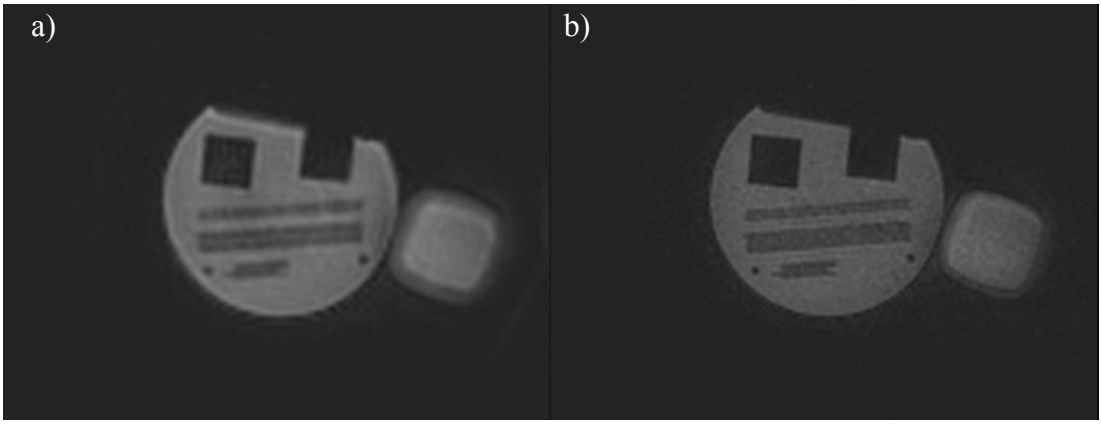

Figure 3.7: Examples of image quality in a resolution phantom (circular object on left of image), with a bottle of oil (square object on right of image) from the optimised split-acquisition sequences, a) HTR sequence, b) HSR sequence

3.4.1 In-vitro Validation

To assess the accuracy of the split-acquisition sequences, an experiment was carried out using the pulsatile flow pump described in section 2.4. The developed split-acquisition sequences were observed to be accurate when compared to a reference standard PCMR gated sequence and the standard real-time sequence (developed in chapter 2), as seen in Figure 3.8.

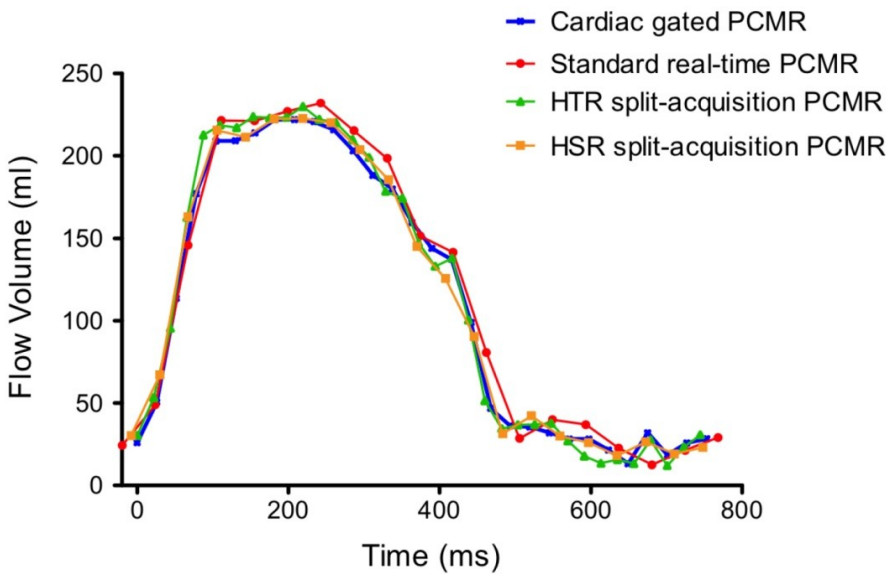

Figure 3.8: Comparison of flow profiles from the pulsatile flow pump between the four sequences tested

For the data shown in Figure 3.8 a good agreement was found in stroke volumes (reference gated PCMR sequence; 86.6 mL/cycle, standard real-time PCMR sequence; 91.9 mL/cycle, HTR split-acquisition sequence; 87.4 mL/cycle, HSR split-acquisition sequence; 87.7 mL/cycle). However in the flow pump there is very little motion, therefore it is not possible to assess the accuracy of the matching algorithm using the pump. Therefore, it was necessary to perform all validation of the matching technique in-vivo.

3.5 Adult Protocol

The adult population consisted of 15 healthy volunteers (7 male, 8 female: median age 39.8: range 25.2-57.9 years), and 5 patients with congenital heart disease (1 male, 4 female: median age 23.4: range 15.2-37.7 years). Additionally the split-acquisition method was tested on a single adult volunteer with an irregular heart rate. Exclusion criteria were;

i) Aortic regurgitation
ii) Aortic surgery
iii) Contraindications for MR such as MR-incompatible implants
iv) Pregnancy

The local research ethics committee approved the study and written consent was obtained from all volunteers and patients.

All imaging was performed at rest, during free-breathing using two three-element spine coils and two three-element body-matrix coils. The SENSE reconstruction algorithm and matching of data was performed online in the Siemens reconstruction environment. The imaging plane for aortic flow assessment was located in the ascending aorta as it passes the bifurcation of the pulmonary arteries.

Flow was measured using four sequences:

i) Cardiac gated PCMR
ii) Interleaved spiral real-time PCMR
iii) Split-acquisition real-time CINE PCMR with a high temporal resolution; 22 ms (spatial resolution; 3.9×3.9 mm)
iv) Split-acquisition real-time CINE PCMR with a high spatial resolution; 2.6×2.6 mm (temporal resolution; 38 ms)

3.5.1 Cardiac Gated PCMR

Cardiac gated PCMR was performed using a retrospectively-gated, velocity-encoded, Cartesian, gradient echo sequence (parameters shown in Table 3.2). Similarly to chapter 2, flow measurements made using this sequence were considered to be the reference standard.

3.5.2 Interleaved Spiral Real-time PCMR

Interleaved spiral real-time (*standard real-time*) PCMR was performed using the sequence developed in chapter 2 (parameters shown in Table 3.2). In this sequence the flow-compensated and flow-encoded data were interleaved in their acquisition. Magnitude and phase images for the un-combined flow-compensated and flow-encoded data were output, along with the combined PC data. Six seconds of real-time data were acquired in order to perform the 'accuracy of matching' experiment detailed below (section 3.6).

3.5.3 Split-acquisition Real-time CINE PCMR

Split-acquisition real-time CINE PCMR was carried out using the same sequence as the standard real-time PCMR sequence, except that flow-compensated and flow-encoded data were split into separate blocks, as described in section 3.3.1. Two split-acquisition real-time CINE flow assessments were carried out; one with a higher temporal resolution, and the second with a higher spatial resolution (parameters shown in Table 3.2).

	Cardiac Gated PCMR	Standard real-time PCMR	HTR split-acquisition PCMR	HSR split-acquisition PCMR
TE/TR	2.7/7.0 ms	1.9/7.3 ms	1.9/7.3 ms	1.9/6.3 ms
Spiral Readouts	-	12	12	24
Acceleration factor	-	4	4	4
Matrix Size	256×192	128×128	128×128	192×192
FOV	~320 mm	500 mm	500 mm	500 mm
Rectangular FOV	75 %	100 %	100 %	100 %
Slice Thickness	6 mm	6 mm	6 mm	6 mm
Flip Angle	30^{o}	25^{o}	25^{o}	25^{o}
Pixel bandwidth	390 Hz/pixel	1860 Hz/pixel	1860 Hz/pixel	1860 Hz/pixel
VENC	180 cm/s	180 cm/s	180 cm/s	180 cm/s
NSAs	3	-	-	-
Total Scan Duration	~2.5 mins	6 sec	6 sec	6 sec
Voxel Size	1.3×1.3 mm	3.9×3.9 mm	3.9×3.9 mm	2.6×2.6 mm
Temporal resolution	30 ms (~33 frames/sec)	44 ms (~23 frames/sec)	22 ms (~45 frames/sec)	38 ms (~26 frames/sec)

Table 3.2: Sequence Parameters for all four sequences tested, in adult study

3.5.4 Experiments

Three experiments were carried out within the adult study;

i) To assess the accuracy of the matching technique

ii) To compare image quality between the sequences

iii) To validate the split-acquisition technique

3.5.5 Data Analysis

All images were processed using in-house plug-ins for the open-source software OsiriX. For each aortic stroke volume measurement, the aorta was manually segmented (by J.A.S) using the modulus images. The plug-in described in section 2.3.6.1 was used for calculation of flow volumes from the split-acquisition data.

All results are expressed as the mean ± standard deviation, where the data is combined for the adult volunteers and patients. Bland-Altman analysis was performed to give measurements of agreement with the cardiac gated flow sequence (119). Additionally, the correlation coefficients were calculated. Comparison of means was performed by using repeated measures ANOVA (analysis of variance) tests with Bonferroni correction for multiple comparisons. All statistical analysis was performed using GraphPad Prism.

3.6 Accuracy of Matching

The purpose of the *accuracy of matching* experiments was to test the assertion that data from adjacent blocks could be matched with sufficient precision to accurately calculate flow.

3.6.1 'Simulated Split-acquisition' Reconstruction

We were able to assess the accuracy of the matching technique described in section 3.3.2, by reconstructing the standard interleaved real-time PCMR data (from the sequence developed in section 2) in two ways;

- 'Conventional' reconstruction
- 'Simulated split-acquisition' reconstruction

The 'conventional' reconstruction used the interleaved flow-encoded and flow-compensated images for subtraction and production of the final phase image. For the 'simulated split-acquisition' reconstruction, the real-time PCMR data was divided into three blocks (of two seconds each). Only the flow-compensated data was used from the first and third blocks, while only flow-encoded data was used from the second block. The 'simulated split-acquisition' data then underwent the matching process described in section 3.3.2. Flow measurements from the same data using the two reconstruction methods were compared for all adult subjects.

In addition, this 'simulated split-acquisition' reconstruction experiment was carried out on one volunteer with an irregular heart rate in order to assess the accuracy of the split-acquisition technique in this population.

3.6.1.1 Results

Mean aortic stroke volumes assessed using the 'conventional' reconstruction method and the 'simulated split-acquisition' reconstruction method were 94.6 ± 21.8 mL/cycle vs. 95.0 ± 21.9 mL/cycle ($r = 0.996$, $p < 0.0001$) respectively. Bland-Altman assessment found a bias of 0.5 mL/cycle with 95% limits of agreement of -3.3 to 4.3 mL/cycle (Figure 3.9);

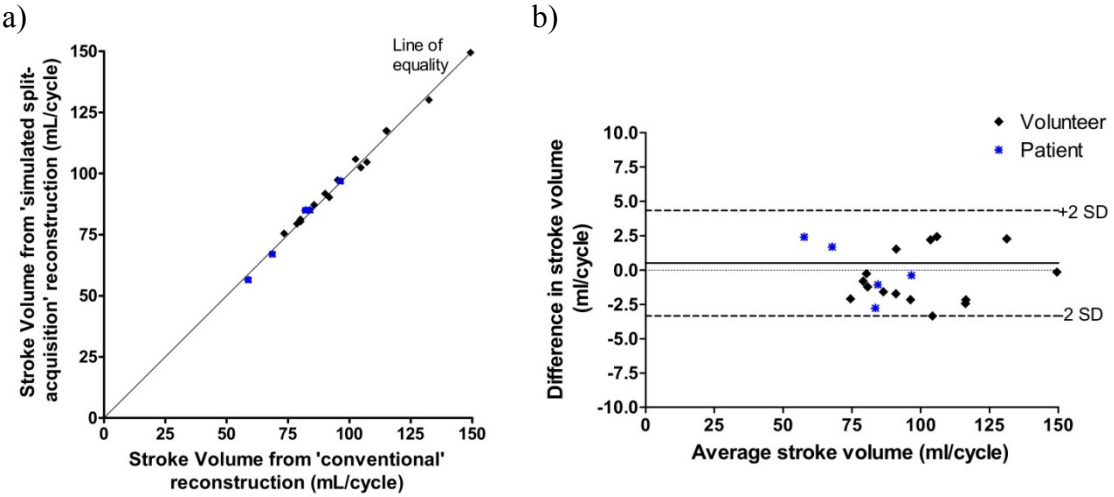

Figure 3.9: Comparison of 'conventional' and 'simulated split-acquisition' reconstructions of the same in-vivo data. a) Correlation of flow measured from both reconstruction techniques. b) Bland-Altman plot of the difference in flow measured using both reconstruction techniques

Comparable flow profiles obtained were obtained for all subjects, using the two reconstruction methods, as seen in Figure 3.10 for one patient.

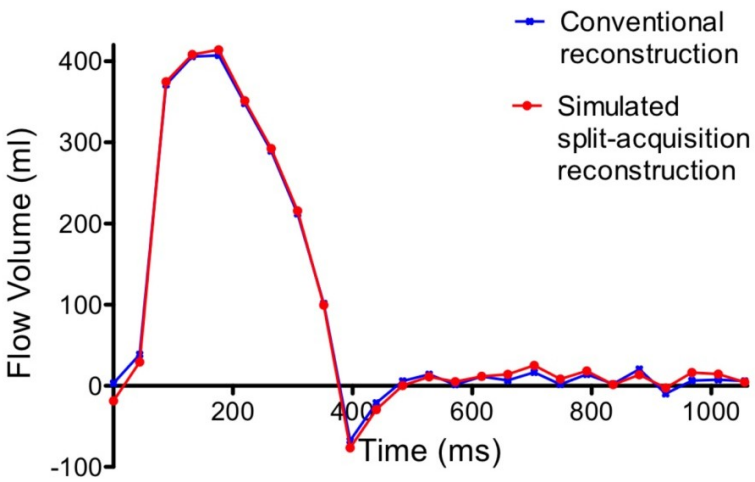

Figure 3.10: Figure from (111). Comparison of flow profiles from one interleaved real-time PCMR adult patient data set, reconstructed using the 'conventional' and 'simulated split-acquisition' reconstruction methods

In one patient with an irregular heart rate, a good agreement in flow profiles between the 'conventional' reconstruction method and the 'simulated split-acquisition' reconstruction method was also found;

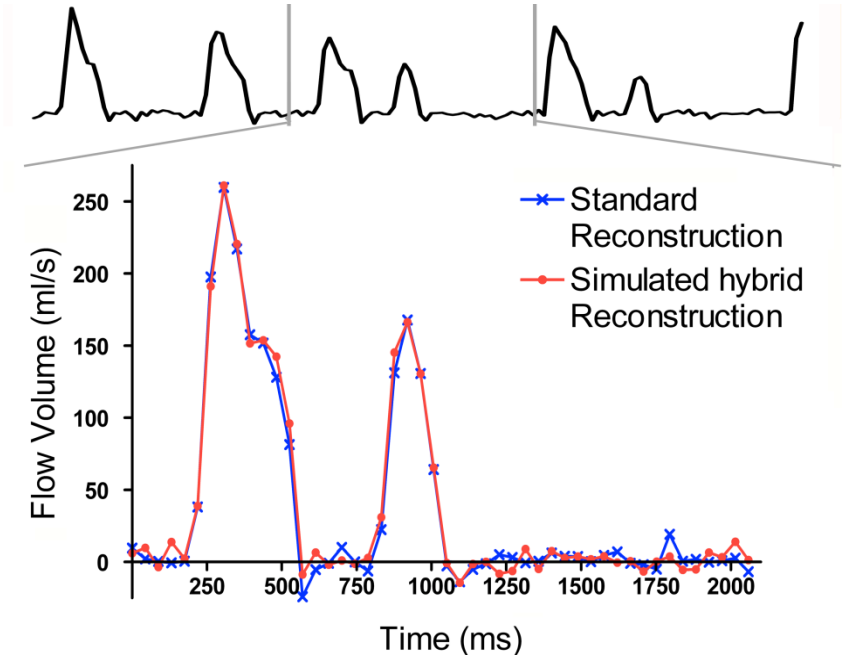

Figure 3.11: Comparison of flow profiles from one patient with an irregular heart rate. Top: flow throughout the 6 seconds of standard interleaved real-time PCMR data (calculated from conventional reconstruction). Bottom: Flow profiles from the middle third of the standard interleaved real-time PCMR data, as calculated from the 'conventional' and 'simulated split-acquisition' reconstruction methods

From the two reconstructed cardiac cycles shown in Figure 3.11, a good agreement in stroke volume was found between the 'conventional' reconstruction method and the 'simulated split-acquisition' reconstruction method; cycle 1: 53.1 mL vs. 54.9 mL, cycle 2: 23.2 mL vs. 23.9 mL, respectively.

3.6.2 Importance of Matching

The importance of accurately matching flow-compensated and flow-encoded data was also assessed. The 'simulated split-acquisition' flow-encoded frame with maximum flow was found and reconstructed using every 'simulated split-acquisition' flow-compensated frame (from the simulated split-acquisition experiment above, section 3.6.1). The resulting flow volumes were compared to the 'conventional' reconstruction for this frame. For each resulting frame the flow error and matching error metric were calculated, giving an indication of the effect of mismatching on the accuracy of the flow assessment.

A further experiment was carried out using this data to demonstrate the need for two flow-compensated blocks; before and after the flow-encoded data. The flow-compensated frame with the minimum matching error metric was found from each block and the flow errors compared. Because these two frames should be in similar position in the cardiac cycle, any differences in flow are thought to be attributed to respiratory cycle mismatching.

3.6.2.1 Results

Figure 3.12 shows the matching error metric calculated between a single flow-encoded frame (during peak systole), and all flow-compensated frames (from both blocks), for one subject. It can be seen that the matching metric has a periodicity, which is equivalent to the heart rate.

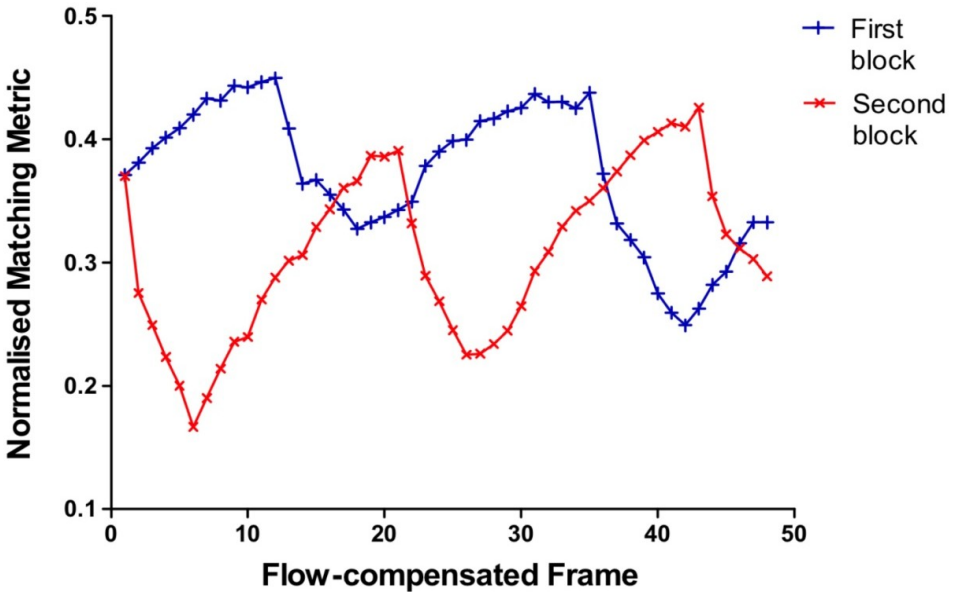

Figure 3.12: Matching error between a single flow-encoded frame and all flow-compensated frames from both blocks

Figure 3.13 shows the relationship between the matching error and the flow error (%) from a single flow-encoded frame as reconstructed with all 96 'simulated split-acquisition' flow-compensated frames, from all adult subjects. It can be seen that a small matching metric leads to a small flow error, and mismatching of frames can lead to high flow errors (up to 80 %);

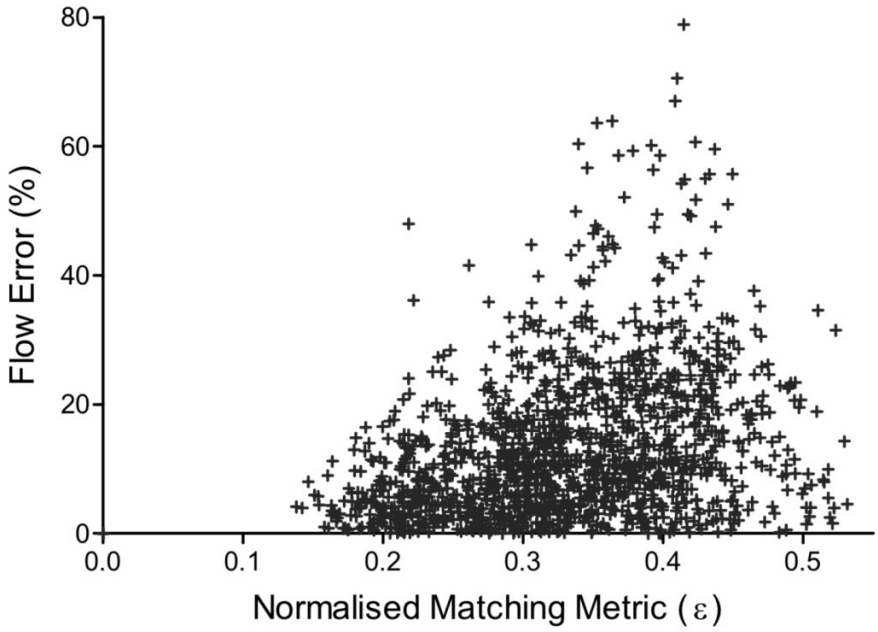

Figure 3.13: Correlation between normalized matching metric and flow error in all adult subjects

The importance of using two blocks of flow-compensated data was demonstrated by assessing flow error from the flow-compensated frame with the minimum matching metric from each 'simulated split-acquisition' block. For example, for the data shown in Figure 3.12, the lowest matching metric from the first flow-compensated block was found in the 42nd frame (matching error: 0.249, flow error: 14.1 %), and from the second flow-compensated block was found in the 6th frame (matching error: 0.167, flow error: 1.9 %). Of these two frames, the one with the lower matching metric gave a lower average flow error, over all adult subjects of 16.1 mL/cycle. In eight subjects, the minimum matching metric was found from the first block and in the remaining twelve subjects from the second block.

3.7 Image Quality

Image quality was assessed using measures of SNR, VNR and edge sharpness during peak systole, using the OsiriX plug-ins described in section 3.3.3.

Figure 3.14 shows examples of the image quality from all four tested sequences. No residual aliasing artefacts were seen over the vessel of interest, in any standard real-time PCMR images or split-acquisition PCMR images. Some image blurring was observed (see Figure 3.14) predominantly in areas of fat. This image blurring was attributed to the sensitivity of the spiral trajectories to off-resonance effects and small k-space trajectory errors.

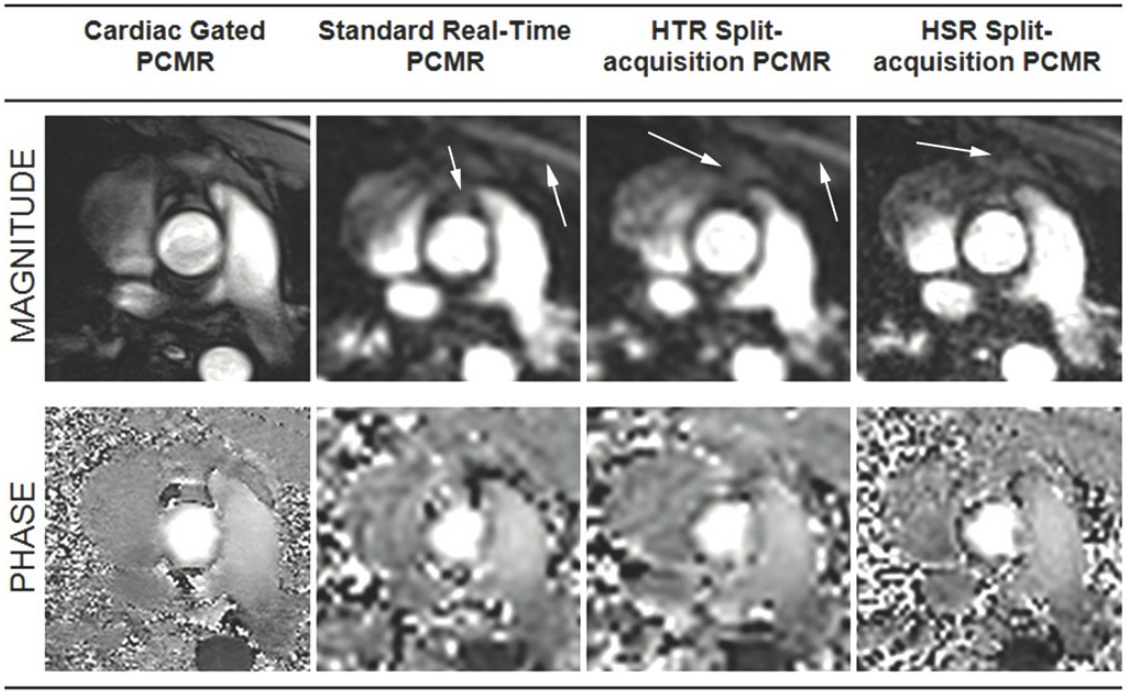

Figure 3.14: Figure from (111). Comparison of image quality from the sequences. Arrows indicate image blurring

Quantitative image quality metrics can be seen in Table 3.3. The cardiac gated PCMR images had the highest estimated SNR, compared to both standard and split-acquisition real-time CINE PCMR data. The HSR split-acquisition images had the lowest estimated SNR and VNR. Estimated velocity noise and VNR were not significantly different in the other three sequences.

Edge sharpness was significantly greater in the cardiac gated PCMR images compared to all of the real-time images (Table 3.3). However, the cardiac gated sequence had the highest standard deviation over all adults. The standard real-time and HTR split-acquisition images had very similar edge sharpness measures. The HSR split-acquisition images had slightly higher edge sharpness than the other real-time images, although this was not found to be statistically significant. A visual improvement in the edge sharpness for this HSR proposed sequence can be seen in Figure 3.14, making segmentation of the images easier.

	Cardiac Gated PCMR	Standard real-time PCMR	HTR split-acquisition PCMR	HSR split-acquisition PCMR
Estimated signal variation: σ_S	4.5 ± 1.1	5.6 ± 1.2*	6.0 ± 1.6*	6.3 ± 1.1*
σ_S / σ_S^{PC}	1	1.3 ± 0.4	1.4 ± 0.5	1.5 ± 0.5
Estimated SNR	50.3 ± 16.1	34.5 ± 10.9*	32.5 ± 10.9*	28.8 ± 8.1*
Estimated velocity variation: σ_V (cm/s)	5.8 ± 1.9	5.5 ± 2.1	5.2 ± 1.8	7.3 ± 2.0*†
σ_V / σ_V^{PC}	1	0.96 ± 0.16	0.92 ± 0.22	1.31 ± 0.24
Estimated VNR	14.9 ± 9.0	15.7 ± 9.0	16.3 ± 11.0	11.2 ± 5.1*†
Edge Sharpness (mm^{-1})	0.97 ± 0.50	0.43 ± 0.21*	0.46 ± 0.21*	0.58 ± 0.26*

* Values are significantly different from cardiac gated PCMR ($p<0.05$)

† Values are significantly different from standard real-time PCMR ($p<0.05$)

Table 3.3: Estimated SNR, VNR and edge sharpness measures for all four sequences

3.8 In-vivo Validation

The split-acquisition sequences were validated in-vivo in all adult subjects, by calculating the aortic stroke volume for each of the four sequences described in section 3.4.1. A good agreement in flow profiles was found for all subjects, as seen in Figure 3.15 for one volunteer;

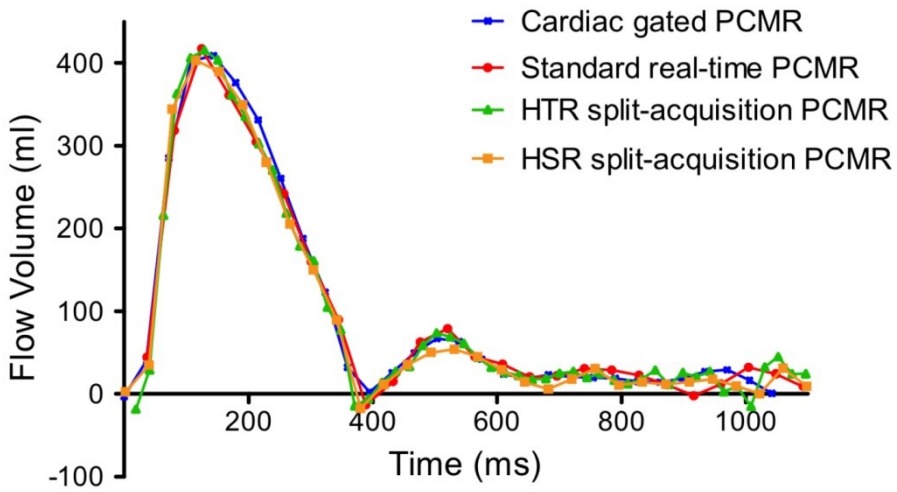

Figure 3.15: Figure from (111). Comparison of flow profiles from all four sequences in one adult volunteer

The stroke volumes calculated from each of the real-time sequences were compared to those from the gold-standard cardiac gated flow sequence and Bland-Altman assessment was carried out. The results can be found in Table 3.4, and Figure 3.16.

	Cardiac Gated PCMR	**Standard real-time PCMR**	**HTR split-acquisition PCMR**	**HSR split-acquisition PCMR**
Stroke Volume (mL)	95.2 ± 20.0	96.2 ± 20.7	95.6 ± 20.1	95.5 ± 20.4
Bias* (mL)	-	1.0	0.4	0.3
Limits of agreement* (mL)	-	-2.2 to 4.1	-3.9 to 4.7	-3.2 to 3.7
Correlation coefficient* (r)	-	0.998	0.994	0.997

*Calculated with cardiac gated PCMR sequence

Table 3.4: Flow volumes for all four sequences tested, in the adult population

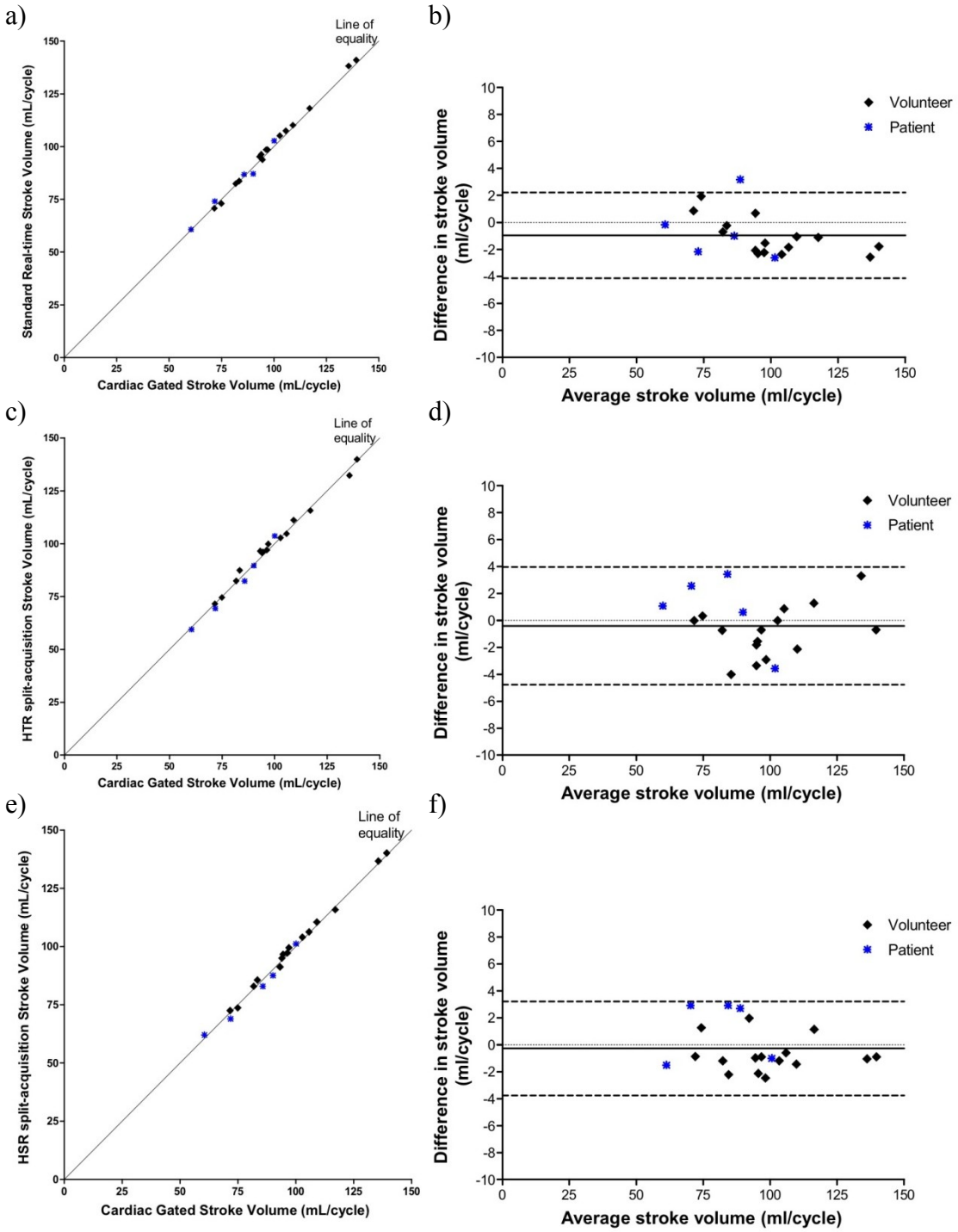

Figure 3.16: Correlation (left) and Bland-Altman analysis (right) of stroke volumes in adult population calculated from: a)-b) cardiac gated PCMR vs. standard real-time PCMR, c)-d) cardiac gated PCMR vs. HTR split-acquisition PCMR, e)-f) cardiac gated PCMR vs. HSR split-acquisition PCMR

An excellent agreement in stroke volumes between all sequences was found, with no statistical differences between any of the sequences. A slight overestimation was found in all real-time sequences, however this was not a clinically significant difference. The average heart rate for all adults was 69 beats per minute.

3.9 Paediatric Utility

To demonstrate the need for higher spatial and temporal resolution in the paediatric population, aortic stroke volumes were compared between;

i) Cardiac gated PCMR
ii) Standard real-time PCMR
iii) Split-acquisition PCMR with a high spatial resolution; ~1.9×1.9 mm (temporal resolution; ~43 ms)

The sequences have been described in section 3.4. The sequence parameters can be assumed to be the same as in Table 3.2, unless otherwise stated below;

	Cardiac Gated PCMR	**Standard real-time PCMR**	**HSR split-acquisition PCMR**
TE/TR	~2.5/7.0 ms	2.1/~7.7 ms	2.1/~7.1 ms
FOV	~250 mm	~350 mm	~350 mm
VENC	~210 cm/s	~210 cm/s	~210 cm/s
Total Scan Duration	~2.5 mins	6 sec	6 sec
Spatial resolution	~1.0×1.0×5.0 mm	~2.8×2.8×5.0 mm	~1.9×1.9×5.0 mm
Temporal resolution	~32 ms (~31 frames/sec)	~46 ms (~22 frames/sec)	~43 ms (~23 frames/sec)

Table 3.5: Sequence Parameters for all three sequences tested, in the paediatric study

The paediatric population consisted of 6 patients with congenital heart disease (3 male: 3 female, median age: 4.8 years, range: 0.2-8.3 years). Aortic stroke volumes were calculated for all three sequences and Bland-Altman analysis was performed to give measurements of agreement with the cardiac gated flow sequence.

3.9.1 Paediatric Results

The average stroke volumes and Bland-Altman assessment from the paediatric study can be seen in Table 3.6 and Figure 3.17;

	Cardiac Gated PCMR	**Standard real-time PCMR**	**HSR split-acquisition PCMR**
Stroke Volume (mL)	20.6 ± 7.6	24.3 ± 9.2†	20.8 ± 7.8
Bias* (mL)	-	3.7	0.3
Limits of agreement* (mL)	-	-0.2 to 7.6	-2.1 to 2.7
Correlation coefficient* (r)	-	0.990	0.995

* Calculated with cardiac gated PCMR sequence

† Value is significantly different from cardiac gated PCMR ($p<0.05$)

Table 3.6: Flow volumes for all three sequences tested, in the paediatric population

There was excellent agreement in stroke volumes between the gold-standard cardiac gated PCMR sequence and the split-acquisition real-time CINE PCMR sequence, with no statistical differences (in this small group) between these two sequences. However, the standard real-time sequence overestimated the stroke volume when compared to the cardiac gated PCMR sequence. The average heart rate for all children was 87 beats per minute.

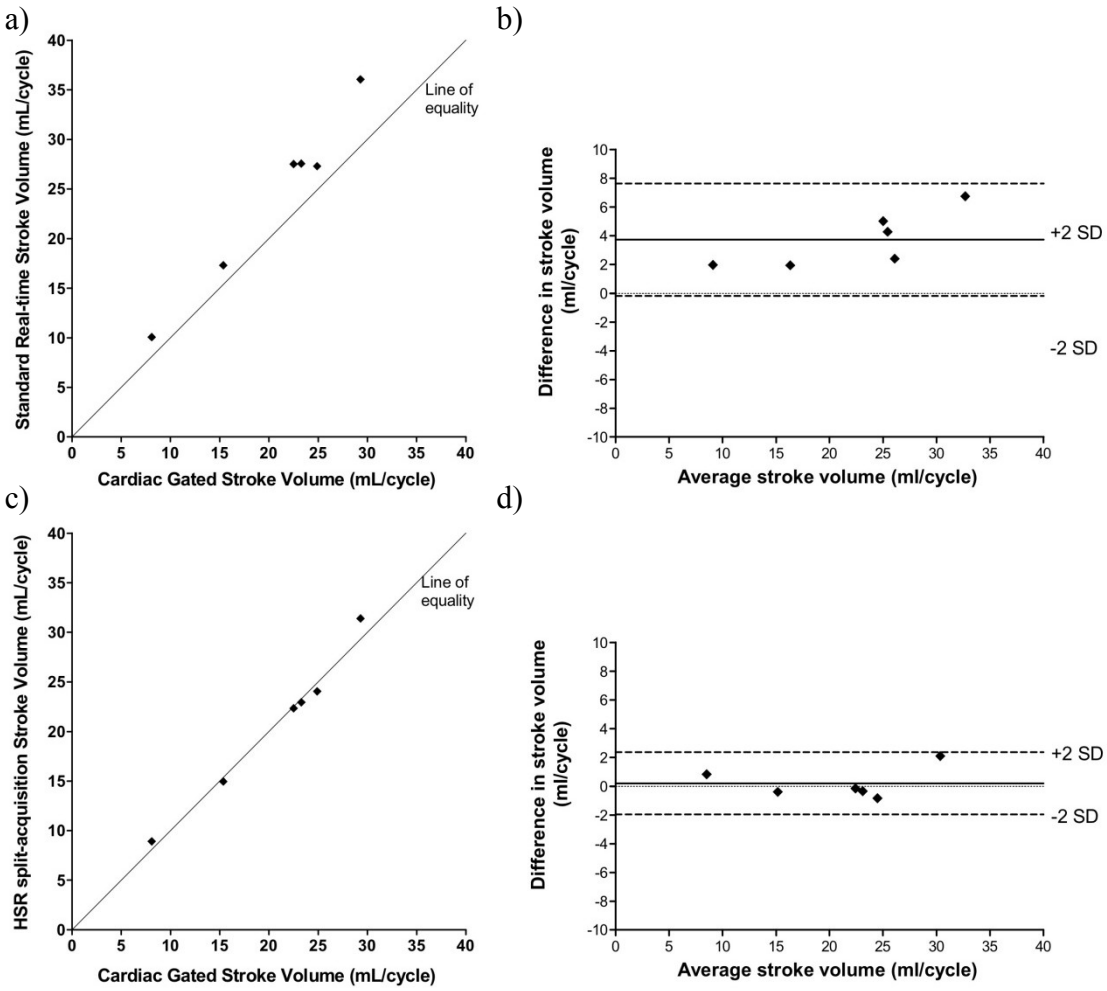

Figure 3.17: Correlation (left) and Bland-Altman analysis (right) of stroke volumes in paediatric population, calculated from: a)-b) cardiac gated PCMR vs. standard real-time PCMR, c)-d) cardiac gated PCMR vs. HSR split-acquisition PCMR

3.10 Discussion

We have demonstrated the feasibility and accuracy of a novel split-acquisition real-time CINE PCMR sequence. Unlike standard real-time PCMR, flow-compensated and flow-encoded data are acquired in separate short blocks and retrospectively matched in the cardio-respiratory cycle. The resulting sequence has the benefit of an effective doubling of the temporal resolution or an increase in the spatial resolution when compared to standard interleaved, real-time PCMR.

3.10.1 Accuracy of Matching

Accurate PCMR assessment relies on cardio-respiratory matching of flow-encoded and compensated data. The reliability of matching was assessed in an adult population by comparing both 'conventional' and 'simulated split-acquisition' reconstructions of the same real-time PCMR data. The excellent agreement in stroke volumes and flow curves, supports the assumption that it is possible to remove background phase offsets using matched data acquired in separate blocks. The importance of matching was further demonstrated by calculating the flow error when frames were purposefully not matched. Errors of up to 80 % were seen if the wrong frame was used for phase subtraction.

Although matching in the cardiac cycle could be performed using an ECG signal (8, 115, 120), image subtraction allows matching in both the cardiac and respiratory cycles in one step (117). This is not only more efficient but also obviates the need for ECG monitoring (116). Alternatively, data from different blocks could be matched using image-based navigators along with motion correction, which has previously been demonstrated in retrospectively enhanced real-time imaging (121).

In one patient with an irregular heart rate the 'conventional' and 'simulated split-acquisition' reconstructions of the same real-time PCMR data also showed good agreement in stroke volumes and flow profiles. This suggests that the split-acquisition method could be used successfully in subjects with an irregular heart rate.

3.10.2 Image Quality

Real-time imaging often trades image quality for speed of acquisition (122). It was observed that in adults the real-time sequences all had significantly lower estimated SNR and edge sharpness than the cardiac gated sequence. Nevertheless, the estimated VNR in adults was not significantly different ($p > 0.05$) between the HTR split-acquisition sequence and cardiac gated sequence. The similar SNR, VNR and edge sharpness between the standard real-time and HTR split-acquisition images in adults suggests that image quality is not seriously affected by matching data from different RR-intervals. The lower SNR and VNR seen in the HSR split-acquisition images was to be expected, given the smaller pixel dimensions.

3.10.3 Adult In-vivo Validation

In adults, there was good agreement between stroke volumes measured using the four different sequences. Importantly, this was true in patients as well as volunteers, suggesting that matching also works in subjects with less regular respiratory patterns. In gated PCMR, variations in stroke volume from breathing are averaged out; however, when analyzing the real-time stroke volumes, a single flow cycle was chosen for comparison. This may explain some of the differences in flow volumes found between the real-time techniques and the gated technique.

3.10.4 Paediatric Utility

In children, standard real-time PCMR was found to overestimate stroke volume, probably due to inadequate spatial resolution. However, there was excellent agreement between the cardiac gated PCMR sequence and the split-acquisition real-time CINE sequence that had a higher spatial resolution.

3.10.5 Advantages of Split-acquisition PCMR

Currently, cardiac gated PCMR is considered the reference standard method of measuring flow in-vivo. It has been validated in numerous studies (58, 60, 91, 93, 94) and due to the high spatial and temporal resolution it is accurate in the paediatric population. However, it is time consuming as it is usually acquired with several signal averages to compensate for respiratory motion. Breath-hold, cardiac gated PCMR is commonly used, however for adequate spatial and temporal resolution the breath-hold time is long. This is problematic when imaging children with congenital heart disease, as they are often unable to perform long breath holds.

Another approach is real-time PCMR, which can be acquired during free breathing in a relatively short length of time. However, as shown in this study, the lower spatial and temporal resolution of standard real-time imaging reduces its accuracy in the paediatric population. The split-acquisition PCMR technique described has all the benefits of standard real-time PCMR, but with improved spatial or temporal resolution. Thus, the split-acquisition technique is accurate even in children and it may be of particular use in the assessment of paediatric heart disease.

3.10.6 Limitations

This study has shown that split-acquisition real-time CINE PCMR technique is accurate in a population of 15 volunteers and 11 patients (5 adult and 6 children). Further work is needed to validate this technique in a larger patient population. In particular the split-acquisition sequence needs to be tested in patients with irregular breathing patterns. Irregular patterns might make it more difficult to match data from different blocks in cardio-respiratory space and may reduce the accuracy of the technique. The split-acquisition technique was demonstrated to be accurate in the *accuracy of matching* experiment in one adult with an irregular heart rate. However this needs to be performed in larger population with this condition, to confirm the accuracy of the technique.

In this initial feasibility study, the split-acquisition technique was only tested in the aorta, as flow quantification has been well validated using MRI in this vessel. One advantage of this technique over other real-time techniques may be its ability to measure flow in smaller vessels, as a higher spatial resolution can be achieved. Further work is required to test this technique in other smaller vessels.

In the future, it may be advantageous to interleave many blocks of flow-compensated and flow-encoded data. This was not carried out in this study due to the long reconstruction times, of approximately 5 minutes per measurement. The matching algorithm was found to only take ~2 % of the reconstruction time, with the non-Cartesian parallel imaging reconstruction taking ~90 % of the total reconstruction time. These long reconstruction times are a drawback, as although the data is acquired in real-time, the images cannot be viewed in real-time. Reconstruction times could be improved by the use of newer multi-processor graphics cards (101, 123), which are well suited to complex iterative reconstruction (see section 5.2.2). This may also allow more complex matching techniques to be carried out, which may involve image registration

3.10.7 Conclusion

In conclusion, we have demonstrated the accuracy and reliability of a novel split-acquisition phase-contrast MR technique in both adults and children. The technique divides the acquisition of flow-compensated and flow-encoded data into separate blocks, and performs automatic matching of this data in cardio-respiratory space. This allows an increase in the temporal or spatial resolution of real-time phase-contrast MR. Split-acquisition PCMR opens up the possibility of real-time scanning of smaller vessels, in patients with higher heart rates, which will be useful in the assessment of congenital heart disease.

CHAPTER 4

Rapid Gated Flow Measurements

4.1 Introduction

Cardiac gated PCMR is a proven method of measuring blood flow in the clinical environment (57-59). It is particularly useful in patients with congenital heart disease (124), where flow assessment often guides clinical decision-making. As we have seen, PCMR is intrinsically slow because each line in k-space must be acquired twice (with different velocity-encodings) in order to perform background phase subtraction. Unfortunately, this prolongs acquisition time and prevents high spatio-temporal resolution cardiac gated PCMR from being performed in a breath-hold within the clinical environment.

We have shown in chapter 2, that it is possible to achieve real-time PCMR with the use of efficient spiral trajectories, combined with parallel imaging techniques. Unfortunately, real-time PCMR comes at the cost of low spatio-temporal resolution and is not well suited to the paediatric population. The split-acquisition technique described in chapter 3, is able to achieve higher spatio-temporal resolution than the real-time technique, however the resolution is still inferior to that desired in the clinical environment for small vessels or in subjects with high heart rates.

Due to the long breath-hold times of high spatio-temporal resolution gated PCMR, multiple signal averages are often used to compensate for respiratory motion in the clinical environment. This results in scan times of approximately 2 minutes and thus in congenital heart disease where flow is often measured in multiple vessels, complete flow assessment can take up to 10 minutes. If spatio-temporal resolution is lowered, gated PCMR can be performed in a breath-hold (97). However, in children with congenital heart disease, high resolution is necessary to assess smaller vessels at higher heart rates. Furthermore, the breath-hold times are often too long (> 15 seconds) for children or sick adults. Thus, in the congenital population there is a need for a high spatio-temporal resolution gated PCMR sequence that can be performed within a short breath-hold.

4.1.1 Aims

The aims of this study were to;

- Develop high spatial and temporal resolution PCMR imaging, using a prospectively-triggered, spiral PCMR sequence accelerated with SENSE, which can be performed in a short breath-hold
- Demonstrate the technique in a population of children and adults with congenital heart disease
- Compare the accuracy of the prospectively-triggered, spiral PCMR sequence against a breath-hold retrospectively-gated Cartesian PCMR sequence

4.1.2 Personal Contribution

To fulfil the above aims I have:

- Designed and developed a prospectively-triggered, spiral PCMR sequence (see section 4.3) in the Siemens, IDEA environment. This is based on the undersampled spiral SENSE sequence developed in chapter 2
- Automated the sequence user interface to allow ease of use (see section 4.3.3)
- Optimised the sequence parameters (see section 4.4)
- Developed an OsiriX plug-in to calculate flow volumes from the prospectively-triggered, spiral PCMR sequence (see section 4.3.4)
- Developed an OsiriX plug-in to correct for residual background phase offsets (see section 4.3.7)
- Performed in-vitro validation of the prospectively-triggered, spiral PCMR sequence (see section 4.5)
- Adapted the SNR and edge sharpness plug-ins for OsiriX (from section 3.3.3), to allow more accurate measures of image quality for this study (see section 4.3.5 and 4.3.6)
- Assessed image quality of the prospectively-triggered, spiral PCMR technique, by quantification of SNR, VNR and edge sharpness (see section 4.8)

- Performed in-vivo validation of the sequence in multiple vessels, in a population of adults and children with congenital heart disease (see section 4.7)
- Assessed intra- and inter-observer variability of the sequence (see section 4.7)

The results from this work are currently in press in Radiology, by J. Steeden, D. Atkinson, M. Hansen, A. Taylor and V. Muthurangu entitled; "Rapid Flow Assessment of Congenital Heart Disease Using High Spatio-Temporal Gated Spiral Phase Contrast MR", (125) (see Appendix 5).

4.2 Literature Overview

In this section previous studies which have performed rapid, gated flow measurements with the use of a SENSE reconstruction algorithm are discussed. This is not an exhaustive review on all rapid, gated flow studies with the use of parallel imaging. I have however highlighted some relevant papers, giving an overview of research in this area. These papers were found using a combination of the search engines *GoogleScholar* and *PubMed*, The search terms used included (a combination of):

- MRI
- Fast
- Flow
- Phase contrast
- SENSE

When a relevant paper was found, the referenced papers were followed up and any subsequent papers which have cited this paper were also followed up.

Beerbaum, et al. (122, 126) investigated flow measurements using a retrospectively-cardiac gated, Cartesian PCMR sequence, undersampled using SENSE factors of 1 (fully sampled, used as the reference), 2 and 3. They measured flow in the ascending aorta (Q_S) and pulmonary artery (Q_P) in a paediatric population (126) and an adult population (122), to allow quantification of Q_P/Q_S ratio during free breathing.

In the first study by Beerbaum, et al. (126), 22 paediatric patients (mean age: 7.2 ± 6.2 years) with cardiac left-to-right shunt were enrolled. The sequence parameters used are shown in Table 4.1;

	SENSE ×1	**SENSE ×2**	**SENSE ×3**
TE/TR	6.5/15.0 ms	6.5/15.0 ms	6.5/15.0 ms
Flip angle	30°	30°	30°
FOV	300	380	380
Rectangular FOV	70 %	100 %	100 %
NSA	2	1	1
VENC	200 cm/s	200 cm/s	200 cm/s
Temporal resolution	30 ms	30 ms	30 ms
Spatial resolution	2.3×3.1×6.0 mm	2.3×3.1×6.0 mm	2.3×3.1×6.0 mm
Scan time	1:37 mins	0:27 mins	0:19 mins
Relative scan time*	-	28 %	19 %

*Percentage of scan time compared to SENSE ×1 (reference) sequence

Table 4.1: Sequence parameters used by Beerbaum, et al. (126) in paediatric study

Beerbaum, et al. demonstrated a good correlation in velocities measured in a pulsatile flow pump between the *bucket and stopwatch* method and both the SENSE ×2 (r = 0.999) and SENSE ×3 (r = 0.999). In-vivo, a negligible difference was found in the stroke volumes (±1 %) and the Q_P/Q_S ratio (±2 %), between the reference PCMR sequence and the undersampled sequences in the paediatric population. SENSE ×3 was found to give slightly more variability than SENSE ×2 (Q_P/Q_S limits of agreement: 124 % to 82 %, and 112 % to 86 %, respectively). Figure 4.1, compares the aortic stroke volumes calculated from the reference (SENSE ×1) sequence with those calculated from the SENSE ×2 sequence.

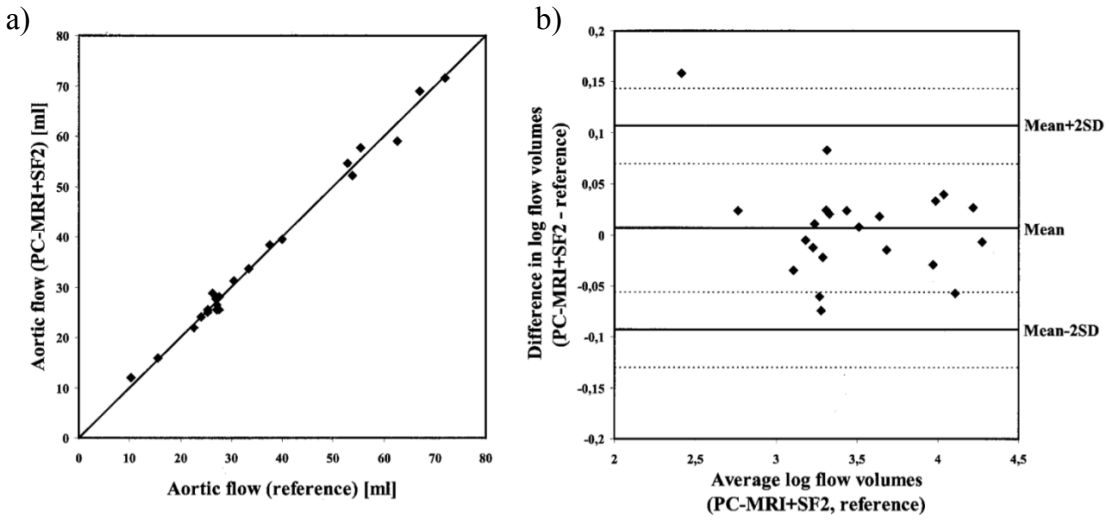

Figure 4.1: From paediatric study by Beerbaum, et al. (126). Comparison of stroke volumes in the aorta for the reference sequence vs. SENSE ×2 sequence; a) Correlation between the two sequences b) Bland-Altman analysis (data log-transformed)

In the second study (122), 13 healthy adults (mean age: 33.0 ± 7.4 years) underwent the same imaging protocol. The sequence parameters were the same as Table 4.1, except an 80 % rectangular FOV was used for all sequences, with average scan times of 2:17 minutes for the reference sequence, 36 seconds for SENSE ×2 and 25 seconds for SENSE ×3.

In this study Beerbaum, et al. (122) demonstrated a good agreement in the Q_P/Q_S ratio in healthy adults, measured by the reference PC sequence (1.03 ± 0.07), SENSE ×2 (1.05 ± 0.13) and SENSE ×3 (1.08 ± 0.11). Negligible differences (between -3 % to 4 %) were found between the reference PC sequence and the undersampled sequences, in terms of stroke volumes in the pulmonary artery and aorta, and the Q_P/Q_S ratio.

Figure 4.2 shows a comparison of the pulmonary artery stroke volumes from the reference sequence and SENSE ×2, as found by Beerbaum, et al. (122);

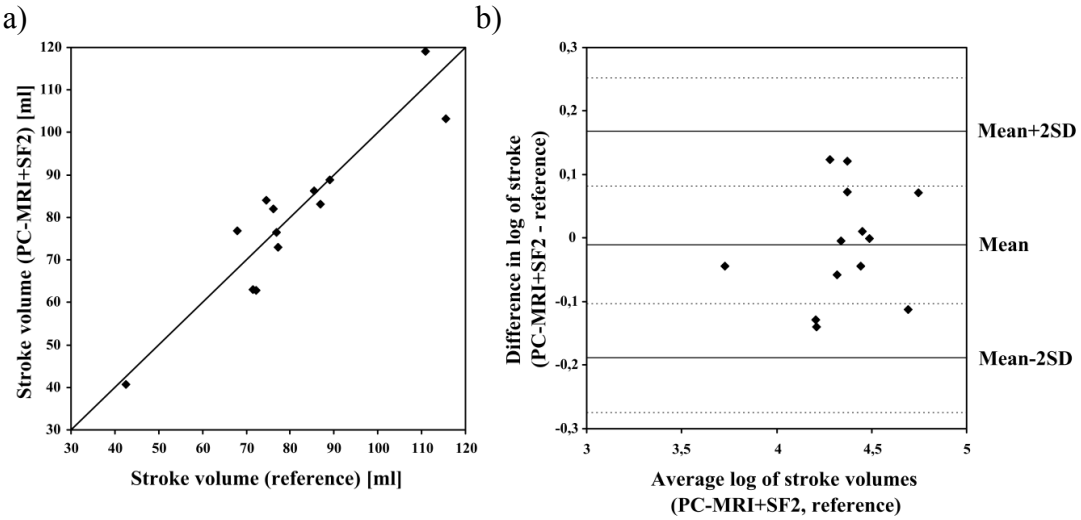

Figure 4.2: From adult study by Beerbaum, et al. (122). Comparison of stroke volumes in the pulmonary artery for a reference sequence vs. SENSE ×2 sequence; a) Correlation between the two sequences b) Bland-Altman analysis (data log-transformed)

In both the paediatric study and the adult study by Beerbaum, et al. the spatial resolution achieved was 2.3×3.1 mm, with a temporal resolution of 30 ms. However, even with a SENSE factor of 3 the scan duration was ~20 seconds, therefore in these studies all data was acquired during free-breathing. Neither of these studies performed any correction for respiratory motion in the undersampled sequences, and only one signal average was used.

A similar study was carried out by Prakash, et al. (127). They achieved higher spatial resolution imaging that Beerbaum, et al. by the use of a smaller FOV, and a larger matrix. Flow volumes were compared from a retrospectively-gated Cartesian PCMR sequence, with a SENSE factors of 1 (reference) and 2. All data was acquired during free-breathing. The sequence parameters used are shown in Table 4.2.

Sequence parameters	
TE/TR	3.1/7.5 ms
Flip angle	20^{o}
FOV	240-350
Matrix	256×160
NSA	2
Views per segment	2
Temporal resolution	30 ms
Spatial resolution	0.94 to 2.2 mm
Scan time	~1:58 mins (with SENSE ×1)
	~0:59 mins (with SENSE ×2)

Table 4.2: Sequence parameters used by Prakash, et al. (127)

Flow was measured in 33 subjects (mean age: 24 years), in the ascending aorta (N = 33) and the pulmonary artery (N = 24). A close correlation in flow measurements was found between the two sequences in the aorta (r = 0.965, mean difference = 0.08 ± 0.3 L/min or 1.0 ± 6.7 %) and in the pulmonary artery (r = 0.965, mean difference = 0.09 ± 0.4 L/min or 1.7 ± 7.0 %), as shown in Figure 4.3.

Using a SENSE factor of 2, Prakash, et al. (127) were able to perform high spatio-temporal resolution imaging during free-breathing with 2 NSAs, in a scan time of 59 ± 19 seconds. They demonstrated the accuracy of this sequence in-vitro and in-vivo.

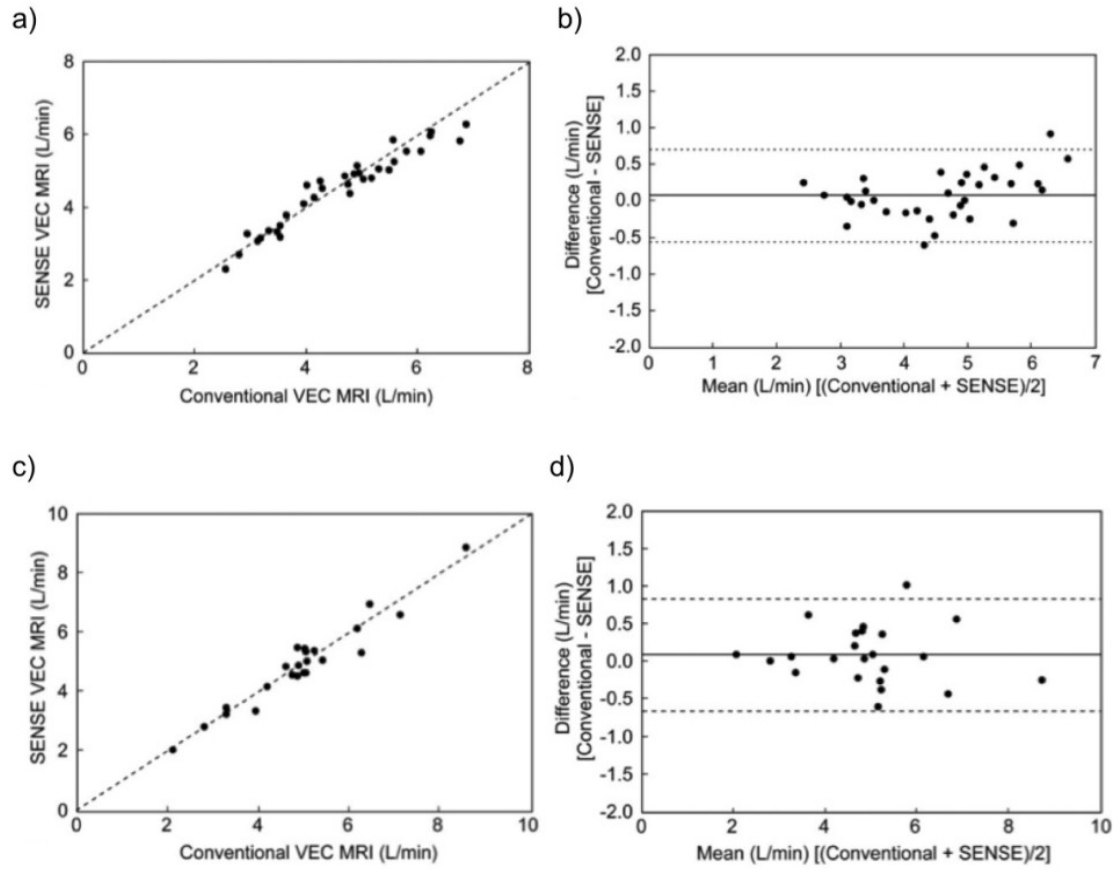

Figure 4.3: From Prakash, et al. (127). Correlation (left) and Bland-Altman analysis (right) between conventional PCMR sequence (SENSE ×1) and SENSE ×2 sequence, as found in a)-b) the aorta, c)-d) the pulmonary artery

Another study by Lew, et al. (128) was able to greatly reduce scan times compared to Beerbaum, et al. and Prakash, et al. allowing the possibility of breath-hold PCMR measurements. A retrospectively-gated, segmented fast gradient echo, Cartesian sequence, accelerated with SENSE factors 1, 2 and 3, was investigated. Stroke volumes were compared from the three sequences in 17 children (average age: 11.8 ± 9.6 years) in the aorta (N = 17) and pulmonary artery (N = 16) during a breath-hold. The sequence parameters are shown in Table 4.3.

Sequence parameters	
TE/TR	~2/~4 ms
Flip angle	15-30^{o}
Matrix	256×160
Slice thickness	5-7 mm
Views per segment	1-6
Scan time	20-30 sec (with SENSE ×1)
	12-20 sec (with SENSE ×2)
	7-10 sec (with SENSE ×3)

Table 4.3: Sequence parameters used by Lew, et al. (128)

Lew, et al. showed a good correlation in the aortic stroke volume, the pulmonary artery stroke volume and the Q_P/Q_S ratio, between the un-accelerated sequence and accelerated sequences. The correlation coefficient was > 0.962 in all cases. For the flow volumes the maximum bias, as found by Bland Altman analysis was 0.12 L/min, with limits of agreement < 0.8 L/min.

Although image quality is not discussed in the paper, the example images are very noisy and the residual aliasing is not completely removed, see Figure 4.4;

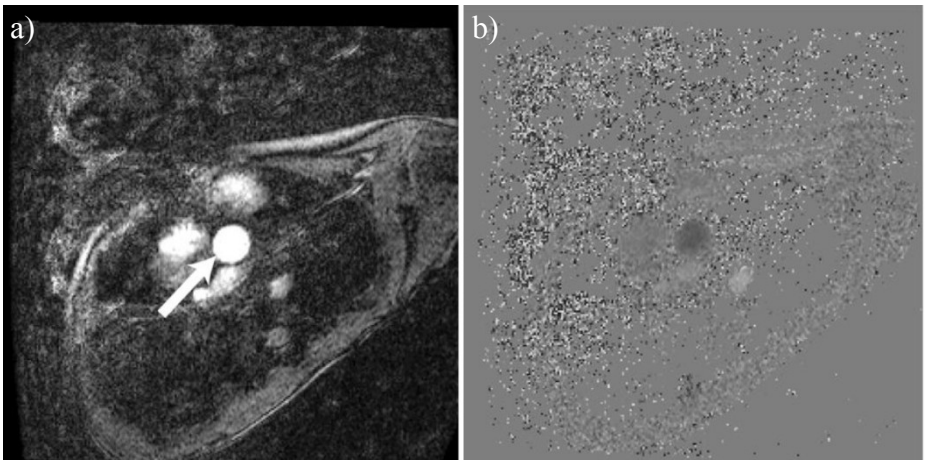

Figure 4.4: From Lew, et al. (128). Resultant image quality from a SENSE×3 sequence; a) magnitude, b) phase. A lot of noise is observed in these images, which Lew, et al. believe comes from noise in the coil sensitivity maps

Although Lew, et al. are able to achieve short breath-hold PCMR scans, which are shown to be accurate in a small number of children, Figure 4.4 shows the resultant image quality to be poor. No details are given as to the temporal or spatial resolution achieved in this study.

All of the studies described, use Cartesian sequences along with SENSE reconstruction algorithms. It is thought that spiral trajectories may be advantageous for flow imaging, due to the very short effTE. Additionally, all of these studies required a calibration scan at the beginning of the examination to calculate the coil sensitivities (~ 1 minute scan by Beerbaum, et al. (122, 126) and ~ 15 seconds for Lew, et al. (128)). This increases the examination time and makes the sensitivity maps susceptible to motion, which may occur during the scan. Lew, et al. (128) observed very noisy images when using a SENSE factor of 3, which they believe was due to noisy sensitivity maps. We do not wish to perform a separate calibration scan, however will calculate high SNR sensitivity maps from the data itself (in the same way as performed in sections 2 and 3).

The studies described here only demonstrate the accuracy of the sequences in the aorta and pulmonary artery. We hope to demonstrate the accuracy of a gated spiral sequence in the aorta, pulmonary artery and in the left and right pulmonary branches.
Additionally, the studies performed by Beerbaum, et al. (122, 126) and Prakash, et al. (127) are unable to reduce the scan times sufficiently to allow breath-hold imaging. Therefore in these studies all data was acquired during free breathing (scan duration > 19 seconds). We wish to reduce the scan duration further than achieved by Lew, et al. (128), to < 7 seconds to enable an achievable breath-hold even for children and sick adults.

4.2.1 Summary

From the literature overview it can be seen that:

- Previous studies have combined gated Cartesian trajectories with SENSE to achieve high resolution PCMR sequences
- These have demonstrated the accuracy of SENSE PCMR in the aorta and pulmonary artery
- Only Lew, et al. (128) were able to reduce the scan times enough to achieve breath-hold imaging
- All of the studies use a calibration scan to calculate the sensitivity maps

4.3 Development

In this study we wished to develop a high spatio-temporal resolution PCMR sequence, with the use of a prospectively-triggered spiral sequence, undersampled using SENSE. The sequence and reconstruction algorithm are based on those developed in chapter 2.

4.3.1 Cardiac Triggering

To develop a prospectively-triggered sequence, the physiological ('*physio*') tab on the UI was enabled, as seen in Figure 4.5. This allowed us to access the ECG trigger data within the sequence;

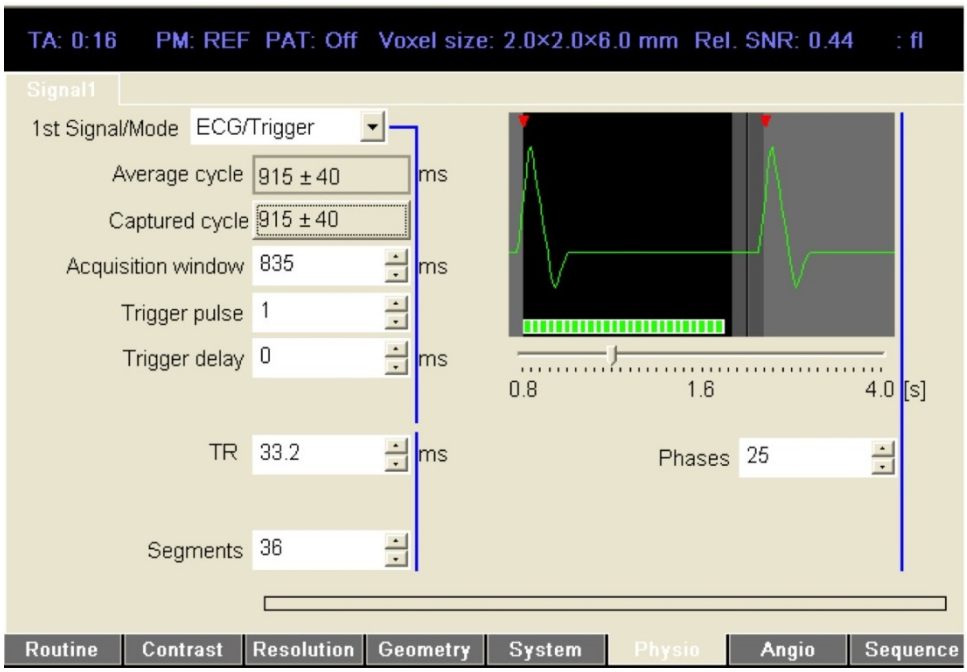

Figure 4.5: The physiological tab was enabled on the UI

In prospectively-triggered sequences (as described in section 1.5.2), it is necessary to leave a trigger window at the end of each RR-interval where the pulse sequence waits for a valid trigger. In this study the available acquisition window was calculated as the average heart rate, minus two times the standard deviation of the heart rate.

As the temporal resolution of the sequence is known (displayed on the UI as 'TR'), it is possible to calculate the maximum number of cardiac phases we are able to capture within the acquisition window. The number of cardiac phases is the calculated as the acquisition window divided by temporal resolution, rounded down to the nearest integer number.

In cardiac gated sequences (as described in section 1.5.2), the detection of an R-wave causes a change in the line that is acquired (38). For spiral imaging the detection of an R-wave, causes a change in the current spiral interleave being acquired. Therefore, if we required 10 spiral interleaves we would need to acquire data over 10 RR-intervals. To reduce the scan time it is possible to segment k-space, where more than one spiral interleave is acquired per RR-interval (in an interleaved fashion). Segmenting k-space therefore affects the temporal resolution of the sequence. For example, by acquiring two spiral interleaves per RR-interleave we only need to acquire data in half the total number of RR-intervals, however the temporal resolution is also halved.

4.3.2 Stimulated Echo's

When acquiring more than one spiral interleave per RR-interval (i.e. segmenting k-space), a hashing artefact was observed in the first few resultant images, as seen in Figure 4.6.

The sequence used to acquire the data in Figure 4.6, has a total of 20 spiral interleaves, with 2 interleaves acquired per RR-interval. No parallel imaging was used to acquire these images. The circular hashing pattern observed in Figure 4.6 in the water phantom, is symmetric about the centre of the image, and is made up of concentric circles in groups of 10. The hashing pattern is not seen in the magnitude images of the oil or the butter. It was observed that by increasing the TR or decreasing the flip angle, this artefact was reduced.

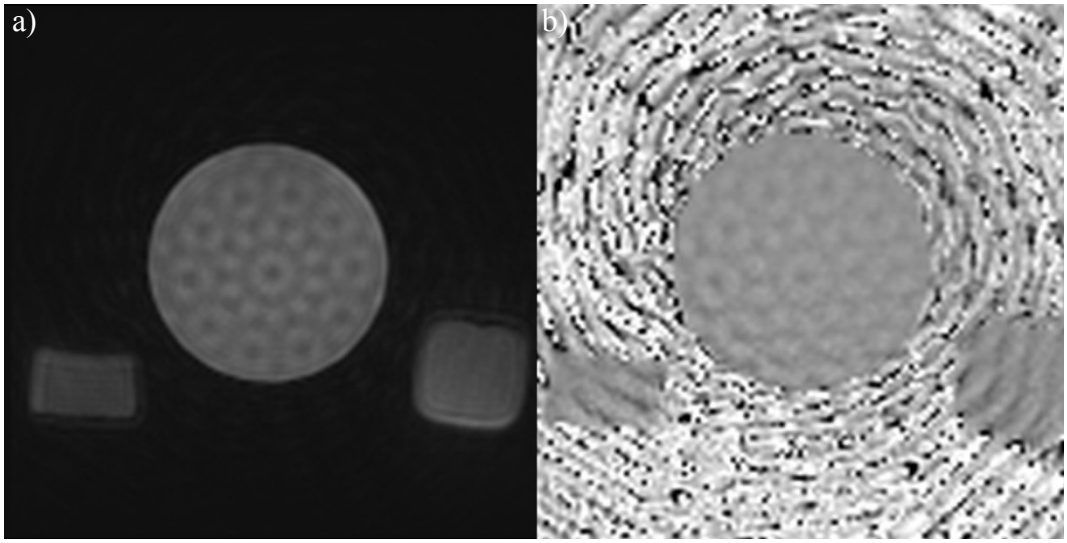

Figure 4.6: Hashing artefact observed when acquiring more than one spiral interleave per RR-interval, in a) Magnitude image, and b) Phase image. The large circular object is a water phantom, and the two smaller objects are oil (right) and butter (left)

These observations suggest that the artefact is caused by a stimulated echo from the first spiral readout, which causes signal during the second spiral readout in each RR-interval. By increasing the TR the transverse magnetization from the first spiral interleave decays, before the second RF-pulse is played out. By decreasing the flip angle the transverse magnetization caused by each RF-pulse is lower, therefore there is less residual transverse magnetization at the end of the TR. This theory is backed up by the fact that the hashing is not observed in the fat phantom, which has a shorter T_1 than water, therefore relaxes faster. Peter Gatehouse deserves special thanks for help getting to the bottom of the cause of this artefact.

In the sequence used to acquire the data in Figure 4.6, a gradient spoiler was applied on the *z*-axis at the end of each TR. No rewinder gradients were applied on the *x*- or *y*-axis. Gradient spoilers are not effective at spoiling transverse steady state magnetization unless the area of the gradient varies from TR to TR (37). When the area of these spoiler gradients varies from TR to TR, the spoiling is not uniform over the FOV, as shown by Bernstein, et al. (37) in Figure 4.7.

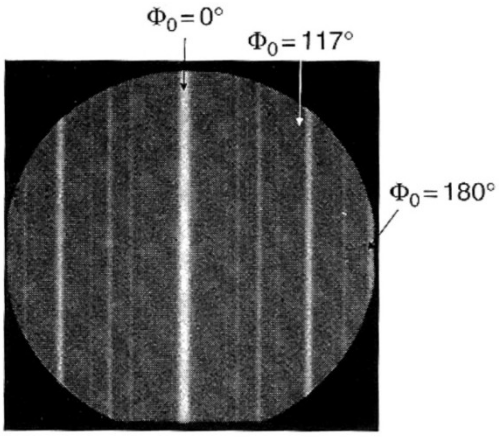

Figure 4.7: From Bernstein, et al. (37). Gradient echo image of a uniform spherical phantom, with no phase-encoding rewinder gradient (i.e. the phase encode gradient is used as a spoiler). The striped pattern demonstrates the spatially non-uniform spoiling caused as the phase-encode gradients produce spatially varying fields

The striped pattern shown in Figure 4.7 is from a Cartesian sequence with variable spoiler gradients in each TR. This striped pattern is similar to the hashing pattern seen in Figure 4.6, from our spiral sequence. In the spiral sequence because the x and y gradients are not rewound, the gradient spoiling at the end of each interleave is variable. This causes spatially non-uniform spoiling, resulting in the circular aliasing pattern.

A better solution to spoiling transverse magnetization, is to perform *RF-spoiling* (129). RF-spoiling was also carried out in the sequence used to acquire the data in Figure 4.6, however the total phase accumulated (due to gradients) in each TR must be the same to ensure spatially-independent RF-spoiling (129). Therefore, it was necessary to rephase the signal in the k_x and k_y dimensions at the end of each readout. The resulting sequence diagram can be seen in Figure 4.8. These rewinder gradients were found to completely remove the aliasing pattern in the resulting images.

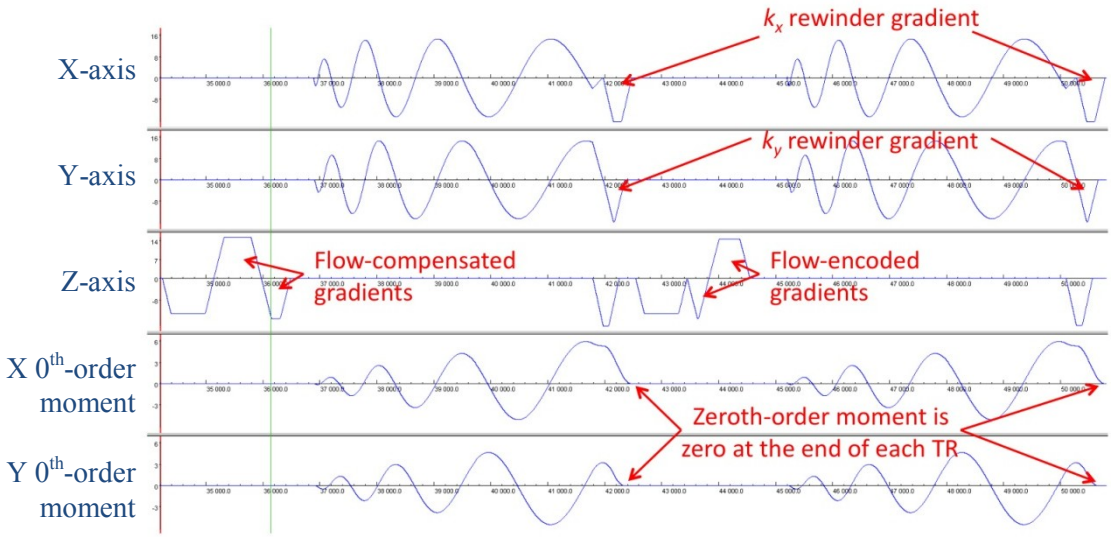

Figure 4.8: Sequence diagram of resultant sequence, showing rewinder gradients after all spiral gradients, which null the zeroth-order moments of all gradients on the x and y axes

This hashing artefact had not been observed in the previous studies, as in both chapters 2 and 3 a large number of dummy pulses were applied at the beginning of the sequence. This means that these stimulated echoes had reached a steady state before the acquisition of data. In the triggered sequence, the trigger window means that the first few frames within any RR-interval are never in a steady state. It was observed that using an additional RR-interval at the beginning of the triggered sequence, which contained dummy pulses, reduced steady state artefacts in the first cardiac phase.

4.3.3 Automating the UI

In order for the triggered sequence to be as easy to use as possible, it was necessary to automate many of the dependent parameters on the UI. For example, the TE and TR should always be minimized to allow the highest temporal resolution. However, when changing some parameters (e.g. when decreasing the bandwidth) it is necessary to increase the TR from its current value, therefore the temporal resolution decreases and the number cardiac phases must be reduced.

These dependent parameters mean that without automating the UI, it is not possible to decrease the bandwidth on the UI without first reducing the number of cardiac phases, and increasing the TR. Once the bandwidth has been set to the required value, the user would then have to minimize the TR, and maximize the number of cardiac phases to allow the highest temporal resolution to be achieved.

Solve-handlers were written to automatically handle these dependent parameters – these ensure the TE and TR are minimized and the number of cardiac phases is maximised after any of the following parameters are changed;

- Bandwidth
- Total number of spiral interleaves
- Number of interleaves acquired per RR-interval
- VENC
- Slice thickness
- FOV
- 'Capture cycle' button is pressed (to capture the current average RR-interval and standard deviation of the RR-interval)

Solver handlers were also written to;

- Automatically decrease the bandwidth when the FOV is reduced, if the current bandwidth is not achievable (due to maximum gradient strength restrictions). This also optimises the TR, and number of cardiac phases for the new bandwidth
- Automatically decrease the bandwidth when the matrix size is increased, if the current bandwidth is not achievable (due to maximum gradient strength restrictions). This also optimises the TR, and number of cardiac phases for the new bandwidth
- Automatically put the coils in triple combine mode when SENSE is on (to output the maximum number of coil elements to the reconstruction process), and automatically put coils in combined mode (to combine the coil elements in hardware before the reconstruction process) when SENSE is off

- Automatically calculate the acquisition window when the 'capture cycle' button is pressed, and optimise the number of cardiac phases achievable within the new acquisition window

4.3.4 Analysis of Flow Data

In chapters 2 and 3, flow volumes were calculated by integrating the flow curve for one cardiac cycle to a 1 ms temporal resolution by Fourier interpolation (see section 2.3.6.1). In this study Fourier interpolation cannot be used as the data points are not evenly distributed, due to the need for a trigger window at the very end of diastole. In this study it was found that on average ~80 ms at the very end of diastole was not sampled, as seen in Figure 4.9;

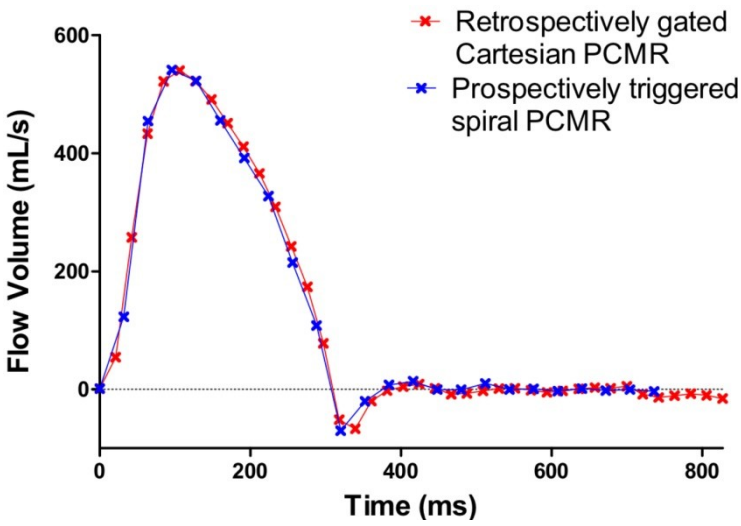

Figure 4.9: Example of a normal flow profile (plotted with linear interpolation) from a retrospectively-gated PCMR sequence, and the prospectively-triggered spiral PCMR sequence. It can be seen that, for this subject, the last 90 ms at the end of diastole is not captured by the prospectively-triggered sequence

It was found that smooth and accurate interpolation between the acquired points could be achieved using a shape preserving piecewise cubic Hermite interpolating polynomial (130) (called '*pchip*' in MATLAB), as seen in Figure 4.10.

From Figure 4.9 it can be seen that missing out the very end of diastole is not important in subjects with normal flow profiles, however is important in patients with regurgitant flow during diastole, as seen in Figure 4.10. Therefore, the missing flow data was predicted by performing a linear interpolation between the last calculated point and the first point, so that the flow profile filled the entire RR-interval (as stored during the acquisition of data from the ECG data), as seen in Figure 4.10;

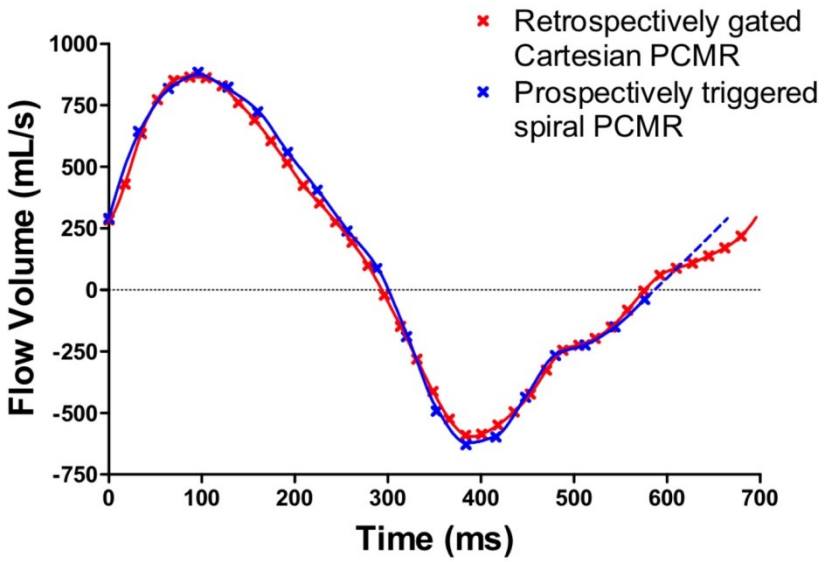

Figure 4.10: Abnormal flow profile, with regurgitant flow during diastole. A cubic interpolation is performed between the acquired data points, and a linear interpolation is used between the last and first points, to ensure the flow profile filled the entire RR-interval

The cubic interpolation (between the acquired points) and the linear interpolation (to ensure the data fills the entire RR-interval) were implemented within a plug-in for OsiriX, as shown in Figure 4.11. The top graph of the plug-in (see Figure 4.11) shows the acquired data points plotted in black (displayed with a linear interpolation) – the corresponding flow volumes are shown in the first column (on the right hand side). The interpolated data is also plotted on the top graph in green and the corresponding flow volumes shown in the second column. This allows the user see the effect of the interpolation – therefore if the interpolation is deemed to be incorrect, the un-interpolated results can still be used. In this study all stroke volumes were calculated from the interpolated flow curves.

For the normal flow curve shown in Figure 4.11, despite the large trigger window (of 167 ms) the stroke volumes calculated with and without interpolation vary by only 0.4 mL/cycle, indicating the accuracy of the cubic interpolation method. This also demonstrates that the linear interpolation does not affect normal stroke volumes, as expected.

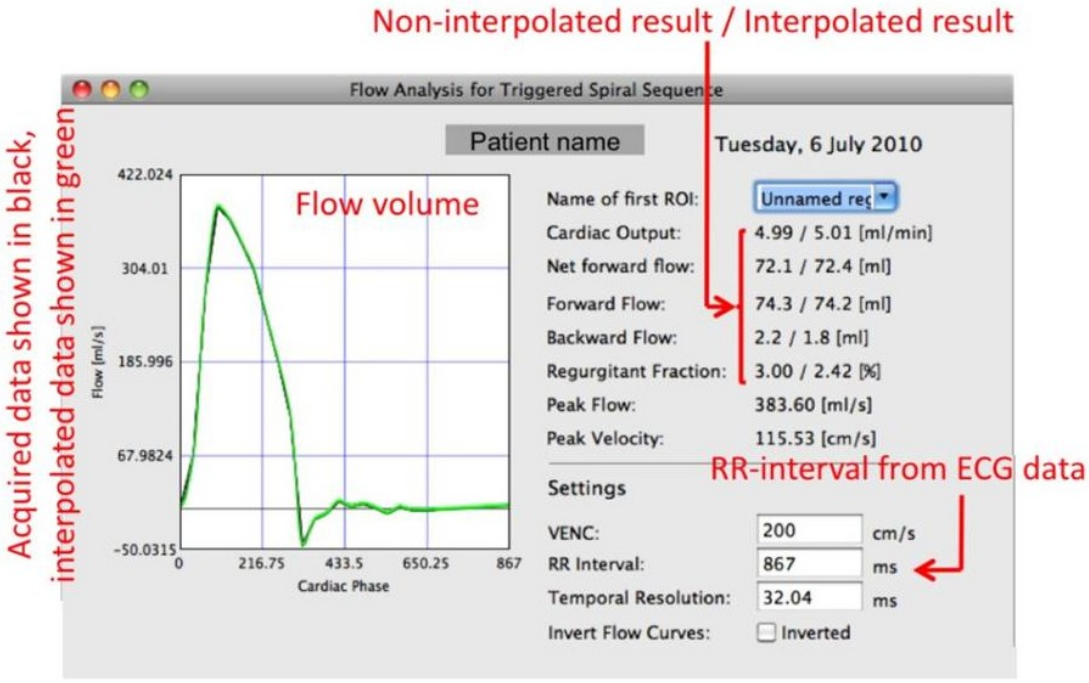

Figure 4.11: OsiriX plug-in developed to analyse flow from the prospectively-triggered PCMR sequence (note: the acquired data is plotted in black behind the interpolated data shown in green). In this subject 22 cardiac phases are captured, meaning the last acquired point is at time 673 ms. As the RR-interval is 867 ms, data for the remaining 167 ms was predicted using linear interpolation

4.3.5 SNR measurements

SNR and VNR measurements were performed in a similar way to that described in section 3.3.3. However, the trigger-window in a prospectively-triggered sequence disturbs the steady state of the sequence, leading to increased signal intensity in the first few cardiac phases – this is known as the *lightning* artefact (38). Therefore, in this study it was necessary to adapt the SNR calculation to take account of this signal intensity variation.

The signal intensity in the prospectively-triggered spiral PCMR sequence was found to decay exponentially. It was therefore necessary to correct for this exponential signal decay, before calculating the estimated signal noise, σ_S. The exponential signal decay was calculated as follows;

- The average signal intensity (I_A) within the stationary ROI (see section 3.3.3) was calculated for each cardiac phase
- The minimum value of I_A across all cardiac phases was found (I_{A_min}), and subtracted from all values of I_A
- The natural log of the offset average intensity values was calculated, and the y-crossing and slope of the resulting line were found
- The exponential fitted curve was calculated, for each cardiac phase, x, as:

$$fitted\_curve(x) = [exp(y\_crossing) \cdot exp(gradient \cdot x)] + I_{A\_min}$$

The corrected signal intensities were calculated by subtracting the fitted exponential value (for the current cardiac phase) from each pixel value in the corresponding image (and adding I_{A_min}). This was implemented in OsiriX. The result of the exponential signal intensity correction is plotted in the plug-in, as seen in Figure 4.12;

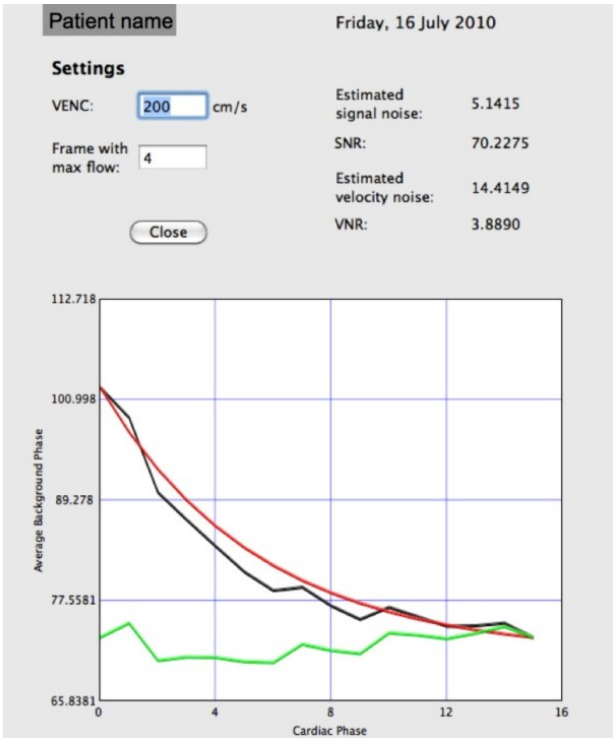

Figure 4.12: Plug-in for SNR quantification, showing the average signal intensity in the stationary ROI (I_A) in the black line, the exponential fitted curve in red, and the corrected signal intensity in green, for a prospectively-triggered spiral PCMR data set

The estimated signal noise and estimated SNR were calculated from the corrected signal intensities (during peak systole), as described in chapter 3. The VNR was calculated in exactly the same way as described in chapter 3.

To allow a fair comparison, SNR was calculated in the same way for all sequences used in this study. Figure 4.13 shows SNR measurements from a retrospectively-gated standard Cartesian sequence and a prospectively-triggered spiral sequence, in the same patient. It can be seen from Figure 4.13 that the exponential fit does not affect the signal intensity in the retrospectively-gated sequence, however does a good job of correcting the exponential decay in the prospectively-gated sequence;

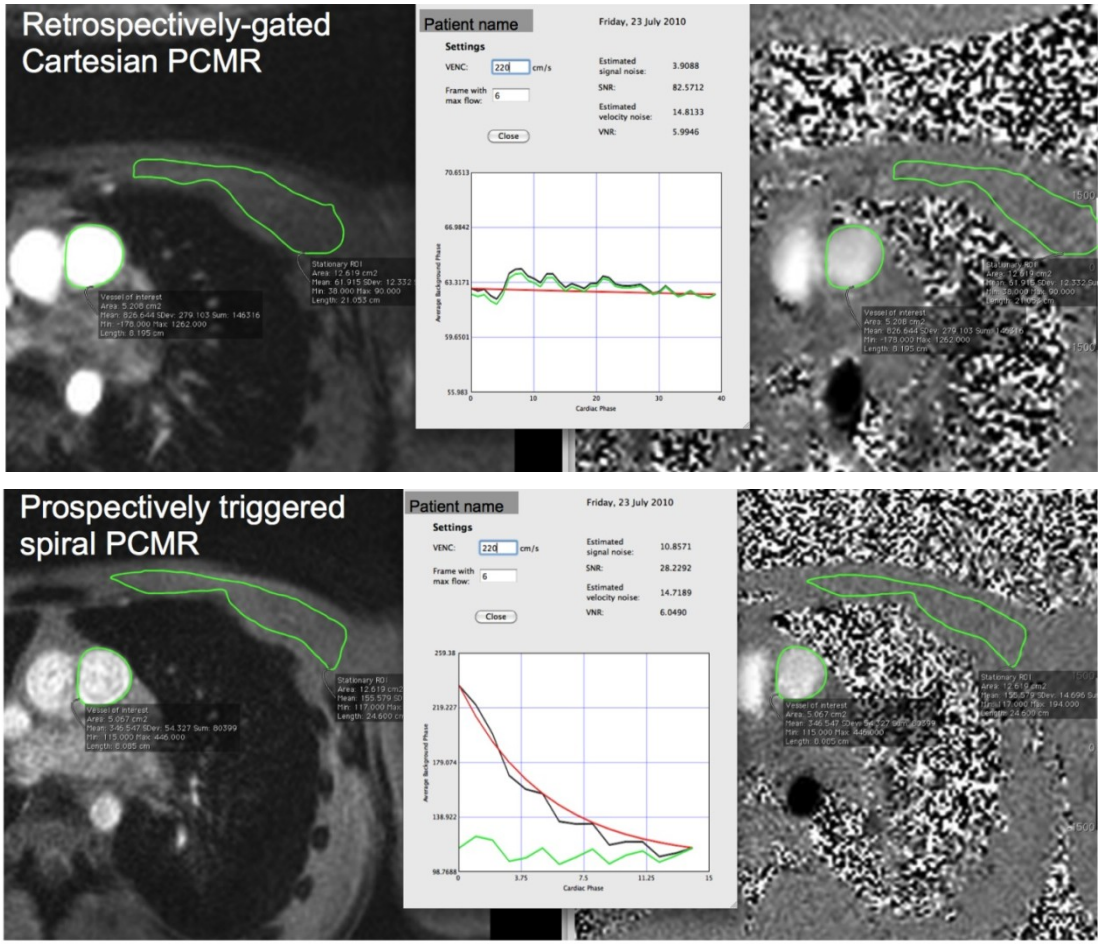

Figure 4.13: SNR measurements with exponential curve fitting from; top) retrospectively-gated Cartesian PCMR sequence, bottom) prospectively-triggered spiral PCMR sequence

4.3.6 Edge sharpness

In this study we wished to quantify edge sharpness, similarly to that carried out in section 3.3.3.4. In the previous study a fifth-order polynomial was fitted to the pixel intensities, to prevent noise providing artificially high gradients (representing sharp edges), see section 3.3.3.4. In this study it was observed that the fifth-order polynomial fit was prone to oscillations caused by noise, which provided artificially high gradients (see Figure 4.14a). This is likely to be because in chapter 3, edge sharpness was only quantified in the aorta, where the edge sharpness was assessed over the border between the aorta and one of the surrounding chambers of the heart. In this study edge sharpness was quantified in the aorta, main pulmonary artery, and pulmonary branches. In the main pulmonary artery, and pulmonary branches edge sharpness was generally quantified over the border between the vessel and the surrounding lung, i.e. noise pixels, leading to artificially high gradients.

It was observed that by filtering the pixel intensities using a Savitzky–Golay filter (131), the edge sharpness algorithm more accurately detected the edge of the vessels in this study, as seen in Figure 4.14.

A Savitzky–Golay filter smoothes data, removing the noise without removing the high frequency components. It works by dividing the data into small windows and performing a polynomial fit on the data within the window (the size of the window and the degree of the polynomial fit are specified by the user from the UI in OsiriX, see Figure 4.14b). For the middle position within the window, the smoothed value is taken to be value at the centre position of the calculated polynomial. The window is stepped through all of the data points, to smooth the data in this way.

a)

b)

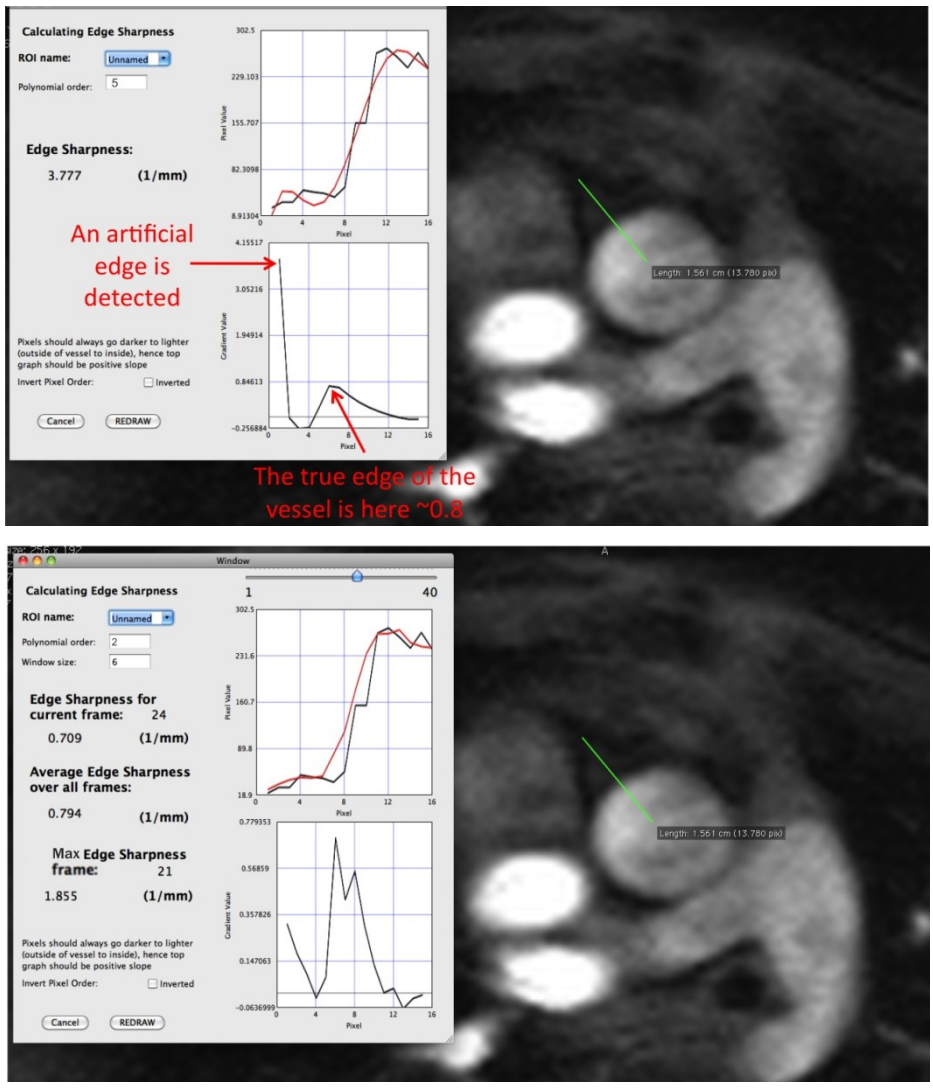

Figure 4.14: Example of edge sharpness calculation for one data set, using; a) fifth-order polynomial fit, b) Savitzky–Golay filter. It can be seen that polynomial fit detects an artificial edge. The Savitzky–Golay filter detects the vessel border correctly

In this application a window size of 6, with a polynomial fit of degree 2, was found to optimally smooth out noise but not smooth out the steep transition at vessel border. These parameters were used for all vessels in this study.

In chapter 3 the edge sharpness was only quantified in one frame during peak systole, however in this study we decided to use an average edge sharpness measure over all frames to give a better indication of overall edge sharpness.

4.3.7 Residual Background Phase Correction

In section 2.3.4 residual background phase offsets (after phase subtraction) were observed to be negligible using a ramp-up time of 10 μs, with a TE delay of 400 μs. However, in this study using the same ramp-up time and TE delay, residual phase offsets were observed (after phase subtraction and Maxwell correction) predominantly when performing PCMR imaging in the pulmonary artery. These additional phase offsets were not observed in chapters 2 or 3 because PCMR was only carried out in the aorta. This may be because the slice position tends to be more angulated when imaging the pulmonary artery, or because the pulmonary artery is further from the isocentre of the magnet.

As described in section 1.6.4, it is possible to predict these background offsets using a similar principle to Walker, et al. (53). This principle uses the assumption that the phase offsets vary smoothly in space. The offsets can therefore be predicted by fitting a surface through the phase of stationary pixels (41, 48, 53).

In this study, the residual phase was observed to be of a low polynomial order and did not change significantly between different cardiac phases. It was observed that these background phase offsets could be accurately predicted by fitting a quadratic surface ($Ax^2+By^2+Cxy+Dx+Ey+F$), through the phase of stationary pixels. The surface was calculated using a Cholesky decomposition algorithm.

In this study background phase correction was implemented in OsiriX (after prototyping in MATLAB). The stationary tissue was identified in two steps;

1. From the pixel intensity in an average magnitude image (over all cardiac phases). This allowed detection of pixels containing tissue
2. From the standard deviation of each pixel in the phase images (through all cardiac phases). This allowed determination of stationary tissue

In OsiriX, an average magnitude image was first calculated and displayed in a new window (see Figure 4.15a). A mask ($mask_{MAGNITUDE}$) was formed using only pixels with values that were greater than a defined threshold (see Figure 4.15a). The default threshold was 10 % of the maximum pixel value in the average magnitude image, however the percentage could be altered from the UI, as seen in Figure 4.15a.

Once the pixels containing tissue had correctly been identified, the stationary tissue was identified from the phase images. Firstly, the standard deviation of each pixel (in the phase images) was calculated through all cardiac phases. This standard deviation image was then masked using the $mask_{MAGNITUDE}$ (see Figure 4.15b). The final mask ($mask_{FINAL}$) was then formed using pixel values in the masked standard deviation image, which were smaller than a defined threshold (see Figure 4.15b). The default threshold was 7 % of VENC, however the percentage could be altered from the UI, as seen in Figure 4.15b.

An average phase image was finally formed over all cardiac phases, and the final mask applied (see Figure 4.15c). The quadratic surface was calculated from the non-zero pixel values, using a Cholesky decomposition (see Figure 4.15c). This surface was subtracted from all phase images, to correct for background phase offsets (see Figure 4.15d). The flow analysis plug-in was then automatically opened to show the effect of the phase correction on the calculated flow volumes (see Figure 4.15e).

a)

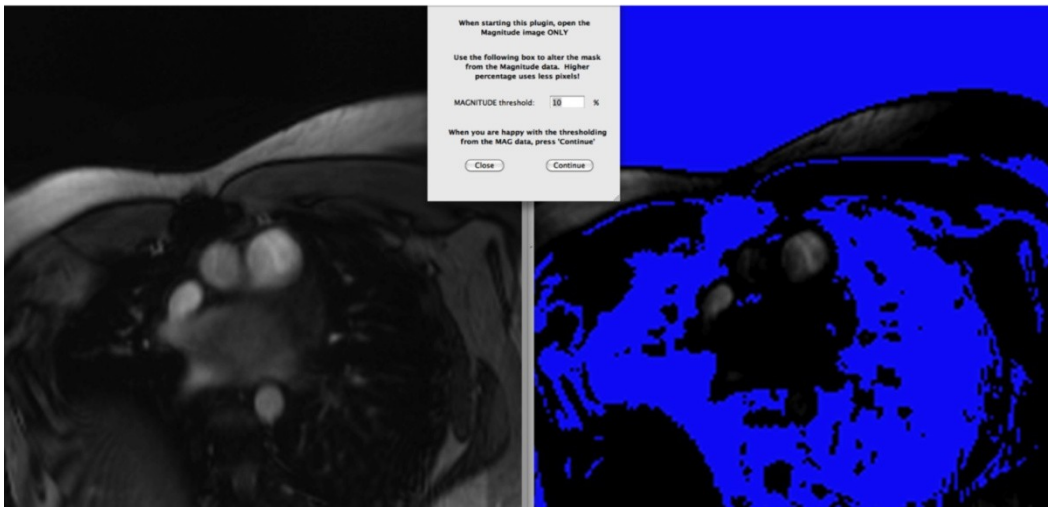
When starting this plugin, open the Magnitude image ONLY
Use the following box to alter the mask from the Magnitude data. Higher percentage uses less pixels!
MAGNITUDE threshold: 10 %
When you are happy with the thresholding from the MAG data, press 'Continue'
Close
Continue

b)

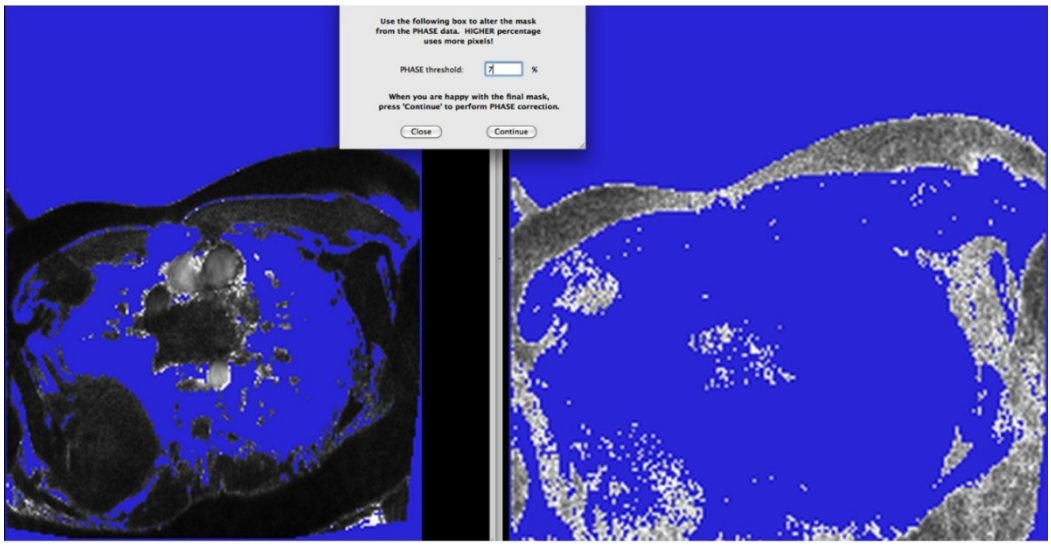
Use the following box to alter the mask from the PHASE data. HIGHER percentage uses more pixels!
PHASE threshold: 7 %
When you are happy with the final mask, press 'Continue' to perform PHASE correction.
Close
Continue

c)

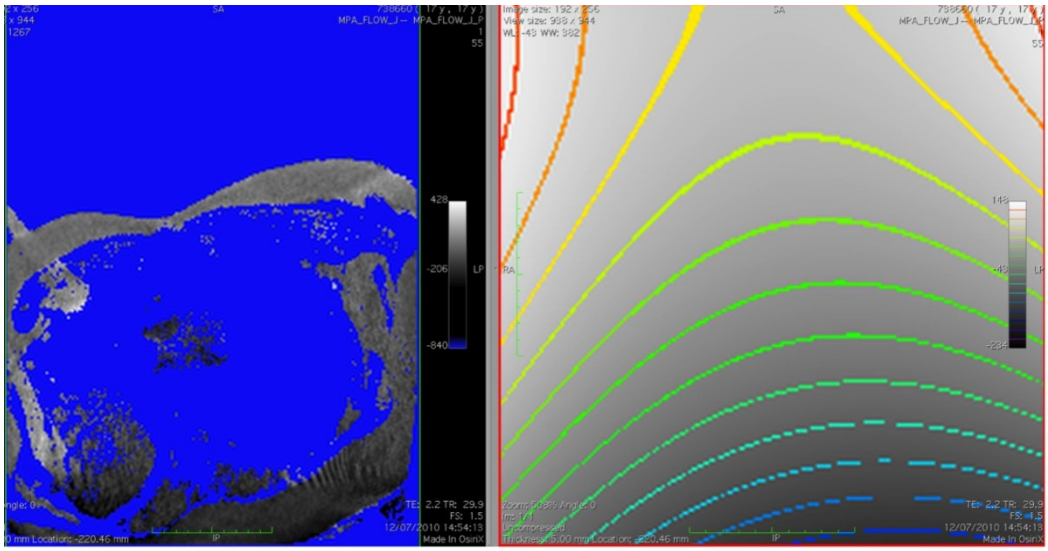

d)

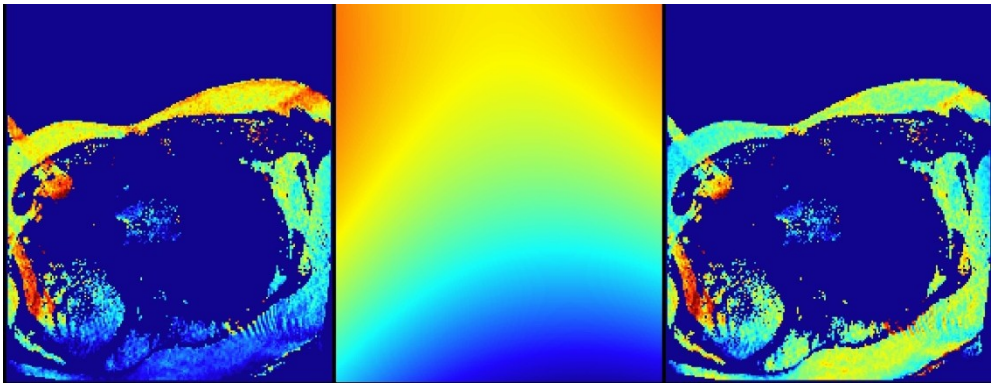

e)

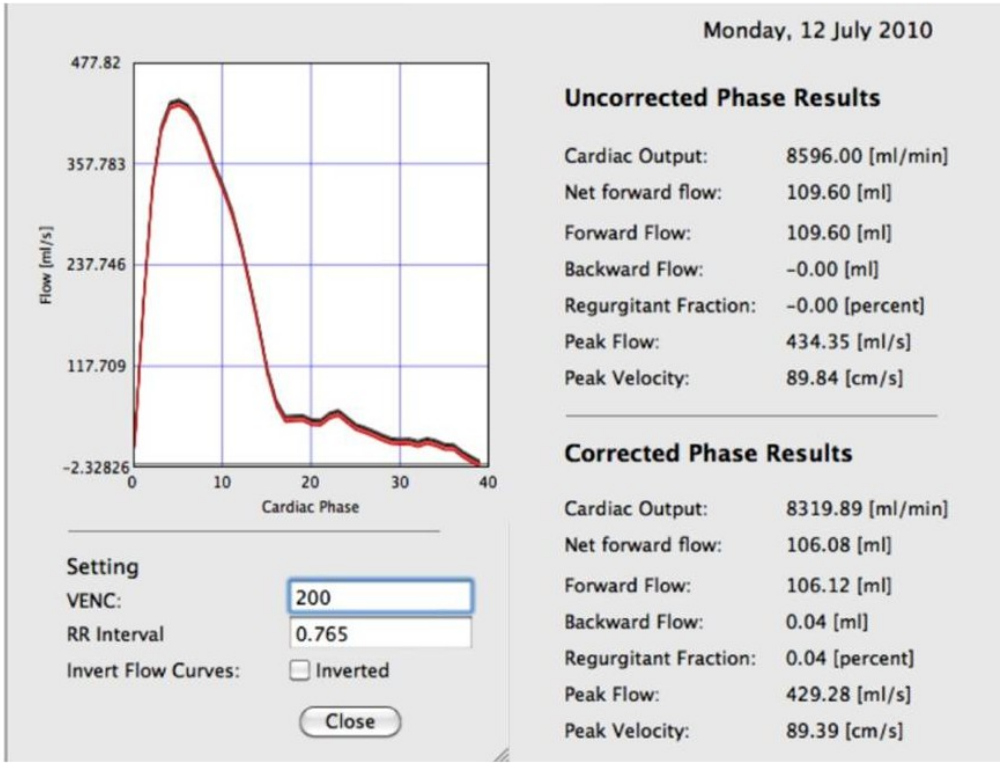

Figure 4.15: Phase correction plug-in as implemented in OsiriX. a) An average magnitude image is formed (left). Using the threshold from the UI, the $mask_{MAGNITUDE}$ is formed (right). Blue pixels show pixels not in the mask. b) The standard deviation of the phase data through all cardiac phases is calculated, and masked using the $mask_{MAGNITUDE}$ (left). Using the threshold from the UI the $mask_{FINAL}$ is formed (right). c) An average phase image is formed and masked with the $mask_{FINAL}$ (left). The pixel values remaining in this image are used to calculate the quadratic correction surface (right). d) The quadratic surface is subtracted from all phase images to correct for offsets. Left; uncorrected average phase image, middle; quadratic surface, right; corrected average phase image. e) Flow analysis is carried out for the uncorrected and corrected phase series, plotted in black and red, respectively

For the subject shown in Figure 4.15, a separate scan was performed on a stationary phantom using identical imaging parameters, immediately after the subject's examination (seen in Figure 4.16a). The phase offset from the stationary phantom and from the quadratic surface were compared in the same ROI as the vessel, as seen in Figure 4.16. This method of phase correction was described in section 1.6.4).

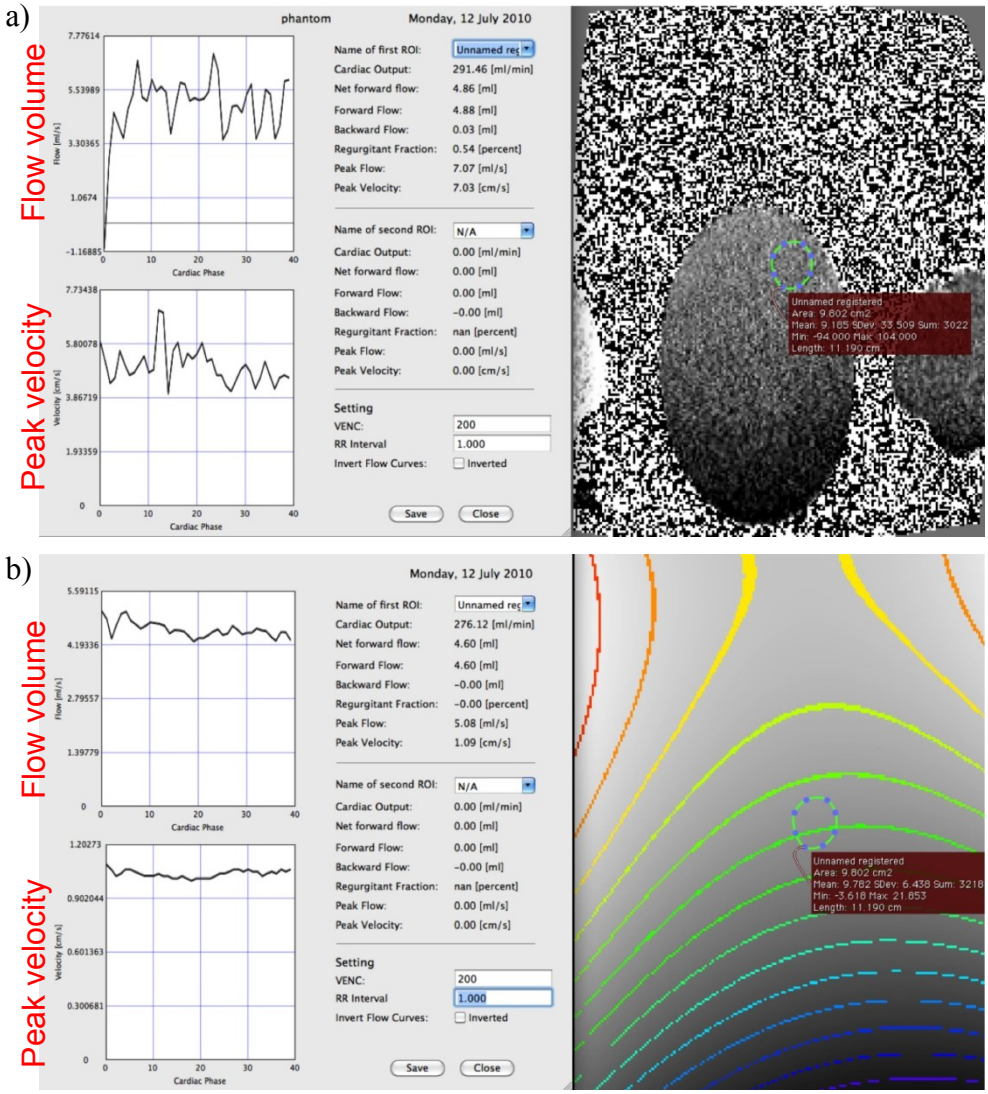

Figure 4.16: a) Phase offsets observed in a stationary water phantom, with identical imaging parameters to those used in the subject from Figure 4.15. The flow volume plug-in was used to calculate the average flow offset (in the same ROI as the vessel) caused by the phase offsets (left). b) The result from the quadratic phase correction, as calculated from the quadratic phase correction shown in Figure 4.15 c).

From Figure 4.16 it can be seen that the average background phase offset calculated from the stationary phantom resulted in an average flow volume offset of 4.86 mL/s, and from the quadratic surface was 4.60 mL/s.

This method of calculating a surface through stationary pixels, can be used on any PCMR sequence. Note, that in Figure 4.15 and Figure 4.16 the phase offsets were assessed from the retrospectively-gated Cartesian PCMR sequence. Figure 4.17 shows an example of the background phase correction used for the prospectively-triggered spiral PCMR sequence in a subject with more severe background phase offsets;

a)

b)

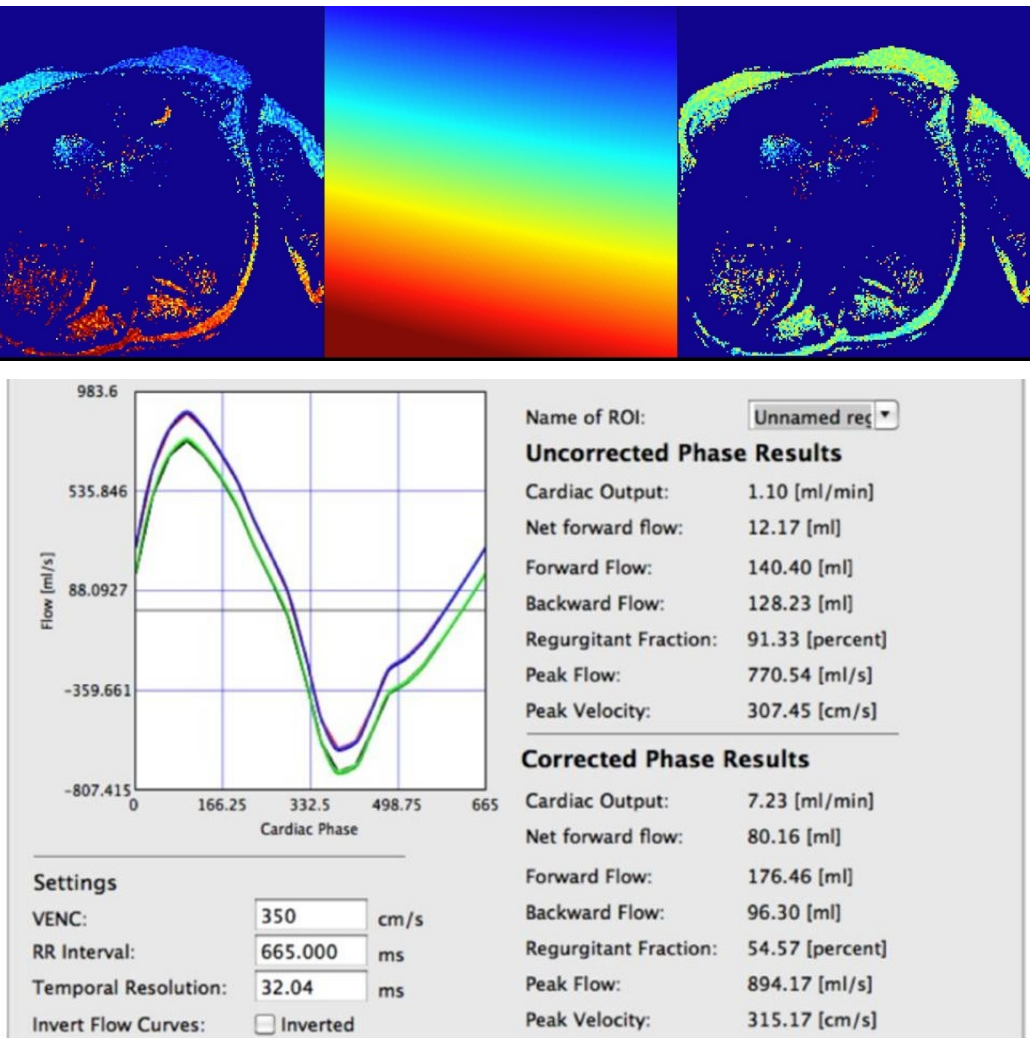

Figure 4.17: Background phase correction for a prospectively-triggered spiral sequence. a) Calculation of quadratic surface, left; average phase image with final mask, middle; quadratic correction surface, right; average phase image with background phase correction. b) Flow analysis for the uncorrected and corrected phase series, plotted in green and blue, respectively

For the subject shown in Figure 4.17, it can be seen that the uncorrected net flow was 12.17 mL/cycle, and the corrected net flow was 80.16 mL/cycle. The net flow for the retrospectively-gated Cartesian PCMR sequence was 81.22 mL/cycle, indicating that the background phase correction does a good job of correcting the stroke volume.

It was important that this background phase correction plug-in did not artificially add phase to images where no background phase offsets were present. Figure 4.18 shows an example of flow volume calculations with and without background phase correction, in a subject where no background phase offsets were present. The uncorrected and corrected stroke volumes differ by only 0.5 mL/cycle;

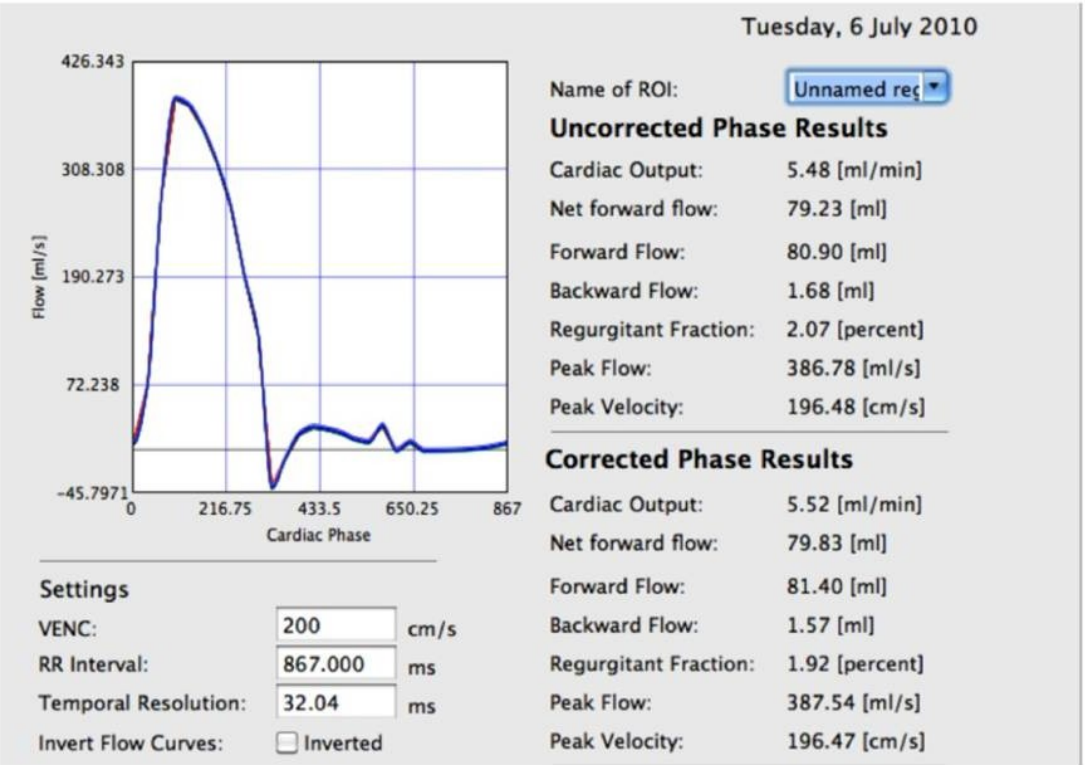

Figure 4.18: Flow analysis for the uncorrected and corrected phase series for a subject with no background phase offsets. It can be seen that the background phase correction has not added artificial phase to the data

Background phase offsets were only observed in a few patients.

4.3.8 Recording Physiological Data

Using the ECG monitor and the respiratory bellows, we were able to record the physiological data during the acquisition of data for all sequences used in this study. This was implemented within the sequence IDEA code. Data was logged from the start of the first dummy pulse, to the end of the last readout. The ECG and respiratory data were written into text files, and processed in MATLAB.

Figure 4.19 shows an example physiological data set acquired for one subject during the prospectively-triggered spiral PCMR sequence;

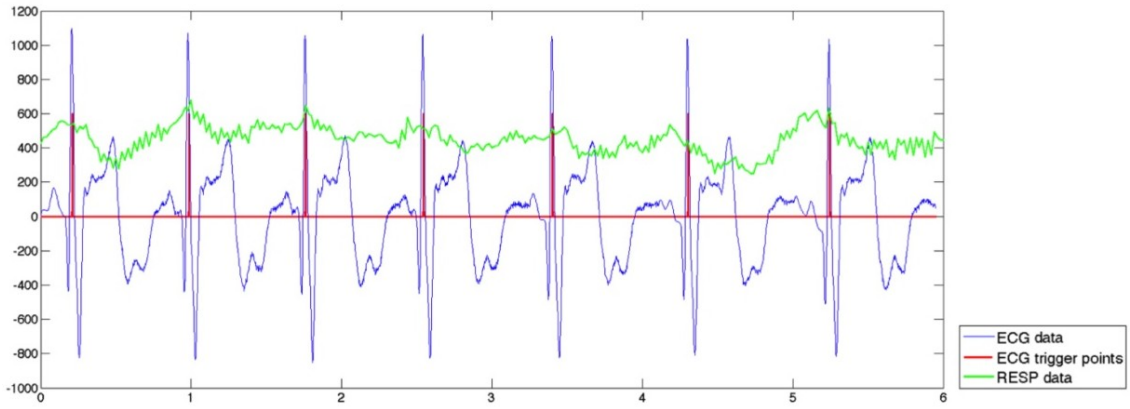

Figure 4.19: Example of physiological data acquired for one subject during the prospectively-triggered spiral PCMR sequence. It can be seen that the sequence correctly triggers at the R-wave in each heart-beat. The respiratory data shows little variation over the 6 second scan

Unfortunately we were not able to quantitatively compare the physiological data between subjects as the data was internally scaled, before being written to the files.

4.4 Optimisation of Sequence Parameters

In this study we wished to acquire high temporal and high spatial resolution images within a short breath-hold. We hoped to achieve a spatio-temporal resolution similar to that of the free breathing, retrospectively-gated sequence used clinically at ICH; ~30 ms temporal resolution and ~1.25 mm spatial resolution. We wished to reduce the scan duration further than achieved by Lew, et al. (128), to < 7 seconds to enable the breath-hold to be achievable even by children and sick adults.

With these specifications we were able to optimise the triggered spiral PCMR sequence. To achieve a high spatial resolution we needed to use a 256 matrix. It was observed that with the use of > 30 spiral interleaves, less image blurring was observed. However, the higher the total number of spiral interleaves, the more RR-intervals needed to acquire data.

With the use of 36 spiral interleaves, a TR of ~8 ms was achieved. This gives a temporal resolution of ~16 ms (for both flow-compensated and flow-encoded readouts), when acquiring just one interleave per RR-interval. Therefore, a temporal resolution of ~32 ms could be achieved by acquiring two spiral interleaves per RR-interval. In this case, 18 RR-intervals were needed to acquire all spiral interleaves with no SENSE acceleration. Using a SENSE factor of 3, allowed all data to be acquired within 6 RR-intervals (plus one RR-interval for the dummy pulses), resulting in a scan time of ~7 seconds (for an RR-interval of 1000ms). These parameters were observed to give the optimal trade-off between temporal resolution and total scan time, whilst maintaining good image quality.

4.4.1 Interleave Ordering

In order to calculate the sensitivity maps from the data itself (in the same way as chapters 2 and 3), it was necessary to rotate the spiral interleaves in each cardiac phase. Therefore, by combining the data from three consecutive cardiac phases, we were able to compute a fully sampled data set with 36 spiral interleaves.

The resulting data acquisition scheme can be seen in Figure 4.20;

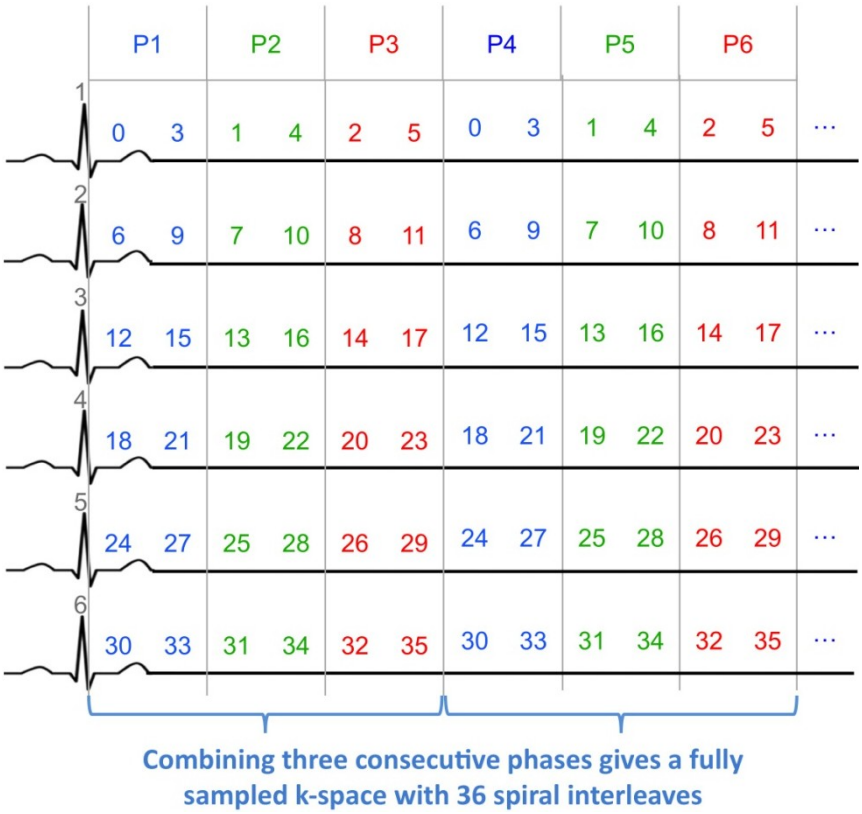

Figure 4.20: The optimised sequence uses a total of 36 spiral interleaves, with 2 interleaves acquired in each RR-interval, undersampled by a factor of 3. The sampling pattern is rotated in each cardiac phase (P, indicated along the top). In total 6 RR-intervals are required to collect all of the data (indicated in gray along the left). The coloured numbers in the boxes, represent which spiral interleaves were acquired – for each spiral interleave the flow-compensated data was acquired first, followed by the flow-encoded data

All data was reconstructed online using the iterative SENSE algorithm developed in chapter 2. The coil-sensitivity information was calculated from the time-averaged (flow-compensated) data from each coil, divided by the sum-of-squares of the time-averaged coil data, in the same way as chapter 2.

4.5 In-vitro Validation

To validate the prospectively-triggered spiral PCMR sequence, an experiment was carried out using the pulsatile flow pump described in section 2.4. The output from the pump was varied from 1.8-4.8 L/min, by changing the stroke volume (30-60 mL/cycle) and the pump rate (55-75 bpm). Flow was quantified at 10 different output volumes.

4.5.1 In-vitro protocol

PCMR images were acquired using a standard, retrospectively-gated Cartesian sequence and the prospectively-triggered spiral PCMR sequence, at the mid-point of the phantom with a transverse imaging plane. The flow volumes measured from the standard, retrospectively-gated Cartesian sequence were assumed to be the true flow volumes. Two three-element spine coils (below the phantom) and two three-element body-matrix coils (above the phantom) were used for imaging. The sequences parameters are shown in Table 4.4.

4.5.2 Image Analysis

All images were processed in OsiriX. Flow images were segmented using the semi-automatic segmentation propagation plug-in described in section 2.7 (by J.A.S. using the modulus images). The pump output was measured.

Results are expressed as the mean ± standard deviation. Measurements of agreement between the standard flow sequence and the real-time flow sequence were performed using Bland-Altman analysis, as well as calculation of correlation coefficients. All statistical analysis was performed using GraphPad Prism.

	Retrospectively-gated Cartesian PCMR	**Prospectively-triggered spiral PCMR**
TE/TR	2.7/7.0 ms	2.3/5.2 ms
GRAPPA (ACL)	2 (24)	-
Spiral readouts	-	36
SENSE factor	-	3
Readouts per RR	2	2
Flip angle	30^{o}	25^{o}
FOV	240×320	375×375
Rectangular FOV	75 %	-
Asymmetric echo	77 %	-
Matrix	192×256	256×256
Pixel Bandwidth	391 Hz/pixel	1395 Hz/pixel
VENC	100 cm/s	100 cm/s
NSA	1	1
Temporal resolution	25.3 ms	30.9 ms
Spatial resolution	1.3×1.3×6.0 mm	1.5×1.5×6.0 mm
Scan Time	~50 seconds (54 RR-intervals)	~5 seconds (6 RR-intervals)

Table 4.4: Sequence parameters in-vitro, for retrospectively-gated Cartesian sequence and prospectively-triggered spiral sequence

4.5.3 In-vitro Results

For each experiment the pump output was calculated using both of the sequences. There was good agreement between the retrospectively-gated Cartesian PCMR sequence and the prospectively-triggered spiral PCMR sequence, throughout the cycle as seen in Figure 4.21.

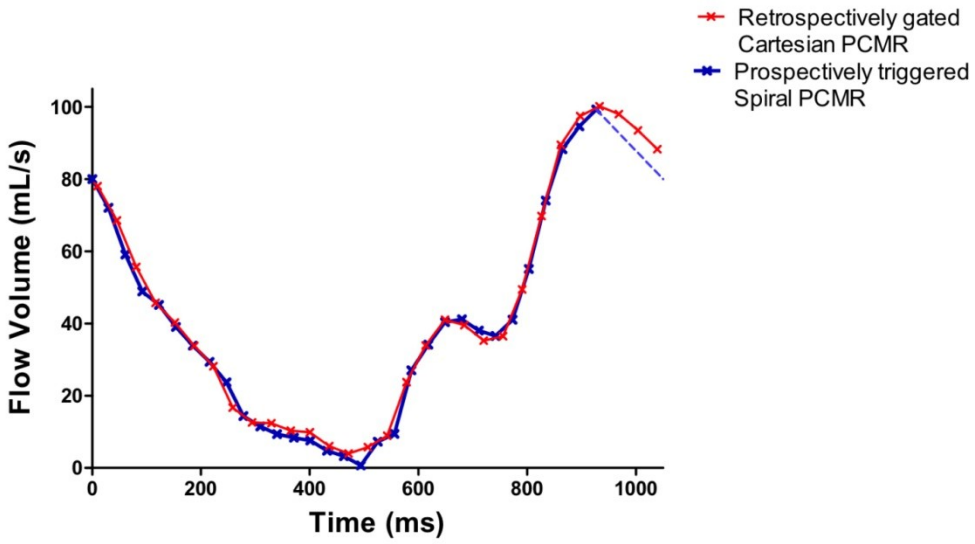

Figure 4.21: Comparison of flow profiles in-vitro

From Figure 4.21 it can be seen that the flow pump triggers during peak systole, therefore the need for a trigger window means that data is not acquired during peak flow. The dashed line at the very end of the RR-interval shows the linear interpolation between the last point and the first point to ensure the prospectively-triggered data fills the entire RR-interval (as described in section 4.3.4).

However, a good agreement was found between the pump output calculated from the retrospectively-gated Cartesian PCMR sequence and prospectively-triggered spiral PCMR sequence (3.24 ± 0.90 L/min vs. 3.15 ± 0.88 L/min, respectively). Bland-Altman analysis of the pump output found the bias was -0.10 L/min, with 95% limits of agreement from -0.29 to 0.09 L/min (as seen in Figure 4.22). The correlation coefficient was 0.994 ($p < 0.005$).

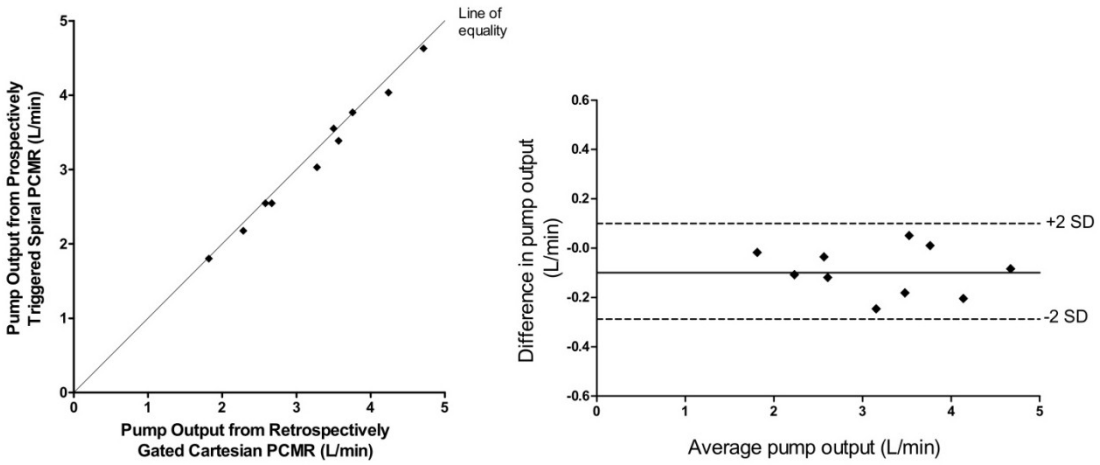

Figure 4.22: Comparison of pump output in-vitro between retrospectively-gated Cartesian sequence and prospectively-triggered spiral sequence. a) Correlation of flow measured from both techniques. b) Bland-Altman plot of the difference in flow measured using both techniques

The prospectively-triggered spiral PCMR sequence is thought to underestimate the pump output compared to the retrospectively-gated Cartesian sequence because the pump is triggered during peak systole. This means that the trigger window always occurs when there is maximum flow, and the linear interpolation does not completely account for the true flow as seen in Figure 4.21.

4.6 In-vivo Protocol

The prospectively-triggered spiral PCMR sequence was validated in-vivo by comparing image quality and flow volumes measured using:

a) Breath-hold spiral SENSE PCMR

b) Standard breath-hold PCMR

c) Reference free-breathing PCMR

4.6.1 Patient population

In July and August 2010, 40 consecutive children and adults (22 male: 18 female) referred for cardiac MR imaging, were enrolled in this study. The median age was 21.4 ± 13.8 years (range: 3.0 to 61.3 years, 17 of whom were less than 16 years old). Their diagnoses were;

- Repaired tetralogy of Fallot/ pulmonary atresia with ventricular septal defect – 15
- Coarctation of the Aorta – 7
- Cardiomyopothy exam – 6
- Pulmonary stenosis – 4
- Transposition of the great arteries repair – 2
- Atrial septal defect - 2, dilated aortic root – 2
- Left pulmonary artery stenosis – 1
- Bicuspid aortic valve – 1

Of these, 5 children were imaged whilst under general anaesthetic. The sample size was chosen to detect a mean difference in stroke volumes of 2 mL with a statistical power of 80 % and a p-value of .05 (means and standard deviation assumed from values found by Sakuma, et al. (97) between CO measurements made during free breathing and small lung volume breath-holding; 6.09 ± 0.49 L/min vs. 5.87 ± 0.53 L/min, respectively). This analysis was performed using open-source

software (G*power 3; University of Dusseldorf, Dusseldorf, Germany) (132) which gave an estimated sample size of 36 (which was increased to 40 for this study).
Inclusion criteria were:

a) Clinical referral for cardiac MR imaging

Exclusion criteria were:

a) Contraindications for MR such as MR-incompatible implants
b) Pregnancy
c) Irregular heart rate

The local research ethics committee approved the study and written consent was obtained from all subjects/guardians.

4.6.2 MR protocol

Imaging was performed on a 1.5 T MR scanner using two spine coils and one body-matrix coil (giving a total of 12 coil elements). A vector ECG system was used for cardiac gating.

All patients underwent a standard clinical cardiac MR examination for diagnostic purposes. Flow imaging was performed in the following vessels as per clinical need, with stented vessels excluded:

- Ascending aorta, AAO (N = 40, including 4 with regurgitation)
- Main pulmonary artery, MPA (N = 38, including 12 with regurgitation)
- Right pulmonary artery, RPA (N = 22, including 10 with regurgitation)
- Left pulmonary artery, LPA (N = 24, including 14 with regurgitation)

Flow assessment was performed in each vessel using the three sequences described below (parameters shown in Table 4.5), before moving to the next vessel.

4.6.2.1 Reference Free-breathing Sequence

The reference standard used in this study was a retrospectively-gated, free-breathing, Cartesian, gradient echo PCMR sequence (provided by the manufacturer). Respiratory motion was compensated by the acquisition of three NSA's. This sequence had high spatial and temporal resolution (Table 4.5) and is well-validated in-vitro and in-vivo (58, 94, 133-135). Therefore in this study the flow volumes measured from this sequence are assumed to be the true flow volumes.

4.6.2.2 Standard Breath-hold Sequence

The standard breath-hold sequence was a retrospectively-gated, Cartesian PCMR sequence (provided by the manufacturer). This sequence was the same as the free-breathing flow sequence described above. However, in order to acquire the data within a breath-hold, spatio-temporal resolution was lowered (Table 4.5).

4.6.2.3 Spiral SENSE Breath-hold Sequence

The spiral sequence was a prospectively-triggered, segmented PCMR sequence, described in section 4.3.

The FOV was not optimized for children, as this would have resulted in a reduction in temporal resolution in the spiral sequence. This is because to reduce the FOV, we must go further out in k-space. Due to limitations in the gradient strength, it is not possible to traverse this outer part of k-space at the sampling bandwidth used in Table 4.5. Therefore a reduction in FOV, results in a reduction in bandwidth for spiral imaging, causing a decrease in the temporal resolution.

	Reference Free-Breathing PCMR	**Standard Breath-hold PCMR**	**Spiral Breath-hold PCMR**
TE/TR	~2.2 / 7.0 ms	~2.2 / 7.0 ms	2.1 / 8.0 ms
Spiral Readouts	-	-	36
Acceleration factor	2 (GRAPPA)	2 (GRAPPA)	3 (SENSE)
Matrix Size	256 × 192	192 × 113	256 × 256
FOV	200 - 400 mm	290 - 400 mm	400 mm
Rectangular FOV	75 %	66 %	100 %
Readouts per segment	3	4	2
Slice Thickness	5 mm	5 mm	5mm
Flip Angle	30^o	30^o	25^o
Pixel bandwidth	543 Hz/pixel	543 Hz/pixel	1220 Hz/pixel
VENC	180 - 400 cm/s	180 - 400 cm/s	180 - 400 cm/s
NSAs	3	1	1
Total Scan Duration	44 - 144 s	11 - 24 s	3 - 8 s
Voxel Size	~ 0.8 – 1.5 mm	~ 1.5 – 2.1 mm	1.6 mm
Temporal resolution	~ 30.0 ms (~33 frames/sec)	~ 40.0 ms (~25 frames/sec)	32.0 ms (31 frames/sec)

Table 4.5: Imaging parameters

4.6.3 Image Analysis

All images were processed in OsiriX by J.A.S. Flow images were segmented using the semi-automatic segmentation propagation plug-in described in section 2.7 (using the modulus images). For each flow measurement the stroke volume (net forward flow) and regurgitation fraction were calculated. Additionally, where flow was measured in both the MPA and AAO (N = 38) the Q_P/Q_S ratio was calculated, and where flow was measured in both the pulmonary branch vessels (N = 20) the *RPA/LPA* ratio was calculated.

In 10 randomly selected patients, the AAO flow data was reanalyzed for all three sequences (J.A.S. – 3 years experience) to determine intra-observer variability. This data was also analyzed by a second operator (V.M. – 8 years experience), to determine inter-observer variability.

4.6.4 Statistical analysis

All statistical analysis was performed using GraphPad Prism. The results were combined for all subjects, and were expressed as the mean ± standard deviation. Comparison of means was performed by using repeated-measures ANOVA tests, with Bonferroni correction for multiple comparisons. A p-value of less than .05 indicated a significant difference. Bland-Altman analysis was performed to give measures of agreement with the free-breathing PCMR sequence (119). Additionally, the correlation coefficients were calculated.

4.7 In-vivo Results

The average heart rate was 76 ± 12 bpm (range: 50 to 111 bpm). For the reference free-breathing sequence, data was acquired over 108 heart-beats, which was 91 ± 17 seconds (range: 44 to 144 seconds). In the standard breath-hold sequence, data was acquired over 18 heart-beats, which was 16 ± 3 seconds (range: 11 to 24 seconds). For the spiral breath-hold sequence, data was acquired over 7 heart-beats, which was 5 ± 1 seconds (range: 3 to 8 seconds).

4.7.1 Physiological Data

Although it was not possible to perform any quantitative analysis of the physiological data, due to internal scaling of the data prior to being recoded (see section 4.3.8), it was observed that some subjects found the breath-hold time for the standard breath-hold sequence too long. This can be seen in Figure 4.23, where subjects 1 and 2 both completed the first half of the breath-hold well, but breathe throughout the second half of the sequence. Figure 4.23 shows that these subjects were able to complete the much shorter breath-hold for the spiral SENSE breath-hold sequence successfully.

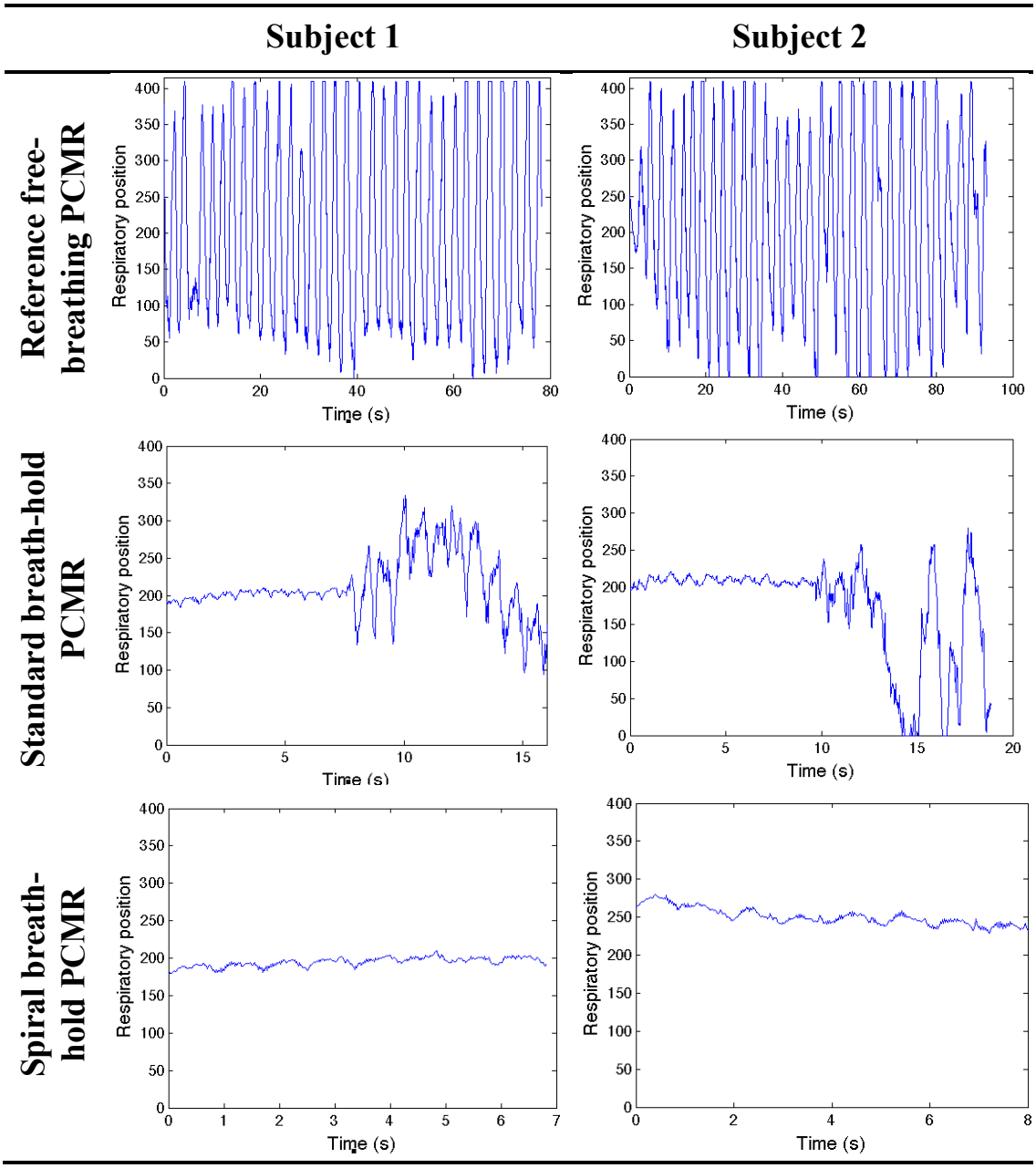

Figure 4.23: Respiratory data recorded from two subjects, for all three sequences. These subjects were able to complete the short breath-hold for the spiral sequence, however were only able to complete about half of the breath-hold for the standard breath-hold sequence. Note: different time axis.

4.7.2 Functional Assessment

A good agreement was seen throughout the cardiac cycle for all sequences, in all vessels, as can be seen for one subject in Figure 4.24;

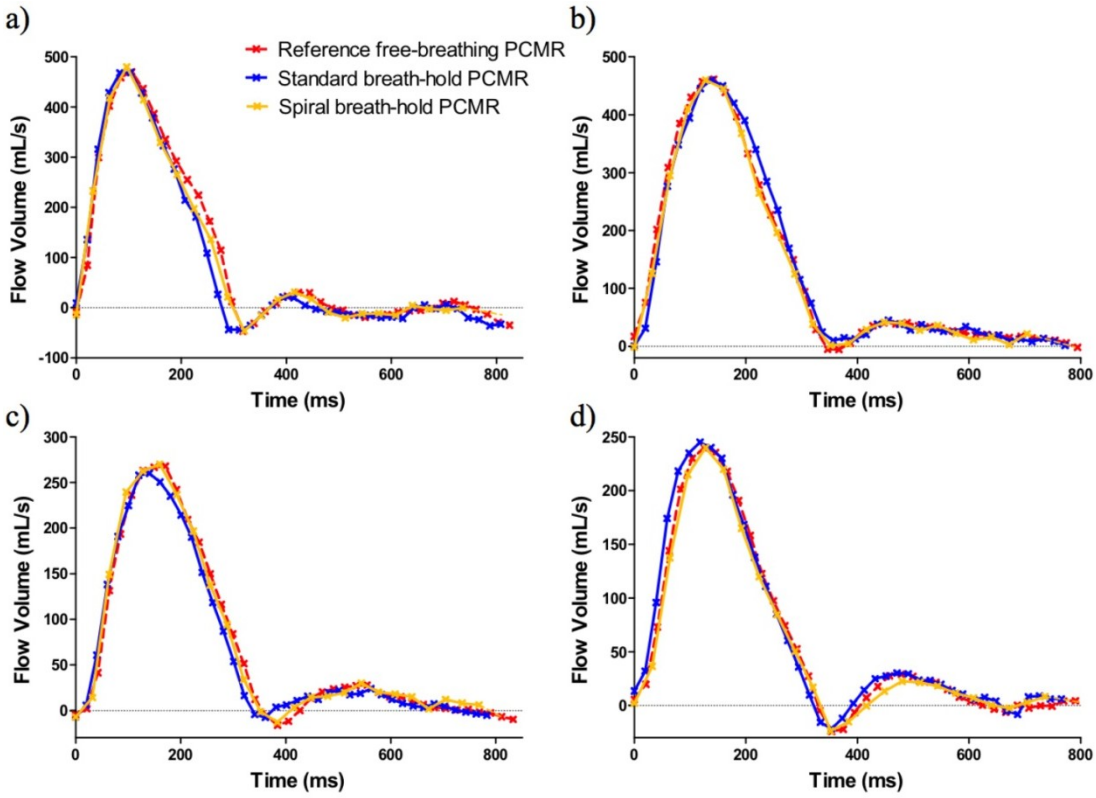

Figure 4.24: Comparison of flow profiles from all three sequences for one patient, for; a) AAO, b) MPA, c) RPA, d) LPA

Combining all vessels (N = 124), there were no statistical differences in mean stroke volume calculated from the reference free-breathing sequence (60.3 ± 27.3 mL/cycle), the standard breath-hold sequence (59.8 ± 27.6 mL/cycle) and the spiral breath-hold sequence (59.5 ± 27.1 mL/cycle). Bland-Altman analyses comparing the breath-hold sequences to the reference free-breathing sequence are shown in Figure 4.25.

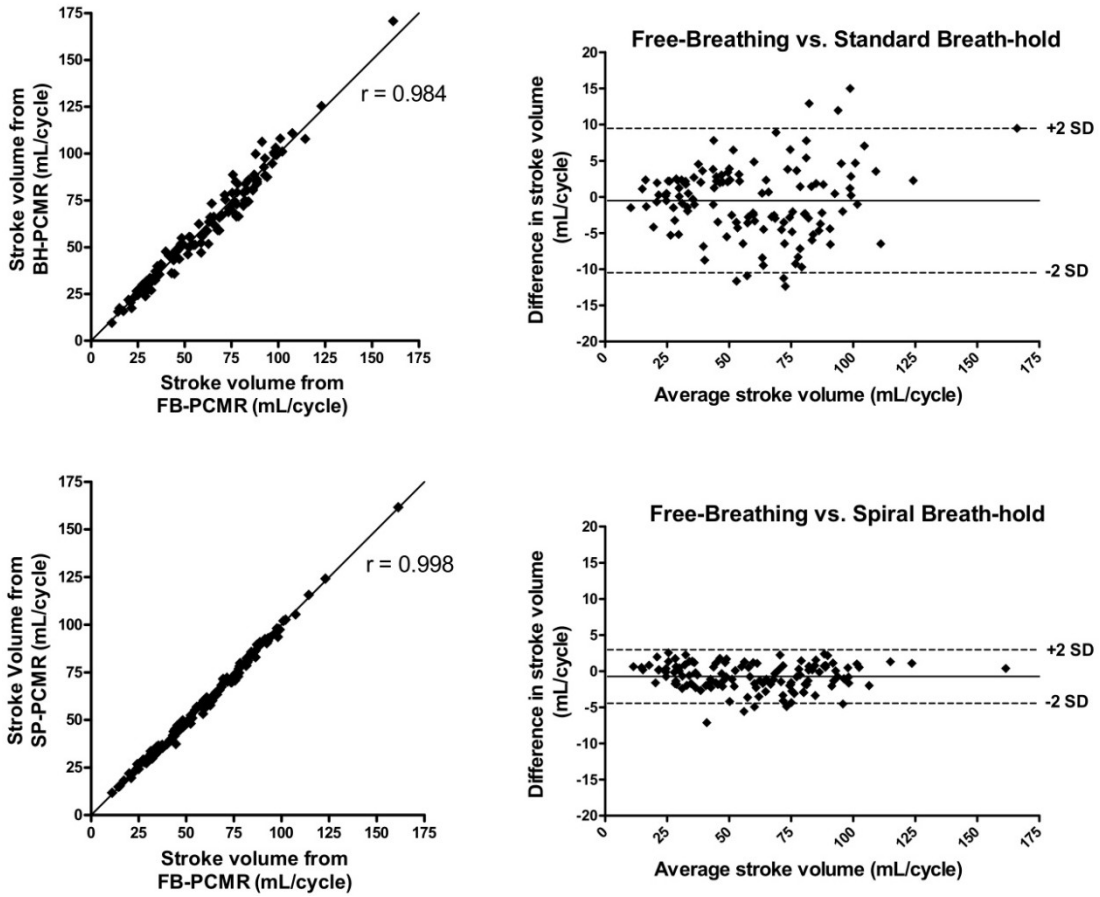

Figure 4.25: Comparisons of stroke volumes in all vessels between reference free-breathing PCMR (FB-PCMR) and standard breath-hold PCMR (BH-PCMR) (top), and between free-breathing PCMR and spiral breath-hold PCMR (SP-PCMR) (bottom). Scatter plots shown on the left and associated Bland-Altman analysis shown on the right

There was no clinically significant bias between the reference free-breathing sequence and either breath-hold sequence (spiral breath-hold: -0.7 mL/cycle, standard breath-hold: -0.5 mL/cycle). However, the 95% limits of agreement were smaller and the correlation better for the spiral breath-hold sequence compared to the standard breath-hold sequence (-4.4 to 2.9 mL/cycle vs. -10.3 to 9.3 mL/cycle, r = 0.984 vs. r = 0.998, respectively).

Separate mean stroke volumes, Bland-Altman analysis and correlations for the AAO, MPA and branch pulmonary arteries are shown in Table 4.6 and Figure 4.26.

	Free-Breathing PCMR	**Standard Breath-hold PCMR**	**Spiral Breath-hold PCMR**
AORTA			
Stroke Volume (mL)	68.6 ± 19.6	67.3 ± 19.6	67.7 ± 19.9
Bias* (mL)	-	-1.3	-0.9
Limits of agreement* (mL)	-	-11.1 to 8.5	-4.6 to 2.8
Correlation coefficient* (r)	-	0.968	0.996
MPA			
Stroke Volume (mL)	76.6 ± 27.6	76.2 ± 29.1	75.9 ± 27.7
Bias* (mL)	-	-0.5	-0.8
Limits of agreement* (mL)	-	-13.1 to 12.1	-4.4 to 2.8
Correlation coefficient* (r)	-	0.976	0.998
PULMONARY BRANCHES			
Stroke Volume (mL)	39.5 ± 18.5	39.7 ± 19.2	38.9 ± 18.1
Bias* (mL)	-	0.2	-0.6
Limits of agreement* (mL)	-	-6.5 to 6.8	-4.2 to 3.1
Correlation coefficient* (r)	-	0.985	0.995

* Compared to free-breathing PCMR sequence

Table 4.6: Comparison of stroke volumes calculated from the three sequences

There were no statistically significant differences in stroke volumes calculated between any of the sequences. Bland-Altman analysis found only a small bias in stroke volume between the free-breathing and both the breath-hold sequences. For all vessels, the limits of agreement were smaller and the correlation was greater for spiral breath-hold acquisition, compared to the standard breath-hold acquisition.

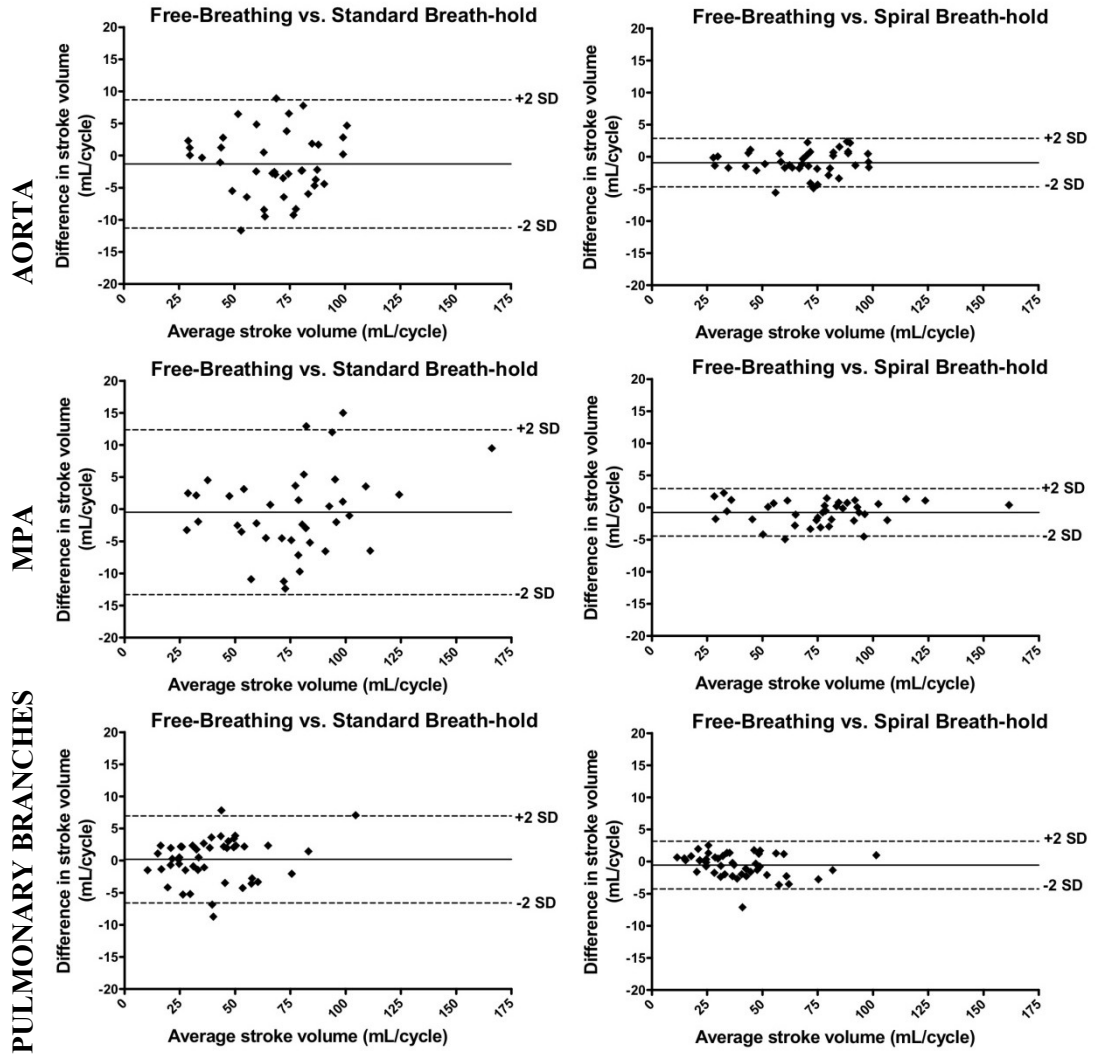

Figure 4.26: Bland-Altman analysis comparing stroke volumes in the aorta, MPA and pulmonary branches between reference free-breathing and standard breath-hold PCMR (left), and between free-breathing PCMR and spiral breath-hold PCMR (right)

Regurgitant flow was found in 40 vessels (see Table 4.7 and Figure 4.27). For free-breathing vs. standard breath-hold PCMR there was no significant difference in regurgitation. However, a small but statistically significant difference was found between the free-breathing and spiral breath-hold PCMR sequences (probably due to the need for a trigger window at the end of diastole in prospective-gating). Despite this, the correlation coefficient was found to be higher and limits of agreement to be lower with the spiral breath-hold acquisition, compared to the standard breath-hold acquisition.

	Free-Breathing PCMR	**Standard Breath-hold PCMR**	**Spiral Breath-hold PCMR**
REGURGITATION (N=40)			
Regurgitation fraction (%)	31.1 ± 14.7	30.0 ± 15.0	29.1 ± 14.2 †
Range (%)	11.16 to 60.8	6.4 to 60.4	8.6 to 55.7
Bias* (%)	-	-1.1	-2.0
Limits of agreement* (%)	-	-8.2 to 5.9	-6.8 to 2.8
Correlation coefficient* (r)	-	0.971	0.986

* Compared to free-breathing PCMR sequence

† Value is significantly different from free-breathing PCMR ($p < 0.05$)

Table 4.7: Comparison of regurgitation fraction calculated from the three sequences

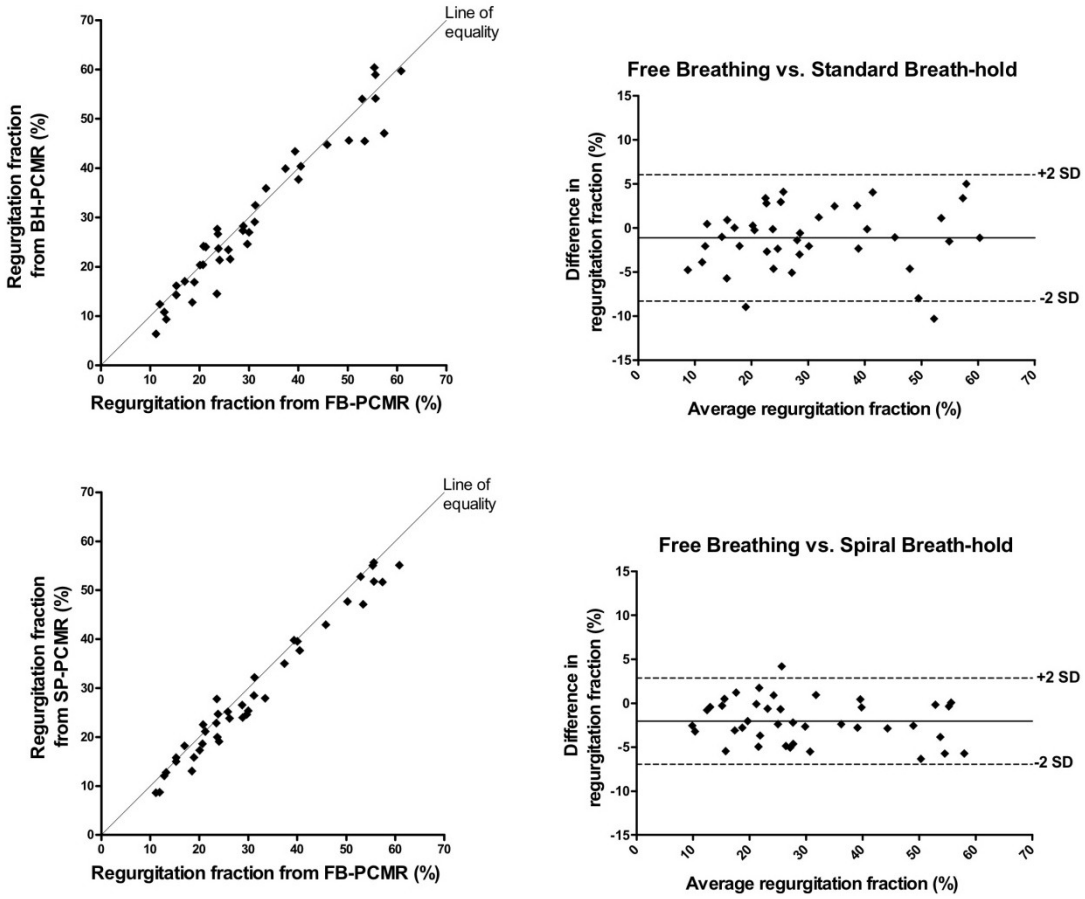

Figure 4.27: Comparisons of stroke volumes in all vessels between reference free-breathing PCMR (FB-PCMR) and standard breath-hold PCMR (BH-PCMR) (top), and between free-breathing PCMR and spiral breath-hold PCMR (SP-PCMR) (bottom). Scatter plots shown on the left and associated Bland-Altman analysis shown on the right

Q_P/Q_S and *RPA/LPA* ratios were calculated where possible (see Table 4.8, Figure 4.28 and Figure 4.29). No significant differences were found between any of the sequences. Bland-Altman analysis found a slightly lower bias, and smaller limits of agreement with the spiral breath-hold acquisition compared to the standard breath-hold acquisition.

	Free-Breathing PCMR	**Standard Breath-hold PCMR**	**Spiral Breath-hold PCMR**
Q_P/Q_S **(N=38)**			
Q_P/Q_S ratio	1.13 ± 0.29	1.15 ± 0.34	1.14 ± 0.30
Range	0.81 to 2.64	0.78 to 2.92	0.83 to 2.73
Bias*	-	0.018	0.006
Limits of agreement*	-	-0.23 to 0.27	-0.08 to 0.10
Correlation coefficient* (r)	-	0.933	0.989
RPA/LPA **(N=20)**			
RPA/LPA ratio	1.44 ± 0.59	1.42 ± 0.65	1.39 ± 0.53
Range	0.55 to 2.78	0.44 to 2.62	0.54 to 2.70
Bias*	-	-0.049	-0.050
Limits of agreement*	-	-0.32 to 0.21	-0.22 to 0.12
Correlation coefficient* (r)	-	0.973	0.991

* Compared to free-breathing PCMR sequence

Table 4.8: Comparison of Q_P/Q_S and *RPA/LPA* ratios calculated from the three sequences

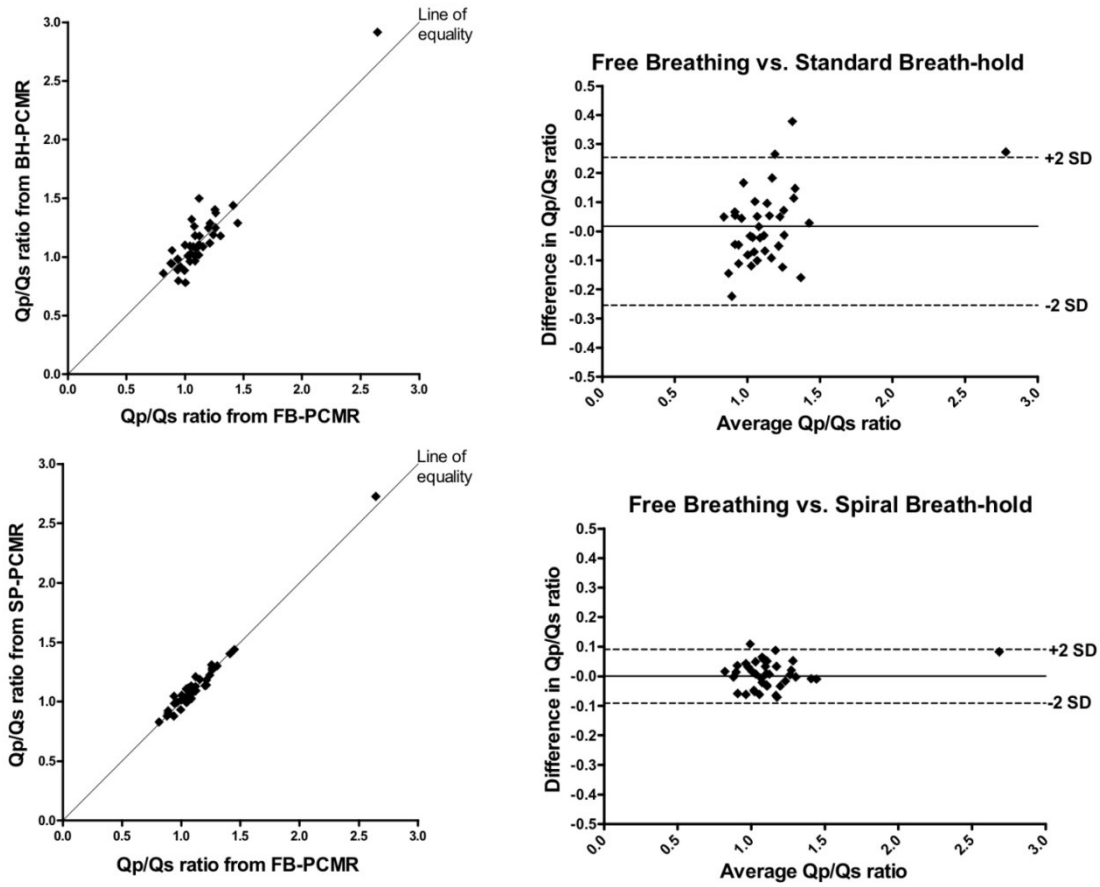

Figure 4.28: Comparisons of Q_P/Q_S ratio in all vessels between reference free-breathing PCMR (FB-PCMR) and standard breath-hold PCMR (BH-PCMR) (top), and between free-breathing PCMR and spiral breath-hold PCMR (SP-PCMR) (bottom). Scatter plots shown on the left and associated Bland-Altman analysis shown on the right

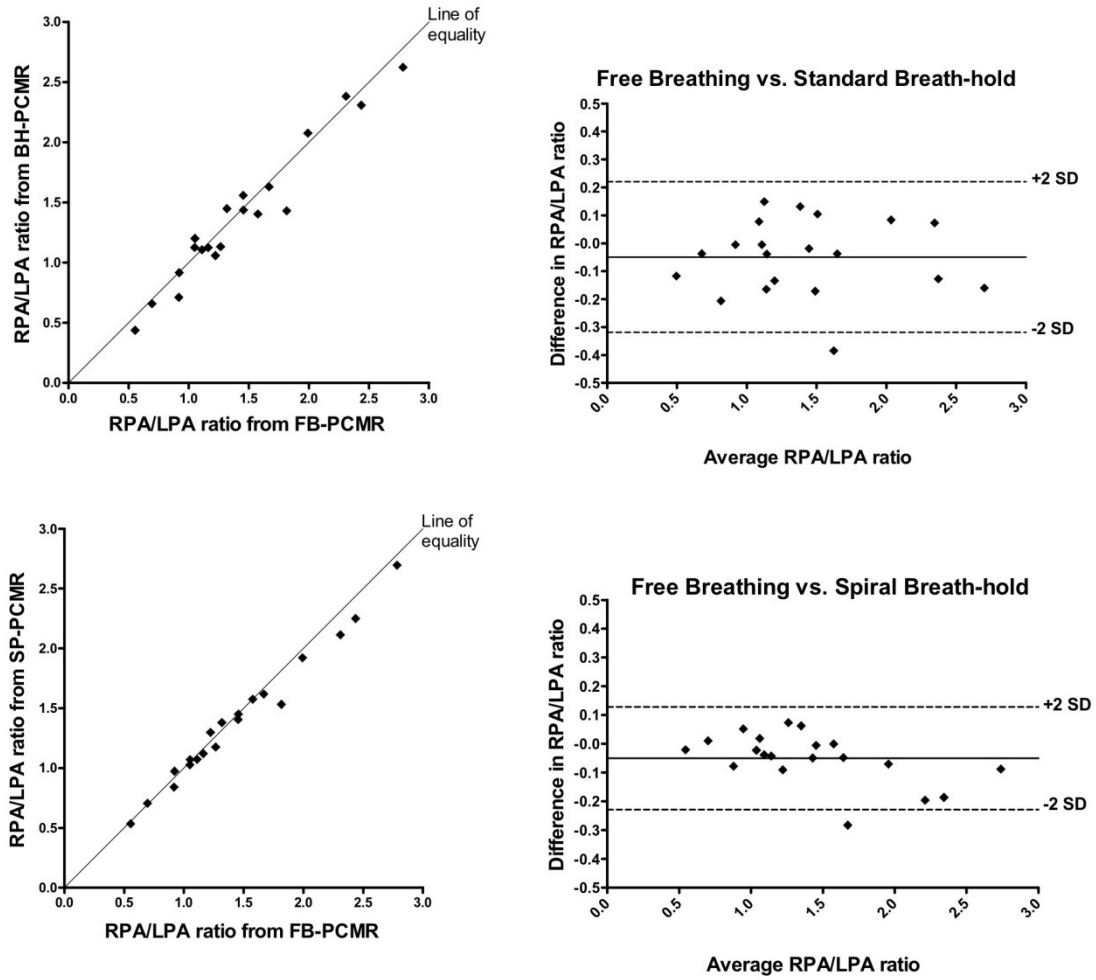

Figure 4.29: Comparisons of *RPA/LPA* ratio in all vessels between reference free-breathing PCMR (FB-PCMR) and standard breath-hold PCMR (BH-PCMR) (top), and between free-breathing PCMR and spiral breath-hold PCMR (SP-PCMR) (bottom). Scatter plots shown on the left and associated Bland-Altman analysis shown on the right.

For 10 randomly selected subjects, the AAO data from all three sequences was re-evaluated by the same observer (J.A.S.). The mean difference in stroke volumes from the free-breathing sequence was 0.5 ± 1.2 % (range: -1.1 to 2.9 %, p = 0.25), for the standard breath-hold sequence was 0.9 ± 2.4 % (range: -3.6 to 5.6 %, p = 0.20) and for the spiral breath-hold was -0.3 ± 1.2 % (range: -2.6 to 1.6 %, p = 0.22), as seen in Figure 4.30. There were no statistically significant differences between the repeated measures for any of the sequences.

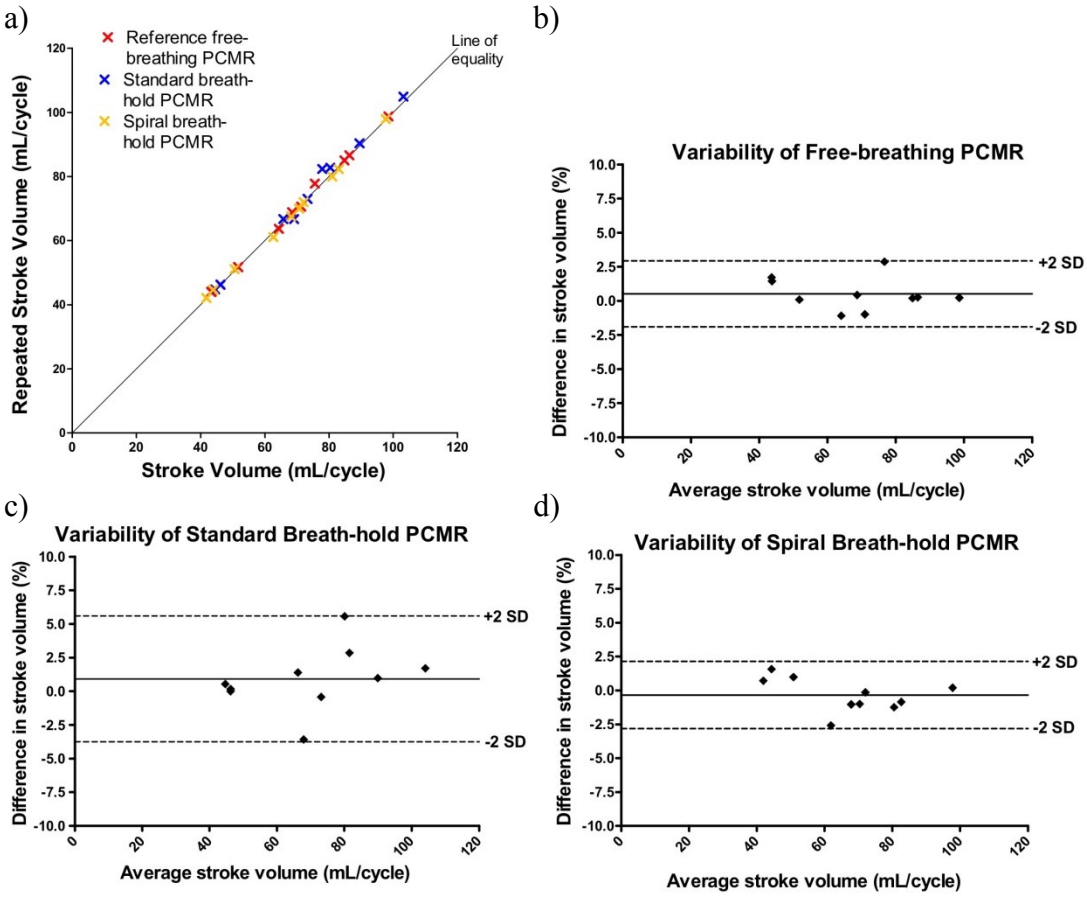

Figure 4.30: Comparisons of intra-observe variability between the three sequences. a) Scatter plot for all three sequences, as well as Bland-Altman analysis for b) reference free-breathing sequence, c) standard breath-hold sequence, and d) spiral breath-hold sequence

These 10 AAO data sets were also independently reviewed by a second observer (V.M.), to assess inter-observer variability. The mean difference in stroke volumes from the free-breathing sequence was 0.1 ± 1.5 % (range: -2.5 to 3.4 %, p = 0.75), for the standard breath-hold sequence was 0.7 ± 2.3 % (range: -3.9 to 3.6 %, p = 0.40) and for the spiral breath-hold was -0.5 ± 1.5 % (range: -2.7 to 2.5 %, p = 0.21), as seen in Figure 4.31. There were no statistically significant differences between the repeated measures for any of the sequences.

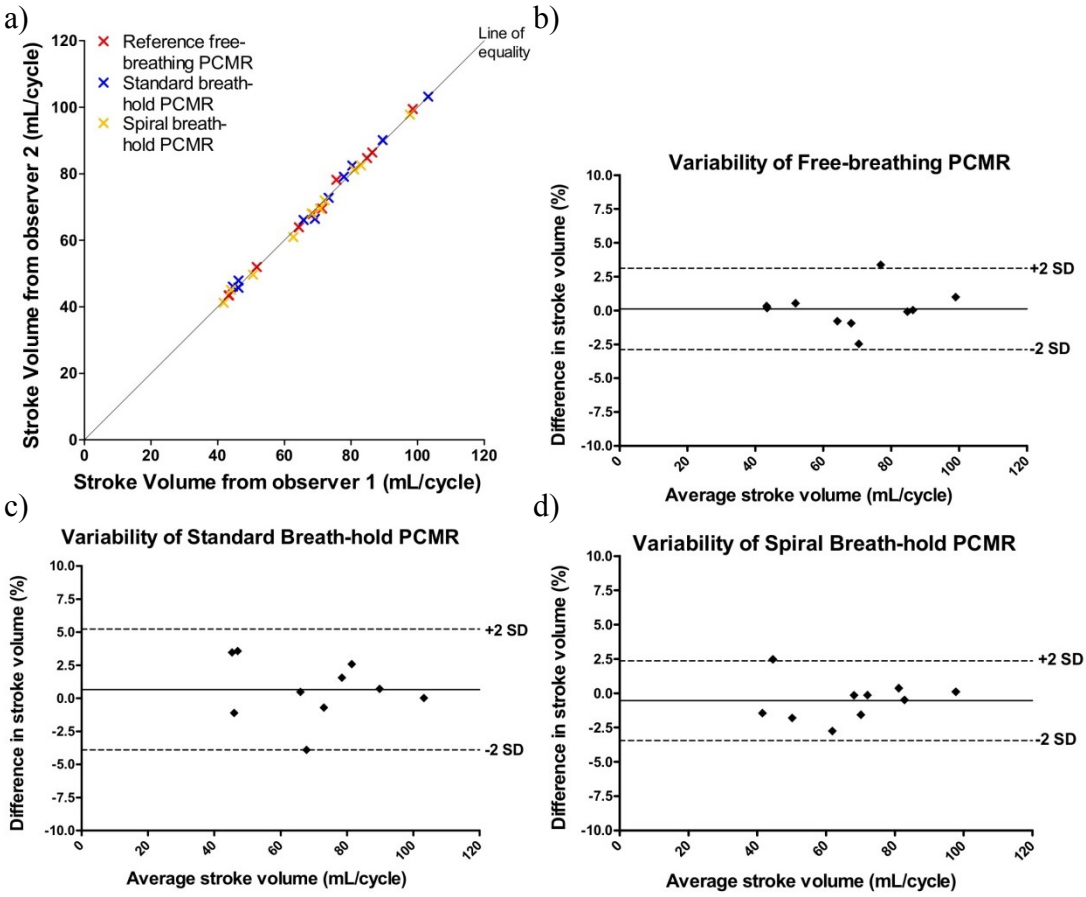

Figure 4.31: Comparisons of inter-observe variability between the three sequences. a) Scatter plot for all three sequences, as well as Bland-Altman analysis for b) reference free-breathing sequence, c) standard breath-hold sequence, and d) spiral breath-hold sequence

4.8 Image Quality

Image quality was assessed for all three sequences using measures of SNR, VNR and edge sharpness, as described in section 4.3.5 and 4.3.6. Figure 4.32 shows examples of the image quality from all three tested sequences in the AAO, MPA, RPA and LPA. Quantitative image quality metrics can be seen in Table 4.9;

	Free-Breathing PCMR	**Standard Breath-hold PCMR**	**Spiral Breath-hold PCMR**
Estimated signal variation: σ_S	5.4 ± 1.4	5.9 ± 1.5†	8.6 ± 2.2†‡
σ_S / $\sigma_{S\ \text{Free-breathing}}$	-	1.1 ± 0.3	1.7 ± 0.6
Estimated SNR	45.6 ± 14.9	41.7 ± 14.2†	31.9 ± 11.6†‡
Estimated velocity variation: σ_V (cm/s)	17.6 ± 9.1	19.5 ± 10.5†	19.7 ± 7.7†
σ_V / $\sigma_{V\ \text{Free-breathing}}$	-	1.1 ± 04	1.2 ± 0.4
Estimated VNR	8.4 ± 4.8	7.4 ± 3.9†	6.7 ± 3.1†‡
Edge Sharpness (mm^{-1})	0.78 ± 0.36	0.74 ± 0.34	0.78 ± 0.35

† Value is significantly different from free-breathing PCMR ($p < 0.05$)

‡ Value is significantly different from standard breath-hold PCMR ($p < 0.05$)

Table 4.9: Image Quality - estimated SNR, VNR and edge sharpness measures for all sequences

The free-breathing PCMR images had the highest estimated SNR and VNR compared to both of the breath-hold PCMR sequences ($p < 0.05$). The spiral breath-hold PCMR images had the lowest estimated SNR and VNR compared to the free-breathing and standard breath-hold PCMR images ($p < 0.05$).

Edge sharpness was not significantly different between any of the sequences (Table 4.9). However, the free-breathing PCMR images and the spiral breath-hold PCMR images had the same average edge sharpness, whereas the edge sharpness was slightly lower in the standard breath-hold PCMR images.

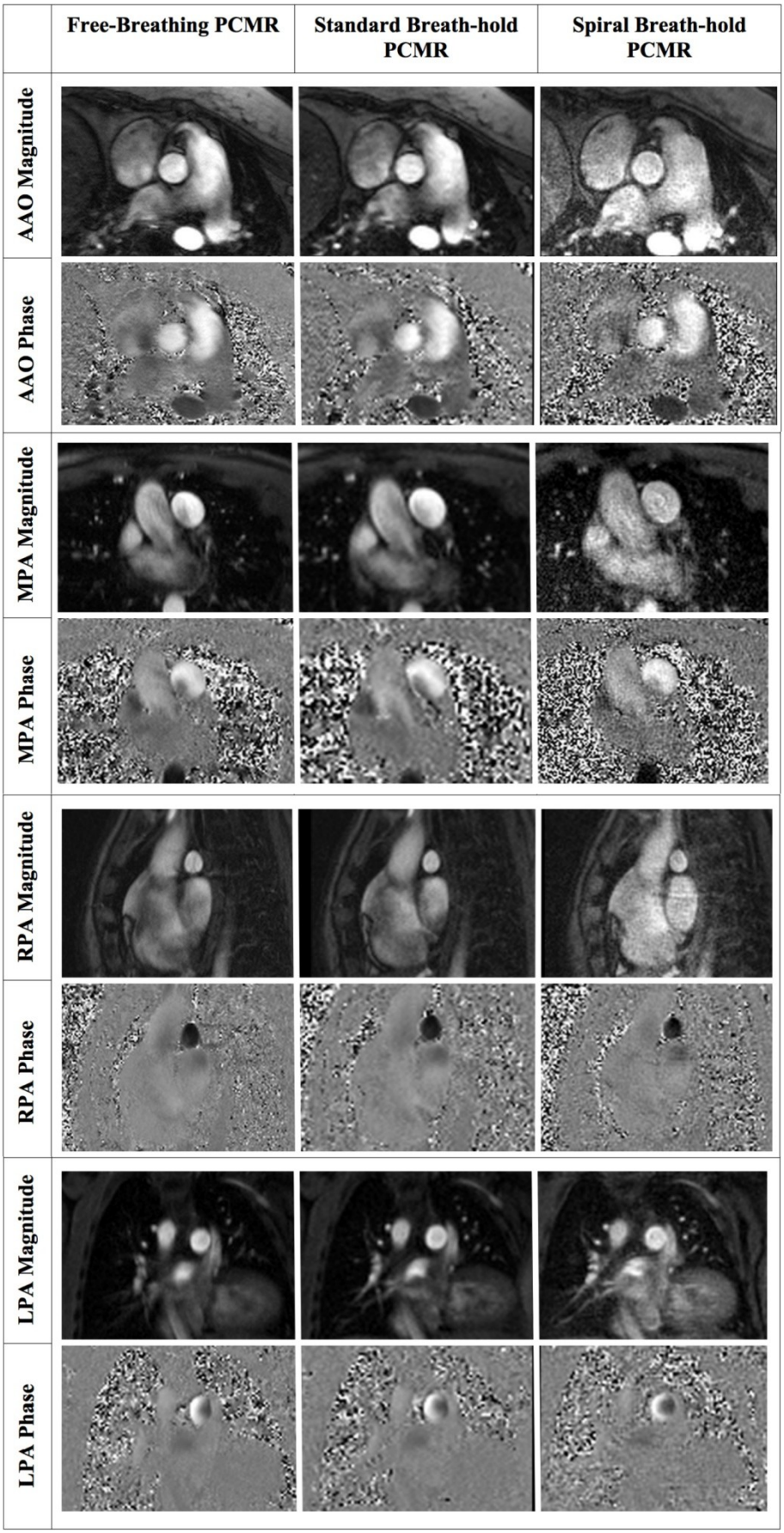

Figure 4.32: Examples of image quality from the three sequences

4.9 Discussion

We have demonstrated that is it possible to use a prospectively-triggered, undersampled spiral PCMR sequence with a SENSE reconstruction algorithm to accurately and reliably measure flow within a short breath-hold (3-8 seconds). Currently the reference standard method of measuring flow in patients with congenital heart disease is high spatio-temporal resolution, free-breathing, cardiac gated PCMR. Unfortunately, due to multiple signal averaging, each flow assessment can take more than 2 minutes to perform. Thus in congenital cardiac MR, where between 4 and 8 separate flow assessments are necessary, flow imaging can take a significant proportion of the total scan time. The spiral breath-hold sequence used in this study should be able to reduce the total duration of flow imaging from an average of 10 minutes, to less than 1 minute. This would lead to a marked reduction in total scan time and has implications for patient throughput and compliance for congenital cardiac MR scanning.

4.9.1 Spiral SENSE PCMR

Achieving high spatio-temporal resolution PCMR in a short breath-hold requires efficient filling of k-space. In this study, spiral trajectories were used to significantly speed up acquisition time. Imaging was further accelerated with non-Cartesian SENSE. The resultant sequence had a breath-hold time of ~5 seconds, compared to ~16 seconds for a standard Cartesian breath-hold PCMR sequence. Furthermore, unlike the standard breath-hold sequence, spatio-temporal resolution was not compromised in order to achieve the short breath-hold. This makes this spiral sequence extremely useful in both children and sick adults who are unable to perform long breath-holds (as demonstrated in Figure 4.23). There are some disadvantages to spiral trajectories and parallel imaging, including off resonance effects and trajectory errors, as well as reduced signal-to-noise. However, these were not seen to affect the accuracy of the spiral PCMR sequence in this study.

4.9.2 Comparison of sequences

For stroke volumes, Q_P/Q_S and *RPA/LPA* ratios, there was an excellent agreement between the spiral breath-hold sequence and the reference free-breathing sequence. Furthermore, the spiral breath-hold sequence was found to be superior to the standard breath-hold sequence in terms of limits of agreement and correlation. This is most likely to be due to the higher temporal and spatial resolution of the spiral breath-hold sequence. It may also be attributed to the shorter breath-hold times, which may prevent residual breathing, as well as limiting heart rate variability during the scan. In addition the intra-observer and inter-observer variability seen in the spiral breath-hold PCMR sequence was good.

There was however, a small, but statistically significant difference in the regurgitation fractions calculated from the free-breathing PCMR sequence and the spiral breath-hold sequence. This was probably due to the interpolation of the flow curve at the very end of diastole in the prospectively-triggered spiral sequence. However, it should be noted that the difference in regurgitant fraction was on average only 2 % and this would not be considered clinically important.

4.9.3 Image quality

The edge sharpness of the spiral breath-hold sequence was found to be similar to the free-breathing sequence, and higher than the standard breath-hold sequence. This is most likely due to the lower spatial resolution of the standard breath-hold PCMR sequence. The good edge sharpness of the spiral breath-hold sequence may have benefits in terms of either manual or automatic segmentation of the vessels compared to standard breath-hold sequences. However, the spiral breath-hold sequence had a lower estimated SNR and VNR than the free-breathing and standard breath-hold sequences. This is due to:

i) Higher acceleration factor used compared to the other two sequences
ii) Much higher bandwidth used compared to the other two sequences
iii) No signal averages (unlike the free-breathing PCMR sequence)
iv) Higher spatial resolution compared to the standard breath-hold sequence

4.9.4 Limitations

The main limitation of using an undersampled spiral trajectory is the need for a large FOV, in order to prevent wrapping of signal and ensure accurate reconstruction of the undersampled data. As we do not use a selective excitation, it is necessary for the FOV to be larger than the object being scanned. In the future, the FOV could be reduced by the use of improved coil configurations, or RF-shielding of the arms and torso (see section 5.2.1). Additionally, a spatially-selective RF-pulse, or saturation bands could be used, however these would increase the scan time, or reduce the temporal resolution (see section 5.2.1).

As seen from the image quality analysis, the spiral breath-hold PCMR sequence has a significantly lower SNR and VNR than the standard breath-hold PCMR sequence, or the free-breathing sequence. Although this is a limitation of the sequence it did not affect the accuracy of the stroke volume measurements made in this study.

4.9.5 Conclusion

Currently, MR flow assessment can take more than 10 minutes in patients with congenital heart disease. Thus it often represents almost 25 % of total scan time. Using the spiral breath-hold sequence validated in this study, all flow imaging could be performed in less than 1 minute. This would significantly reduce total scan time without compromising the accuracy of the flow assessment. The benefits of this would be twofold. Firstly, in the paediatric population a shorter total scan time would be less demanding on the patients and improve compliance. Secondly, shorter scan times should improve patient throughput. Therefore, we believe that this sequence has significant benefits in congenital CMR.

CHAPTER 5

Conclusions and Future Work

5.1 Summary

The present work has focussed on the development of fast and accurate methods of measuring blood flow, using undersampled spiral SENSE PCMR.

Chapter 2 presented a real-time spiral PCMR sequence, which was used to measure flow during the continuation of exercise, using an up-down ergometer. The flow data was combined with simultaneous blood pressure measurements to allow quantification of vascular resistance and compliance during exercise, in a population of 20 healthy volunteers. This technique was shown to successfully measure the hemodynamic response to exercise using MRI for the first time.

The sequence presented in chapter 2 was able to achieve a high temporal resolution of 40.4 ms, however the low spatial resolution (of 3.9x3.9 mm) means that this sequence is not suitable for quantification of flow volumes in small vessels or in children. To achieve higher spatial resolution imaging, during free-breathing, chapter 3 presented a split-acquisition PCMR technique. In this study the acquisition of flow-compensated and flow-encoded data was split into short blocks. By comparing magnitude images, the closest flow-compensated frame in the cardio-respiratory cycle was determined for each flow-encoded frame, allowing higher temporal or spatial resolution compared to conventional interleaved real-time PCMR. This technique was shown to be accurate in a population of 15 healthy adults, and 5 adult patients. Additionally, in 6 paediatric patients it was found that this split-acquisition sequence was more accurate than conventional interleaved real-time PCMR, due to the higher spatial resolution achieved.

Although the split-acquisition PCMR sequence (presented in chapter 3) was able to achieve a higher spatial resolution than the real-time PCMR sequence (presented in chapter 2), the resolution was still inferior to that desired clinically in patients with congenital heart disease. Chapter 4 therefore presented a high spatio-temporal resolution, prospectively triggered (interleaved) PCMR sequence. This sequence was demonstrated to accurately and reliably measure flow within a short breath-hold, in a population of 40 patients with congenital heart disease. This sequence allowed

comparable resolution to the clinical reference free-breathing, Cartesian PCMR sequence, however in ~5 seconds compared to ~90 seconds. The prospectively triggered spiral breath-hold sequence was shown to be accurate in terms of stroke volumes, Q_P/Q_S and *RPA/LPA* ratios. A small, but statistically significance difference was found in terms of regurgitation fraction calculated from the sequence, although this was not clinically significant. This sequence is now being widely used at ICH, leading to a marked reduction in total scan time. This has implications for patient throughput and compliance for congenital cardiac MR scanning.

5.2 Future Work

The studies described in this work all use undersampled spiral trajectories, with an iterative conjugate gradient SENSE algorithm. In all of these studies the main limitations were:

- The use of a large FOV, which was necessary to prevent wrapping of signal and ensure accurate reconstruction of the undersampled spiral data
- Long reconstruction times, due to the complex, iterative conjugate gradient algorithm used

Thus, future work could be directed towards addressing these limitations.

Additionally, future developments related to the studies described in this work include:

- 4D flow measurements
- Fourier velocity encoding (FVE)
- Fourier acceleration encoding (FAE)

5.2.1 Reducing the FOV

In the studies described in this work, the FOV was always > 400 mm in adults (and > 350 mm in children). This was necessary to ensure that the arms of the subjects were included in the FOV, therefore preventing ambiguity between aliasing caused by undersampling of data and aliasing caused by wrapping of signal.

The FOV could be reduced by the use of:

- Improved coil configurations
- RF-shielding of the arms and torso
- Spatially-selective RF-pulses
- Saturation bands

5.2.1.1 Improved Coil Configurations

Improved coil configurations may allow a reduction in the FOV, as smaller coils cannot 'see' as far as large coils (136). Therefore it is possible that by using specialist coils containing an array of smaller coils, the arms will not be 'seen' by the coils allowing a reduction in the FOV. The use of more coil elements may also improve the parallel imaging reconstruction algorithm or may allow higher acceleration factors to be achieved. However, the use of more coil elements would increase the reconstruction time.

5.2.1.2 RF-Shielding

RF-shielding of the arms and torso offers a very simple way to reduce the FOV. RF shields work by absorbing the RF signal, so that spins within the shield are not excited. *Accusorb* (137) offer advanced flexible RF absorbers, which are shaped to fit around the arms and torso, as seen in Figure 5.1;

Figure 5.1: From (137). Accusorb shields for the arms (left) and the torso (right)

We have carried out some preliminary experiments with these *Accusorb* RF shields over the arms of the subject. For the exercise study described in chapter 2, the shields allowed a reduction in FOV from 500 mm to 400 mm in adult subjects. This allowed an increase in the spatial resolution (from 3.9×3.9 mm to 3.1×3.1 mm), as well as greatly improving the image quality, as seen in Figure 5.2.

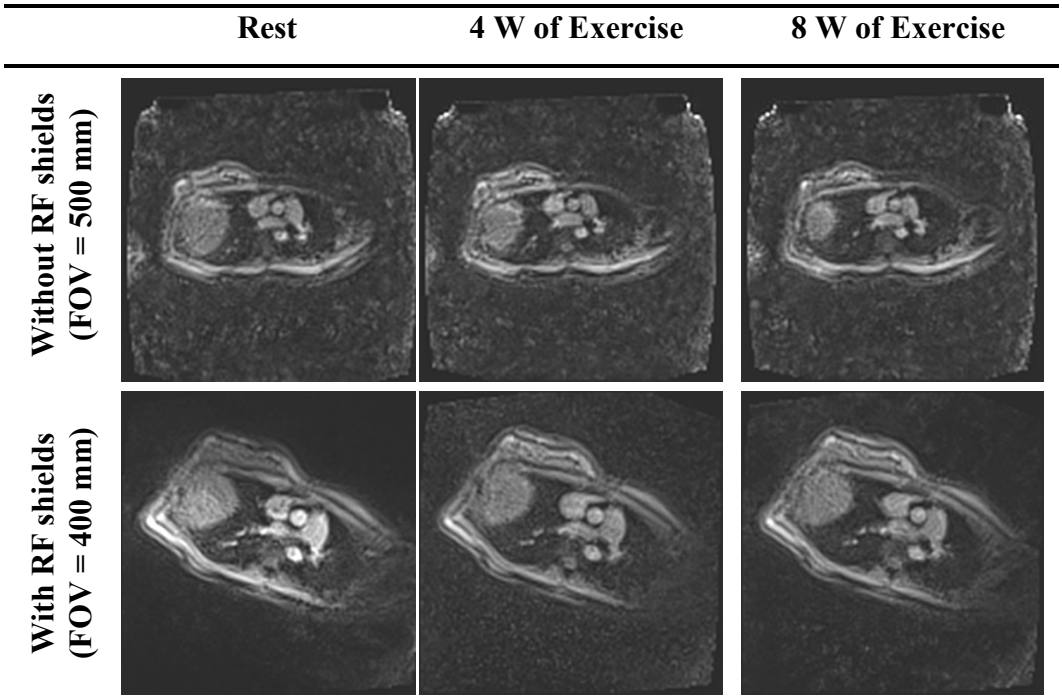

Figure 5.2: Effect of *Accusorb* RF arm shields in the same subject, from the real-time PCMR sequence described in chapter 2, at rest and during exercise

5.2.1.3 Spatially-selective RF-pulses

Spatially-selective RF-pulses could be used to only excite the tissue around the vessel of interest, allow significant reductions in the FOV. 2D spatially-selectivite RF-pulses are achieved by playing out appropriate gradients on two independent gradient axes, simultaneously with the RF waveform (138). Often the gradient waveforms used resemble the time-reversed spiral trajectories, described in this work.

Additionally, a spectral-spatial RF-pulse could be used (139), which would excite magnetization in a specified location and with a specified spectral content. This would allow one chemical species (e.g. water) to be excited, while leaving others virtually unaffected (e.g. lipids). This may be advantageous in spiral imaging due to the sensitivity of spiral trajectories to off-resonance effects. The biggest disadvantage of using selective RF-pulses is their long duration, which would conversely decrease the temporal resolution. For example, the study by Nayak, et al. (65) described in section 2.2.1.1 used a water-selective spectral-spatial excitation pulse which had a duration of 7 ms, compared to the non-selective RF-pulse with duration 600 μs used in this work.

5.2.1.4 Saturation bands

Saturation bands could also be used to reduce the FOV by attenuating signal from spins outside the FOV. Saturation bands are created by applying 90^{o} spatially selective RF-pulses over the desired area(s), prior to the excitation pulse (140). These saturation pulses are followed by large dephasing gradients to create maximal phase dispersion across the saturated band. This results in minimal transverse magnetization in the saturation band during the subsequent readout, allowing a smaller FOV to be imaged without wrap. Saturation pulses are typically played out in every TR. Like selective RF-pulses, the use of saturation bands would decrease the resultant temporal resolution.

5.2.2 Speeding up the Reconstruction

The largest limitation found in all of the studies described in this work, were the long reconstruction times. These long reconstruction times mean that although the data is acquired rapidly, the user had to wait before the images could be viewed (~5 minutes in chapters 2 and 3, and ~30 seconds in chapter 4). This greatly limits the use of these sequences, as it is not clinically feasible to wait more than a few seconds for the images to reconstruct. Reconstruction times could be improved by the use of newer multi-processor graphics cards, which are well suited to complex iterative reconstructions.

Previous studies have shown the use of graphics cards (GPU's) for the speedup of complex reconstruction algorithms. Hansen, et al. (123) used a GPU to perform fast Cartesian SENSE and k-t SENSE reconstructions. The SENSE inversion step was shown to be up to 146 times faster on a GPU compared to a CPU. However, the total speedup achieved between a CPU reconstruction and a GPU reconstruction was in the order of 20 (due to the data transfer overhead cost).

Sørensen, et al. (101) have shown the use of GPU's for non-equispaced fast Fourier transform (NFFT). In this paper the NFFT was used for reconstruction of radial and spiral MRI data. For the NFFT algorithm the GPU implementation was found to be up to 85 times faster than a CPU implementation. However, the overall speedup in reconstruction time was in the order of 20.

Additionally, Sørensen, et al. have shown the use of GPUs for the reconstruction of real-time radial SENSE data in cardiac imaging, and real-time radial k-t SENSE data in speech imaging (141). The GPU NFFT gridding was found to be accurate compared to a CPU based NDFT (non-equispaced discrete Fourier transform): mean error; 0.0024 vs. 0.0022, respectively. The overall acceleration factor achieved using the GPU implementation was between 10-12, compared to the CPU reconstruction.

If an overall speed-up between 10-fold and 20-fold could be achieved for the studies described in this work, the reconstruction times for chapters 2 and 3 could be reduced from 5 minutes to ~15-30 seconds. This would make these techniques clinically useable.

At ICH, Grzegorz Kowalik has already developed a fully integrated platform within the MRI environment, to send raw data to a networked GPU. The complex reconstruction of MR data can be performed on the GPU and fed back to the scanner. At the moment this is used for T2 IDEAL (iterative decomposition of water and fat with echo asymmetry and least-squares estimation) (142), however we hope that in the near future an iterative CG SENSE algorithm can be implemented for a GPU reconstruction of undersampled spiral data.

5.2.3 4D Flow Measurements

Time-resolved 3D PCMR imaging using three-directional velocity encoding (known as *4D PCMR*), allows quantification of flow in any imaging plane, in addition to the visualization of complex flow patterns (143). However, 4D PCMR is rarely used in the clinical setting due to long acquisition times (144). As we have shown in this work, the use of efficient trajectories in addition to parallel imaging can greatly reduce the scan times in 2D PCMR. It may be possible to use efficient spiral trajectories, along with parallel imaging to greatly reduce the acquisition times for 4D PCMR.

Preliminary work has been carried out to develop a 4D PCMR sequence from the prospectively triggered spiral sequence described in chapter 4. A 3D volume is imaged using a slab-selective RF-excitation (to limit wrap in the z-direction) and an additional phase encode gradient is used on the z-axis to encode slice information (see Figure 5.3). The x and y gradients remain the same as described previously. Additionally, in each cardiac phase a flow-compensated readout plus the three flow-encoded readouts (one for each direction) were repeatedly acquired, as seen in Figure 5.3;

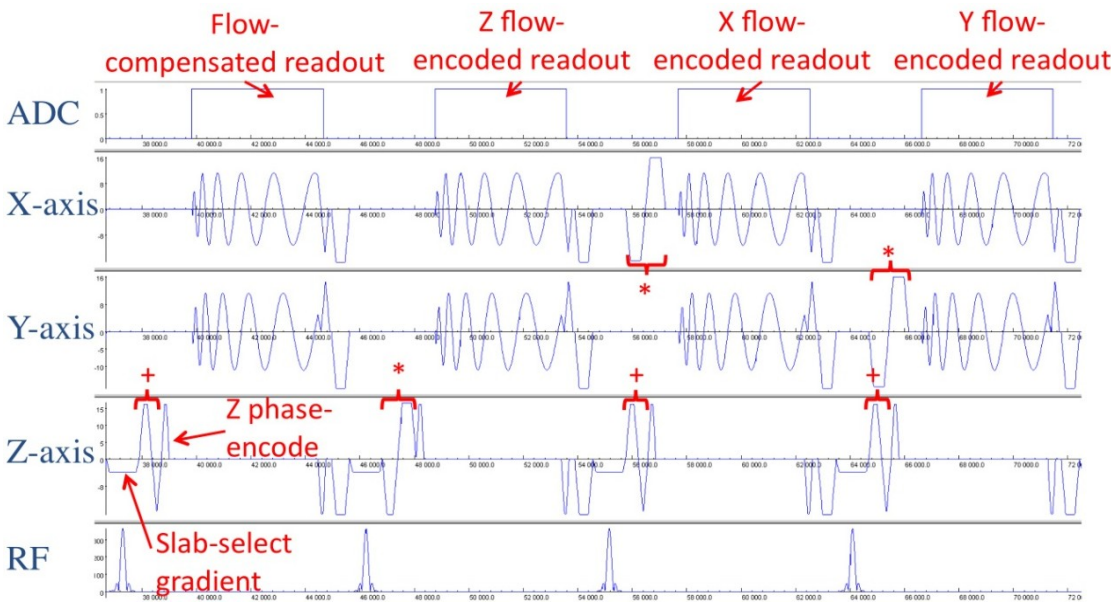

Figure 5.3: Sequence diagram for spiral 4D PCMR sequence. + indicates flow-compensated gradients, * indicates flow-encoding gradients

The sequence parameters used in these preliminary experiments were;

Sequence Parameters	
TE/TR	2.6/9.85 ms
Spiral interleaves	16
SENSE	4
Flip angle	25°
FOV	500×500×180 mm
Matrix	192×192
VENC	180 cm/sec
Temporal resolution	39.4 ms (~25 frames/sec)
Spatial resolution	2.6×2.6×5 mm

Table 5.1: Sequence parameters used for 4D PCMR sequence

Imaging was performed in the transverse plane, with 36, 5 mm thick slices. Two body coils and 2 spine coils were used (giving a total of 12 elements). Data was acquired during free-breathing, with 2 signal averages to reduce respiratory motion. In total data was acquired over 288 RR-intervals, giving a scan time of ~4 minutes.

The sampling pattern was rotated for each cardiac phase so that four consecutive cardiac phases comprised a fully-sampled k-space with 16 spiral readouts. The undersampled data was reconstructed online using an iterative SENSE algorithm (with a 3D reconstruction kernel). Coil sensitivity information was calculated for each slice, from the time-average of each coil (over all flow-compensated phases), divided by the sum-of-squares of the time-averaged coil data (for the respective slice). The reconstruction time was ~20 minutes.

There was a good agreement in stroke volumes measured in the descending Aorta between the 4D PCMR sequence and a standard 2D PCMR sequence, (51.5 ml/cycle vs. 53.2 ml/cycle), as seen in Figure 5.4.

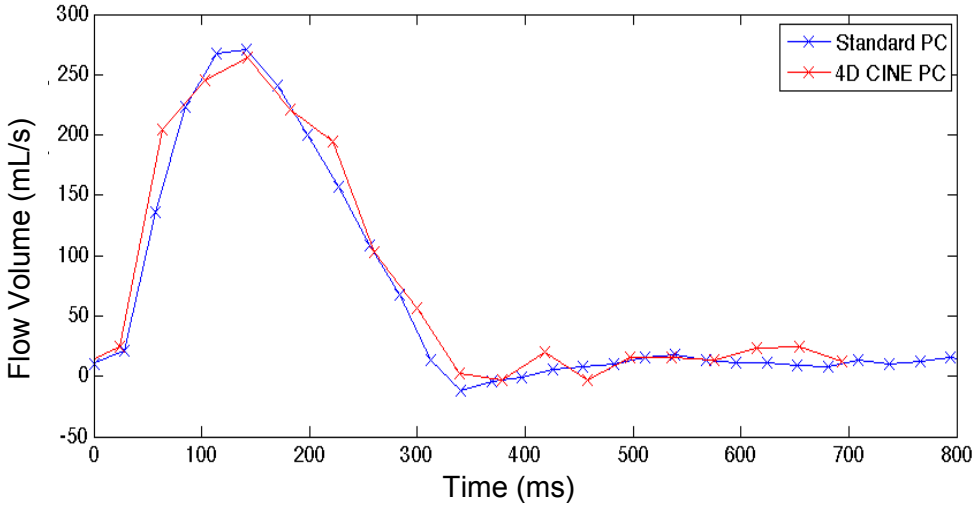

Figure 5.4: Comparison of flow profiles between standard PCMR and the 4D CINE PCMR sequence

Particle tracking was also performed in MATLAB, as shown in Figure 5.5;

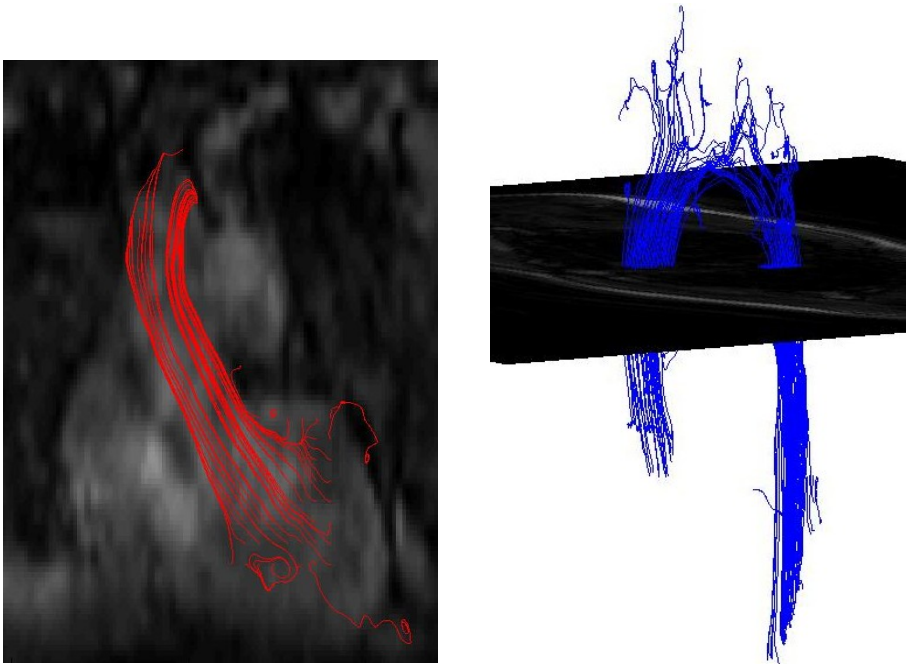

Figure 5.5: Streamlines from the 4D PCMR sequence performed in MATLAB. a) Streamlines seeded in the left ventricle, showing path through aorta, b) Streamlines seeded in the ascending and descending aorta, showing the aortic arch

By combining spiral readouts with 2D SENSE we were able to achieve high spatio-temporal resolution 4D PCMR, within a reasonable scan time. In this initial work no respiratory gating was used, nevertheless flow volumes and streamlines appear valid.

Further work is ongoing to implement respiratory navigation. Additionally acceleration in the slice direction may allow isotropic spatial resolution to be achieved without increasing the scan time.

5.2.4 Fourier Velocity Encoding and Fourier Acceleration Encoding

Standard PCMR averages blood velocity within each pixel and therefore tends to underestimate peak velocities. An alternative MR approach is Fourier Velocity Encoding (FVE), which acquires multiple phase contrast data sets with different velocity sensitivities. From this, a velocity spectrum and peak blood velocity can be reconstructed for each image pixel (40, 145, 146). Unfortunately FVE is not commonly used due to long acquisition times. With the use of undersampled spiral trajectories it may be possible to reduce the acquisition times of FVE, making this technique clinically useful.

Peak velocities measured using FVE could be used to calculate pressure using the modified Bernoulli equation (147). Measuring blood pressure gradients is vital in the evaluation of patients with valvular heart disease and vessel stenosis. These diseases are becoming more common as the population ages, with > 50 % of over 75 year olds having valvular heart disease.

The ‘gold standard’ method of measuring pressure gradients is invasive catheterization, however this is not practical as part of routine clinical management. Normally Doppler ultrasound measurements are used to calculate peak velocities however Doppler is limited by the restricted viewing angles and the penetration depth. Quantification of velocities using MRI is free from the restrictions of ultra-sound. Thus FVE MRI may represent a more robust, non-invasive method of measuring pressure drops.

Although FVE provides accurate measures of peak velocity, calculation of pressure gradients is still susceptible to the significant assumptions of the Bernoulli equation. A better approach would be to measure blood acceleration and use it as an input to the Navier-Stokes equation for the calculation of pressures (148). Acceleration could be computed from temporal and spatial derivatives of velocity, but this is subject to noise and requires multiple velocity measures for finite differencing (149).

A more accurate pressure calculation could be obtained from direct measures of acceleration, which is possible with MRI by using an extension of the phase contrast method (150). However, similar to phase contrast velocity MRI, this method would only provide average blood acceleration within each pixel. To measure peak acceleration, Fourier Acceleration Encoding (FAE) may be used (151), where multiple data sets with different acceleration encodings are acquired (149, 152).

To provide accurate pressure calculations from MRI data, future work may include:

- The development of a FVE sequence (with ~ 16 velocity sensitivities)
- The development of acceleration encoded PCMR sequence
- The development of a FAE sequence (with ~ 16 acceleration sensitivities)

To make these sequences clinically useful the acquisition times must be relatively short. This could be achieved using undersampled spiral trajectories, as described in this work. Validation of these sequences would be carried out in-vitro and in-vivo. Additionally the accuracy of pressure calculations from PCMR, FVE, acceleration PCMR, FAE and Doppler could be compared to invasive catheter manometers.

5.3 Conclusion

This thesis has investigated the use of novel acquisition strategies and reconstruction algorithms for PCMR. These studies have provided benefits to the research and clinical environment. For example, the real-time sequence in chapter 2 provides a novel method of researching the hemodynamic response to physical and mental stress using MRI. Additionally this real-time sequence can be used in the clinical environment in subjects with irregular heart-beats where conventional gated sequences fail.

The prospectively triggered sequence described in chapter 4 has had the largest clinical impact, providing high spatio-temporal resolution PCMR imaging in a short breath-hold. This allows a significant reduction in total scan time, improving patient compliance and increasing throughput. It is hoped that future work could continue to bring additional benefits to the clinical environment.

References

1. *F. Bloch, Nuclear induction. Physical review, 1946. **70**(7-8): p. 460.*
2. *E.M. Purcell, H.C. Torrey, and R.V. Pound, Resonance Absorption by Nuclear Magnetic Moments in a Solid. Physical review, 1946. **69**(1-2): p. 37.*
3. *P.C. Lauterbur, Image Formation by Induced Local Interactions: Examples Employing Nuclear Magnetic Resonance. Nature, 1973. **242**(5394): p. 190-191.*
4. *A N Garroway, P K Grannell, and P. Mansfield, Image formation in NMR by a selective irradiative process. Journal of Physics C: Solid State Physics, 1974. 7(24): p. L457.*
5. *K.T. Block and J. Frahm, Spiral imaging: A critical appraisal. Journal of Magnetic Resonance Imaging, 2005. **21**(6): p. 657-668.*
6. *G.H. Glover, Simple analytic spiral K-space algorithm. Magnetic Resonance in Medicine, 1999. **42**(2): p. 412-415.*
7. *C.H. Meyer, B.S. Hu, D.G. Nishimura, and A. Macovski, Fast Spiral Coronary Artery Imaging. Magnetic Resonance in Medicine, 1992. **28**(2): p. 202-213.*
8. *P.D. Gatehouse, D.N. Firmin, S. Collins, and D.B. Longmore, Real time blood flow imaging by spiral scan phase velocity mapping. Magnetic Resonance in Medicine, 1994. **31**(5): p. 504-512.*
9. *K.F. King, T. K. F. Foo, and C.R. Crawford, Optimized gradient waveforms for spiral scanning. Magnetic Resonance in Medicine, 1995. **34**(2): p. 156-160.*
10. *P. Boernert, H. Schomberg, B. Aldefeld, and J. Groen, Improvements in spiral MR imaging. Magma, 1999. **9**(1-2): p. 29.*
11. *J.D. O'Sullivan, A Fast Sinc Function Gridding Algorithm for Fourier Inversion in Computer Tomography. Medical Imaging, IEEE Transactions on, 1985. **4**(4): p. 200-207.*

12. *H. Schomberg and J. Timmer, The gridding method for image reconstruction by Fourier transformation. Medical Imaging, IEEE Transactions on, 1995.* ***14****(3): p. 596-607.*
13. *J.I. Jackson, C.H. Meyer, D.G. Nishimura, and A. Macovski, Selection of a convolution function for Fourier inversion using gridding [computerised tomography application]. Medical Imaging, IEEE Transactions on, 1991.* ***10****(3): p. 473-478.*
14. *K.P. Pruessmann, M.k. Weiger, P. Bornert, and P. Boesiger, Advances in sensitivity encoding with arbitrary k-space trajectories. Magnetic Resonance in Medicine, 2001.* ***46****(4): p. 638-651.*
15. *K.P. Pruessmann, M. Weiger, M.B. Scheidegger, and P. Boesiger, SENSE: Sensitivity encoding for fast MRI. Magnetic Resonance in Medicine, 1999.* ***42****(5): p. 952-962.*
16. *J. Tsao, P. Boesiger, and K.P. Pruessmann, k-t BLAST and k-t SENSE: Dynamic MRI with high frame rate exploiting spatiotemporal correlations. Magnetic Resonance in Medicine, 2003.* ***50****(5): p. 1031-1042.*
17. *P. Kellman, F.H. Epstein, and E.R. McVeigh, Adaptive sensitivity encoding incorporating temporal filtering (TSENSE). Magnetic Resonance in Medicine, 2001.* ***45****(5): p. 846-852.*
18. *D.K. Sodickson and W.J. Manning, Simultaneous acquisition of spatial harmonics (SMASH): Fast imaging with radiofrequency coil arrays. Magnetic Resonance in Medicine, 1997.* ***38****(4): p. 591-603.*
19. *M.A. Griswold, P.M. Jakob, R.M. Heidemann, M. Nittka, V. Jellus, J. Wang, B. Kiefer, and A. Haase, Generalized autocalibrating partially parallel acquisitions (GRAPPA). Magnetic Resonance in Medicine, 2002.* ***47****(6): p. 1202-1210.*
20. *F. Huang, J. Akao, S. Vijayakumar, G.R. Duensing, and M. Limkeman, k-t GRAPPA: A k-space implementation for dynamic MRI with high reduction factor. Magnetic Resonance in Medicine, 2005.* ***54****(5): p. 1172-1184.*
21. *M.A. Griswold, F. Breuer, M. Blaimer, S. Kannengiesser, R.M. Heidemann, M. Mueller, M. Nittka, V. Jellus, B. Kiefer, and P.M. Jakob, Autocalibrated coil sensitivity estimation for parallel imaging. NMR in Biomedicine, 2006.* ***19****(3): p. 316-324.*

22. C.A. McKenzie, E.N. Yeh, M.A. Ohliger, M.D. Price, and D.K. Sodickson, Self-calibrating parallel imaging with automatic coil sensitivity extraction. Magnetic Resonance in Medicine, 2002. **47**(3): p. 529-538.
23. Y. Qian, Z. Zhang, V.A. Stenger, and Y. Wang, Self-calibrated spiral SENSE. Magnetic Resonance in Medicine, 2004. **52**(3): p. 688-692.
24. K. Heberleins and X. Hu, Auto-calibrated parallel spiral imaging. Magnetic Resonance in Medicine, 2006. **55**(3): p. 619-625.
25. B. Madore, G.H. Glover, and N.J. Pelc, Unaliasing by Fourier-encoding the overlaps using the temporal dimension (UNFOLD), applied to cardiac imaging and fMRI. Magnetic Resonance in Medicine, 1999. **42**(5): p. 813-828.
26. J. Shewchuk, Conjugate gradient without the agonizing pain. 1994, Carnegie Mellon University: Pittsburgh.
27. M.T. Heath, Scientific Computing: An Introductory Survey. Second ed. 2002: McGraw-Hill.
28. M. Bydder, J.E. Perthen, and J. Du, Optimization of sensitivity encoding with arbitrary k-space trajectories. Magnetic Resonance Imaging, 2007. **25**(8): p. 1123-1129.
29. P.C. Hansen, Rank-deficient and discrete ill-posed problems: numerical aspects of linear inversion. 1998: Society for Industrial Mathematics.
30. L. Ying, D. Xu, and Z.P. Liang. On Tikhonov regularization for image reconstruction in parallel MRI. in Engineering in Medicine and Biology Society, 2004. IEMBS '04. 26th Annual International Conference of the IEEE. 2004.
31. K. King, SENSE image quality improvement using matrix regularization. Proceedings of the 9th Annual Meeting of ISMRM, Glasgow, Scotland, 2001: p. 1771.
32. F.H. Lin, K.K. Kwong, J.W. Belliveau, and L.L. Wald, Parallel imaging reconstruction using automatic regularization. Magnetic Resonance in Medicine, 2004. **51**(3): p. 559-567.
33. J. Tsao, K. Pruessmann, and P. Boesiger, Feedback Regularization for SENSE Reconstruction Proceedings of the 10th Annual Meeting of ISMRM, 2002. : p. 739.
34. D. Rosenfeld, New approach to gridding using regularization and estimation theory. Magnetic Resonance in Medicine, 2002. **48**(1): p. 193-202.

35. *H. Eggers and P. Boesiger, Improved Preconditioning for the Non-Cartesian SENSE Reconstruction with Regularization. Proceedings of the 11th Annual Meeting of ISMRM, Kyoto, 2004: p. 2409.*

36. *D. Firmin, J. Keegan, P. Gatehouse, P. Jhooti, and Y. Guang Zhong. Flow and motion: implications on cardiac MR. in Medical Imaging and Augmented Reality, 2001. Proceedings. International Workshop on. 2001.*

37. *M.A. Bernstein, K.F. King, and X.J. Zhou, Handbook of MRI Pulse Sequences. 2004: Elsevier Academic Press.*

38. *G.W. Lenz, E.M. Haacke, and R.D. White, Retrospective cardiac gating: A review of technical aspects and future directions. Magnetic Resonance Imaging, 1989. **7**(5): p. 445-455.*

39. *J.L. Duerk and O.P. Simonetti, Review of MRI gradient waveform design methods with application in the study of motion. Concepts in Magnetic Resonance, 1993. **5**(2): p. 105-122.*

40. *P.R. Moran, A flow velocity zeugmatographic interlace for NMR imaging in humans. Magnetic Resonance Imaging, 1982. **1**(4): p. 197-203.*

41. *G. Greil, T. Geva, S.E. Maier, and A.J. Powell, Effect of acquisition parameters on the accuracy of velocity encoded cine magnetic resonance imaging blood flow measurements. Journal of Magnetic Resonance Imaging, 2002. **15**(1): p. 47-54.*

42. *C. Tang, D. Blatter, D., and D. Parker, L. , Accuracy of phase-contrast flow measurements in the presence of partial-volume effects. Journal of Magnetic Resonance Imaging, 1993. **3**(2): p. 377-385.*

43. *M.A. Bernstein, X.J. Zhou, J.A. Polzin, K.F. King, A. Ganin, N.J. Pelc, and G.H. Glover, Concomitant gradient terms in phase contrast MR: Analysis and correction. Magnetic Resonance in Medicine, 1998. **39**(2): p. 300-308.*

44. *K. King, F., A. Ganin, X.J. Zhou, and M.A. Bernstein, Concomitant gradient field effects in spiral scans. Magnetic Resonance in Medicine, 1999. **41**(1): p. 103-112.*

45. *A. Chernobelsky, O. Shubayev, C.R. Comeau, and S.D. Wolff, Baseline Correction of Phase Contrast Images Improves Quantification of Blood Flow in the Great Vessels. Journal of cardiovascular magnetic resonance, 2007. **9**(4): p. 681-685.*

46. *T. Miller, A. Landes, and A. Moran, Improved accuracy in flow mapping of congenital heart disease using stationary phantom technique. Journal of cardiovascular magnetic resonance, 2009.* ***11****(1): p. 52.*

47. *A. Caprihan, S.A. Altobelli, and E. Benitez-Read, Flow-velocity imaging from linear regression of phase images with techniques for reducing eddy-current effects. Journal of Magnetic Resonance, 1990.* ***90****(1): p. 71-89.*

48. *J.-W. Lankhaar, M.B.M. Hofman, J.T. Marcus, J.J.M. Zwanenburg, T.J.C. Faes, and A. Vonk-Noordegraaf, Correction of phase offset errors in main pulmonary artery flow quantification. Journal of Magnetic Resonance Imaging, 2005.* ***22****(1): p. 73-79.*

49. *P. Gatehouse, M. Rolf, M. Graves, M. Hofman, J. Totman, B. Werner, R. Quest, Y. Liu, J. von Spiczak, M. Dieringer, D. Firmin, A. van Rossum, M. Lombardi, J. Schwitter, J. Schulz-Menger, and P. Kilner, Flow measurement by cardiovascular magnetic resonance: a multi-centre multi-vendor study of background phase offset errors that can compromise the accuracy of derived regurgitant or shunt flow measurements. Journal of cardiovascular magnetic resonance, 2010.* ***12****(1): p. 5.*

50. *J. Lotz, C. Meier, A. Leppert, and M. Galanski, Cardiovascular Flow Measurement with Phase-Contrast MR Imaging: A Basic Facts and Implementation. RadioGraphics, 2002.* ***22****(3): p. 651-671.*

51. *J. Keegan, D. Firmin, P. Gatehouse, and D. Longmore, The application of breath hold phase velocity mapping techniques to the measurement of coronary artery blood flow velocity: Phantom data and initial in vivo results. Magnetic Resonance in Medicine, 1994.* ***31****(5): p. 526-536.*

52. *B. Holland, B. Printz, and W. Lai, Baseline correction of phase-contrast images in congenital cardiovascular magnetic resonance. Journal of cardiovascular magnetic resonance, 2010.* ***12****(1): p. 11.*

53. *P.G. Walker, G.B. Cranney, M.B. Scheidegger, W. Gena, G.M. Pohost, and A.P. Yoganathan, Semiautomated method for noise reduction and background phase error correction in MR phase velocity data. Journal of Magnetic Resonance Imaging, 1993.* ***3****(3): p. 521-530.*

54. *Z. Chang and Q.-S. Xiang, Nonlinear phase correction with an extended statistical algorithm. Medical Imaging, IEEE Transactions on, 2005.* ***24****(6): p. 791-798.*

55. *E.H. Hardy, J.r. Hoferer, D. Mertens, and G. Kasper, Automated phase correction via maximization of the real signal. Magnetic Resonance Imaging, 2009.* ***27****(3): p. 393-400.*

56. *J.P. Singh, M.G. Larson, T.A. Manolio, C.J. O'Donnell, M. Lauer, J.C. Evans, and D. Levy, Blood Pressure Response During Treadmill Testing as a Risk Factor for New-Onset Hypertension : The Framingham Heart Study. Circulation, 1999.* ***99****(14): p. 1831-1836.*

57. *D.N. Firmin, G.L. Nayler, R.H. Klipstein, S.R. Underwood, R.S.O. Rees, and D.B. Longmore, In Vivo Validation of MR Velocity Imaging. Journal of Computer Assisted Tomography, 1987.* ***11****(5): p. 751-756.*

58. *P. Beerbaum, H. Korperich, P. Barth, H. Esdorn, J. Gieseke, and H. Meyer, Noninvasive Quantification of Left-to-Right Shunt in Pediatric Patients : Phase-Contrast Cine Magnetic Resonance Imaging Compared With Invasive Oximetry. Circulation, 2001.* ***103****(20): p. 2476-2482.*

59. *A.C. Van Rossum, F.C. Visser, K.H. Peels, J. Valk, and J.P. Roos, An in vivo validation of quantitative blood flow imaging in arteries and veins using magnetic resonance phase-shift techniques. European Heart Journal, 1991.* ***12****(2): p. 117.*

60. *W.G. Hundley, R.A. Lange, G.D. Clarke, B.M. Meshack, J. Payne, C. Landau, R. McColl, D.E. Sayad, D.L. Willett, J.E. Willard, L.D. Hillis, and R.M. Peshock, Assessment of Coronary Arterial Flow and Flow Reserve in Humans With Magnetic Resonance Imaging. Circulation, 1996.* ***93****(8): p. 1502-1508.*

61. *B. Beleslin, M. Ostojic, J. Stepanovic, A. Djordjevic-Dikic, S. Stojkovic, M. Nedeljkovic, G. Stankovic, Z. Petrasinovic, L. Gojkovic, and Z. Vasiljevic-Pokrajcic, Stress echocardiography in the detection of myocardial ischemia. Head- to-head comparison of exercise, dobutamine, and dipyridamole tests. Circulation, 1994.* ***90****(3): p. 1168-1176.*

62. *P.S. Nandi and D.H. Spodick, Recovery from exercise at varying work loads. Time course of responses of heart rate and systolic intervals. Br. Heart J., 1977.* ***39****(9): p. 958-966.*

63. *B. Hargreaves. http://mrsrl.stanford.edu/~brian/vdspiral/. 2001.*

64. *J.A. Steeden, D. Atkinson, A.M. Taylor, and V. Muthurangu, Assessing vascular response to exercise using a combination of real-time spiral phase*

*contrast MR and noninvasive blood pressure measurements. Journal of Magnetic Resonance Imaging, 2010. **31**(4): p. 997-1003.*

65. *K.S. Nayak, J.M. Pauly, A.B. Kerr, B.S. Hu, and D.G. Nishimura, Real-time color flow MRI. Magnetic Resonance in Medicine, 2000. **43**(2): p. 251-258.*
66. *C. Klein, S. Schalla, B. Schnackenburg, A. Bornstedt, E. Fleck, and E. Nagel, Magnetic resonance flow measurements in real time: Comparison with a standard gradient-echo technique. Journal of Magnetic Resonance Imaging, 2001. **14**(3): p. 306-310.*
67. *H. Korperich, J. Gieseke, P. Barth, R. Hoogeveen, H. Esdorn, A. Peterschroder, H. Meyer, and P. Beerbaum, Flow Volume and Shunt Quantification in Pediatric Congenital Heart Disease by Real-Time Magnetic Resonance Velocity Mapping: A Validation Study. Circulation, 2004. **109**(16): p. 1987-1993.*
68. *K.P. Pruessmann, M. Weiger, and P. Boesiger, Sensitivity encoded cardiac MRI. Journal of cardiovascular magnetic resonance, 2001. **3**(1): p. 1-9.*
69. *R. Nezafat, P. Kellman, A. Derbyshire, and E. McVeigh, R. , Real-time blood flow imaging using autocalibrated spiral sensitivity encoding. Magnetic Resonance in Medicine, 2005. **54**(6): p. 1557-1561.*
70. *R. Nezafat, P. Kellman, J.A. Derbyshire, and E.R. McVeigh, Real Time High Spatial-Temporal Resolution Flow Imaging with Spiral MRI using Auto-Calibrated SENSE. Engineering in Medicine and Biology Society, 2004. IEMBS '04. 26th Annual International Conference of the IEEE, 2004. **1**: p. 1914-1917.*
71. *D.S. Dymond, C. Foster, R.P. Grenier, J. Carpenter, and D.H. Schmidt, Peak exercise and immediate postexercise imaging for the detection of left ventricular functional abnormalities in coronary artery disease. The American Journal of Cardiology, 1984. **53**(11): p. 1532-1537.*
72. *H. Hecht, L. DeBord, N. Sotomayor, R. Shaw, R. Dunlap, and C. Ryan, Supine bicycle stress echocardiography: peak exercise imaging is superior to postexercise imaging. Journal of the American Society of Echocardiography, 1993. **6**(3): p. 265-271.*
73. *R.H. Mohiaddin, P.D. Gatehouse, and D.N. Firmin, Exercise-related changes in aortic flow measured with spiral echo-planar MR velocity mapping. Journal of Magnetic Resonance Imaging, 1995. **5**(2): p. 159-163.*

74. *E.M. Pedersen, S. Kozerke, S. Ringgaard, M.B. Scheidegger, and P. Boesiger, Quantitative abdominal aortic flow measurements at controlled levels of ergometer exercise. Magnetic Resonance Imaging, 1999.* ***17****(4): p. 489-494.*

75. *E.M. Pedersen, E.V. Stenbog, T. Frund, K. Houlind, O. Kromann, K.E. Srensen, K. Emmertsen, and V.E. Hjortdal, Flow during exercise in the total cavopulmonary connection measured by magnetic resonance velocity mapping. Heart, 2002.* ***87****(6): p. 554-558.*

76. *M. Jekic, E. Foster, M. Ballinger, S. Raman, and O. Simonetti, Cardiac function and myocardial perfusion immediately following maximal treadmill exercise inside the MRI room. Journal of cardiovascular magnetic resonance, 2008.* ***10****(1): p. 3.*

77. *C.A. Taylor, C.P. Cheng, L.A. Espinosa, B.T. Tang, D. Parker, and R.J. Herfkens, In Vivo Quantification of Blood Flow and Wall Shear Stress in the Human Abdominal Aorta During Lower Limb Exercise. Annals of biomedical engineering, 2002.* ***30****(3): p. 402-408.*

78. *C.P. Cheng, D.F. Schwandt, E.L. Topp, J.H. Anderson, R.J. Herfkens, and C.A. Taylor, Dynamic exercise imaging with an MR-compatible stationary cycle within the general electric open magnet. Magnetic Resonance in Medicine, 2003.* ***49****(3): p. 581-585.*

79. *C.P. Cheng, R.J. Herfkens, A.L. Lightner, C.A. Taylor, and J.A. Feinstein, Blood flow conditions in the proximal pulmonary arteries and vena cavae: healthy children during upright cycling exercise. Am J Physiol Heart Circ Physiol, 2004.* ***287****(2): p. H921-926.*

80. *C.P. Cheng, R.J. Herfkens, C.A. Taylor, and J.A. Feinstein, Proximal pulmonary artery blood flow characteristics in healthy subjects measured in an upright posture using MRI: The effects of exercise and age. Journal of Magnetic Resonance Imaging, 2005.* ***21****(6): p. 752-758.*

81. *A.S. Tenforde, C.P. Cheng, G.Y. Suh, R.J. Herfkens, R.L. Dalman, and C.A. Taylor, Quantifying in vivo hemodynamic response to exercise in patients with intermittent claudication and abdominal aortic aneurysms using cine phase-contrast MRI. Journal of magnetic Resonance Imaging, 2010.* ***31****(2): p. 425-429.*

82. *V.E. Hjortdal, K. Emmertsen, E. Stenbog, T. Frund, M.R. Schmidt, O. Kromann, K. Sorensen, and E.M. Pedersen, Effects of Exercise and*

Respiration on Blood Flow in Total Cavopulmonary Connection: A Real-Time Magnetic Resonance Flow Study. Circulation, 2003. ***108****(10): p. 1227-1231.*

83. *L.M. Pedersen, T.A.L. Pedersen, E.M. Pedersen, H. Hojmyr, K. Emmertsen, and V.E. Hjortdal, Blood flow measured by magnetic resonance imaging at rest and exercise after surgical bypass of aortic arch obstruction. Eur J Cardiothorac Surg, 2010.* ***37****(3): p. 658-661.*
84. *P. Gatehouse, J. Keegan, L. Crowe, S. Masood, R. Mohiaddin, K.-F. Kreitner, and D. Firmin, Applications of phase-contrast flow and velocity imaging in cardiovascular MRI. European Radiology, 2005.* ***15****(10): p. 2172-2184.*
85. *A.A.W. Roest, P. Kunz, H.J. Lamb, W.A. Helbing, E.E. van der Wall, and A.d. Roos, Biventricular response to supine physical exercise in young adults assessed with ultrafast magnetic resonance imaging. The American Journal of Cardiology, 2001.* ***87****(5): p. 601-605.*
86. *A.A.W. Roest, W.A. Helbing, P. Kunz, J.G. van den Aardweg, H.J. Lamb, H.W. Vliegen, E.E. van der Wall, and A. de Roos, Exercise MR Imaging in the Assessment of Pulmonary Regurgitation and Biventricular Function in Patients after Tetralogy of Fallot Repair. Radiology, 2002.* ***223****(1): p. 204-211.*
87. *P. Lurz, V. Muthurangu, S. Schievano, J. Nordmeyer, P. Bonhoeffer, A.M. Taylor, and M.S. Hansen, Feasibility and Reproducibility of Biventricular Volumetric Assessment of Cardiac Function During Exercise Using Real-Time Radial k-t SENSE Magnetic Resonance Imaging. Journal of Magnetic Resonance Imaging, 2009.* ***29****: p. 1062-1070.*
88. *V. Muthurangu, P. Lurz, J. Critchely, J. Deanfield, A. Taylor, and M.S. Hansen, Real-time Assessment of Right and Left Ventricular Volumes and Function in Patients with Congenital Heart Disease by Using High Spatiotemporal Resolution Radial k-t SENSE. Radiology, 2008.* ***248****(3): p. 782-791.*
89. *P. Segers, S. Brimioulle, N. Stergiopulos, N. Westerhof, R. Naeije, M. Maggiorini, and P. Verdonck, Pulmonary arterial compliance in dogs and pigs: the three-element windkessel model revisited. Am J Physiol Heart Circ Physiol, 1999.* ***277****(2): p. 725-731.*
90. *Z. Liu, K.P. Brin, and F.C. Yin, Estimation of total arterial compliance: an improved method and evaluation of current methods. Am J Physiol Heart Circ Physiol, 1986.* ***251****(3): p. 588-600.*

91. *V. Muthurangu, A. Taylor, R. Andriantsimiavona, S. Hegde, M.E. Miquel, R. Tulloh, E. Baker, D.L.G. Hill, and R.S. Razavi, Novel Method of Quantifying Pulmonary Vascular Resistance by Use of Simultaneous Invasive Pressure Monitoring and Phase-Contrast Magnetic Resonance Flow. Circulation, 2004.* ***110****: p. 826-834.*

92. *V. Muthurangu, D. Atkinson, M. Sermesant, M.E. Miquel, S. Hegde, R. Johnson, R. Andriantsimiavona, A.M. Taylor, E. Baker, R. Tulloh, D. Hill, and R.S. Razavi, Measurement of total pulmonary arterial compliance using invasive pressure monitoring and MR flow quantification during MR-guided cardiac catheterization. AJP - Heart and Circulatory Physiology 2005.* ***289****: p. 1301-1306.*

93. *V.S. Lee, C.E. Spritzer, B.A. Carroll, L.G. Pool, M.A. Bernstein, S.K. Heinle, and J.R. MacFall, Flow quantification using fast cine phase-contrast MR imaging, conventional cine phase-contrast MR imaging, and Doppler sonography: in vitro and in vivo validation. Am. J. Roentgenol., 1997.* ***169****(4): p. 1125-1131.*

94. *A.J. Evans, F. Iwai, T.A. Grist, H.D. Sostman, L.W. Hedlund, C.E. Spritzer, R. Negro-vilar, C.A. Beam, and N.J. Pelc, Magnetic Resonance Imaging of Blood Flow with a Phase Subtraction Technique: In Vitro and In Vivo Validation. Investigative Radiology, 1993.* ***28****(2): p. 109-115.*

95. *M.F. Wilson, B.H. Sung, G.A. Pincomb, and W.R. Lovallo, Exaggerated pressure response to exercise in men at risk for systemic hypertension. The American Journal of Cardiology, 1990.* ***66****(7): p. 731-736.*

96. *E. Raaijmakers, T.J.C. Faes, R.J.P.M. Scholten, H.G. Goovaerts, and R.M. Heethaar, A meta-analysis of three decades of validating thoracic impedance cardiography. Critical Care Medicine, 1999.* ***27****(6): p. 1203-1213.*

97. *H. Sakuma, N. Kawada, H. Kubo, Y. Nishide, K. Takano, N. Kato, and K. Takeda, Effect of breath holding on blood flow measurement using fast velocity encoded cine MRI. Magnetic Resonance in Medicine, 2001.* ***45****(2): p. 346-348.*

98. *M.H. Frick and T. Somer, Base-line effects on response of stroke volume to leg exercise in the supine position. J Appl Physiol, 1964.* ***19****(4): p. 639-643.*

99. *Y. Ichihara, J. Ohno, M. Suzuki, T. Anno, M. Ugino, and K. Nagata, Blunt circulatory response to exercise in coronary high-risk subjects among*

apparently healthy Japanese. Circulation journal: A official journal of the Japanese Circulation Society, 2004. ***68****(4): p. 286-293.*

100. *M.S. Hansen, C. Baltes, J. Tsao, S. Kozerke, K.P. Pruessmann, and H. Eggers, k-t BLAST reconstruction from non-Cartesian k-t space sampling. Magnetic Resonance in Medicine, 2006.* ***55****(1): p. 85-91.*
101. *T.S. Sorensen, T. Schaeffter, K.O. Noe, and M.S. Hansen, Accelerating the Nonequispaced Fast Fourier Transform on Commodity Graphics Hardware. Medical Imaging, IEEE Transactions on, 2008.* ***27****(4): p. 538-547.*
102. *K. Mortensen, J. Steeden, J. Panzer, A. Taylor, and V. Muthurangu, Isometric exercise in cardiac magnetic resonance imaging: an initial experience using fast imaging. Journal of cardiovascular magnetic resonance, 2011.* ***13****(Suppl 1): p. P386.*
103. *D.J. Burkart, J.P. Felmlee, C.D. Johnson, R.L. Wolf, A.L. Weaver, and R.L. Ehman, Cine phase-contrast MR flow measurements: improved precision using an automated method of vessel detection. J. Comput Assist Tomogr, 1994.* ***18****: p. 469-475.*
104. *A. Lalande, P.K. van Kien, N. Salvé, D.B. Salem, L. Legrand, P.M. Walker, J.E. Wolf, and F. Brunotte, Automatic determination of aortic compliance with cine-magnetic resonance imaging: an application of fuzzy logic theory. Invest Radiol, 2002.* ***37****(685-691): p. 685.*
105. *S. Kozerke, R. Botnar, S. Oyre, M.B. Scheidegger, E.M. Pedersen, and P. Boesiger, Automatic vessel segmentation using active contours in cine phase contrast flow measurements. Journal of magnetic Resonance imaging, 1999.* ***10****: p. 41-51.*
106. *S. Oyre, S. Ringgaard, S. Kozerke, W.P. Paaske, M.B. Scheidegger, P. Boesiger, and E.M. Pedersen, Quantitation of circumferential subpixel vessel wall position and wall shear stress by multiple sectored three-dimensional paraboloid modeling of velocity encoded cine MR. Magnetic Resonance in Medicine, 1998.* ***40****: p. 645-655.*
107. *F. Odille, J. Steeden, V. Muthurangu, and D. Atkinson, Automatic Segmentation Propagation of the Aorta in Real-Time Phase Contrast MRI using Nonrigid Registration. Journal of Magnetic Resonance Imaging, 2011.* ***33****(1): p. 232-238.*

108. *L.R. Dice, Measures of the amount of ecologic association between species. Ecology, 1945.* ***26****: p. 297-302.*

109. *A. Jones, J. Steeden, J. Pruessner, A. Taylor, A. Deanfield, and V. Muthurangu, Detailed Assessment of The Hemodynamic Response to Psychosocial Stress using Real-Time MRI. Journal of Magnetic Resonance Imaging, 2011.* ***33****(2): p. 448-454.*

110. *K. Dedovic, R. Renwick, N.K. Mahani, V. Engert, S.J. Lupien, and J.C. Pruessner, The Montreal Imaging Stress Task: using functional imaging to investigate the effects of perceiving and processing psychosocial stress in the human brain. J Psychiatry Neurosci, 2005.* ***30****(5): p. 319-325.*

111. *J.A. Steeden, D. Atkinson, A.M. Taylor, and V. Muthurangu, Split-Acquisition Real-time CINE Phase-Contrast MR Flow Measurements Magnetic Resonance in Medicine, 2010.* ***64****(6): p. 1664-1670.*

112. *L.-C. Man, J.M. Pauly, D.G. Nishimura, and A. Macovski, Nonsubtractive spiral phase contrast velocity imaging. Magnetic Resonance in Medicine, 1999.* ***42****(4): p. 704-713.*

113. *J.-F. Nielsen and K.S. Nayak, Referenceless phase velocity mapping using balanced SSFP. Magnetic Resonance in Medicine, 2009.* ***61****(5): p. 1096-1102.*

114. *R.H. Mohiaddin, P.D. Gatehouse, J.C.C. Moon, M. Youssuffidin, G.Z. Yang, D.N. Firmin, and D.J. Pennell, Assessment of Reactive Hyperaemia Using Real Time Zonal Echo-Planar Flow Imaging. Journal of cardiovascular magnetic resonance, 2002.* ***4****(2): p. 283-287.*

115. *K.S. Nayak and B.S. Hu, Triggered real-time MRI and cardiac applications. Magnetic Resonance in Medicine, 2003.* ***49****(1): p. 188-192.*

116. *A.C. Larson, R.D. White, G. Laub, E.R. McVeigh, D. Li, and O.P. Simonetti, Self-gated cardiac cine MRI. Magnetic Resonance in Medicine, 2004.* ***51****(1): p. 93-102.*

117. *C.J. Bakker, J.H. Seppenwoolde, L.W. Bartels, and R. van der Weide, Adaptive subtraction as an aid in MR-guided placement of catheters and guidewires. Journal of Magnetic Resonance Imaging, 2004.* ***20****(3): p. 470-474.*

118. *O. Dietrich, J.G. Raya, S.B. Reeder, M.F. Reiser, and S.O. Schoenberg, Measurement of signal-to-noise ratios in MR images: Influence of multichannel coils, parallel imaging, and reconstruction filters. Journal of Magnetic Resonance Imaging, 2007.* ***26****(2): p. 375-385.*

119. *J.M. Bland and D.G. Altman, Statistical methods for assessing agreement between two methods of cliical measurement. Lancet, 1986.* ***i****: p. 307-310.*

120. *P. Lanzer, E. Botvinick, N. Schiller, L. Crooks, M. Arakawa, L. Kaufman, P. Davis, R. Herfkens, M. Lipton, and C. Higgins, Cardiac imaging using gated magnetic resonance. Radiology, 1984.* ***150****(1): p. 121-127.*

121. *P. Kellman, C. Chefd'hotel, C.H. Lorenz, C. Mancini, A.E. Arai, and E.R. McVeigh, Fully automatic, retrospective enhancement of real-time acquired cardiac cine MR images using image-based navigators and respiratory motion-corrected averaging. Magnetic Resonance in Medicine, 2008.* ***59****(4): p. 771-778.*

122. *P. Beerbaum, H. Körperich, J. Gieseke, P. Barth, M. Peuster, and H. Meyer, Blood flow quantification in adults by phase-contrast MRI combined with SENSE--a validation study. Journal of cardiovascular magnetic resonance, 2005.* ***7****(2): p. 361-369.*

123. *M.S. Hansen, D. Atkinson, and T.S. Sorensen, Cartesian SENSE and k-t SENSE reconstruction using commodity graphics hardware. Magnetic Resonance in Medicine, 2008.* ***59****(3): p. 463-468.*

124. *S. Rees, D. Firmin, R. Mohiaddin, R. Underwood, and D. Longmore, Application of flow measurements by magnetic resonance velocity mapping to congenital heart disease. The American Journal of Cardiology, 1989.* ***64****(14): p. 953-956.*

125. *J.A. Steeden, D. Atkinson, A.M. Taylor, and V. Muthurangu, Rapid Flow Assessment of Congenital Heart Disease Using High Spatio-Temporal Gated Spiral Phase Contrast MR. Radiology, 2010.* ***In Press****.*

126. *P. Beerbaum, H. Korperich, J. Gieseke, P. Barth, M. Peuster, and H. Meyer, Rapid Left-to-Right Shunt Quantification in Children by Phase-Contrast Magnetic Resonance Imaging Combined With Sensitivity Encoding (SENSE). Circulation, 2003.* ***108****(11): p. 1355-1361.*

127. *A. Prakash, R. Garg, E.N. Marcus, G. Reynolds, T. Geva, and A.J. Powell, Faster flow quantification using sensitivity encoding for velocity-encoded cine magnetic resonance imaging: In vitro and in vivo validation. Journal of Magnetic Resonance Imaging, 2006.* ***24****(3): p. 676-682.*

128. C.D. Lew, M.T. Alley, R. Bammer, D.M. Spielman, and F.P. Chan, Peak Velocity and Flow Quantification Validation for Sensitivity-Encoded Phase-Contrast MR Imaging. Academic Radiology, 2007. **14**(3): p. 258-269.

129. Y. Zur, M.L. Wood, and L.J. Neuringer, Spoiling of transverse magnetization in steady-state sequences. Magnetic Resonance in Medicine, 1991. **21**(2): p. 251-263.

130. C. Molar, Interpolation, in Numerical Computing with MATLAB. 2004, SIAM.

131. A. Savitzky and M.J.E. Golay, Smoothing and Differentiation of Data by Simplified Least Squares Procedures. Analytical Chemistry, 1964. **36**(8): p. 1627-1639.

132. F. Faul, E. Erdfelder, A.-G. Lang, and A. Buchner, G*power 3: A flexible statistical power analysis program for the social, behavioral, and biomedical sciences. Behavior Research Methods, 2007. **39**(2): p. 175-191.

133. A.J. Powell, S.E. Maier, T. Chung, and T. Geva, Phase-Velocity Cine Magnetic Resonance Imaging Measurement of Pulsatile Blood Flow in Children and Young Adults: In Vitro and In Vivo Validation. Pediatric Cardiology, 2000. **21**(2): p. 104-110.

134. R. Frayne, D.A. Steinman, B.K. Rutt, and C.R. Ethier, Accuracy of MR phase contrast velocity measurements for unsteady flow. Journal of Magnetic Resonance Imaging, 1995. **5**(4): p. 428-431.

135. D. Meier, S. Maier, and P. Bösiger, Quantitative flow measurements on phantoms and on blood vessels with MR. Magnetic Resonance in Medicine, 1988. **8**(1): p. 25-34.

136. M.A. Ohliger and D.K. Sodickson, An introduction to coil array design for parallel MRI. NMR in Biomedicine, 2006. **19**(3): p. 300-315.

137. Accusorb. http://www.magmedix.com/default.htm. 2006.

138. P. Börnert and B. Aldefeld, On spatially selective RF excitation and its analogy with spiral MR image acquisition. Magnetic Resonance Materials in Physics, Biology and Medicine, 1998. 7(3): p. 166-178.

139. C.H. Meyer, J.M. Pauly, A. Macovskiand, and D.G. Nishimura, Simultaneous spatial and spectral selective excitation. Magnetic Resonance in Medicine, 1990. **15**(2): p. 287-304.

140. *J.P. Felmlee and R.L. Ehman, Spatial presaturation: a method for suppressing flow artifacts and improving depiction of vascular anatomy in MR imaging. Radiology, 1987.* ***164****(2): p. 559-564.*

141. *T.S. Sorensen, D. Atkinson, T. Schaeffter, and M.S. Hansen, Real-Time Reconstruction of Sensitivity Encoded Radial Magnetic Resonance Imaging Using a Graphics Processing Unit. Medical Imaging, IEEE Transactions on, 2009.* ***28****(12): p. 1974-1985.*

142. *H. Yu, C.A. McKenzie, A. Shimakawa, A.T. Vu, A.C.S. Brau, P.J. Beatty, A.R. Pineda, J.H. Brittain, and S.B. Reeder, Multiecho reconstruction for simultaneous water-fat decomposition and T2* estimation. JOURNAL OF MAGNETIC RESONANCE IMAGING, 2007.* ***26****(4): p. 1153-1161.*

143. *M. Markl, F.P. Chan, M.T. Alley, K.L. Wedding, M.T. Draney, C.J. Elkins, D.W. Parker, R. Wicker, C.A. Taylor, R.J. Herfkens, and N.J. Pelc, Time-resolved three-dimensional phase-contrast MRI. Journal of Magnetic Resonance Imaging, 2003.* ***17****(4): p. 499-506.*

144. *D.N. Firmin, P.D. Gatehouse, J.P. Konrad, G.Z. Yang, P.J. Kilner, and D.B. Longmore. Rapid 7-dimensional imaging of pulsatile flow. in Computers in Cardiology 1993, Proceedings. 1993.*

145. *J. Carvalho, J. Nielsen, and K. Nayak, Validation of the spiral Fourier velocity encoding method. Journal of cardiovascular magnetic resonance, 2008.* ***10****(Suppl 1): p. A403.*

146. *C. Baltes, M.S. Hansen, J. Tsao, S. Kozerke, R. Rezavi, E.M. Pedersen, and P. Boesiger, Determination of Peak Velocity in Stenotic Areas: Echocardiography versus kt SENSE Accelerated MR Fourier Velocity Encoding. Radiology, 2007.* ***246****(1): p. 249.*

147. *N.B. Wood, Aspects of Fluid Dynamics Applied to the Larger Arteries. Journal of Theoretical Biology, 1999.* ***199****(2): p. 137-161.*

148. *J.-P. Tasu, O. Jolivet, and J. Bittoun, From flow to pressure: estimation of pressure gradient and derivative by MR acceleration mapping. Magnetic Resonance Materials in Physics, Biology and Medicine, 2000.* ***11****(1): p. 55-57.*

149. *F. Balleux-Buyens, O. Jolivet, J. Bittoun, and A. Hermet, Velocity encoding versus acceleration encoding for pressure gradient estimation in MR haemodynamic studies. Physics in Medicine and Biology, 2006.* ***51****(19): p. 4747.*

150. *J.-P. Tasu, O. Jolivet, E. Mousseaux, A. Delouche, B. Diebold, and J. Bittoun, Acceleration mapping by fourier acceleration-encoding: in vitro study and initial results in the great thoracic vessels. Magnetic Resonance in Medicine, 1997.* ***38****(1): p. 110-116.*

151. *J. Bittoun, O. Jolivet, A. Herment, E. Itti, E. Durand, E. Mousseaux, and J.P. Tasu, Multidimensional MR mapping of multiple components of velocity and acceleration by fourier phase encoding with a small number of encoding steps. Magnetic Resonance in Medicine, 2000.* ***44****(5): p. 723-730.*

152. *J.-P. Tasu, E. Mousseaux, P. Colin, M.S. Slama, O. Jolivet, and J. Bittoun, Estimation of left ventricular performance through temporal pressure variations measured by MR velocity and acceleration mappings. Journal of Magnetic Resonance Imaging, 2002.* ***16****(3): p. 246-252.*